UNIVERSITY OF CAPE TOWN
IYUNIVESITHI YASEKAPA • UNIVERSITEIT VAN KAAPSTAD

The Response of Partially-confined Right-circular Cylinders to Internal Blast Loading

Thesis presented in partial fulfilment of the requirements
of the degree MSc (Mechanical Engineering)

Adam Ozinsky

Supervisor
A/Prof Genevieve Langdon

10 December 2012

Blast Impact and Survivability Research Unit
Department of Mechanical Engineering
University of Cape Town

Abstract

This report presents results of an experimental and numerical investigation into the response of partially-confined, thin-walled, stainless steel cylinders subjected to internal blast loading. "Partial-confinement" refers to an enclosure that may retain a significant, quasi-static pressure following an internal explosion, while "thin-walled" implies that the cylinder wall thickness is small relative to other geometric dimensions. The cylinder deformation is used to gauge the level of blast damage.

The chosen cylinders are of length $l = 300$mm, inner radius $a = 150$mm, and wall thickness $h = 2$mm, and cut from seamless 304 stainless steel pipe. Partial-confinement is achieved by keeping one end of the cylinders closed in all tests.

The experimental tests are conducted on the horizontal ballistic pendulum at the Blast Impact and Survivability Research Unit (BISRU), University of Cape Town. The blasts are generated by detonating radially-centred, spherical PE4 charges inside the cylinders.

The charge mass is varied between 20g and 75g at two axial charge positions, specifically 150mm and 225mm, relative to the closed end. These axial positions are denoted $0.5l$ and $0.75l$ respectively. Polystyrene annuli are used to position the charges within the cylinders, and the influence of this polystyrene on the cylinder deformation is briefly investigated as an additional parameter.

Details are presented of the development of an LS-DYNA Release 6.0.0 computational model that simulates the cylinder response to blast loading. Several 1D and 2D preliminary simulations and convergence studies are presented, the results of which inform the mesh sizes in the final model. The air and explosive are modelled using solid Arbitrary-Lagrange-Euler (ALE) elements, and the cylinders are modelled using Lagrange solids. Since the cylinders and explosive are all circular in section, the simulations are performed in 2D axisymmetry to reduce computational expense.

The maximum cylinder deflections and selected final profiles, as well as the impulses imparted to the pendulum, are compared to the corresponding experimental results. With the exception of the $0.75l$ tests at larger charge masses, the results exhibit generally good experimental-simulation correlation.

For the $0.5l$ tests, the cylinders exhibit a linear increase in deformation with increasing charge mass, while the relationship is an exponential increase for the $0.75l$ axial charge position. For charges below 45g, the deformations from both axial charge positions are similar, however the responses diverge with increasing charge mass, indicating that the confinement effect of the cylinders is a function of the axial position and is influential only beyond a given mass of explosive. This confinement effect is greater when the charge is located nearer the open end of the cylinder.

The computational models provide insight into the transient behaviour of the systems which cannot be achieved experimentally. The influence of the charge position is confirmed by comparing the simulated deformation-time histories for the different axial charge positions.

Two pressure fronts are evident in the simulations: one moving radially and one axially. The significant structural damage is caused by the radial pressure incident on the cylinder wall, while the laterally moving pressure drives gas out from the open end. In the case of the $0.75l$ simulations, the pressure incident on the cylinder wall has longer to act before it is expelled by the laterally moving pressure. For higher charge masses, the high pressure acting during this additional time is the cause of late-time deformation.

Two tests are performed using a half-annulus of polystyrene. Relative to the other tests, these two exhibit greater radial disparity, with the deformation biased to the side *with* polystyrene. This preliminary result suggests that placing polystyrene between the charge and the cylinder increases the structural deformation, and necessitates further investigation.

Declaration

I know the meaning of plagiarism and declare that all the work in this document, save for that which is properly acknowledged, is my own.

Signed by candidate

Adam Ozinsky
10 December 2012

Acknowledgements

The author would like to thank the following people for their significant contributions to the present work:

- A/Prof Genevieve Langdon for her considerable effort in supervising this project, and her willingness to find time regardless of her numerous commitments and the often-late notice. It has been a pleasure to work with you.
- Prof Gerald Nurick for his overall guidance and genuine care.
- Dr Steeve Chung Kim Yuen for his help during the initial testing and his constant advice around the laboratory.
- Carlo Geretto for his introduction to LS-DYNA and much support that followed.
- Trevor Cloete, Richard Curry and Victor Balden for expending much effort on trying to make high strain rate tensile testing of the curved cylinder specimens a reality. Unfortunately this did not happen, though your willingness to engage on any topic is appreciated.
- Erik Pickering for always being willing to help and share his experience.
- Gregory Sinclair for his steadfast moral advice and unwavering assistance, and for his skill in drawing many of the shock phenomena images in the present work. You have been a true help.
- Wei-chi Lee and Travis Henchie for being supportive office mates.
- Stanley Johannes for cutting many cylinders and specimens. The contributions of the other workshop staff, particularly Glen Newins and Pierre Smith, are also acknowledged.
- The National Research Foundation (NRF) and UCT University Research Council for their significant financial support of the present work.

Table of Contents

List of Tables

List of Figures

Chapter 1

Introduction

A brief background to the present work is presented in this section, followed by the objectives and outline of this report.

1.1 Background

The risk of explosions, occurring as a result of a terrorist attack, accidentally in industry, or otherwise, is a real and dangerous possibility. Regardless of the source or reason for the explosion, the loading imposed on structures occurs significantly more quickly than the quasi-static loads for which most structures have typically been designed. Consequently, owing to the different nature of the loading, the resulting structural responses and damage mechanisms are of concern.

Such an explosion may be broadly classed as confined or unconfined, depending on the geometry of the structure in which it occurs. A confined explosion is regarded as an explosion occurring in any volume in which there exists a significant, long-term accumulation of gas pressure, for example subway tunnels, shipping containers, and litter bins. Silvestrini et al [1] have shown that explosions in (partially-)confined spaces lead to the concentration of explosive energy that would be hundreds of times greater than that in an unconfined explosion. This makes such structures attractive as terror targets as the level of damage may be significantly magnified compared to a similar unconfined explosion, with recent terrorist attacks on subway systems in London and Madrid being grave reminders of the consequences. This threat has been realised as evidenced by the on-going removal of litter bins from high-risk public spaces, particularly transport hubs [2–4].

The potential damage from such explosions could be further mitigated by better understanding the response of simple confined geometries to internal blast loading. Research in this field has in the past been predominantly experimental, where scale and expense are significant limiting factors. However the relatively recent improvement in numerical codes and computational power, presents a quicker, lower-cost opportunity to gain insight into the behaviour of such systems.

A series of experiments is performed to investigate the structural response of partially-confined (one end open, one end closed), thin-walled, right-circular cylinders to internal blast loading. Such a configuration is chosen to approximately simulate a simple case of a bomb in a bin-like structure. The effects of the mass of explosive and the axial charge position within the structure on the response of the cylinders are considered.

The experimental programme is simulated in LS-DYNA to gain insight into the transient behaviour of the systems that is not attainable solely from the experiments. Particularly, the behaviour of the pressure inside the cylinders and the influence of the axial position of the explosive charge are of interest. The results of the simulations are validated against the experimentally-measured diametric deformation of the cylinders, as well as the impulse imparted to the systems during testing.

All work in this report is undertaken at the Blast Impact and Survivability Research Unit

(BISRU), University of Cape Town. The principle objectives of this work are summarised here:

- investigate experimentally the effect of the mass of explosive and axial charge position on the structural response of partially-confined cylinders
- develop a robust computational model to simulate both the loading and structural response of the systems
- validate the computational model by comparing its results with those measured experimentally
- use both the experimental and simulated results to comment on the behaviour of the systems.

1.2 Report outline

This report takes the following structure:

- Literature Review (Chapter 2)
  - Review of general shock wave and blasting phenomena
  - Review of pressure behaviour and structural response due to confined explosions
- Preliminary Analytical Modelling (Chapter 3)
  - Review and modification of Benham and Duffey [5] analytical solution
  - Cylinder geometry and material selection for the present work
- Experimental Details and Results (Chapter 4)
  - Details of experimental programme
  - Results from experimental programme
- Numerical Details and Results (Chapter 5)
  - General formulations used for all simulations
  - Mesh convergence and other preliminary simulations
  - Details of the final numerical model for the present work
  - Results from simulations
- Discussion (Chapter 6)
  - Correlation of experimental and simulated results
  - Effect of axial charge position on structural response and pressure behaviour
  - Comparison of results with modified analytical solution
  - Early insight into the effect of polystyrene annuli on structural response
- Conclusions (Chapter 7)
  - Validity of experimental and numerical set ups
  - Effect of tested parameters on structural response
- Recommendations
- References

- Appendices
  - Derivation of pendulum-impulse theory
  - Details on material characterisation
  - Drawings for test rig design
  - Ethics declaration

Chapter 2

Literature Review

This section presents general background to the present work, followed by an overview of several key works pertaining to the pressure behaviour and structural response due to confined explosions.

2.1 Explosions

Baker [6] referred to an explosion as a process during which a rapid release of energy generates a pressure wave of finite amplitude. The source of the energy is unimportant, but the release must be so rapid as to cause a local accumulation of energy at the site of the explosion [7]. In order for the energy release to be classified as an explosion, Martin et al [8] required that a significant quantity of work pV is done on the environment and this can only occur if a gas is involved. The magnitude of an explosion is defined by the amount of energy released during the explosion and is typically expressed in joules J.

Explosions may be classified as being physical, nuclear or chemical depending on the source. Physical explosions occur as the result of a physical process, for example the bursting of a pressure vessel. Nuclear explosions are caused by the redistribution of subatomic particles in the interaction between nuclei. The most well known of such explosions are the nuclear fission and fusion processes. Chemical explosions occur as the result of either a decomposition or combination chemical reaction. An example of a chemical explosion is the detonation of an explosive material like Trinitrotoluene (TNT) [9,10]. Such explosions are considered in the present work.

2.2 Shock phenomena

Cooper [11] presents an overview of shock phenomena. The concepts relevant to the current work are presented in this section.

2.2.1 Characteristics of shock waves

The compressive stress-strain behaviour of most materials exhibits three regions: elastic behaviour at relatively low strains, elastic-plastic combined behaviour at intermediate strains, and plastic behaviour at higher strains. For shock applications, materials typically exhibit plastic flow behaviour, similar to a fluid [11].

The sound velocity of a material is proportional to the ratio of pressure P and density ρ and is given by

$$C = \sqrt{\frac{\mathrm{d}P}{\mathrm{d}\rho}} \tag{2.1}$$

In the elastic region the sound velocity is constant, which defines a linear relationship between pressure and density. However in the plastic region, the sound velocity increases with pressure or density, so that pressure and density are no longer linearly related. The increase in sound velocity with increasing pressure has major implications in shock dynamics [11].

Figure 2.1 shows three points of interest on a typical pressure wave in the plastic region. At each point we refer to the sound, particle and pressure wave velocities, where the wave velocity is equal to the sum of the other two. At point 'A' the pressure is low and by Equation 2.1 the sound velocity is similarly low. The local material speed, referred to as the particle velocity, is also fairly low resulting in a low wave velocity [11]. At point 'B', the pressure is higher than at 'A' giving a higher sound velocity. The particle velocity is also higher at 'B' and consequently the pressure wave is travelling faster at 'B' than it is at 'A'. For the same reasons, the wave is travelling fastest at point 'C'. The result of the wave velocity discrepancies, is that the upper section of the pressure wave catches up to the lower section. The wave eventually assumes a vertical front and this is known as a shock wave. This changing wave front is shown in Figure 2.2.

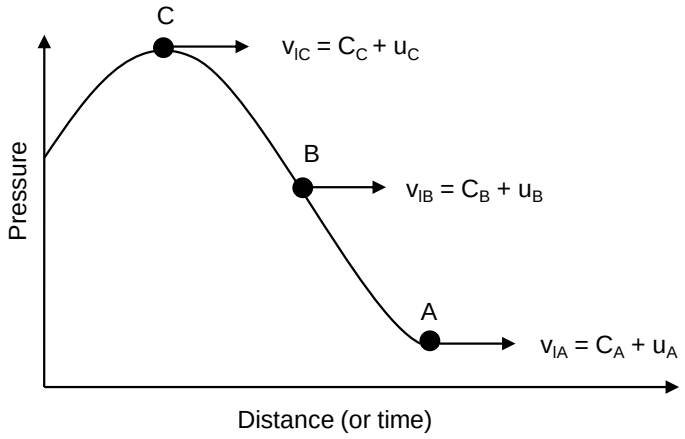

Figure 2.1: Typical pressure wave in the plastic region adapted from Cooper [11].

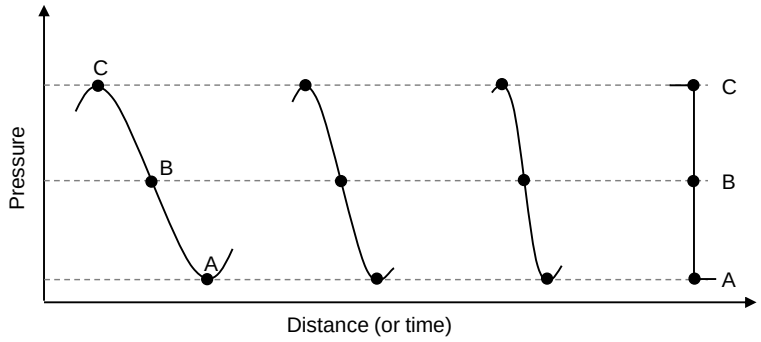

Figure 2.2: Upper section of wave front catching up to lower section adapted from Cooper [11].

2.2.2 Attenuation behind shock waves

Figure 2.3 shows a square pulse shock wave where the front of the wave is a shock. Because the back of the wave is following the shock front, it is travelling into a region of higher density than the front of the wave. Point 'A' is at high pressure and is travelling into the higher density region. Its particle velocity is also greater than that at the front of the wave. The result is that the back of the wave has a higher wave velocity than the front, and so rapidly catches up with the front of the wave. Point 'C' is at low pressure and has a lower wave velocity than the other points, both at the front and back. Consequently point 'C' lags behind the rest of the wave.

The back side of the wave is known as a rarefaction wave. Since the upper and lower sides of the rarefaction wave are travelling at significantly different velocities, the wave spreads out over time. When the upper part of the rarefaction wave catches the front portion of the wave, it causes a reduction in pressure to the elastic region. Once this occurs the wave is known as a sound wave [11]. The process is shown in Figure 2.4.

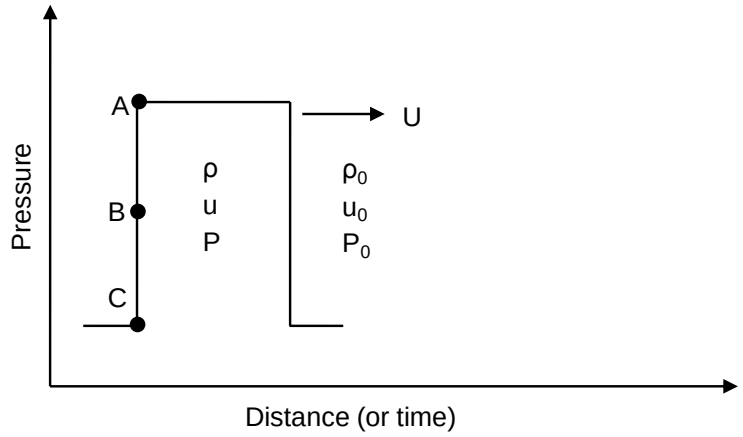

Figure 2.3: Square pulse shock wave adapted from Cooper [11].

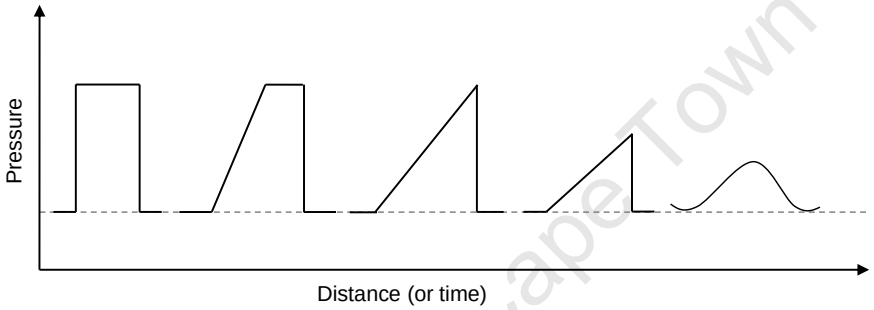

Figure 2.4: Rarefaction spreading out over time adapted from Cooper [11].

2.2.3 Rankine-Hugoniot jump equations

Cooper [11] describes the shock front as a discontinuity across which, the material jumps from the non-shocked to the shocked state. That is, there is no gradual change from one state to the other, rather an instantaneous, path-independent change. Figure 2.5 shows a shock front travelling to the right at velocity U through a volume of material. The non-shocked material ahead of the shock front is in its original state, described by particle velocity u_0, density ρ_0, internal energy E_0 and pressure P_0. The shocked material behind the shock front has particle velocity u_1, density ρ_1, internal energy E_1 and pressure P_1.

To solve for these five variables, five equations and/or relationships are required. Three equations may be derived by considering the conservation of mass, momentum and energy across the shock front. These equations are path-independent and depend only on the initial and final states of the material. The set of equations is known as the Rankine-Hugoniot jump equations, and is presented in detail by Cooper [11]. Since the equations are similar to those described in Section 2.3.2, they are not reproduced here.

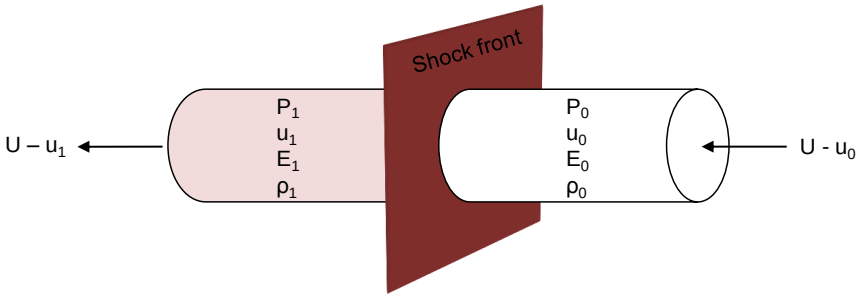

Figure 2.5: Shocked and non-shocked states separated by shock front adapted from Cooper [11].

2.2.4 The Hugoniot

Two further relationships are required to solve the five variables that fully describe a shock wave. An example of such a relationship is an equation of state (EOS). The ideal gas EOS is a general relationship but is not suitable for shock applications. However, if there were an EOS such that $e = f(P, v)$, then the energy term e could be eliminated by combining it with the energy jump equation, resulting in a relationship of the form

$$P = f(v) \tag{2.2}$$

Equation 2.2 is the Hugoniot equation, representing the locus of all possible material states behind the shock front.

An alternative to the EOS-derived Hugoniot is to determine a relationship between any two of the variables in the mass and momentum jump equations. Of all the combinations $U - u$, $P - v$ and $P - u$ are found to be most useful [11].

A typical $P - v$ Hugoniot is shown in Figure 2.6. The line joining the initial and final states on the Hugoniot (Points 'A' and 'B' respectively) represents the jump discontinuity described in Section 2.2.3. This line is known as the Rayleigh line and its slope is proportional to the shock velocity. The Rayleigh line may be used to determine the final $P - v$ state of a shock, if its initial state and shock velocity are both known.

The Hugoniot on the $P - u$ plane is given by

$$P_1 = \rho_0 u_1 (C_0 + s u_1) \tag{2.3}$$

A right-going shock is one for which the shock travels from left to right. For a right-

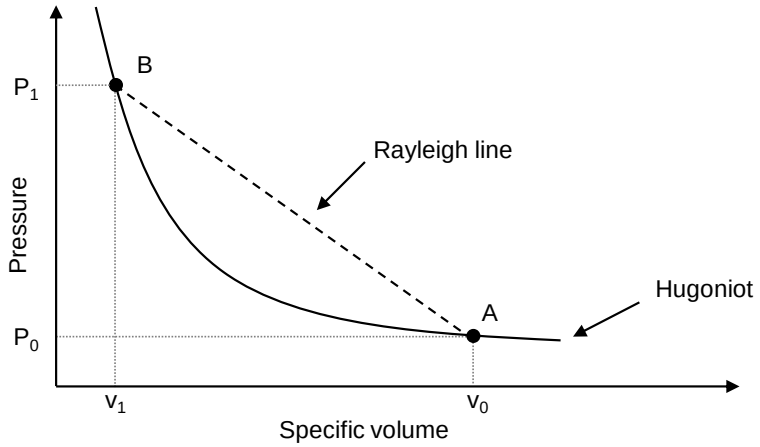

Figure 2.6: Typical $P - v$ Hugoniot curve adapted from Cooper [11].

going shock, the slope of the straight line joining the initial and final states on the $P - u$ Hugoniot is $\rho_0 (U - u_0)$. For a left-going shock, the slope is $-\rho_0 (U - u_0)$. In these slope expressions, U is the shock velocity in Eulerian coordinates, while $(U - u_0)$ is the shock velocity relative to the material for an arbitrary initial material velocity.

These slope quantities are used to solve interactions of shocks. Two different $P - u$ Hugoniots along with the Rankine-Hugoniot jump equations provide five equations for the five unknowns of this section. Further, by using the slope expressions above, shock interactions may be solved while specifying only the initial conditions [11].

2.3 Detonation phenomena

Combustion describes any oxidation reaction regardless of whether it requires oxygen or has it in excess. In explosive materials, the combustion process is known as deflagration or detonation, depending on the rate of combustion.

Deflagration occurs in materials where the decomposition takes place at a rate well below the speed of sound in the material. Since the combustion is subsonic, no shock front is produced, and the deflagration is propagated by the heat liberated from the reaction [8,9]. This is not of interest in the current work.

When the explosive decomposition occurs at a rate above the speed of sound in the material, the combustion process is called detonation [12]. Since the process is supersonic, a high intensity shock front is produced, which causes the formation of large pressure and temperature gradients as the uncreated explosive is converted to hot, dense, high pressure gas [12]. The detonation process may be split into initiation and propagation. For the purpose of analysis, the latter is considered a steady-state process and is described in this section.

Zukas and Walters [13] list four common behavioural phenomena seen in the steady-state propagation of a detonation wave:

- the propagation wave velocity is greater than the speed of sound of the unreacted material into which it is travelling
- the wave velocity is constant in any given explosive material
- the wave velocity is proportional to the density of the explosive material
- the wave velocity decreases with decreasing charge diameter for a given material, and propagation is not possible below some minimum charge diameter.

2.3.1 The simple model

Cooper [11] describes in detail the simple model of steady-state ideal detonation, also referred to as the ZND detonation model. The simple model is based on several simplifying assumptions:

- the detonation wave is uni-axial i.e. the detonation front is an infinite plane, and the wave is travelling in a direction normal to the front
- the wave front is discontinuous

- the reaction product gases leaving behind the detonation front are in chemical and thermodynamic equilibrium and the chemical reaction is complete
- the chemical reaction is completed instantly resulting in a reaction zone of zero length
- the detonation rate or velocity is constant
- the products leaving the detonation front remain at the same state independent of time.

Within the framework of these assumptions, detonation may be viewed as a shock wave moving through an explosive material at a constant velocity [13]. As the shock wave proceeds, it rapidly compresses and heats the explosive material ahead of it, causing an exothermic reaction. The reaction is completed instantly and the energy released drives the shock wave forward. The gases released behind the shock front continue to expand and a rarefaction wave moves forward in the same direction as the shock wave. The shock front, chemical reaction and the leading edge of the rarefaction are all in equilibrium and move at the same speed known as the detonation velocity.

The detonation jump from unreacted explosive to shock-compressed reaction product gases is shown on the $P - v$ plane in Figure 2.7. On this plane the gradients of the Hugoniot curves are indicative of velocity. Note that the Rayleigh line is tangent to the Hugoniot of the reaction products. If it were not, for instance the line labelled "*over*" in Figure 2.7, then two states would be possible for the detonation products, one at each intersection (points 'F' and 'E'). The gradient of the Hugoniot at point 'F' is greater than the gradient of the Rayleigh line indicating that the reaction zone and the rarefaction wave would be travelling faster than the shock front. Similarly at point 'E' the gradient is less, indicating that the shock front would be pulling away from the reaction zone and rarefaction. Neither situation satisfies the conditions of equilibrium.

The only point on the Hugoniot where the conditions of equilibrium are satisfied and the shock wave, reaction zone and rarefaction wave travel at the same velocity, is where the Rayleigh line is tangent to the Hugoniot (point 'B'). This point is known as the Chapman-Jouguet state (CJ state).

The Von Neumann spike is the shock state that initiates the reaction. In the simple model, the Von Neumann spike is ignored resulting in a reaction zone of zero thickness. This is illustrated in Figure 2.8 which shows the profile of a detonation wave in the pressure-distance $P - x$ plane.

The rarefaction wave which describes the expansion of the product gases from the CJ state to ambient conditions is known as the Taylor wave. The Taylor wave is not a characteristic

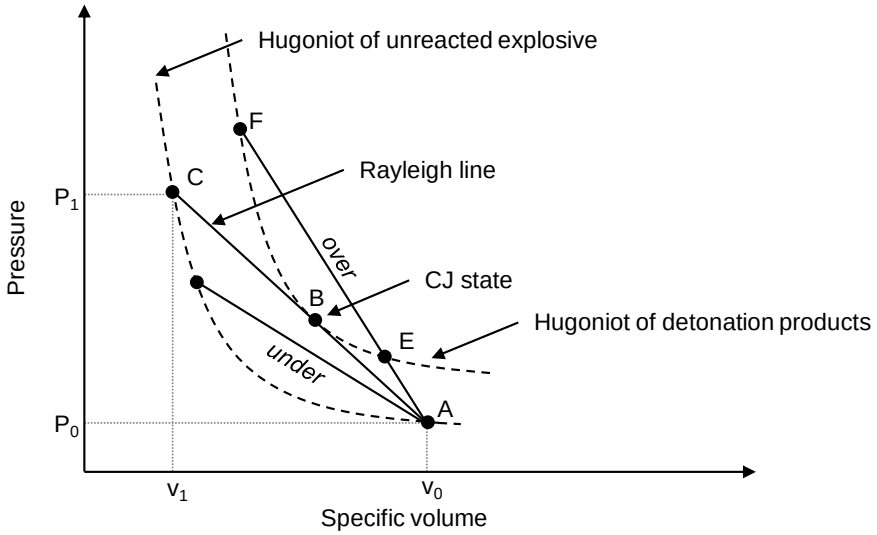

Figure 2.7: Possible Rayleigh positions in the $P - v$ plane [11].

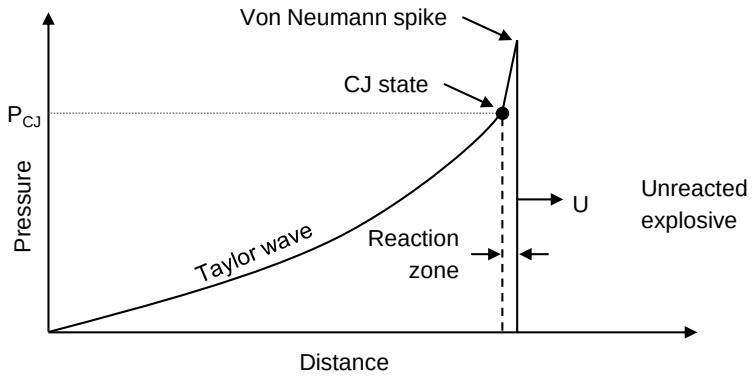

Figure 2.8: Profile of a detonation wave in the $P - x$ plane adapted from Cooper [11].

of the explosive, rather it is dependent on the geometry of the explosive and the degree of confinement. A confined explosion has a longer and higher Taylor wave than an unconfined explosion.

2.3.2 Detonation Rankine-Hugoniot jump equations

Recall the shock front discontinuity of Section 2.2.3. In a detonation, the initially undisturbed material is compressed across the shock front and immediately exists at the highly compressed CJ state. The Rankine-Hugoniot jump equations may then be written as

Mass balance

$$\frac{\rho_{CJ}}{\rho_0} = \frac{v_0}{v_{CJ}} = \frac{D}{D - u_{CJ}} \tag{2.4}$$

Momentum balance

$$P_{CJ} = \rho_0 u_{CJ} D = \frac{u_{CJ} D}{v_0} \tag{2.5}$$

Energy balance

$$e_{CJ} - e_0 = \frac{1}{2}\left(P_{CJ} + P_0\right)\left(v_0 - v_{CJ}\right) \tag{2.6}$$

In these equations ρ is the density, v is the specific volume, D is the detonation velocity, u is the particle velocity, P is the pressure and e is the specific internal energy. The subscripts $_{CJ}$ and $_0$ indicate the CJ and initial states respectively [13].

Similar to the typical shock of Section 2.2, seven unknowns are required to fully describe the detonation jump. Two of these, the initial pressure P_0 and density ρ, are specified as boundary conditions. This leaves five unknowns in the three jump equations. Two further relationships are again required.

2.3.3 The CJ state

Several methods exist for determining the detonation velocity, including analysis of the chemical composition, chemical structure and thermodynamic properties [13]. Dobratz and Crawford [14] present data for an empirical relationship of the form

$$D = j + k\rho_0 \tag{2.7}$$

where j and k are constants chosen for a particular explosive. The detonation velocity is the easiest of the CJ state parameters to measure accurately and is used to determine the other CJ state parameters [13].

Unlike the typical shock wave described in Section 2.2, no empirical $U - u$ relationship exists for a detonation. However Cooper [11] presents a similar empirical relationship relating the initial and CJ densities

$$\rho_{CJ} = 1.386\rho_0^{0.96} \tag{2.8}$$

The CJ pressure can then be estimated by combining this relationship with the mass and momentum detonation jump equations

$$P_{CJ} = \rho D^2 \left(1 - \frac{\rho_0}{\rho_{CJ}}\right) = \rho D^2 \left(1 - 0.7215\rho_0^{0.04}\right) \tag{2.9}$$

This enables all of the CJ state parameters to be determined and thus the detonation jump is fully described.

2.4 Equations of state

An equation of state (EOS) is a relationship between state variables of matter under given physical conditions. Zukas and Walters [13] provide an overview of the several equations of state pertinent to explosive application. The equations of state most relevant to the present work are described here.

2.4.1 Linear polynomial (and gamma law)

The linear polynomial EOS describes a linear relationship between the pressure and internal energy of a material, given by

$$p = C_0 + C_1\mu + C_2\mu^2 + C_3\mu^3 + \left(C_4 + C_5\mu + C_6\mu^2\right) E \tag{2.10}$$

where C_0 through C_6 are polynomial coefficients to be calibrated, E is the internal energy, and $\mu = \rho/\rho_0 - 1$ in which ρ and ρ_0 are the current and initial densities of the material respectively.

By setting the appropriate polynomial coefficients, the linear polynomial EOS may be used to approximate gases according to the gamma law EOS

$$p = (\gamma - 1)\frac{\rho}{\rho_0}E \tag{2.11}$$

where γ is the adiabatic exponent or ratio of specific heats.

2.4.2 Ideal gas

The ideal gas EOS is

$$pv = RT \tag{2.12}$$

where p is the pressure, v is the volume, R is the universal gas constant and T is the temperature.

When the gas molecules are far apart relative to their dimensions, this equation of state provides a good approximation. However in shock applications where the gas densities are high, the approximation fails to describe reality. In limited regions, the polytropic gas equation given by Equation 2.13, may be used to gain a qualitative understanding of system behaviour. In such cases, the adiabatic exponent γ must be adjusted to fit data in the region of interest [13].

$$E = \frac{pv}{\gamma - 1} \tag{2.13}$$

where E is the internal energy and γ is the adiabatic exponent or ratio of specific heats.

2.4.3 Jones-Wilkins-Lee

For shock and explosive applications a widely used equation of state is the Jones-Wilkins-Lee (JWL) equation given by

$$p = A\left(1 - \frac{\omega}{R_1 V}\right)e^{-R_1 V} + B\left(1 - \frac{\omega}{R_2 V}\right)e^{-R_2 V} + \frac{\omega e}{V} \tag{2.14}$$

where p is the pressure, V is the volume ratio and e is the energy per unit volume. A, B, R_1, R_2 and ω are constant parameters to be calibrated. Values for these parameters have been calculated for many common explosives and are available in the literature [14].

The JWL EOS is favoured in many computer codes as it is easily recalibrated to fit experimental data. The parameters should be considered an interdependent set and should not be modified unilaterally. Further, should pressures significantly exceed the CJ pressure of the material, the exponential terms may give rise to unrealistic behaviour [15].

2.5 Blast phenomena

When an explosive is detonated, the unreacted solid explosive is rapidly converted to hot, dense, pressurised gases. The rapid expansion of the hot gas creates a layer of compressed air in front of it, which contains most of the energy liberated by the explosion. The compressed air layer expands outwards as a spherical front from the point of detonation. This layer of compressed air is known as a blast wave [12, 16].

The outward expansion of a blast wave is illustrated in Figure 2.9 for a free-air burst blast. As the blast wave expands outwards, it decays in strength, increases in duration and decreases in velocity. These phenomena are caused by a combination of spherical divergence and the completion of the chemical reaction [12].

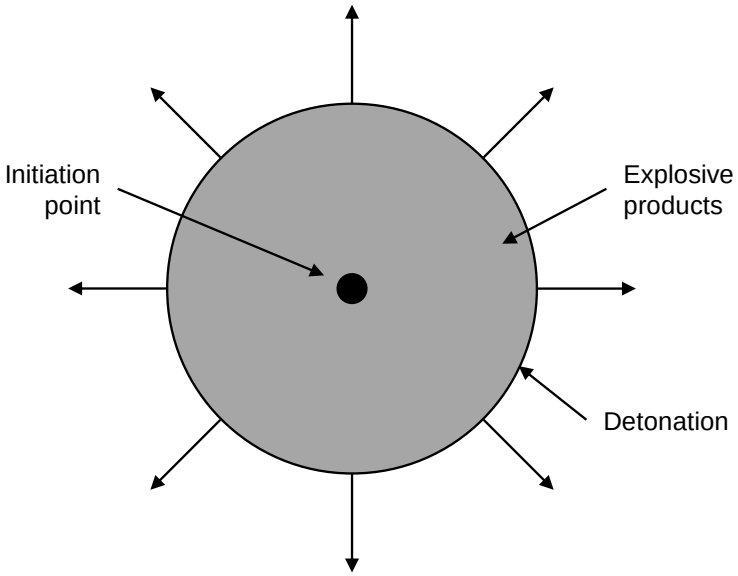

Figure 2.9: Spherically-outward expansion of blast wave for free-air blast adapted from Rinehart and Pearson [17].

Any structures in the path of the blast wave are subjected to shock pressure loads as the blast wave impinges on it. The magnitude and distribution of the pressure loads on the structures are determined by: the type and mass of the explosive, the distance between the detonation and the structure, and the interaction of the pressure with other surfaces in the vicinity [12]. These factors are detailed in this section.

2.5.1 Explosives

Explosive materials may be classified according to their physical state as either solid, liquid or gas. However explosives are typically classified by either their sensitivity to ignition or rate of decomposition.

Depending on their sensitivity to ignition, explosives may be classed as either primary or secondary explosives. Primary explosives are highly sensitive and may be easily detonated from a spark, flame or impact. Examples of primary explosives include mercury fulminate and lead azide [16].

Secondary explosives are less sensitive than primary explosives, requiring a shock or sudden temperature rise to initiate detonation. Since secondary explosives are stable and therefore able to be safely handled and stored, secondary explosives are typically used in blast testing environments. Plastic Explosive 4 (PE4), Composition 4 (C4), and Trinitrotoluene (TNT) are common secondary explosives

When the rate of decomposition through the explosive material is used a criterion, explosives may be classed as either high or low explosives. High explosives have high burn velocities relative to low explosives. The blast effects, including pressures, impulses and load durations are "well established" [12] for high explosives.

2.5.2 TNT equivalence

Two parameters that are important in all blasting applications are the amount of energy liberated by the explosion and the distance from the source of the explosion to the structure of interest. The explosive energy is assumed to be proportional to the charge mass [16].

UFC 3-340-02 [12] presents extensive blast effect data for bare, spherical TNT charges. Such data may be used for other explosives by relating the explosive energy of a given mass of an explosive to that of an equivalent mass of TNT [9,18]. For explosive materials of similar shape, the TNT-equivalent charge mass may be found by relating the heats of detonation of the explosives according to

$$W_E = \frac{H^d_{\mathrm{EXP}}}{H^d_{\mathrm{TNT}}} W_{\mathrm{EXP}} \tag{2.15}$$

where W_E is the TNT-equivalent charge mass, W_{EXP} is the non-TNT explosive mass, H^d_{EXP} is the heat of detonation of the non-TNT explosive, and H^d_{TNT} is the heat of detonation of the TNT.

A list of TNT conversion factors for many explosives is presented by Baker [19], for instance PE4 which has a TNT-equivalent mass of approximately 1.3 per unit mass of TNT.

UFC 3-340-02 [12] notes that the TNT-equivalent charge mass predicted by Equation 2.15 is based on the explosive output for unconfined explosions. Consequently the TNT-equivalent charge mass for confined explosions is expected to differ.

2.5.3 Scaled distance

In addition to the explosive charge mass, the other pertinent factor in all blast effects is the distance from the point of detonation to a point of interest, often referred to as the stand off distance (SoD) [16].

Hopkinson's law establishes that similar blast waves are produced at identical scaled distances, when different masses of the same explosive are detonated under the same conditions [20].

Consequently any distance from the point of detonation R of a charge mass, can be written as a scaled distance given by

$$Z = \frac{R}{\sqrt[3]{W_E}} \tag{2.16}$$

where W_E is the TNT-equivalent charge mass. The masses for explosives other than TNT may be obtained through the concept of TNT equivalence as described in Section 2.5.2.

The scaled distance parameter provides a convenient parametric correlation between a particular explosion and a standard charge of the same material [16]. This method of scaling is used in Section 3.3 for the experimental design in the present work.

2.5.4 Blast loading categories

Depending on the degree of confinement of an explosion, a blast load may be classified as either unconfined or confined. Within these two groups, a blast load may be further classed according to its interaction with surrounding structures [12].

Definitions for the six blast loading categories are presented in UFC 3-340-02 [12] and these are outlined below.

- **Unconfined explosions**

  Free-air burst

  An explosion which occurs in free air, resulting in a shock wave that propagates away from the point of detonation. The shock wave is not amplified before it interacts with structures in its path.

  Burst

  An explosion which occurs in air at some distance from the ground and/or surrounding structures, such that the ground reflections of the shock wave occur before the shock interacts with structures in its path.

  Surface burst

  An explosion which occurs close to, or on the ground, such that the initial shock wave is amplified owing to the ground reflections.

- **Confined explosions**

  Fully-vented

  An explosion which occurs within or immediately adjacent to a barrier or structure with at least one surface open to the atmosphere. The initial shock wave, which is amplified by interactions with the structure, along with the products of detonation are vented to the atmosphere, resulting in a shock wave that propagates away from the structure.

  Partially-confined

  An explosion which occurs within a structure with limited size openings to the atmosphere. The initial shock wave, which is amplified by interactions with the structure, along with the products of detonation, are vented to the atmosphere after a finite time period. The confinement of hot, high pressure gaseous products, causes an accumulation of quasi-static pressure. The quasi-static pressure has a time duration that is long relative to that of the shock pressure. The quasi-static pressure may be referred to as the "gas pressure" [12].

  Fully-confined

  An explosion which occurs within a structure which is totally contained or near-totally contained, such that there are no significant openings to the atmosphere. The initial shock wave is unvented and amplified by interactions with the structure. The quasi-static pressures are of a very long duration relative to the other confinement configurations.

Based on these definitions, the cylinders in the present work are considered partially-confined since they are expected to contain a significant quasi-static pressure.

2.5.5 Pressure-time history

A typical unconfined blast wave pressure-time history is shown in Figure 2.10. Time t_A is the time taken from detonation for the blast wave to reach a point of interest. The atmospheric pressure is denoted by P_0. On arrival at the point of interest, the pressure jumps immediately to a value well above atmospheric pressure, known as the peak overpressure P_{so}. Over some time t_d, this pressure decays and may drop below atmospheric pressure, creating a partial vacuum. The maximum value of this negative pressure is known as the peak underpressure P_{so}^-. After a further time t_d^-, the pressure returns to ambient conditions.

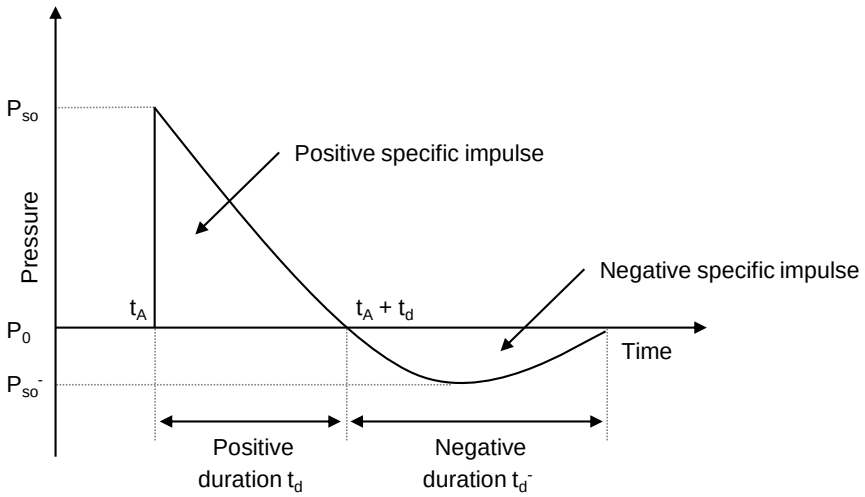

Figure 2.10: Typical pressure-time history adapted from Ngo [16].

The portion of the pressure-time history that is above ambient conditions is known is as the positive phase, while the portion below is called the negative phase. The negative phase is typically of a significantly lower amplitude and longer duration than the positive phase.

This treatment of the blast wave is generalised, and the magnitudes and durations of the pressures vary depending on the degree of confinement [12]. This is discussed in Section 2.5.6.

2.5.6 Effects of confinement

The pressures associated with a confined explosion are amplified by shock reflections within the structure. The accumulation of gaseous products from the explosion results in additional pressures and an increased load duration relative to an unconfined explosion.

The pressure due to the incident blast wave is known as the "shock pressure", while the additional accumulated pressure is referred to as the quasi-static or "gas pressure" [12].

The reflected shock pressures and the addition of the quasi-static pressure are what distinguishes a confined explosion from one that is unconfined.

The onsets of the shock and quasi-static pressures are not coincident, with the onset of

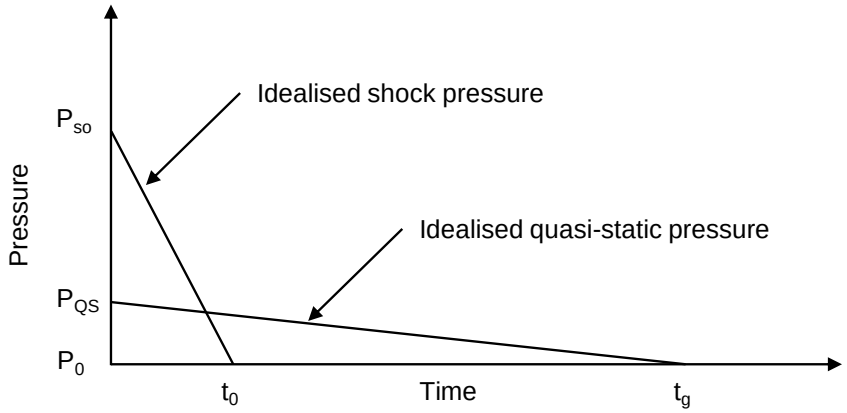

Figure 2.11: Idealised pressure-time history for a confined explosion adapted from UFC 3-340-02 [12].

The magnitude and duration of the quasi-static pressure loading is a function of the charge mass, the degree of confinement and the volume of the enclosure. The magnitude of the quasi-static pressure is generally less than that of the shock pressure, and of a significantly longer duration. In general, as the the opening-enclosed volume ratio decreases, the magnitude and duration of the quasi-static pressure loading increases. For very small openings, the duration of the quasi-static pressure is "very long" [12] relative to the natural period of the structure. As described in Section 2.5.4, structures in which the quasi-static pressure accumulation is insignificant are referred to as fully-vented structures.

For relatively small structures, the magnitude of the quasi-static pressure may be considered uniform throughout the structure. However for structures that are biased in one direction as is the case in the present work (e.g. tubes or cylinders), the magnitude of the quasi-static pressure varies along the length of the structure [12].

2.5.7 Prediction of blast pressure

Brode [21] provides equations for estimating the peak overpressure due to a spherical blast

$$P_{so} = \begin{cases} \dfrac{0.975}{Z} + \dfrac{1.455}{Z^2} + \dfrac{5.85}{Z^3} - 0.019 & \text{if } 0.1 < P_{so} < 10 \\ \dfrac{6.7}{Z^3} + 1 & \text{if } P_{so} > 10 \end{cases} \tag{2.17}$$

where P_{so} is given in bars and Z is the scaled distance parameter of Equation 2.16.

Mills [22] presents a similar expression for peak overpressure

$$P_{so} = \frac{1772}{Z^3} - \frac{114}{Z^2} + \frac{108}{Z} \tag{2.18}$$

where P_{so} is in kPa and Z is again the scaled distance for an equivalent kg mass of TNT.

Similar equations for predicting blast pressures are introduced by others in the literature [23], while extensive design charts are given in UFC 3-340-02 [12].

2.5.8 Impulse

Recall the pressure-time history of Figure 2.10. The area under the curve from the arrival time t_a to the end of the positive phase at time $t_a + t_d$ is known as the "specific impulse" [9]. Mathematically this is represented as

$$i = \int_{t_a}^{t_a+t_d} P(t)\,\mathrm{d}t \tag{2.19}$$

Impulse is used to quantify the damage potential of a blast and is dependent on the peak overpressure, blast duration and the rate of decay. Because the peak overpressure is significantly larger than the peak underpressure, the negative phase of the pressure-time history is typically neglected for unconfined blasts [24].

2.5.9 Friedlander equation

The quasi-exponential pressure fall in the pressure-time history may be described by the Friedlander equation

$$P(t) = P_{so}\left[1 - \frac{t}{t_d}\right] e^{-\alpha t/t_d} \tag{2.20}$$

where α is a decay parameter chosen so that the pressure-time relationship gives a suitable value for the blast impulse. Smith and Hetherington [9] provide several values for α based on the scaled distance parameter Z.

2.5.10 Reflections

Reflections occur when a blast wave encounters a solid surface or any medium more dense than the one in which it is propagating. The simplest case is a blast wave impinging normally on an infinitely large, rigid wall. As the blast wave is brought to rest against the wall, it is further compressed, resulting in a reflected overpressure which is higher than the incident overpressure. The peak reflected overpressure P_r is given by

$$P_r = 2P_{so}\left[\frac{7P_0 + 4P_{so}}{7P_0 + P_{so}}\right] \tag{2.21}$$

The peak reflected overpressure is typically between 2 and 8 times greater than the peak incident overpressure [9].

The scenario above describes one limiting case where the angle of incidence α_I between the incident blast wave and the surface normal is zero. The other limiting case is where $\alpha_I = 90°$ and no reflection occurs. For reflections between these limits, either regular reflection or Mach reflection is exhibited. The threshold angle of incidence α_I is dependent on the peak incident overpressure [9].

Regular reflection

Regular reflection typically occurs for lower angles of incidence α_I, where the blast wave is said to "bounce" off the reflecting surface. There exists an α_I above which the reflected pressure P_r is greater than that for the case of normal incidence described above. In air

this angle is approximately 40°. The angle of reflection α_r increases with the angle of incidence α_I [9]. Regular reflection is illustrated in Figure 2.12a.

Mach reflection

At higher angles of incidence α_I Mach reflection occurs. Smith and Hetherington [9] describe a Mach reflection as a "skimming" off the reflected surface. The reflected wave catches up with the incident wave, merging at some point to form a new wave front known as the Mach stem. Mach reflections are typically seen in above-ground detonations and for confined explosions, where the angles of incidence with the various surfaces of the structure vary significantly [9]. Mach reflection is illustrated in Figure 2.12b.

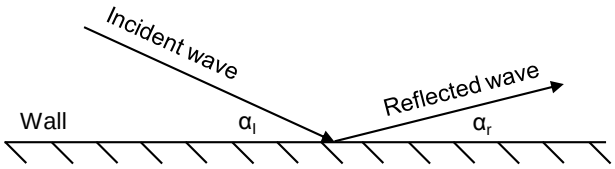

(a) Regular reflection.

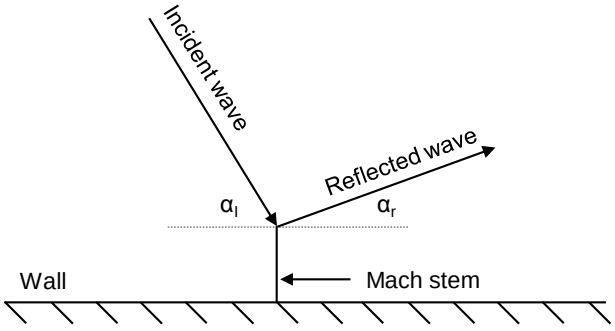

(b) Mach reflection.

Figure 2.12: Reflection of a plane shock wave.

2.5.11 Afterburning

During an explosion the primary source of energy comes form the short-duration detonation process which occurs on a timescale in the order of microseconds. Under certain chemical and physical conditions, a late-time, longer-duration (milliseconds) combustion process may release further energy into the system. This phenomenon is known as afterburning [25], and may result in additional damage or structural deformation beyond that caused by the detonation.

In the case of fuel-rich explosives[1], for instance TNT, PE4 and C4, three general conditions are required for afterburning to occur:

- presence of sufficient surrounding oxygen,
- adequate mixing of the detonation products and the surrounding oxygen,
- temperatures above the ignition temperatures of the reacted fuels [25].

For fully-vented explosions, the temperature and pressure near to the reaction zone decay quickly, precluding the reactions necessary to produce the afterburning effect. However, in the case of partially- or fully-confined explosions, the temperature and pressure decay relatively slowly resulting in the conditions that promote afterburning. Additionally the confinement enhances the mixing between the detonation products and surrounding oxygen, further promoting the possibility of afterburning [25].

2.5.12 Blast testing

When the blast waves described in the preceding sections interact with structures they impose blast loads on the structures. These loads are complex and are often simplified to be either impulsive or quasi-static for the purpose of analysis [24].

The Steel Construction Institute [24] defines an impulsive blast load as one where the duration of the load is significantly less than the natural period of the structure. This means that under impulsive loading conditions, higher loads can be tolerated since the structure does not have sufficient time to fully respond to the blast load. The damage caused is thus dependent on the impulse and not the peak load.

[1]Explosives with a negative oxygen balance are said to be fuel-rich, while those with a positive oxygen balance are said to be oxygen-rich. Oxygen balance and the associated chemistry is beyond the scope of the present work; a good overview is presented by Cooper [11].

If the duration of the load is much longer than the natural period of the object, the blast load is said to be quasi-static. In such a case the structure sees the full effect of the blast load and thus the damage is dependent on the peak load [24].

Loading in between these two cases is termed dynamic loading, and the damage is a result of both the impulse and peak load [24]. Such a load case is typical in confined explosions where the duration of the load is increased owing to limited venting.

2.5.13 Charge mass

The charge mass is the mass of explosive used in a blast test and is used to control the impulse in the test. At the Blast Impact and Survivability Research Unit (BISRU), disc- or cylindrical-shaped charges charges have been used in many studies [26–29], while spherical charges have been used successfully elsewhere [5, 30]. For such charge shapes the mass is given by

$$m_c = \begin{cases} \rho_c h_c \dfrac{\pi d_c^2}{4} & \text{for cylindrical charges} \\ \\ \rho_c \dfrac{\pi d_c^3}{6} & \text{for spherical charges} \end{cases} \tag{2.22}$$

where ρ_c is the charge density, h_c is the charge height and d_c is the charge diameter.

2.6 Confined pressure phenomena

The process of blast wave reflection and its importance in pressure growth in partially-vented and unvented spaces was first identified in World War II research on the effects of bombs detonated within enclosures [31]. However, the earliest attempt to relate the physical processes involved was presented later by Weibull [32] in 1968. This section presents details of several key works on the behaviour of pressure in spherical or cylindrical confinements.

2.6.1 Peak quasi-static pressure

Weibull [32]

Weibull [32] correlated the peak quasi-static pressure with charge mass and enclosure volume for TNT detonated in "partially-closed" [32] enclosures. Weibull [32] noted that though termed "partially-closed" [32], the areas of the openings were very small relative to the total enclosing area of the enclosures. Thus the structures are more likely to be classified as fully-confined based on the definitions in Section 2.5.4.

The results of the experiments are shown in Figure 2.13. The straight line is a linear best-fit to the experimental data and is not founded in theory. The "fairly good" [32] correlation between the experimental data and the fitted curve, suggests that the peak quasi-static pressure is linearly proportional to the charge mass-volume ratio.

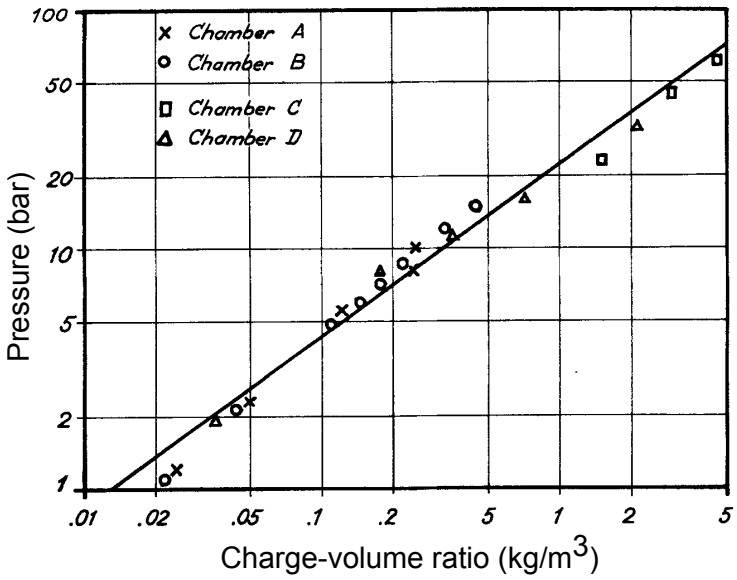

Figure 2.13: Peak quasi-static pressure as a function of charge mass-structure volume ratio [32].

Kingery et al [33]

Kingery et al [33] investigated the pressure history at the walls of suppressive structures subjected to internal blast loading. Kingery et al [33] listed two difficulties in determining the peak quasi-static pressure. Firstly, the quasi-static pressure is generated while the repeated, reflected shocks are occurring, thus obscuring the value of the peak quasi-static pressure on the recorded pressure history. Secondly, in cases where the vent area is large, the quasi-static pressure is generated while the reflected shock pressures decay.

To overcome these difficulties, the authors [33] proposed two methods for determining the peak quasi-static pressure. The first method was to fit an exponential curve to the decaying pressure-time curve and extrapolate back to time $t = 0$. While not explicitly stated, it appears this method was also used by Weibull [32]. The second method used by Kingery et al [33] was to take the average pressure at time $t = W^{2/3}$ where W is the charge mass in pounds and t is the time in milliseconds. The smaller the relative vent area to the total enclosed volume, the closer the two pressure predictions will be to each other [31].

Baker et al [31]

Because several reflections must occur before the shock energy is converted to quasi-static pressure, Baker et al [31] regarded the method of extrapolation back to time $t = 0$ as "inappropriate" [31]. Rather the authors [31] recommended allowing "some time" [31] for establishing the peak quasi-static pressure, more in line with the second method proposed by Kingery et al [33]. It should be noted that Kingery et al [33] found "excellent agreement" [33] between the quasi-static pressures predicted using the extrapolation method and those predicted by the INBLAST computer code.

A further problem cited by Baker et al [31] is accurate determination of the quasi-static pressure *duration*. Even though the shock reflections have decayed (see Section 2.6.2), the pressure approaches ambient conditions asymptotically, making it difficult to accurately determine the duration of the pressure load.

Baker et al [31] present an extensive analysis of quasi-static pressures from internal explosions. From the data of 177 experiments, Baker et al [31] developed an equation for the peak quasi-static pressure as a function of charge mass W and enclosure volume V.

The equation is a result of best-fit curves to the experimental data and takes the form

$$\begin{aligned}\log\left(P_{QS}\right) = {} & 0.30759 + 0.51815\left[\log(W/V)\right] - 0.150534\left[\log(W/V)^2\right] \\ & + 0.31892\left[\log(W/V)^3\right] + 0.10434\left[\log(W/V)^4\right] \\ & - 0.14138\left[\log(W/V)^5\right] - 0.019206\left[\log(W/V)^6\right] \\ & + 0.021486\left[\log(W/V)^7\right]\end{aligned} \tag{2.23}$$

Baker et al [31] noted that the peak quasi-static pressure was independent of the of the area of the openings, and dependent on the ratio of charge mass to volume of the enclosure.

2.6.2 Mechanisms of pressure growth

Karpp et al [34]

Karpp et al [34] investigated the pressure loading on the walls of spherical containment vessels by simulating the detonation of high explosive using a hydrocode. The structure was taken as a 352mm diameter sphere subjected to loading from a centrally-located 25.4mm diameter spherical charge. The explosive products were modelled using the JWL EOS, and the air was approximated using the linear polynomial EOS. The same EOS combination is used in the present work.

The results exhibited the formation of two shocks following the detonation. Figure 2.14 shows the two shocks $40\mu s$ after detonation, just prior to interaction with the shell wall. The main shock, denoted 'M' in Figure 2.14, is followed by a secondary shock 'S' which travels inwards relative to the moving explosive products. The secondary shock causes the formation of a high density region between the main shock and the air-explosive interface, as indicated in Figure 2.14b.

Following the reflection of the main shock with the vessel wall, it next interacts with the air-explosive interface. Owing to the high density in this region, a "substantial" [34] portion of the shock wave is reflected back toward the vessel wall, resulting in a second loading pulse on the wall. These two loading pulses are evident in Figure 2.15a which shows the pressure on the vessel wall for $200\mu s$ following detonation.

The other portion of the main shock is eventually reflected from the centre of the vessel and impinges on the vessel wall causing the next major pressure load at approximately 240μs. This is illustrated in Figure 2.15b where several subsequent reflected pressure

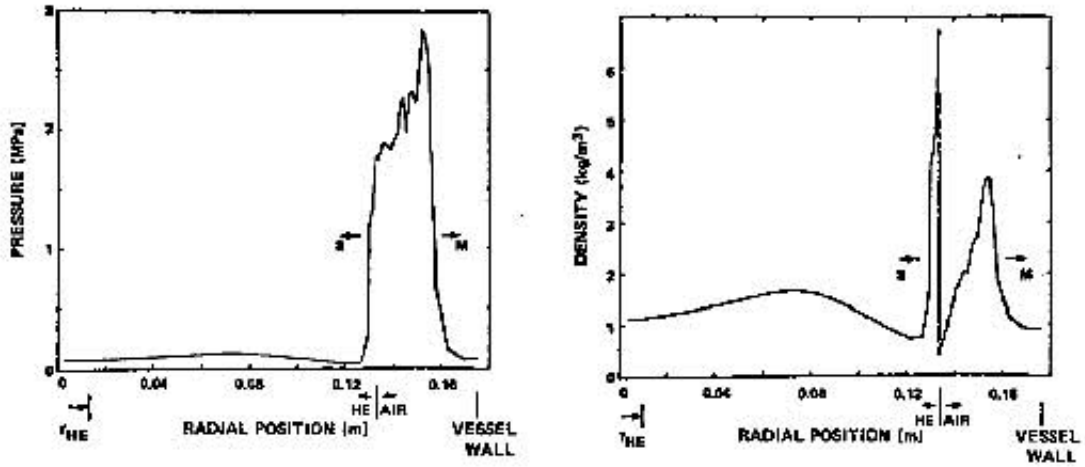

(a) Pressure distribution. (b) Density distribution

Figure 2.14: Pressure and density distributions 40μs after detonation [34].

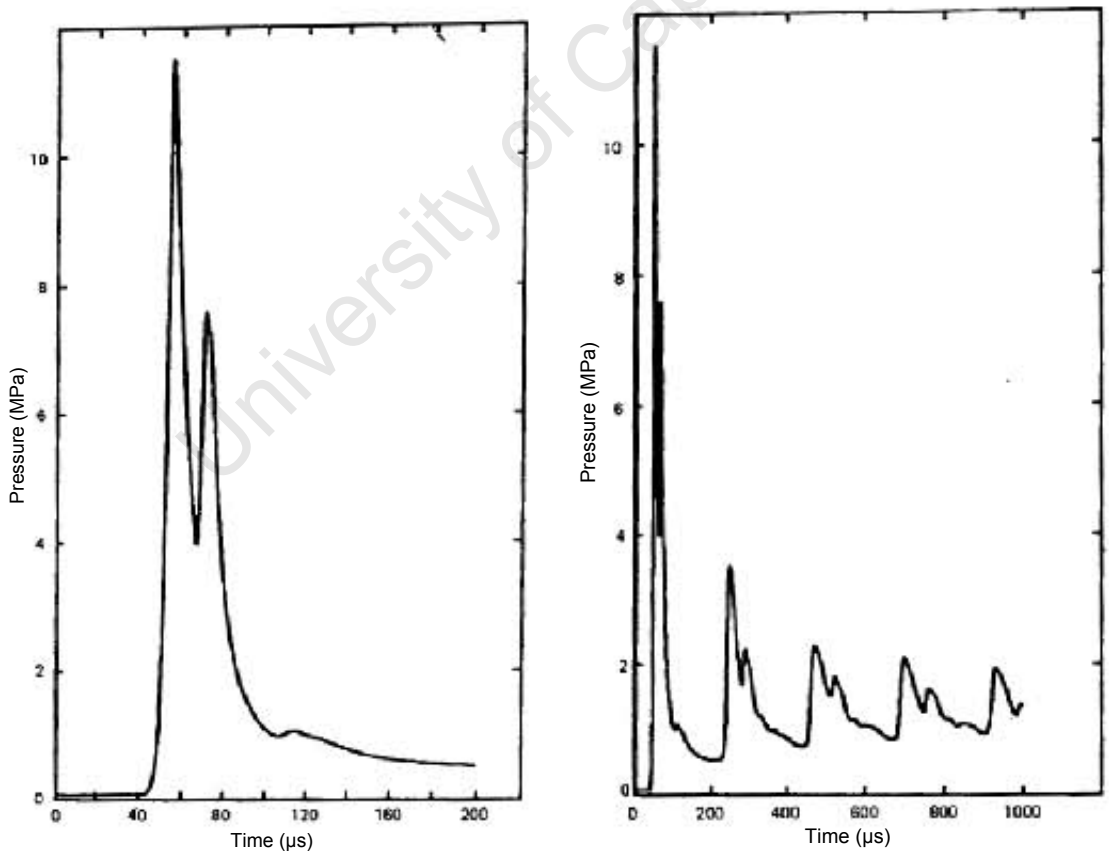

(a) 200μs. (b) 1000μs.

Figure 2.15: Pressure pulse on shell wall for different times following detonation [34].

loads are also evident. Each major pulse exhibits the "double peaked" [34] behaviour described above owing to reflection at the air-explosive interface.

Karpp et al [34] noted that a change in the size of the explosive charge resulted in a pressure pulse of a different shape. With a particular charge size, specifically 14% of the vessel radius, they found the second pressure pulse owing to reflection at the air-explosive interface, was larger than that caused by the initial shock front.

The authors found "good qualitative agreement" [34] between the simulated pressures and those measured experimentally. However the simulated values significantly overestimated the experimental values, particularly for the initial shock front.

2.6.3 Pressure relief and afterburning behaviour

Edri et al [35]

Recent work has focussed on the late-time pressure relief behaviour from partially-confined explosions. Edri et al [35] experimentally investigated the pressure behaviour on the walls of cuboid structures, with particular interest on the relationship between charge mass W and structure volume V on the peak, relatively late-time quasi-static pressure P_{QS}, as defined in Section 2.5.6. Note that the charge mass and structure volume parameters are often expressed as the ratio W/V, and recall that the terms gas pressure and quasi-static pressure may be used interchangeably.

The structure used in the experiments was an almost-cubicle, reinforced concrete room of dimensions ($l \times w \times h$) 2.9m×2.9m×2.7m. The walls were of thickness 0.35m and considered rigid for all tests. The edges of the walls were truncated as indicated in the section and plan views in Figure 2.16, which also shows the circular, central opening in the roof section which remained open to the atmosphere in all tests. The makers in the section view of Figure 2.16 represent the locations of the pressure gauges used in the experiments. The blast loads were generated by detonating centrally-located cuboid TNT charges, and the charge mass was varied in 0.5kg increments between 0.5kg and 4.0kg.

The authors [35] compared the measured pressure values from gauges at the corner P_{corner} of the structure with those measured near the centre P_{centre}. The ratio of $P_{\text{corner}}/P_{\text{centre}}$ increased with increasing charge mass, indicating that the corner pressures become more influential at larger charge masses. However the corner pressures were consistently *lower* than those measured at the centre, which the authors [35] note contradicts the work of Baker [19]. The same behaviour was exhibited by the corner and central impulse values.

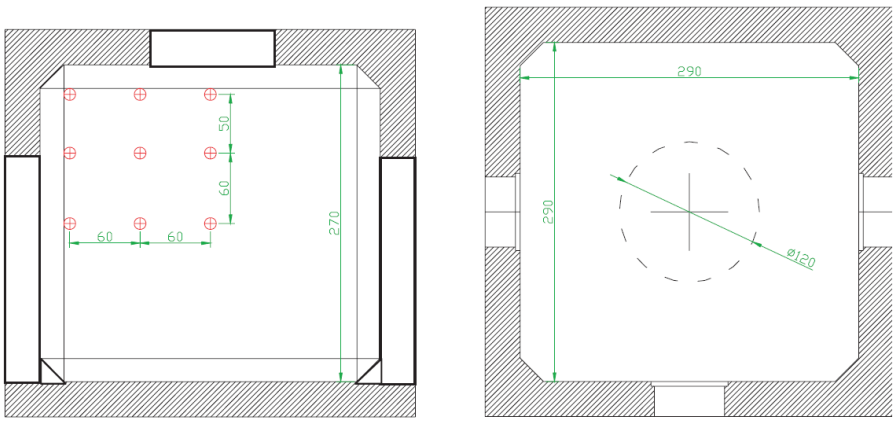

Figure 2.16: Section (left) and plan views of structure used in experiments by Edri et al [35].

Since the present work is concerned only with cylinders, the effect corner amplification is not considered further.

Edri et al [35] analysed the measured pressure-time histories from all the tests, and a typical response is shown in Figure 2.17. With increasing charge mass, the impulse was seen to increase and the arrival time decreased as expected. A second order polynomial, least-squares curve was fit to the measured pressure data. The fitted curve was projected back to time $t = 0$, and the intersection of the projection and the increasing measured pressure signal was defined as the peak quasi-static pressure. This is similar to one of the methods proposed by Kingery et al [33] in Section 2.6.1. As shown in Figure 2.17, there is good agreement between the impulse obtained from the measured pressure signal, and that found by integrating the curve fit.

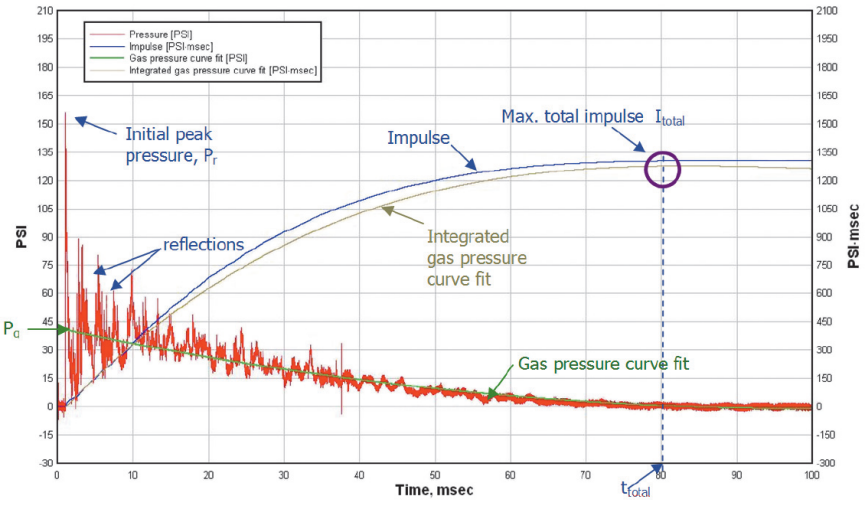

Figure 2.17: Typical pressure-time history from experiments by Edri et al [35].

The peak quasi-static pressures were compared with those predicted according to UFC 3-340-02 [12]. The experimental pressures were consistently 27% lower than those predicted,

which the authors [35] attributed to the subjective nature of the definition of peak quasi-static pressure.

Feldgun et al [36]

Following the experimental work reported by Edri et al [35] described previously, Feldgun et al [36] performed a numerical investigation into the same problem with the aim of adding insight to several aspects of the problem, with particular attention on the late-time pressure attenuation.

The numerical analysis was performed in AUTODYN. The air was modelled as an ideal gas, and the TNT was modelled using the JWL EOS. The material characteristics were taken directly from the AUTODYN material library. The corners of the structure used in the experiments were truncated. In the numerical study, both a truncated and an non-truncated domain were investigated, and the pressure-time history from gauges near the corners were compared. Typical pressure-time histories for a 2D simulation are shown in Figure 2.18. Feldgun et al [36] reported that in 2D and 3D the pressure-time history was both qualitatively and quantitatively affected by the truncation. This effect was considerably smaller for gauges further from the corners, with the differences only apparent following several pressure peaks.

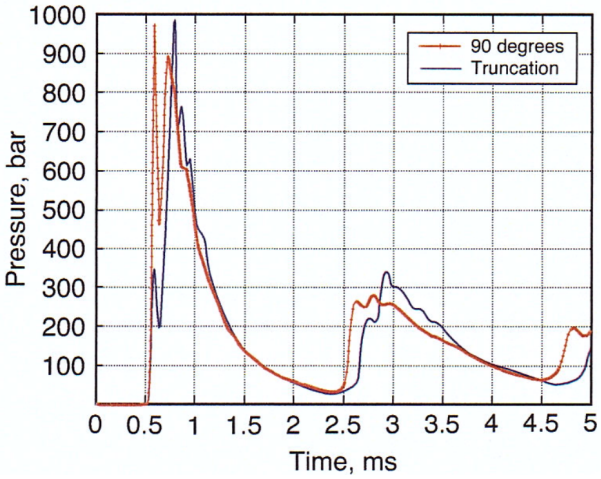

Figure 2.18: Typical pressure-time history from 2D simulations with and without truncations by Feldgun et al [36].

As a means of validating the numerical models, the authors [36] compared the numerical pressure-time histories from a 4kg TNT simulation, with that found both experimentally and from UFC 3-340-02 [12]. In all cases the numerical results were taken from simulations *with* truncated corners, and a typical pressure-time history result is shown in Figure 2.19. The simulated and experimental pressure-time histories exhibited good correlation for the initial pressure peaks, however in the intermediate and late-time range the simulations

significantly underestimated the measured responses. Feldgun et al [36] suggested that this underestimation may be due to the mesh size sensitivity of the numerical model, in which case the quality of the model is questionable. An alternative explanation is that the model ignores the afterburning effect (see Section 2.5.11) which is beyond the scope of the Feldgun et al [36] paper.

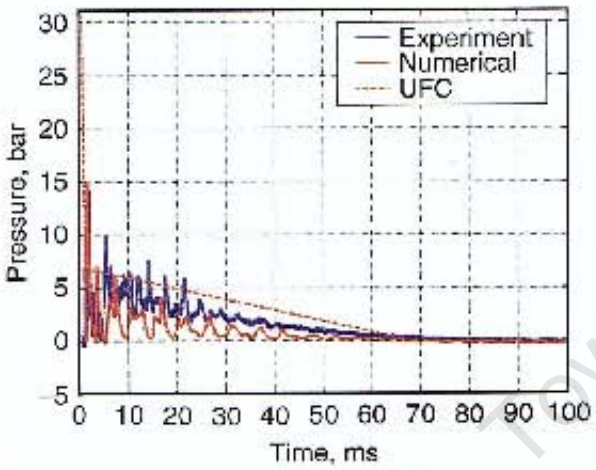

Figure 2.19: Experimental-simulated pressure-time history comparison from 3D simulations by Feldgun et al [36].

To better describe the late-time pressure response, the authors [36] consider the pressure history in two regions: the early, short-duration phase and the longer-duration, late-time relief phase. To better describe this late-time pressure response, Feldgun et al [36] developed a simplified model based on the Bernoulli equation given by

$$p\,(t) = p_{\infty}\left[\frac{M(t)/\Theta}{\rho_{\infty}}\right]^{\gamma} \tag{2.24}$$

where p_{∞} and ρ_{∞} are respectively the atmospheric pressure and original density of the air, Θ is the structure volume, $M(t)$ is the mass of gas filling the structure at time t, and γ is the adiabatic index. The initial pressure P_b and density ρ_b conditions at the start of the relief phase were calculated from an approximate analytical formula [37] based on the energy conservation law. The full derivation of Equation 2.24 is presented by Feldgun et al [36] in the literature.

Figure 2.20 compares the simplified model of Equation 2.24 with the experimental work reported by Edri et al [35] and a prediction from UFC 3-340-02 [12]. The simplified model shows good agreement with the experimental data, and the correlation is significantly better than that of the UFC 3-340-02 [12] prediction which overestimates the experimental response, particularly in the intermediate time range.

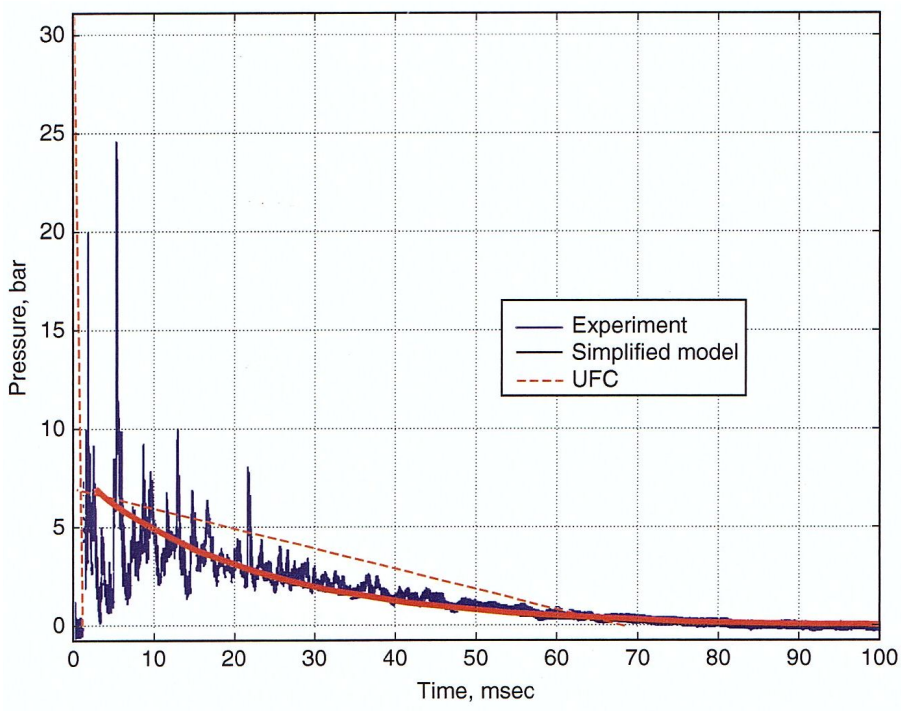

Figure 2.20: Experimental-simulated pressure-time history comparison from 3D simulations using the proposed simplified model for the late-time response by Feldgun et al [36].

Edri et al [25]

The underprediction of the simulated pressure-time histories reported by Feldgun et al [36], prompted Edri et al [25] to study the influence of TNT afterburning on the simulated pressure-time history.

Feldgun et al [37] presented an equation for the residual quasi-static pressure following a fully-confined explosion. Rearranged this equation takes the form

$$P = \left[\frac{P_\infty}{\gamma_\infty - 1}\left(V - v_E\right) + Q\rho_E v_E\right]\frac{\gamma - 1}{V} \tag{2.25}$$

where P_∞ is the atmospheric pressure, γ and γ_∞ are respectively the adiabatic indices of the detonation product-fuel mixture and of pure air, V and v_E are respectively the volumes of the structure and of the charge, and ρ_E is the charge density. The parameter Q is the detonation energy released during the explosion.

Edri et al [25] suggested that, for fully-confined explosions, the afterburning effect may be captured simply by using different values of Q depending on the ratio between the charge mass W and the volume of the structure V.

However for partially-confined explosions, finding this Q value analytically is significantly

more complex, if even possible [25]. Consequently, to account for the afterburning effect, the authors [25] proposed a numerical approach where an amount of additional energy is added to the system after some time. Based on a chemical analysis, the authors [25] found the theoretical energy release ΔH_{ab} due to full afterburning of TNT was 10.01MJ/kg-TNT.

Using the same numerical model as that presented by Feldgun et al [36] and described previously in this section, the authors [25] investigated the effect of incorporating the afterburning effect on the simulated pressure-time histories. The standard JWL EOS does not account for any additional energy to due afterburning. However Edri et al [25] captured this effect in AUTODYN by specifying additional energy into the explosive over a given time interval. This is an optional feature for the JWL EOS in AUTODYN[2], where the required input parameters are: energy per unit mass, initiation time T_0, and termination time T_1.

The time-dependent additional energy curve specified by Edri et al [25] is shown in Figure 2.21. The authors [25] took T_0 as the time when the first shock wave reflected from the nearest wall, and T_1 was specified as the time when the temperature was below the average ignition temperature of the fuels. The maximum value of the additional energy was specified as the theoretical afterburning energy (10.01MJ/kg-TNT).

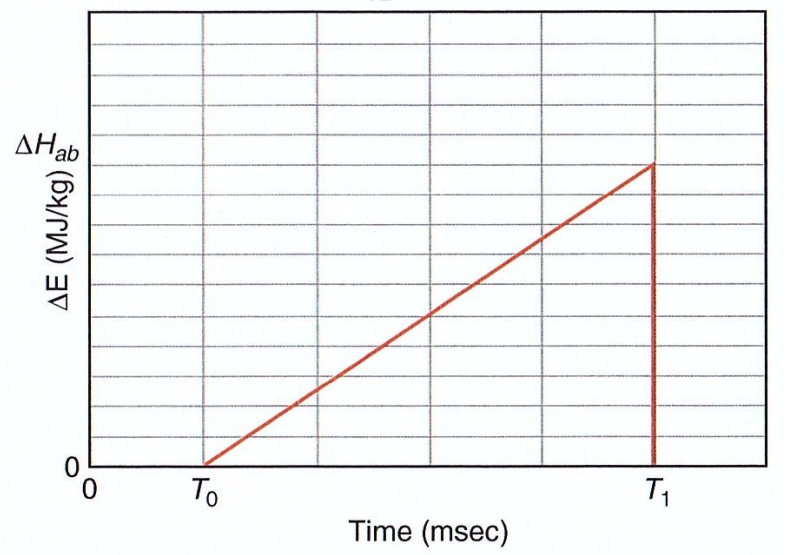

Figure 2.21: Linear time-dependent additional energy used to approximate afterburning in simulations by Edri et al [25].

The authors [25] performed two sets of simulations with a 4kg TNT charge mass: one set ignoring the additional afterburning energy, and one accounting for it. For the case ignoring the additional energy, the experimental and simulated pressure-time curves exhibited good agreement for the first pressure peaks, however the later peaks exhibited

[2]Note that no such option is available in LS-DYNA.

poor agreement as shown in Figure 2.22. Additionally the simulated impulse was significantly lower than that found from the experimental data. Figure 2.23 shows that when the afterburning energy was considered, the experimental and simulated pressure-time curves exhibited a significant improvement in correlation regarding the magnitudes and arrival times of the later pressure peaks. The simulated impulse was also significantly closer to that found experimentally.

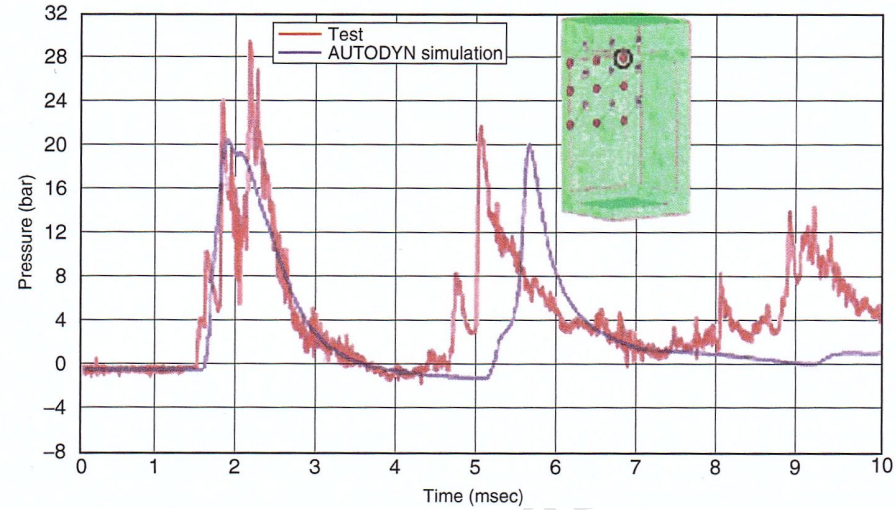

Figure 2.22: Experimental-simulated pressure-time history comparisons for simulations ignoring afterburning by Edri et al [25].

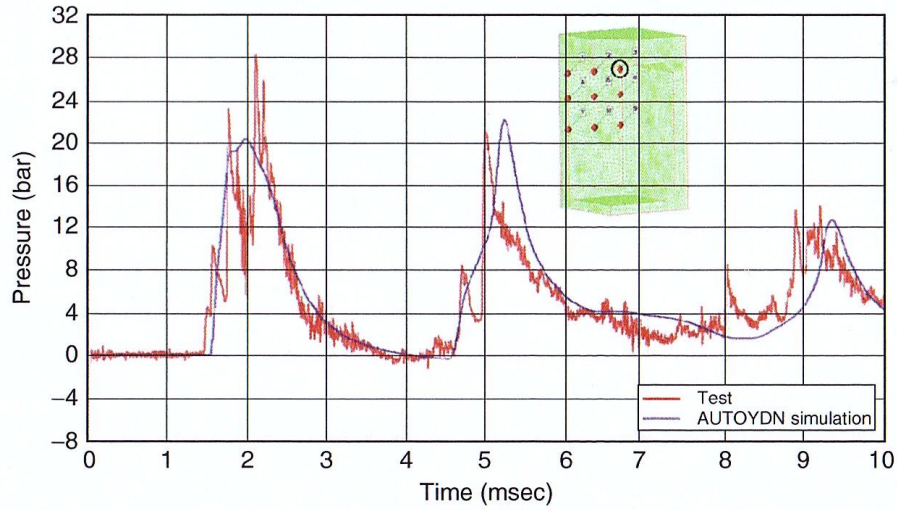

Figure 2.23: Experimental-simulated pressure-time history comparisons for simulations considering afterburning by Edri et al [25].

2.7 Structural response to internal blast loading

Spherical and cylindrical structures are used in several applications to mitigate the effects of internal explosions. Such structures are classified as multiple- or single-use depending on their structural response to blast loading [38].

Structures may be designed for multiple uses in which case the response remains in the elastic regime. Examples of such uses are the testing of explosive components and bomb disposal [38]. If structures are designed for only a single use, they may be designed to absorb significant strain energy as they undergo large plastic deformations [38].

Several major works in understanding the response of such structures to internal explosions are presented in this section. First the response of the spherical vessels is detailed and then that of cylinders.

2.7.1 Response of spherical structures

Baker et al [39, 40]

Baker [40] extended work based on the thin-shell equation of motion for elastic shells [39], to include the elastic-plastic response of the shells. Baker [40] presented two approaches in developing the theory: one which neglected the effects of shell thinning and dilation, and one which considered these effects. The first method lead to a relatively simple linear solution, and a transient equation for radial displacement of the shell wall. The latter solution lead to a relatively complex, non-linear second order differential equation, which must be solved numerically.

Baker [40] considered a small steel shell of radius 15in. (381mm) and thickness 1/16in. (1.6mm) and used the theory to predict the response of the shell to loading from spherical explosive charges detonated at its centre. The pressure-time histories imparted to the shell were predicted from experimental data presented by Hoffman and Mills [41].

As a means of validating the theory, Baker [40] performed several experiments on shells of similar dimensions and properties to those considered above. The shells were made from steel segments that were welded together to form a crude sphere. To determine the elastic response, the shells were subjected to a blast load from a 0.016lb (7.3g) Tetryl charge. The plastic response was obtained by detonating a 0.125lb (56.7g) Pentolite charge, though the shells ruptured at the welds under this load. However, maximum strains were recorded on most of the strain gauge channels before failure of the gauge leads.

Results of the experiments compared favourably with the theory, exhibiting "quite good" [40] quantitative agreement for both the elastic and elastic-plastic responses. Additionally the general form of the measured responses was similar to that predicted by the theory.

Baker [40] noted that a more precise set of experiments on better fabricated shells was required in order to compare the merits of using the simple linear theory as opposed to the relatively complex non-linear theory.

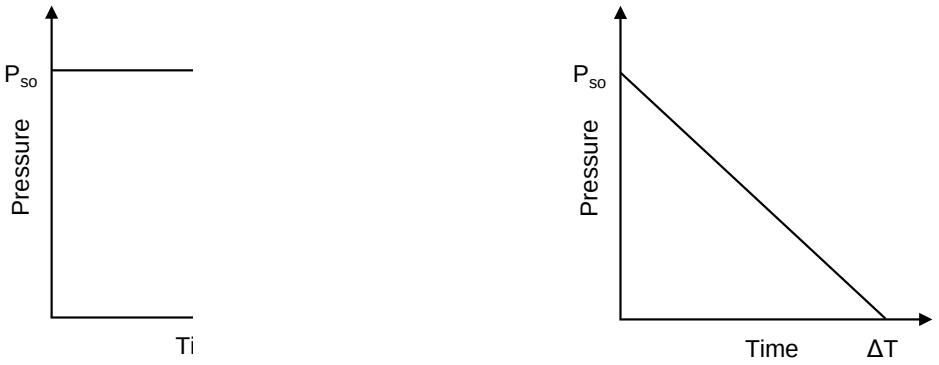

(a) Rectan (b) Triangular pulse.

Figure 2.24: Shapes of pressure pulses considered by Karpp et al [34] in the analysis of shell motion.

The loading was assumed to be a simple rectangular or triangular pressure pulse of amplitude P_{so} and duration ΔT, as illustrated in Figure 2.24. From the one-dimensional equation of motion for a thin spherical shell, Karpp et al [34] determined the strain in the shell wall u given by

$$u = \begin{cases} \dfrac{P_{so}}{\rho h \omega^2} \left[1 - \cos \omega t\right] & \text{for } 0 \leq t \leq \Delta T \\ \\ \dfrac{P_{so}}{\rho h \omega^2} \left[\cos \omega \left(t - \Delta T\right) - \cos \omega t\right] & \text{for } t > \Delta T \end{cases} \tag{2.26}$$

where ρ is the density of the shell material, h is the wall thickness and ω is given by

$$\omega = \sqrt{\frac{2E}{\rho a^2 (1-\nu)}} \tag{2.27}$$

in which E is the Young's modulus, a is the shell radius and ν is Poisson's ratio.

The authors [34] determined the maximum induced strain in the shell wall for two load cases depending on the duration of the pressure pulse. Where the duration of the pressure load was significantly smaller than the natural period of the structure, the response was independent of the pulse shape. Loads of this duration are defined as purely impulsive as detailed in Section 2.5.12.

However, where the duration of the load was not small relative to the natural period of the structure, the effects of the pulse shape were *not* insignificant [34], and thus blast loads of equal magnitudes (but different shapes) may cause different peak strains [34].

The structural response of the vessels was investigated in both 1D and 2D. For the 1D case the calculations gave reasonable quantitative estimates of the initial peak strains with the calculations mostly over-estimating the experimental values. The 2D motion was analysed using the ADINA finite element code. Using only one element through the shell thickness, "fairly good" [34] agreement between the simulated and measured strain histories was reported. The strain-time histories are shown in Figure 2.25 for a typical case [34].

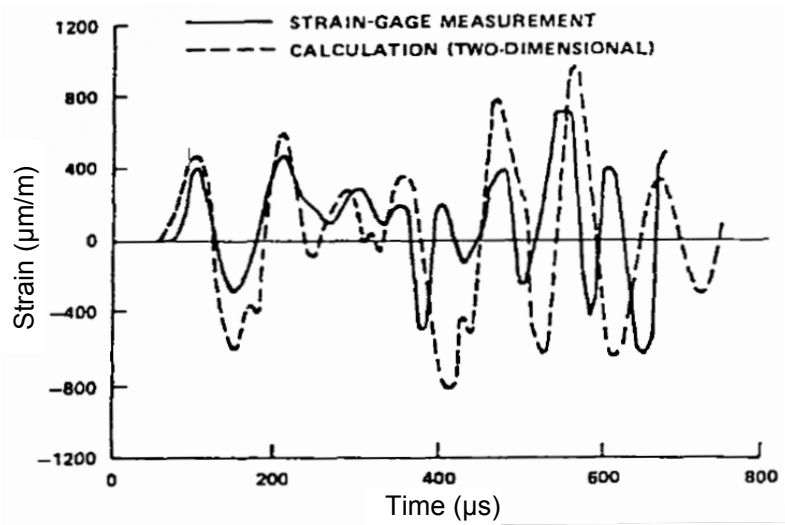

Figure 2.25: Comparison between simulated and experimental strain in the vessel wall by Karp et al [34].

Giglio [42]

In a more recent study, Giglio [42] numerically investigated the response of a spherical vessel to loading due to a centrally-located explosion. Only the initial impulsive loading and ensuing response were considered in the analysis. Giglio [42] considered a spherical steel, air-filled vessel of initial dimensions and properties identical to those studied by Karpp et al [34]. Loading was due to detonation of a centrally-located 25.4mm spherical charge of PBX-9404.

The analytical pressure loading on the vessel was calculated from the fundamental equations of fluid dynamics, assuming the air in the system behaved as an ideal gas. Such an approach avoided the use of the JWL EOS which requires calibration. Giglio [42] compared the experimentally-measured pressure-time history at the vessel wall with that from Karpp et al [34]. Qualitatively the calculated pressure histories showed good agreement.

The structural response of the vessel was investigated using ABAQUS by performing a decoupled analysis using the pressure history calculated previously. The circumferential stress history is shown in Figure 2.26. Giglio [42] noted "substantial" [42] qualitative agreement between the circumferential strain history and that reported by Karpp et al [34]. Quantitatively and qualitatively the stress history was similar to that from the experimental results of Karpp et al [34].

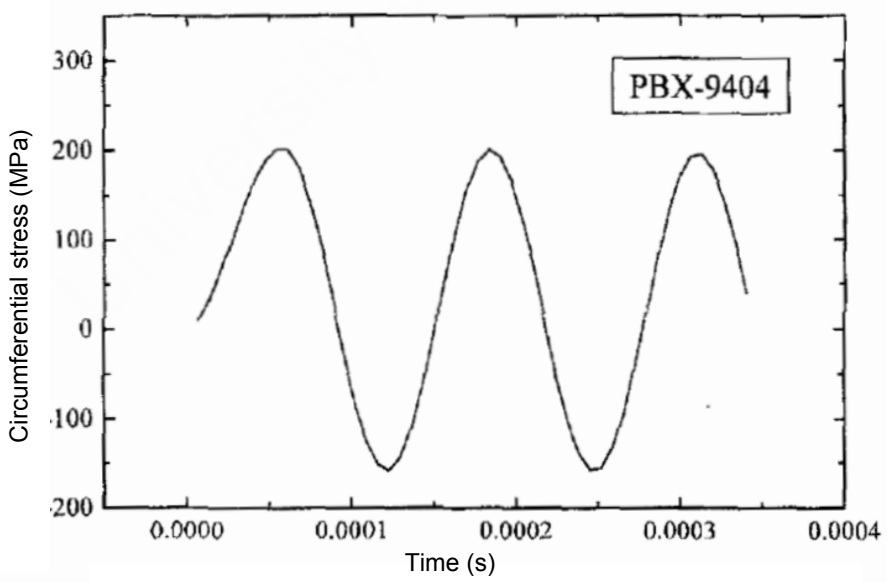

Figure 2.26: Circumferential stress-time history measured by Giglio [42] for shell subjected to load from a 25.4mm spherical PBX-9404 charge.

2.7.2 Strain growth phenomenon

Dong et al [43]

In the preceding studies [31–34], the analyses neglected the structural response of the shell. That is, the shell had been considered as a rigid body for the purposes of determining the primary shock. This method was adopted as it has been reported that the structural response of the shell has negligible effect on the primary shock [43].

While Karpp et al [34] recognised the mechanisms of the reflected shock waves, their importance with respect to the late-time structural response of the shell was not considered until the strain growth phenomenon was observed [43].

Using finite element simulations in LS-DYNA, Dong et al [43] studied the dynamic elastic response of spherical vessels subjected to internal blast loading. This was used as a basis to comprehensively explore the relationship between the shell response and the reflected shock waves.

In accordance with Baker [40] and Karpp et al [34], Dong et al [43] assumed a transient triangular pressure pulse of duration ΔT as illustrated previously in Figure 2.24b. Five different triangular pressure pulses were considered in the study, with each one delivering the same impulse but with different peak pressures and durations.

By comparing the displacement-time histories of a cylindrical shell loaded by these five pressure pulses, Dong et al [43] showed that the displacement of the shell depended mainly on the impulse when the duration of the loading pressure pulse was less than $T_0/4$. When the duration exceeded $T_0/4$, the shell response depended on both the impulse and pulse shape (i.e. peak pressure and duration), and this dependence was enhanced for durations exceeding $3T_0/8$. Here T_0 is the period of the shell breathing mode, given by

$$T_0 = \frac{2\pi a}{\sqrt{\frac{2E}{\rho\,(1-\nu)}}} \tag{2.28}$$

where a is the shell radius, E is the Young's modulus, ρ is the shell density, and ν is the Poisson's ratio [40].

Dong et al [43] investigated the influence of the shell response on calculating the amplitude of the primary shock. The authors [43] ran side-by-side simulations where the shells were assumed to be rigid and elastic. The differences resulting from rigid and elastic simulations were found to be small, supporting the use of a rigid shell for determining the primary shock [43].

When considering the effects of shock reflections on the late-time response of the shells, Dong et al [43] defined a strain growth factor as the ratio of the maximum strain to the first peak strain. The authors [43] used this factor to compare the influence of shock reflections on the structural response of the vessels.

The displacement-time histories of two shells are shown in Figure 2.27 and Figure 2.28. In Figure 2.27, the displacement amplitudes exhibit no sign of gradual growth giving a strain growth factor of 1.042. In this case the frequencies of the displacement and shock reflection histories are far apart.

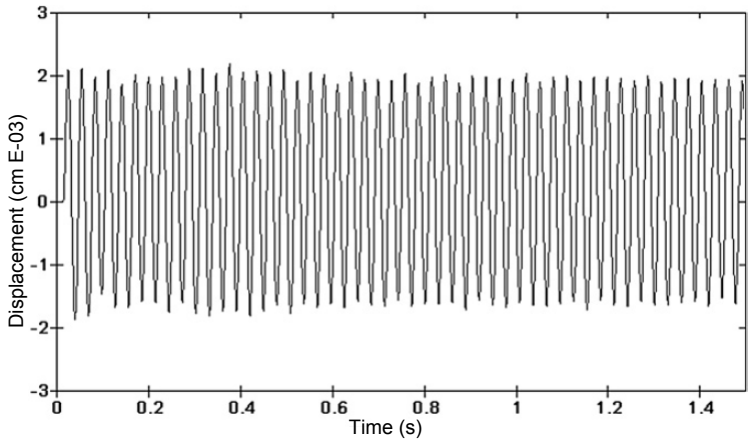

Figure 2.27: Radial displacement-time history for a shell tested by Dong et al [43] with no indication of strain growth.

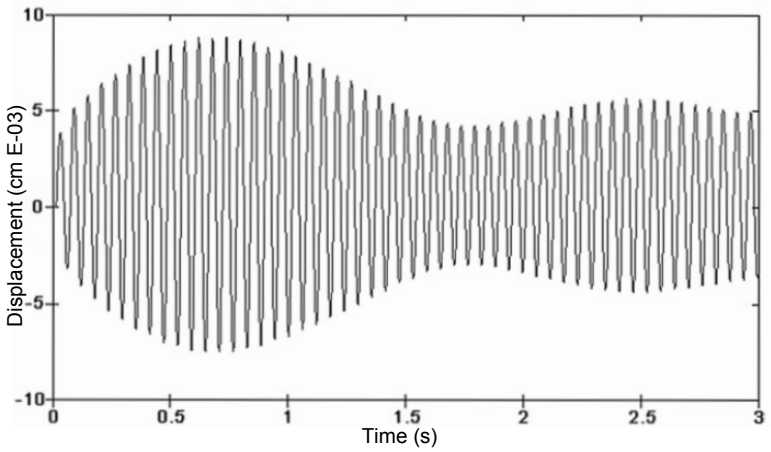

Figure 2.28: Radial displacement-time history for a shell tested by Dong et al [43] with increasing displacements indicating strain growth.

In Figure 2.28, the early peak displacements are amplified to some maximum value before reducing, after which this increase-decrease trend perpetuates. In this case the strain growth factor is 2.283, and the frequencies of the displacement and shock reflection histories are 17.0kHz and 16.6kHz respectively. Since the two frequencies are close together,

and the shell exhibits appreciable strain growth, it suggests that the influence of the reflected shock waves is significant in the late-time response of the shells [43].

It was noted that the displacement of the shell may be amplified or attenuated, depending on the relationships of the frequency and phase between the reflected pressure waves and the shell vibration [43]. When the reflected pressure waves and the displacement history of the shell were in phase, the vibration was amplified, while it was attenuated when they had opposite phases. Further Dong et al [43] observed that when the interaction between the reflected pressure and the shell response was significant, the vibration of the shell influenced the reflected pressure waves.

Figure 2.29 and Figure 2.30 compare the pressure-time histories respectively for a rigid and an elastic shell subjected to the same pressure load. Where the shell vibration is ignored (rigid shell), the reflected pressure pulses gradually attenuate. However when the shell vibration is considered (elastic shell), it is seen that the amplitude of the reflected pressure waves gradually increases when the amplitude of the shell vibration decreases, and vice versa. In cases where the interaction between the reflected pressure and the shell response is insignificant, the pressure-time histories for both rigid and elastic shells are similar.

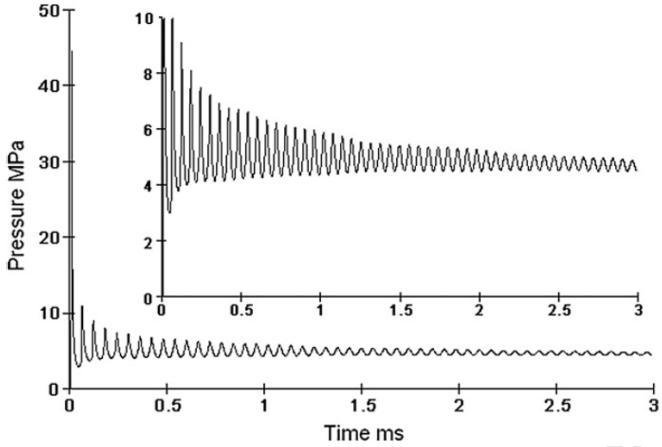

Figure 2.29: Pressure-time history for a rigid shell tested by Dong et al [43] with gradually attenuating pressures.

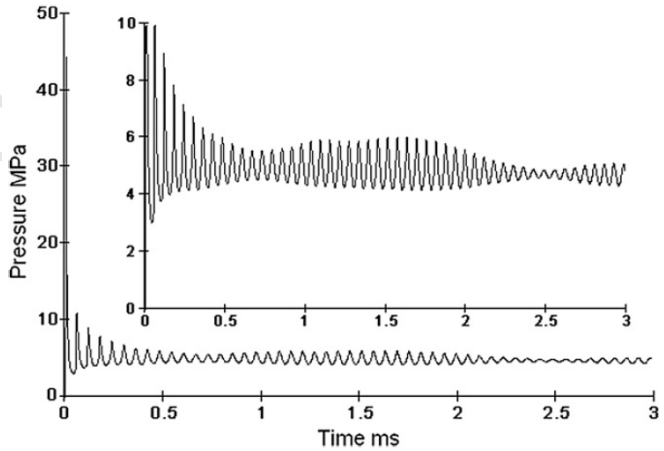

Figure 2.30: Pressure-time history for an elastic shell tested by Dong et al [43] with late-time pressure amplification.

2.7.3 Response of cylindrical structures

Proctor [44]

One of the earliest significant works on cylinders was on the containment ability of closed, water-filled, right-circular cylinders by Proctor [44]. The author [44] developed equations to predict the maximum charge mass from which a cylinder may sustain an internal explosion without rupture. The equations were written in terms of the geometries and basic material properties of the vessel. A comprehensive set of experiments was performed as calibration and validation.

The equations were developed for a water-filled, right-circular cylinder of internal radius R_i, external radius R_e, internal length L, and wall thickness h. The explosive charge was taken as TNT of radius R_c. The following assumptions were made:

- $L \geq 4R_i$
- $10 \leq R_i/h \leq 40$
- $h = R_e - R_i$
- $R_i \geq 3R_c$
- the water is in a liquid state
- the cylinder material is homogeneous and isotropic
- the explosive charge is compact (length $\approx$ diameter) and detonated at the centroid of the vessel
- the cylinder contains no discontinuities.

Proctor [44] performed approximately 100 experiments to determine the value of a lumped parameter function required for the containment equations. Several cylinders of various lengths, diameters, wall thickness and materials were investigated. The cylinders were filled with water and loaded by detonating a compact Pentolite charge at the centroid of the vessel. At least four cylinders with different charge masses were tested for each combination of size and material. The deformation-time history was recorded with a high-speed camera and a typical, uniform deformation progression is shown in Figure 2.31.

For explosions in both water and air, Proctor [44] found that there was no significant cylinder deformation beyond an axial length of four times the cylinder radius. With the data from these experiments, Proctor [44] produced an "explosion containment equation" [44] for ideal cylinders.

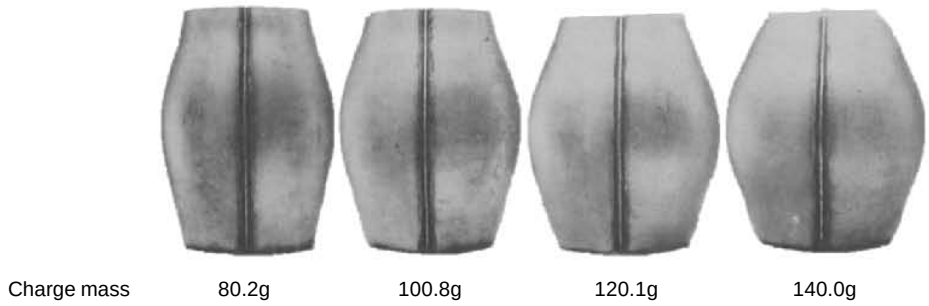

Figure 2.31: Typical uniform deformation increase with charge mass for water-filled cylinders tested by Proctor [44].

The average deviation of the experimental results from this equation was $+5\%/-6\%$ which the author considered "excellent" [44] in the light of the repeatability of explosive phenomena. It should be noted that while not all the experimental data were used to calibrate the ideal containment equation, it is nonetheless unsurprising that the analytical and experimental data are in close agreement.

Youngdahl [45]

Youngdahl [45] studied the dynamic plastic response of long cylinders loaded by internal pressure pulses of different shapes. In a purely theoretical investigation considering a rigid-perfectly plastic cylinder, Youngdahl [45] showed that neither pulse shape nor peak overpressure were important in determining the plastic deformation of the cylinders.

Duffey and Mitchell [30]

According to Duffey and Mitchell [30], the work of Proctor [44] was not suitable for basic design calculations since it did not predict the deformation profile or strain distribution. Furthermore the study was based on water-filled cylinders [30]. The Youngdahl [45] study lacked validation, as it did not present any comparison of the theory with experimental work.

Duffey and Mitchell [30] developed a theoretical solution for determining the final deformation of air-filled, right-circular cylinders, subjected to loading from centrally-located explosive charges. The theory was compared with a set of experiments for validation.

To predict the loading on the cylinder wall, the authors [30] considered a generic point q on the wall of a long cylinder with radius a and thickness h. The point is located an axial distance x from the charge which is at the centroid of the structure. This geometric arrangement is shown in Figure 2.32. The loading was assumed to comprise only an initial shock phase, which was taken as a purely impulsive load with an instantaneous

application time. The long-term quasi-static pressure was neglected as it was not thought to cause additional structural deformation.

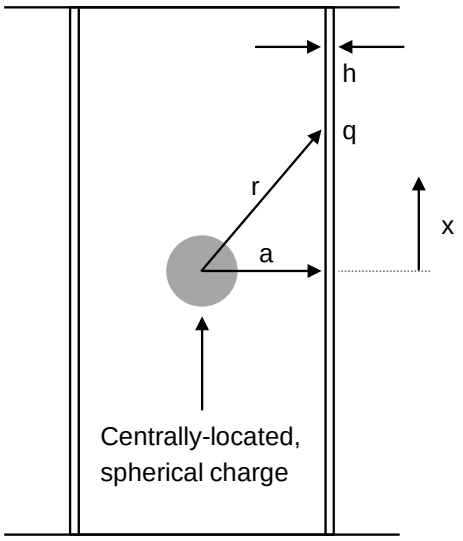

Figure 2.32: Geometry of the analytical problem adapted from Duffey and Mitchell [30].

The effective impulse imparted to the cylinder at point q is given approximately by

$$I_{\text{eff}} = (I_{nr} - I_{so}) \frac{a}{\sqrt{a^2 + x^2}} + I_{so} \tag{2.29}$$

where I_{nr} is the resultant impulse imparted to the wall at normal incidence, and I_{so} is the side-on impulse. At small stand off distances, the resultant impulse is small relative to the side-on impulse and was consequently ignored by Duffey and Mitchell [30] in Equation 2.29. The authors [30] obtained values for these impulses from expressions presented by Goodman [46].

To predict the structural response of the cylinder wall, Duffey and Mitchell [30] assumed a cylinder material that was rigid-plastic with linear strain hardening. Strain rate sensitivity was included according to the form

$$\frac{\sigma_y^D}{\sigma_y} = 1 + \left(\frac{\dot{\epsilon}}{D}\right)^{1/q} \tag{2.30}$$

where σ_y^D is the material dynamic yield strength, σ_y is the static yield strength, $\dot{\epsilon}$ is the strain rate, and D and q are the Cowper-Symonds [47] calibration constants.

The cylinder was taken to be sufficiently long as to negate the effects of the boundary conditions at the ends of the cylinder. By neglecting the axial bending moment, the motion of axially adjacent cross sections was decoupled, reducing the problem to a 1D stress state [30].

Because the loading was considered purely impulsive, the peak radial deflection was found by equating the initial kinetic energy of the shell with the plastic strain energy of deformation, giving an equation for the radial strain as function of axial position x

$$\epsilon(x) = \left[\frac{1}{\lambda^2} + \frac{I_{\text{eff}}^2(x)}{\rho h^2 \lambda \sigma_y^D}\right]^{1/2} - \frac{1}{\lambda} \tag{2.31}$$

where λ is the linear strain hardening parameter.

To validate the theoretical predictions, Duffey and Mitchell [30] performed a series of experiments on annealed mild steel cylinders. All cylinders were loaded by detonating centrally-located, spherical C4 charges, and radial strain measurements were taken at various axial positions.

For the mild steel cylinders, Duffey and Mitchell [30] found "reasonable" [30] agreement between the predicted peak strains and those measured experimentally. An example of the results is shown in Figure 2.33 where the two experimental strain curves are diametrically opposite. The predicted peak strains were consistently lower than the measured strains, which the authors [30] attributed to the strain rate sensitivity approximation.

Figure 2.34 compares the theoretical peak strains with experimental values from Wise and Proctor [48] for 304 stainless steel cylinders, the same material used in the present work. In Wise and Proctor [48] the effect of strain rate sensitivity was ignored and it is clear that the correlation is again very good.

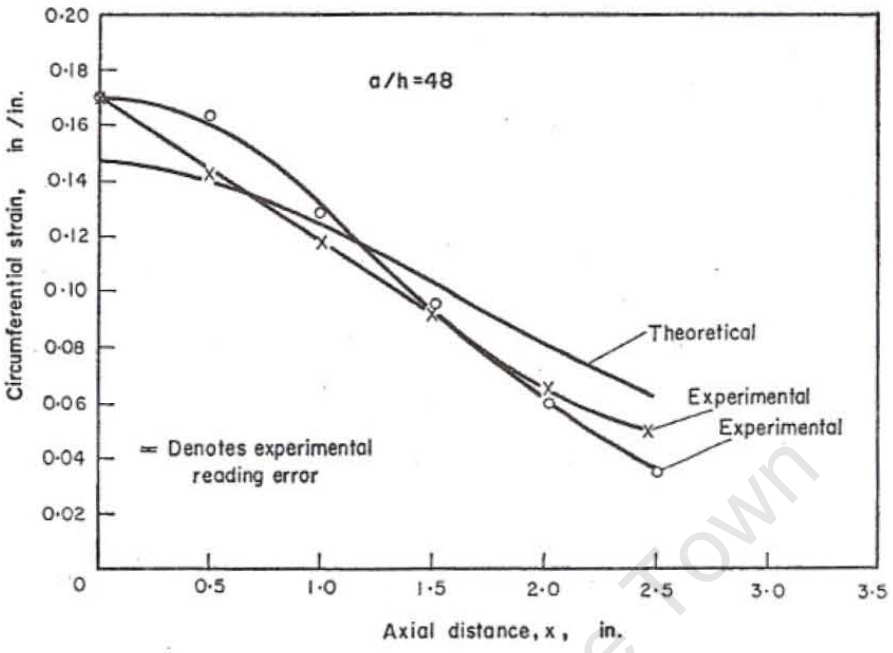

Figure 2.33: Comparison of predicted and experimental strain profiles for a mild steel cylinder subjected to a blast load from an 80g C4 charge [30].

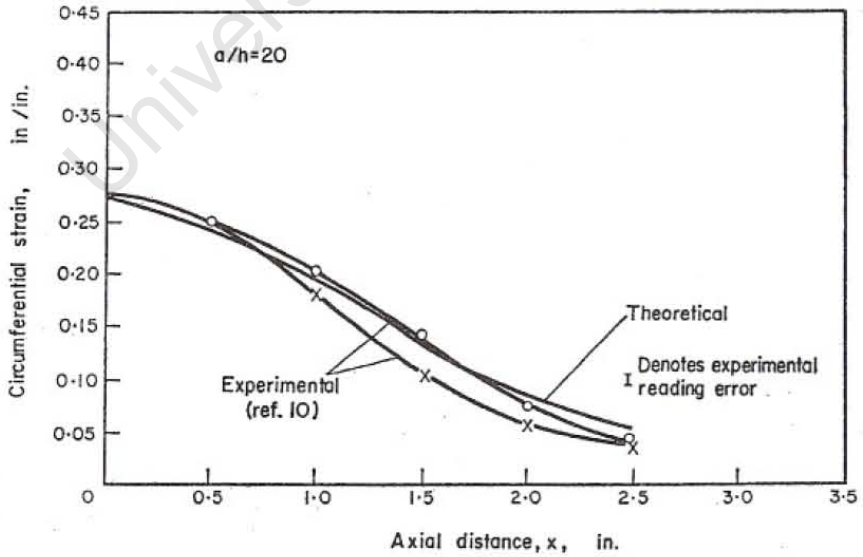

Figure 2.34: Comparison of predicted and experimental strain profiles for a stainless steel cylinder subjected to a blast load from a 50g Pentolite charge [30].

Benham and Duffey [5]

In a follow on study, Benham and Duffey [5] considered the effects of end caps on the containment ability of air-filled cylinders. The authors [5] developed a theoretical equation to predict the peak radial deformation of the cylinder wall, and this was compared to the results of experiments for validation. The background to this study is presented in detail in Section 3.1, where it is used as the basis for the experimental design in the present work.

The load applied to the cylinder wall was assumed to comprise an initial impulse I_0, followed after some delay time T by an exponentially decaying, quasi-static pressure of peak magnitude P_0. The form of this pressure load is shown later in this report in Figure 3.1.

From the equation of motion for the purely radial response of the cylinder wall and the strain displacement relationship $\epsilon = \omega/a$, Benham and Duffey [5] present the following differential equation

$$\frac{\mathrm{d}^2\omega}{\mathrm{d}t^2} + \frac{\lambda\sigma_y^D}{\rho a^2}\omega + \frac{\sigma_y^D}{\rho a} = \frac{I_0}{\rho h}\delta\left(t\right) + \frac{P_0}{\rho h}U\left(t-T\right)e^{\left[-\alpha(t-T)\right]} \tag{2.32}$$

Two solution methods arise from this differential equation: one each both ignoring and considering the effect of strain rate sensitivity. If the effect of strain rate sensitivity is ignored (i.e. for constant σ_y^D), and for initial conditions $w(0) = 0$ and $\mathrm{d}w/\mathrm{d}t(0-) = 0$, a closed-form solution to this differential equation exists. However where σ_y^D is taken as variable, no closed-form solution is possible and the differential equation must be solved numerically. These solutions are presented in more detail in Section 3.1.4 and Section 3.1.5 respectively.

Benham and Duffey [5] noted that, depending on the solution method, Equation 2.32 produces the theoretical lower and upper bounds on the peak final deformation of the cylinder. The lower bound is given by ignoring strain rate effects and assuming no quasi-static pressure build up. The upper bound is given by the numerical solution to Equation 2.32, with the quasi-static pressure applied immediately.

To investigate the validity of the theoretical predictions, Benham and Duffey [5] performed several experiments on steel cylinders of length 21in. (533.4mm), diameter 10.5in. (266.7mm), and wall thickness 0.25in. (6.35mm). The cylinders were placed between massive end caps which were bolted together, as illustrated in Figure 2.35. Loading was achieved by detonating a bare, spherical charge of C4 located at the centroid of the structure.

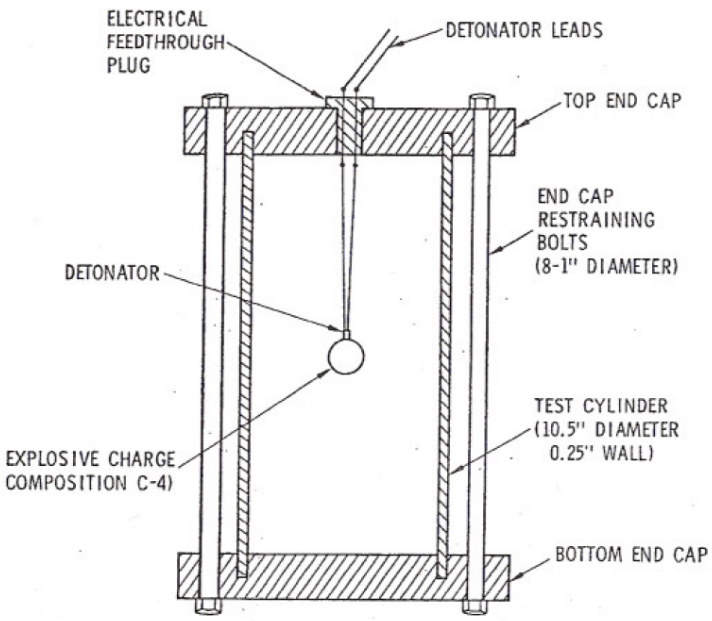

Figure 2.35: Schematic of the experimental set up used by Benham and Duffey [5].

Figure 2.36 compares the theoretical and experimental final deformations of the cylinders as a function of charge mass. The curves are the theoretical predictions and the data points are the experimental results.

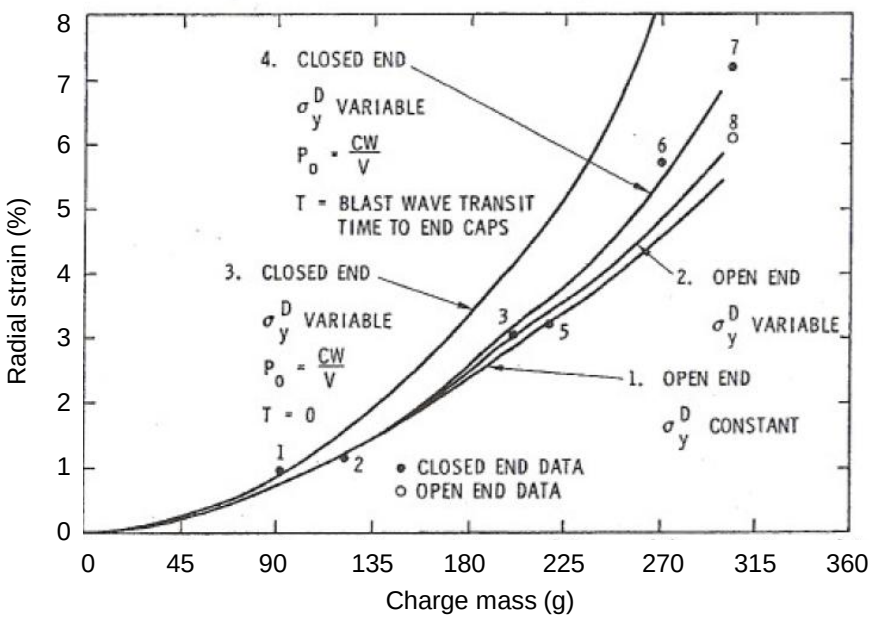

Figure 2.36: Comparison of the theoretical and experimental peak radial deformations for various charge masses [5].

Benham and Duffey [5] noted the following about the four theoretical curves:

- Curve 1 is the closed-form solution to Equation 2.32 for an open-ended cylinder ($P_0 = 0$) with a constant dynamic yield stress. This is the lower bound on the peak final strain of the cylinder.
- Curve 2 is the numerical solution to Equation 2.32 for an open-ended cylinder ($P_0 = 0$) with a variable dynamic yield stress.
- Curve 3 is the numerical solution to Equation 2.32 for a closed-ended cylinder with a variable dynamic yield stress. The effect of the quasi-static pressure acts with a zero delay time ($T = 0$). Since these conditions are the worst-case loading scenario, this is the upper bound on the peak final strain of the cylinder.
- Curve 4 is similar to Curve 3 except that the quasi-static pressure is applied after a non-zero delay time. The delay was taken as the time for the shock wave to propagate from the charge to the end cap as described previously.

The authors [5] found the level of agreement between the predictions (particularly Curve 4) and the experimental results "remarkable" [5] in the light of the number of approximations used to develop the theory. From Figure 2.36 it is clear that the influence of the quasi-static pressure is more significant at higher charge masses.

To investigate the influence of the quasi-static pressure, Benham and Duffey [5] defined an "effective internal pressure ratio" [5] given as

$$\bar{\eta} = \frac{CW}{V}\frac{a\sigma_u}{h}\left(\frac{t_{\max} - T}{t_{\max}}\right) \quad \text{where } \bar{\eta} = 0 \text{ for } T > t_{\max} \tag{2.33}$$

where $t_{\max}$ is the time to peak deformation, and σ_u is the material ultimate tensile strength. The ratio is the effective ratio of theoretical quasi-static pressure to static burst pressure of the cylinder. If $T > t_{\max}$ then the final deformation is unaffected by the quasi-static pressure.

The influence of the quasi-static pressure is isolated from the impulsive loading in Figure 2.37, where the ratio of peak strains for closed-ended cylinders to open-ended cylinders is plotted as a function of the effective internal pressure ratio. The influence of the quasi-static pressure is indicated by the divergence of the curve from unity, where further away indicates more influential. The closed- and open-ended strains were calculated using the theory of Curves 4 and 2 respectively. For the configurations tested, the quasi-static pressure had negligible effect where $\bar{\eta} < 0.3$. Where $0.3 < \bar{\eta} < 0.8$, the influence was

significant, while for $\bar{\eta} > 0.8$ the reliability of the theory is questionable owing to the steepness of the curve in this region [5].

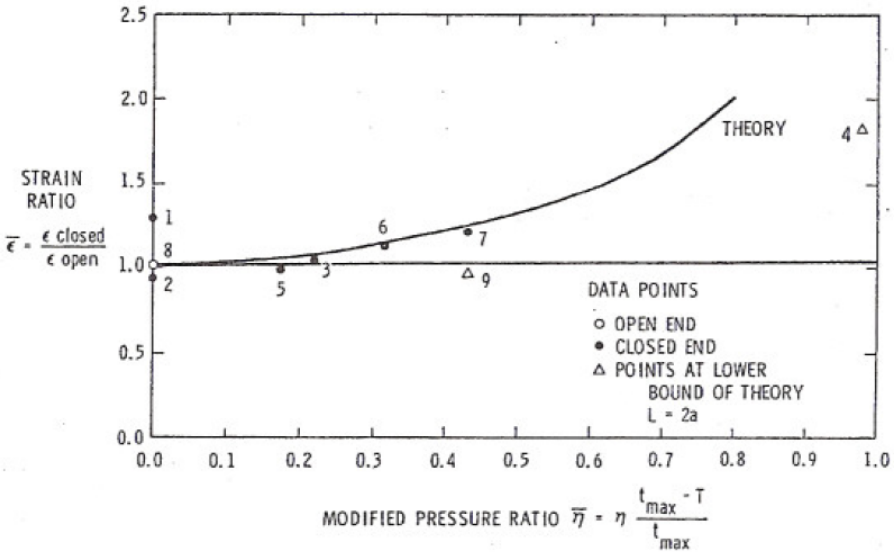

Figure 2.37: The influence of the quasi-static pressure on the final deformation cylinders [5]. Greater influence is indicated by greater divergence from unity.

Rushton [49]

Rushton et al [49] present a more recent study on the internal blast loading of steel pipes, in order to determine the failure mechanism of pipe at high loading rates. The study compared previous theoretical work [50, 51] with numerical simulations and experiments by Rushton et al [49].

Experiments were performed on open-ended, seamless, mild steel pipes of length 800mm, diameter 324mm, and wall thickness 9.5mm. The pipes were loaded by detonating a charge of PE4 located at the centroid of the pipe. The explosive charge was shaped as a circular cylinder and detonated at both flat ends as illustrated in Figure 2.38. The charge was detonated at both ends to improve the symmetry of the problem, and to amplify the impulsive loading due to the interaction of two shock waves at the centre of the pipe [49].

Simulations were performed using AUTODYN with both the von Mises and Johnson-Cook [52] material models, and the plastic hoop strains predicted by these models for various charge masses were compared. The results are shown in Figure 2.39 where the strains were recorded from strain gauges attached to the pipes. The disparity between the two simulated plots in Figure 2.39 illustrates the significance of strain rate sensitivity in predicting the response of the pipes. It is also clear that the correlation between the two experimental results and the Johnson-Cook [52] prediction is very good.

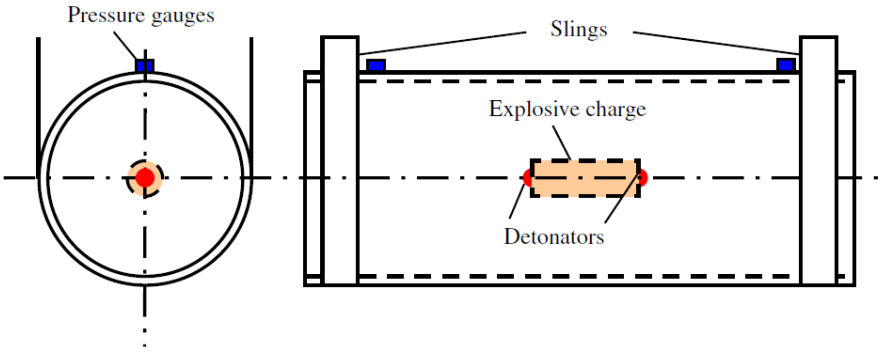

Figure 2.38: Schematic of the experimental set up used by Rushton et al [49].

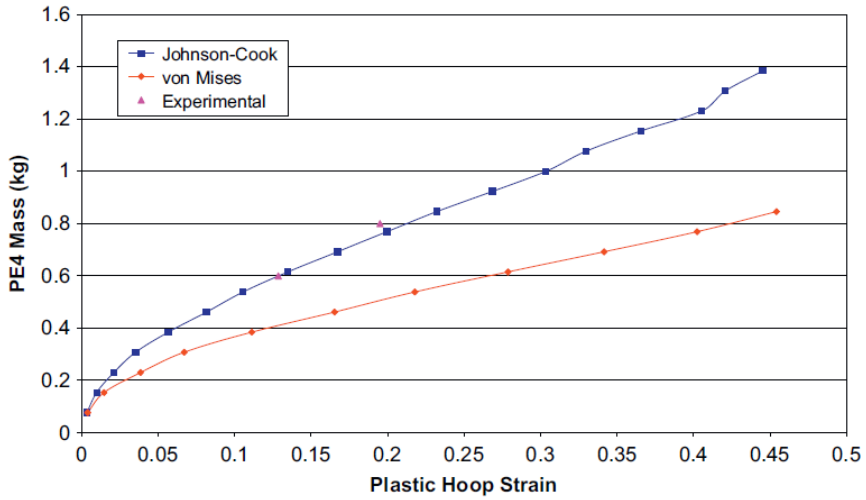

Figure 2.39: Comparison of the maximum plastic hoop strain predicted by different AUTODYN material models, as well as experimental data points [49].

Rushton et al [49] investigated the effect of charge shape on the response of the pipes using AUTODYN. For the cylindrical charge as the ratio of radius to length (r/l) decreases, a significant increase in peak pressure and impulse was observed. When the charge shape was spherical and detonated at its centre, the pipe deformation was less than that due to an equivalent mass cylindrical charge detonated at both ends. Based on this, the authors [49] suggested that the shock transmission through the explosive had a significant effect on the impulsive loading [49]. It should be noted that Rushton et al [49] came to this conclusion from only a single simulation and without any experimental support.

For the analytical analysis, the impulse acting on the pipes was taken from the extensive data in TM5-1300 [53], and the plastic hoop strain was predicted using the analytical models proposed by Duffey and Micthell [30], Fanous and Greimann [50], and Clayton [51]. However no comparison was provided with the experimental results since the data from TM5-1300 [53] is based on spherical charges, and the experiments used cylindrical charges detonated at both ends [49].

2.8 Numerical modelling with hydrocodes

A hydrocode is a computational tool for modelling the behaviour of continua. Hydrocodes describe fluid flow at various speeds and have been adapted to handle material strength and rheology. Collins [54] outlines the fundamentals of hydrocodes and the relevant areas are presented in this section.

2.8.1 Basic procedure

The geometry of the continuum system of interest is discretized into cells of finite dimension which is referred to as the domain or the mesh. The code considers both the internal and external forces acting on each element in the mesh. Over a short period of time known as the timestep, these forces are assumed constant and their effect is used to adjust to the geometry of the mesh. The forces are then recalculated and the process repeats until a satisfactory solution is found.

Typically three relations are used to determine the forces acting on the mesh: the conservation laws, an EOS, and a constitutive relationship. The conservation laws are a set of differential equations that describe the balance of mass, momentum and energy in the system. The EOS relates pressure to density and internal energy and thus accounts for compressibility effects and irreversible thermodynamic processes. The constitutive model describes the effect of material deformation by relating stress to some combination of strain, strain rate, internal energy and damage [54].

2.8.2 Lagrangian and Eulerian descriptions

The conservation equations may be represented either with respect to the material itself, or with respect to a fixed point in space. The former is known as the Lagrangian or material description and the latter as the Eulerian or spatial description. The Lagrangian description is typically used for modelling solids, while the Eulerian is used for modelling fluids.

Lagrangian description

In the Lagrangian description, the mesh is attached to the material and deforms with the material as it deforms as illustrated in Figure 2.40. The forces acting on each cell are computed and the deformation is calculated from the constitutive relations for force and deformation. Mass, momentum and energy are transported by material flow. The mass

of each cell is constant, thus changes in density are a result of changes in cell volume only. Since the history of the material within a cell is tracked, the Lagrangian description is able to describe history-dependent phenomena such as strain hardening or plastic work. However the description may be inaccurate when cells experience large deformations [54].

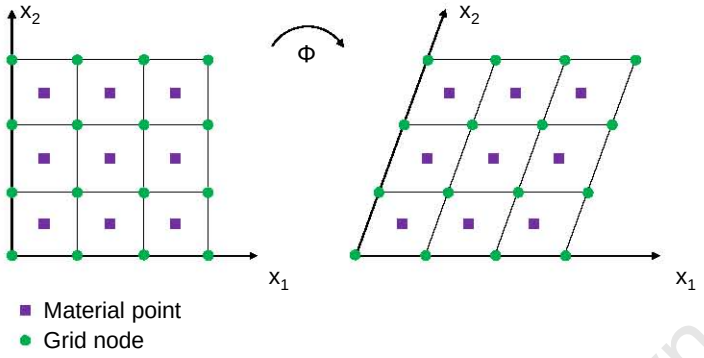

Figure 2.40: Illustration of mesh moving with material under deformation.

Eulerian description

In the Eulerian description, the mesh is fixed in space and the material flows through the mesh as illustrated in Figure 2.41. Mass, momentum and energy flow across cell boundaries. The volume of each cell is constant, thus changes in density are a result of changes in cell mass only. Since the material flows through the mesh the space around the body must be modelled, and consequently a larger number of cells is required to achieve the same spatial resolution as the Lagrangian description for a given body. This may add significantly to the computational expense [54]. An advantage of the Eulerian description is that it allows for mixing of materials within cells referred to as multi-material (MM) cells.

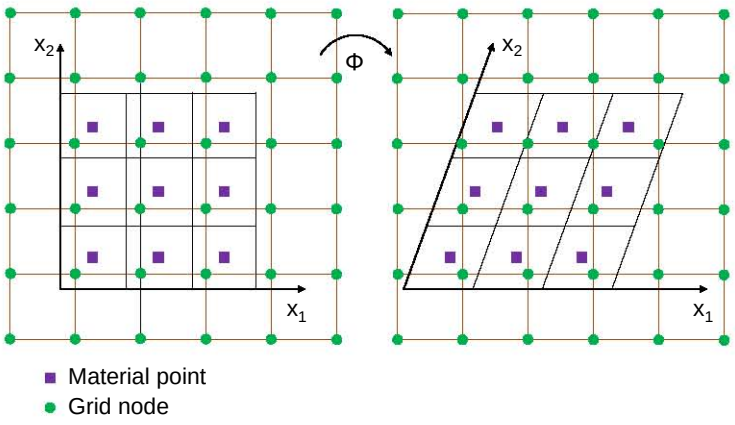

Figure 2.41: Illustration of material moving through mesh under deformation.

2.8.3 Discretization

In the same way that the continuum system of Section 2.8.2 is discretized, so too the governing differential equations must be discretized to be computed numerically. Three techniques are used to do so: the finite element method (FEM), the finite difference method (FDM) and smooth particle hydrodynamics (SPH) [54].

Finite difference method

In the finite difference method (FDM), the derivatives in the conservation equations are replaced by difference equations. The difference equations are calculated at discrete points in the mesh, that is the continuous space is discretized point-wise. For some function F calculated at spatial point x_n or temporal pointt_n, the centrally-approximated, first- and second-order spatial derivatives, as well as the first- and second-order time derivatives are respectively

$$\frac{\partial F(x_n)}{\partial x} = \frac{F(x_n + 1) - F(x_n - 1)}{2\Delta x} \tag{2.34}$$

$$\frac{\partial^2 F(x_n)}{\partial x^2} = \frac{F(x_n + 1) - 2F(x_n) + F(x_n - 1)}{\Delta x^2} \tag{2.35}$$

$$\frac{\partial F(t_n)}{\partial t} = \frac{F(t_n + 1) - F(t_n - 1)}{2\Delta t} \tag{2.36}$$

$$\frac{\partial^2 F(t_n)}{\partial t^2} = \frac{F(t_n + 1) - 2F(t_n) + F(t_n - 1)}{\Delta t^2} \tag{2.37}$$

The FDM typically requires a structured mesh, that is the cells must be arranged in rows and columns. Consequently additional techniques may be required to solve problems with complex geometries.

Finite element method

In the finite element method (FEM), the continuous space is divided into discrete elements. The elements may be either rectilinear or curved and need not be structured. Consequently the FEM is better suited to problems with complex geometries than is the FDM. The necessary equations are solved on an element-by-element basis and then combined. This enables the FEM code to take advantage of parallel processing thus reducing computation time [54].

Smooth particle hydrodynamics

Smooth particle hydrodynamics (SPH) involves the motion of a set of points for which the velocity and thermal energy are always known. Each point is assigned a mass and thus the points are referred to as particles. Using complex interpolation techniques, the forces experienced by each particle are calculated and the particles moved accordingly. SPH is inherently Lagrangian but the particles are not connected, and thus it does not suffer under large deformations. SPH codes are favoured for fluid flow problems involving relatively small density changes and simple boundary conditions as well as impact/penetration problems [54, 55].

2.8.4 Stability

Hydrocodes suffer from numerical instabilities inherent in the discretization schemes. Unexpected large, high frequency oscillations in either space or time may be a result of numerical instability. Limiting conditions on the timestep may be used as a method for mitigating numerical instability. Collins [54] describes three such conditions:

1. The timestep $\mathrm{d}t$ should not exceed the time taken for sound to cross a cell, that is

$$\mathrm{d}t < \min\left(\frac{\mathrm{d}x}{c}, \frac{\mathrm{d}y}{c}\right) \tag{2.38}$$

   where $\mathrm{d}x$ and $\mathrm{d}y$ are the cell dimensions, and c is the speed of sound in the material for a rarefaction wave, or the shock front velocity for shock wave. The min implies the minimum of all cells in the mesh. This is known as the Courant condition on sound signal propagation.

2. The timestep dt should be chosen to ensure that fluid cannot be moved more than approximately one cell width per timestep, that is

$$\mathrm{d}t < \min\left(\frac{\mathrm{d}x}{|u|}, \frac{\mathrm{d}y}{|v|}\right) \tag{2.39}$$

where u and v are the velocities in the x and y directions respectively. This is known as the Cauchy or convective flux limit.

3. A further condition exists for cases where viscous effects are included. The timestep $\mathrm{d}t$ should be small enough so that momentum diffuses less than a single cell width per timestep, that is

$$\mathrm{d}t < \frac{\rho \mathrm{d}x^2 \mathrm{d}y^2}{2\left(\lambda + 2\eta\right)\left(\mathrm{d}x^2 + \mathrm{d}y^2\right)} \tag{2.40}$$

where λ and η are the bulk and shear viscosities respectively.

Chapter 3

Preliminary Analytical Modelling

The experiments in the present work are concerned with the structural response of partially-confined, right-circular cylinders subjected to internal blast loading from spherical PE4 charges. The experimental geometry is derived from scaling previous work by Benham and Duffey [5], while the material is chosen subject to acceptable local availability.

The experiments are performed on the horizontal ballistic pendulum at the Blast Impact and Survivability Research Unit (BISRU). A test rig is designed to attach the cylinders to the pendulum.

In this section the analytical solutions of Benham and Duffey [5] are presented in detail from first principles. These solutions are then solved numerically in MATLAB R2010a. Several of the experiments performed by Benham and Duffey [5] are simulated using LS-DYNA Release 6.0.0, and the results of these simulations are compared with the analytically predicated solutions.

Details of the cylinder geometry and material used in the present work are described and the analytical equations are then adapted to the present work and the resulting predictions are presented.

3.1 Development of the analytical solutions

As presented in Section 2.7, Duffey and Mitchell [30] studied the structural response of right-circular cylinders to loading from centrally-located explosive charges. The Benham and Duffey [5] paper extended this work to consider the effects of end caps on the containment ability of the cylinders. That is, where Duffey and Mitchell [30] considered only open-ended geometries, Benham and Duffey [5] investigated the more complex case of closed-ended configurations. Regardless of the approach used for the analytical models, a simplified pressure load must be assumed. A brief overview of several such assumed loads is given in the following section, after which the Benham and Duffey [5] methodology is detailed starting in Section 3.1.2.

3.1.1 Overview of analytical pressure-time descriptions

As shown previously in Section 2.6, the pressure-time history for a confined explosion is characterised by a short-duration, initial peak, followed by several subsequent peaks of significantly smaller magnitude. In a partially-confined explosion, the openings enable the pressure to vent so that it approaches atmospheric conditions with sufficient time. The rate at which the pressure in the structure converges is dependent on the size and positions of the openings.

Several possibilities exist to describe the complex pressure growth and decay phenomenon analytically. Regardless of the chosen approach, it remains an approximation of reality.

Benham and Duffey [5] present a load of the form shown in Figure 3.1. The load comprises an initial impulse I_0 delivered to the cylinder at time $t = 0$. After some delay time T, the cylinder is loaded by an exponentially decaying, quasi-static pressure of peak magnitude P_0. T is taken as the earliest possible time for P_0 to occur, that is the time it takes for the blast wave to reach the end caps.

Mathematically the pressure pulse is defined as

$$p(t) = I_0\delta(t) + P_0U(t-T)e^{-\alpha(t-T)} \tag{3.1}$$

in which $\delta(t)$ is the delta function, $U(t)$ is the Heaviside step function, P_0 is the peak magnitude of the quasi-static pressure, and I_0 is the specific impulse due to the shock loading.

Note that this analytical description is highly simplified and the smooth relief curve does

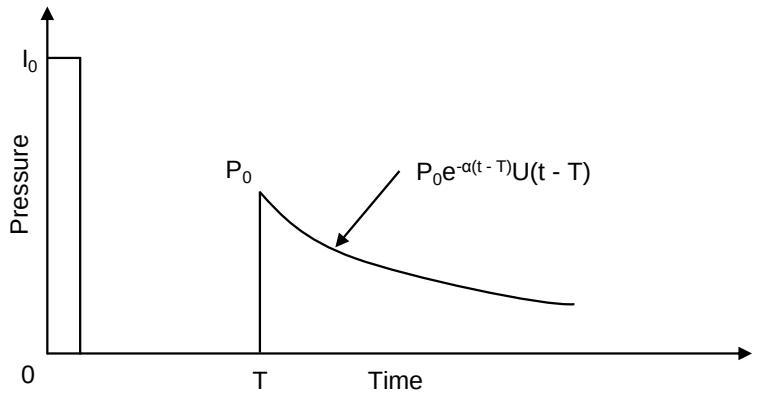

Figure 3.1: Form of assumed pressure load by Benham and Duffey [5].

not capture the multi-peaked nature typical of a confined pressure-time curve. Additionally there is uncertainty about the rate at which the quasi-static portion of the curve should decay.

Another possible analytical curve of the form shown in Figure 3.2 is presented by Baker et al [19]. In this description the pressure peaks are assumed to be triangular, and the magnitude of a given peak is half that of the preceding peak. The duration of each pressure peak is constant and given as $T_R = 2t_a$, where t_a is the arrival time, that is time taken for the blast wave to reach the cylinder wall.

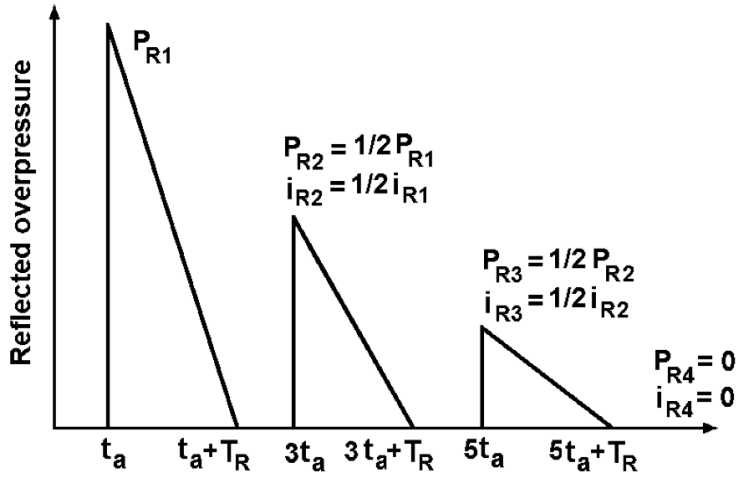

Figure 3.2: Form of proposed pressure load by Baker et al [19].

Edri et al [35] noted that this description makes no accommodation for the late-time quasi-static pressure that remains following confined explosions, and there is no recommendation for determining the magnitude of the first pressure peak, which is dependent on the explosive type and structure volume. Additionally, the discontinuous nature of this description makes it arduous for implementing mathematically, which is needed if it is to be used as the forcing function for an equation describing a structural response of a

cylinder.

Figure 3.3 shows a more recent pressure-time curve presented by Orlenko [56] and reported by Edri et al [35]. It is clear from Figure 3.3 that this curve is significantly closer to a "real" pressure response than the two curves presented previously.

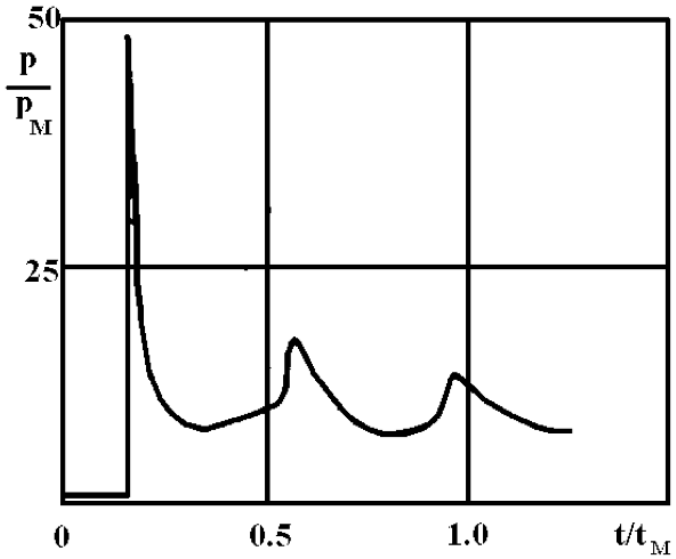

Figure 3.3: Form of proposed pressure load by Orlenko [56].

In this description, the pressure is normalised relative to atmospheric pressure P_M, and the time is presented relative to an unnamed parameter t_M given by r_E/μ_M. Here r_E is the charge radius, and u_M is the speed of sound in air given by $\sqrt{P_M/\rho_M}$, where ρ_M is the original air density.

Orlenko [56] gives the following equation to calculate the magnitude of the i-th pressure peak

$$P_i = \begin{cases} P_D \left[1 + \dfrac{\gamma+1}{4\gamma} + \sqrt{1 + \left(\dfrac{\gamma+1}{4\gamma} \right)^2} \right] & \text{if } i = 1 \\ \dfrac{P_D}{2} + \left(P_1 - \dfrac{P_D}{2} \right) \left(\dfrac{r_0}{D t_i} \right)^{\alpha} & \text{if } i \geq 2 \end{cases} \tag{3.2}$$

In Equation 3.2, $\alpha = 1$ applies for cylindrical structures and $\alpha = 1.2$ for spherical structures, P_D is the pressure at the incident detonation wave with velocity D, γ is the adiabatic index of the detonation products, r_0 is the distance from the charge centre to the structure wall, and t_i is the arrival time for the i-th pressure peak.

Orlenko [56] also presents an approximate equation to describe the continuous pressure-

time response in between the peaks described by Equation 3.2. This is given as

$$P_i(t) = 0.37D + \left(P_i - 0.37P_D \left(\frac{t_i}{t} \right)^{4+N} \right) \tag{3.3}$$

where $N = 1$ applies for cylindrical structures and $N = 2$ for spherical structures. The value of the arrival time t_i of the i-th peak is found according to

$$t_i = \begin{cases} \dfrac{r_0}{D} & i = 1 \\ \dfrac{3.90r_0}{D} & i = 2 \ \& \ N = 1 \\ \dfrac{3.55r_0}{D} & i = 2 \ \& \ N = 2 \\ \dfrac{6.90r_0}{D} & i = 3 \ \& \ N = 1 \\ \dfrac{6.15r_0}{D} & i = 3 \ \& \ N = 2 \\ t_3 + (i-3)\dfrac{\alpha r_0}{D} & i \geq 4 \end{cases} \tag{3.4}$$

The analytical description of Figure 3.3 is certainly a qualitative improvement over the preceding two descriptions in this section. However, the highly piece-wise definition of this description makes it mathematically difficult to include as a forcing function in an equation of motion, as required by the analytical procedure of the following sections. Additionally there is no comparison with experimental data precluding important comment regarding its quantitative accuracy.

3.1.2 Benham and Duffey analytical methodolgy

To develop an analytical model for the response of a cylinder to an internal blast load, Benham and Duffey [5] consider a cylinder of length L, inner radius a, and thickness h, where the length was subject to the constraint $L \geq 2a$. The end caps are considered massive (undeformable) relative to that of the cylinder and are attached at both ends in a pressure-tight manner.

Three possibilities for the analytical load to be applied to the cylinder wall were detailed in the previous section. It is required that the mathematical description of the pressure load be as simple as possible, making it suitable for design calculations, and so that it is easily incorporated as a forcing function in the equations of motion. The complex

and highly piece-wise definition of the description presented by Orlenko [56] is thus not suitable.

Both the descriptions presented by Benham and Duffey [5] and Baker et al [19] are plausible for use in the analytical model. While not ideal, the Baker et al [19] load could be incorporated by including several delta functions in the mathematical description (one for each load pulse). However the Benham and Duffey [5] pressure form is chosen for use in the analytical model, based on the good experimental-analytical correlation reported by the authors [5] when using this description.

Recall that the pressure pulse is defined mathematically as

$$p(t) = I_0\delta(t) + P_0U(t-T)e^{-\alpha(t-T)} \tag{3.5}$$

in which $\delta(t)$ is the delta function, $U(t)$ is the Heaviside step function, P_0 is the peak magnitude of the quasi-static pressure, and I_0 is the specific impulse due to the shock loading.

The specific impulse and the magnitude of the quasi-static pressure are found from Equations 3.6 and 3.7 respectively.

$$\frac{I_0}{\bar{P}_0^{2/3}W^{1/3}} = \frac{b_1}{\left(\bar{P}_0^{1/3}Z\right)} + \frac{b_2}{\left(\bar{P}_0^{1/3}Z\right)^2} + \frac{b_3}{\left(\bar{P}_0^{1/3}Z\right)^3} \tag{3.6}$$

$$b_1 = 0.1204,\ b_2 = 0.1384,\ b_3 = 0.003708$$

$$P_0 = \frac{CW}{V}\ \left(\frac{\text{lb}_\text{f}}{\text{in}^2}\right) \tag{3.7}$$

In these equations, W is the charge mass in lb, $\bar{P}_0$ is the ambient pressure in atm, Z is the scaled distance according to $Z = a/W^{1/3}$, V is the volume of the cylinder in ft^3, and C is a constant depending on the explosive type. The authors use $C = 3000\text{lb}^{-1}\text{ft}^3\text{psi}$ which is common for many secondary explosives [5].

The cylinder material is assumed to be rigid-plastic with linear strain hardening and

non-liner strain rate sensitivity. These relationships are given by

$$\sigma = \sigma_y^D \left[1 + \lambda\epsilon\right] \tag{3.8}$$

and

$$\frac{\sigma_y^D}{\sigma_y} = 1 + \left(\frac{\dot{\epsilon}}{D}\right)^{1/q} \tag{3.9}$$

in which σ_y^D is the material dynamic yield strength, λ is the linear strain hardening parameter, ϵ is the current strain, σ_y is the static yield strength, $\dot{\epsilon}$ is the current strain rate, and D and q are the Cowper-Symonds [47] strain rate calibration constants.

By neglecting the axial stress and bending moment the structural response becomes purely radial. This simplification is in the interests of producing simple solutions suitable for design purpose [5], and is reasonable given the good experimental-theoretical correlation reported by Behnam and Duffey [5], using such an assumption. Under these conditions the equation of motion per unit length of the cylinder wall, directly in line with the centre of the charge is

$$\frac{\mathrm{d}^2\omega}{\mathrm{d}t^2} + \frac{\sigma}{\rho a} = \frac{p(t)}{\rho h} \tag{3.10}$$

where ω is the outward radial displacement, ρ is the cylinder material density, σ is the radial stress, and $p(t)$ is the time-dependent pressure previously defined.

Combining these equations and the strain-displacement relationship $\epsilon = \omega/a$, Benham and Duffey [5] present a differential equation for the motion of the cylinder wall. This is Equation 2.32 from Section 2.7 and is reproduced here for ease of reference

$$\frac{\mathrm{d}^2\omega}{\mathrm{d}t^2} + \frac{\lambda\sigma_y^D}{\rho a^2}\omega + \frac{\sigma_y^D}{\rho a} = \frac{I_0}{\rho h}\delta\left(t\right) + \frac{P_0}{\rho h}U\left(t - T\right)e^{\left[-\alpha(t-T)\right]} \tag{3.11}$$

From Equation 3.11, two possible solutions arise: one each where the dynamic yield stress is considered as constant or variable. These are considered in the following sections.

3.1.3 Cylinder geometry and material properties

The geometry of the cylinders considered by Benham and Duffey [5] is illustrated in Figure 3.4. These cylinders are of length $l = 533.4$mm, inner radius $a = 127$mm, and wall thickness $h = 6.35$mm, where the values have been converted from imperial to metric units for convenience.

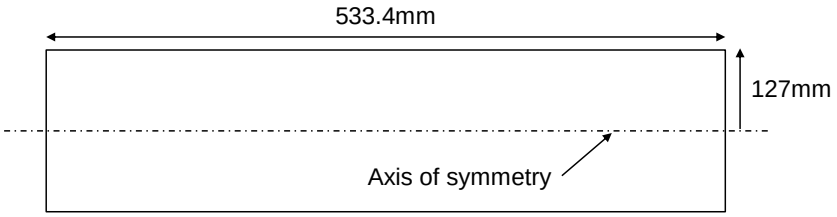

Figure 3.4: Geometry of cylinders for Benham and Duffey [5] analytical solution.

Two different specifications of mild steel are used with respective yield stresses σ_y of 248.21MPa and 296.47MPa, and a material density ρ of 7790.75kg/m^3. In both cases the linear strain hardening parameter λ is assumed to be 0.01, and the strain rate sensitivity is captured with the typical mild steel Cowper-Symonds [47] coefficients, D and q, of 40s^{-1} and 5 respectively.

The cylinder geometry and material parameters are summarised in Table 3.1.

Description	**Symbol**	**Units**	**Value**
Length	l	mm	533.4
Inner radius	a	mm	127
Wall thickness	h	mm	6.35
Yield stress 1	σ_y	MPa	248.21
Yield stress 2	σ_y	MPa	296.47
Strain hardening	λ	-	0.01
Cowper-Symonds 1	D	s^{-1}	40.4
Cowper-Symonds 2	q	-	5

Table 3.1: Cylinder geometry and material properties used by Benham and Duffey [5].

3.1.4 Analytical solution with constant yield

If the dynamic yield stress σ_y^D is taken as invariant a closed-form solution to Equation 3.11 exists. To solve this, the authors [5] assume that the dynamic yield stress σ_y^D is based on the initial strain rate $\dot{\epsilon}_1$ (not current strain rate $\dot{\epsilon}$), which may be approximated by

$$\dot{\epsilon}_1 = \frac{I_0}{\rho h a} \tag{3.12}$$

The resulting, constant dynamic yield stress is given by

$$\sigma_y^D = \sigma_y \left[1 + \left(\frac{\dot{\epsilon}_1}{D}\right)^{1/q}\right] \tag{3.13}$$

Imposing this constraint, as well as the initial conditions $\omega(0) = 0$ and $\frac{\mathrm{d}\omega}{\mathrm{d}t}(0-) = 0$, Equation 3.11 becomes

$$\omega(t) = \frac{\mu}{\beta^{\frac{1}{2}}} \sin \beta^{\frac{1}{2}} t - \frac{\gamma}{\beta}\left(1 - \cos \beta^{\frac{1}{2}} t\right) + \zeta U(t-T)\left(\frac{e^{[-\alpha(t-T)]}}{\alpha^2+\beta} + \frac{\sin\left(\beta^{\frac{1}{2}}(t-T) - \xi\right)}{\beta^{\frac{1}{2}}(\alpha^2+\beta)^{\frac{1}{2}}}\right) \tag{3.14}$$

with

$$\beta = \frac{\lambda \sigma_y^D}{\rho a^2},\ \gamma = \frac{\sigma_y^D}{\rho a},\ \mu = \frac{I_0}{\rho h},\ \zeta = \frac{P_0}{\rho h},\ \text{and}\ \xi = \arctan\left(\frac{\beta^{\frac{1}{2}}}{\alpha}\right)$$

The peak radial strain may be found by maximising Equation 3.14, that is solving for t in $\frac{\mathrm{d}\omega}{\mathrm{d}t} = 0$, and substituting the resulting t value into Equation 3.14.

The input parameters used to solve Equation 3.14 are summarised in Table 3.2. By incrementing the charge mass W and solving again, a solution of the peak radial strain as a function of charge mass is produced. The results are presented in Section 3.1.6.

Description	Symbol	Units	Curve 1
Charge mass (C4)	W	g	0 - 350
Inner radius	a	mm	127
Wall thickness	h	mm	6.35
Static yield stress	σ_y	MPa	248.21 or 296.47[a]
Dynamic yield stress	σ_y^D	MPa	Equation 3.13[b]
Material density	ρ	kg/m^3	7790.75
Strain hardening	λ	-	0.01
Cowper-Symonds 1	D	s^{-1}	40.4
Cowper-Symonds 2	q	-	5
Initial strain rate	$\dot{\epsilon_1}$	s^{-1}	Equation 3.12[b]
Specific impulse	I_0	lbf.s.in^{-2}	Equation 3.6[b]
Quasi-static pressure	P_0	atm	0
Quasi-static delay time	T	s	0
[a] Depending on material specification. [b] Varies with charge mass.			

Table 3.2: Input parameters used by Benham and Duffey [5] for closed-form solutions.

3.1.5 Analytical solution with variable yield

If the dynamic yield stress is taken as a function of the current strain rate, no closed-form solution to Equation 3.11 exists, and a solution must be found numerically [5].

To achieve this the numerical solution is found using the *ode45* function in MATLAB. *ode45* is a Runge-Kutta method solver for ordinary differential equations. A variable timestep is used to improve computational efficiency.

In order to use *ode45*, the second order differential equation of Equation 3.11 is first rewritten as a series of first order differential equations. That is, from rewriting Equation 3.11 with the form

$$\frac{\mathrm{d}^2\omega}{\mathrm{d}t^2} = -\frac{\lambda\sigma_y^D}{\rho a^2}\omega - \frac{\sigma_y^D}{\rho a} + \frac{I_0}{\rho h}\delta(t) + \frac{P_0}{\rho h}U(t-T)\,e^{[-\alpha(t-T)]} \tag{3.15}$$

a vector **w** is defined such that

$$w(1) = \omega$$

$$w(2) = \frac{\mathrm{d}\omega}{\mathrm{d}t}$$

and consequently

$$\frac{\mathrm{d}}{\mathrm{d}t}w(1) = w(2)$$

$$\frac{\mathrm{d}}{\mathrm{d}t}w(2) = -\frac{\lambda\sigma_y^D}{\rho a^2}\omega - \frac{\sigma_y^D}{\rho a} + \frac{I_0}{\rho h}\delta(t) + \frac{P_0}{\rho h}U(t-T)\,e^{[-\alpha(t-T)]}$$

Additionally *ode45* requires initial conditions for the values contained in **w**, that is both the initial radial displacement $\omega(0)$ and the initial velocity $\frac{\mathrm{d}\omega}{\mathrm{d}t}(0)$ are required. The initial radial displacement $\omega(0)$ is plainly 0, however no detail on the initial conditions for the initial velocity $\frac{\mathrm{d}\omega}{\mathrm{d}t}(0)$ is presented by Benham and Duffey [5].

Consequently the initial velocity in this section is taken from Section 3.1.4. This is found by differentiating Equation 3.14 and solving $\frac{\mathrm{d}\omega}{\mathrm{d}t}$ at $t = 0$. The resulting initial velocity is thus given by

$$\frac{\mathrm{d}\omega}{\mathrm{d}t}(0) = \frac{aI_0}{\rho h a} \tag{3.16}$$

A vector **input** is defined containing the initial conditions and other parameters that are passed to the series of first order differential equations to solve them. Different solution cases may be solved by modifying the **input** vector. The values contained in **input** are listed in Table 3.3 for the two cases solved in this section. Curve 1 is omitted from the table since it is solved using the closed-form solution detailed in Section 3.1.4.

The *ode45* function produces two outputs: a time vector **t** and a matrix of solutions **w**. **t** represents the independent variable and contains the times at which each of the solutions in the **w** matrix are calculated. **w** contains all the dependent variables where each column of **w** is a separate variable and each row corresponds to a fixed point in time. In this case, the first column of **w** (that is, $w(1)$ as defined previously) gives all the solutions of ω, while the second column (that is, $w(2)$) gives $\frac{\mathrm{d}\omega}{\mathrm{d}t}$.

The peak radial strain is found by extracting the maximum value of ω for all time values in **t**. Using a *for loop*, the value for the charge mass W that is contained in the **input** vector is incremented from 0g to 350g and a new peak radial strain is found. This produces a solution of the peak radial strain as a function of charge mass, the results of which are presented in the following section.

Description	Symbol	Units	Curve 2	Curve 3
Charge mass	W	g	0 - 350	
Inner radius	a	mm	127	
Wall thickness	h	mm	6.35	
Static yield stress	σ_y	MPa	248.21 or 296.47[a]	
Dynamic yield stress	σ_y^D	MPa	Equation 3.9[b]	
Material density	ρ	kg.m^{-3}	7790.75	
Strain hardening	λ	-	0.01	
Cowper-Symonds 1	D	s^{-1}	40.4	
Cowper-Symonds 2	q	-	5	
Specific impulse	I_0	lbf.s.in^{-2}	Equation 3.6[b]	
Quasi-static pressure	P_0	atm	0	Equation 3.7[b]
Quasi-static delay time	T	s	0	
Initial displacement	$\omega(0)$	mm	0	
Initial velocity	d$w(0)$	mm.s^{-1}	Equation 3.16[b]	
[a] Depending on material specification. [b] Varies with charge mass.				

Table 3.3: Input parameters used by Benham and Duffey [5] for numerical solutions.

3.1.6 Results of analytical solution

Figure 3.5 presents the three analytically-derived relationships between peak radial strain and charge mass that have been described in the preceding sections. These are Curves 1 to 3 as labelled by Benham and Duffey [5], and the charge mass has been converted from imperial to metric units for consistency with the rest of this document. Additionally the radial strains have been normalised by a factor of 36/43 (the ratio of the two different material yield stresses) to make Figure 3.5 comparable with a similar graphical solution presented by Benham and Duffey [5].

In Figure 3.5:

- Curve 1 is the solution to Equation 3.14 for an open-ended cylinder ($P_0 = 0$) with a constant dynamic yield stress. This is the lower bound on the peak final strain of the cylinder.
- Curve 2 is the numerical solution to Equation 3.11 for an open-ended cylinder ($P_0 = 0$) with a variable dynamic yield stress.
- Curve 3 is the numerical solution to Equation 3.11 for a closed-ended cylinder with a variable dynamic yield stress. The effect of the quasi-static pressure given by Equation 3.7 acts with zero latency ($T = 0$). Since these conditions are the worst-case loading scenario, this is the upper bound on the peak final strain of the cylinder.

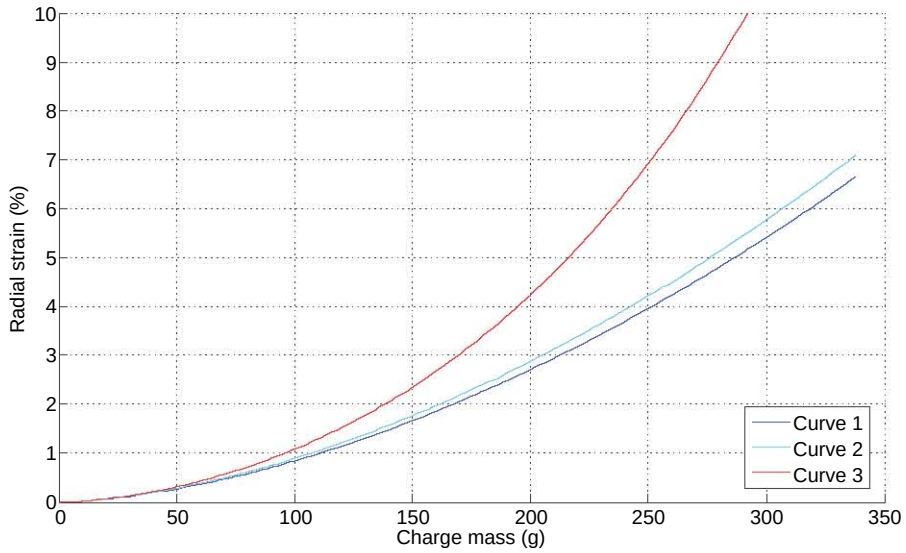

Figure 3.5: Results of analytical solution methods proposed by Benham and Duffey [5].

Figure 2.36 in Section 2.7 is the graphical solution presented by Benham and Duffey [5]. Comparing Figures 3.5 and 2.36, it is clear that the analytical solutions have been successfully reproduced in this section.

Note that Figure 2.36 includes an additional curve (Curve 4) which considers the effect of the quasi-static pressure with a non-zero delay time. No attempt is made in this section to find this solution, since it is sensitive to the exponential decay α and quasi-static delay time T parameters, neither of which is listed by the authors [5].

3.2 Simulation of Benham and Duffey experiments

The results of the numerical simulation of the experiments performed by Benham and Duffey [5] are presented in this section. While presented early in this document, these simulations are performed after the preliminary tests presented in Section 5.4, and the findings from that section are used accordingly. These simulations are performed to provide a reference for the validity of the simulation techniques to be used in the final model, as well as a benchmark between the simulated results and those predicted analytically.

The fundamental modelling technique follows closely that detailed in Section 5.1, with the only significant distinctions between Section 5.1 and the present section being the problem geometries. Thus for brevity several details including the methods for defining the Arbitrary-Lagrange-Euler (ALE) and Lagrange domains, explosive regions, and material and equation of state (EOS) details are *not* repeated in this section.

Instead details of mainly the geometries of the constituent domains for the simulations are presented first in this section, followed by the results and a brief comparison with the analytical work previously presented.

3.2.1 Cylinder geometry and material properties

The cylinder geometry and material properties are detailed in Section 3.1.3. The important parameters are reproduced here for ease of reference where all cylinders are of:

- length $l = 533.4$mm
- inner radius $a = 127$mm
- wall thickness $h = 6.35$mm.

Two different mild steels are tested and these are identified by their respective yield stresses. Imperial units have been converted to metric units for convenience. Only a selection of the experiments are simulated in this section, and these are listed as Tests 1 to 4 in the test matrix of Table 3.4.

Description	**Units**	**Test 1**	**Test 2**	**Test 3**	**Test 4**
Charge mass	g	89.8	119.8	200.0	309.8
Yield stress	MPa	248.21			296.47
Radial deformation	mm	1.49	1.74	4.47	9.26

Table 3.4: Test matrix for simulations of Benham and Duffey [5] experiments.

3.2.2 Air and explosive model

The cylinders tested by Benham and Duffey [5] are of outer radius and axial length 133.35mm and 533.4mm respectively. Consequently the width of the ALE domain is chosen to allow sufficient space into which the cylinder will deform radially, while the length of the domain corresponds with the axial length of the cylinders. Since the cylinders and charges used in the experiments are all circular in section, the experiments are modelled in 2D axisymmetry. This results in an ALE domain of overall dimensions 533.4mm×185mm.

The ALE domain is meshed with solid multi-material (MM) elements and the whole region is filled with air following the techniques outlined in Section 5.1. In accordance with the findings of Section 5.4, the ALE domain is modelled with elements of size 1mm×1mm. It is shown in that section that there is no significant accuracy gain derived from the use of smaller elements, nor is it practically feasible to do so with rapidly increasing computational expense.

In the experiments the authors [5] use radially- and axially-centred, spherical charges in all the tests, which are detonated from the centre. The geometry of the explosive region in the simulations is chosen to replicate this as far as possible, where the 2D axisymmetric representation of a centrally-located sphere is a semi-circle centred on the axis of symmetry. The area of this region is adjusted according the desired mass of explosive. The characteristic dimensions of the ALE domain and the explosive region are illustrated in Figure 3.6.

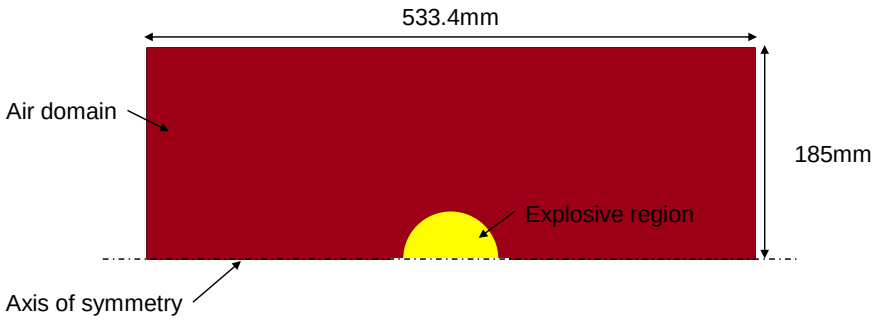

Figure 3.6: ALE domain and explosive region for Benham and Duffey [5] simulations.

3.2.3 Cylinder model

The cylinders used in the experiments [5] have a wall thickness and axial length of 6.35mm and 533.4mm respectively. The width of the Lagrange domain is chosen to correspond to a wall thickness.

In the simulations the axial length exposed to blasting is controlled by restricting the ALE domain to a length equal to the internal axial length of the experimental cylinders (see Section 3.2.2). However to allow for the application of boundary conditions, the axial length of the Lagrange domain is extended beyond the ALE domain by 25mm on both ends. Since the extension is beyond the boundary of the ALE domain, the cylinder length exposed to blasting remains unchanged. The resulting Lagrange domain is of width and length 6.35mm×583.4mm respectively. The Lagrange domain is illustrated in Figure 3.7, where the extended, clamped regions are also indicated.

Figure 3.7: Cylinder domain and blast-exposed region for Benham and Duffey [5] simulations.

The element size for the Lagrange domain is chosen to be a quarter that of the air domain, that is 0.25mm×0.25mm. As shown in Section 5.4.6, elements of this size have produced acceptable structural responses relative to smaller elements, in addition to minimising material transport (leakage) through the cylinder domain.

The stress-strain relationship is captured using a modified Johnson-Cook [52] constitutive model. This model is chosen as the best approximation to the rigid-linear plastic model assumed by Benham and Duffey [5].

In the analytical work the cylinder material is idealised as rigid-linear plastic, with non-linear strain rate sensitivity. As presented previously, the stress-strain relationship is given mathematically by Equation 3.8 and Equation 3.9.

Combining Equation 3.8 and Equation 3.9 leads to

$$\sigma = \left[\underbrace{\sigma_y}_{\text{A}} + \underbrace{\lambda\sigma_y\epsilon}_{\text{B}}\right]\left[1 + \left(\frac{\dot{\epsilon}}{D}\right)^{1/q}\right] \tag{3.17}$$

In LS-DYNA a modified form of the Johnson-Cook [52] model is a available which captures the strain rate sensitivity according to the Cowper-Symonds [47] relation. This modified model is given by

$$\sigma = [A + B\epsilon^n]\left[1 + \left(\frac{\dot{\epsilon}}{D}\right)^{1/q}\right][1 - T^m] \tag{3.18}$$

By setting $A = \sigma_y$, $B = \lambda\sigma_y$, $n = 1$, and m sufficiently small, Equations 3.17 and 3.18 become equivalent. Consequently this material model is used in the simulations of Benham and Duffey [5].

3.2.4 Boundary conditions

Figure 3.8 shows a typical model set up. As detailed in Section 5.1.7, the left and right boundaries of the ALE domain, corresponding to the end caps of the cylinders, are modelled as either flow out or reflective boundaries, depending on whether the simulation is to be open- or closed-ended. In this section, only closed-ended experiments are simulated and consequently only reflective boundaries are used. Material flow is permitted across all other boundaries.

In order to constrain the Lagrange domain, the velocity of the boundaries of the extended sections is set to zero in either the x- or y-directions. This approximates the clamping set up used in the experiments. The zero-velocity boundary conditions are indicated in the zoomed section of Figure 3.8.

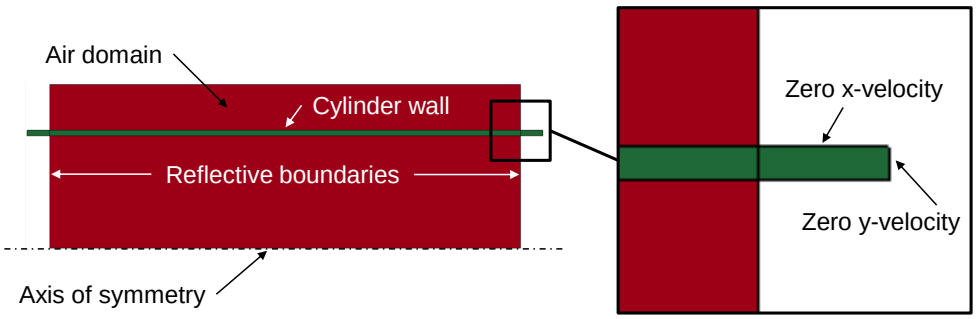

Figure 3.8: Boundary conditions set up for numerical model.

3.2.5 Summary of model dimensions

Details were presented in Section 3.2.1 to Section 3.2.4, of the LS-DYNA model used to simulate the experiments of Benham and Duffey [5]. The domain dimensions and element sizes are summarised below:

- the ALE domain is of dimensions 533.4mm×185mm,
  with element sizes of 1mm×1mm
- the Lagrange domain is of dimensions 583.4mm×6.35mm,
  with element sizes of 0.25mm×0.25mm.

3.2.6 Simulation results

In Figure 3.9 the simulated peak radial deflections are compared with those measured experimentally by Benham and Duffey [5]. The solid line $y = x$ corresponds to perfect correlation between simulated and experimental results. The distance from this line is indicative of the deviation of the simulated values from those found experimentally. The parallel, red, dashed lines correspond to error bounds of ± 1 wall thickness (in this case 6.35mm), which for plates tested at BISRU is approximately the bounds of experimental repeatability.

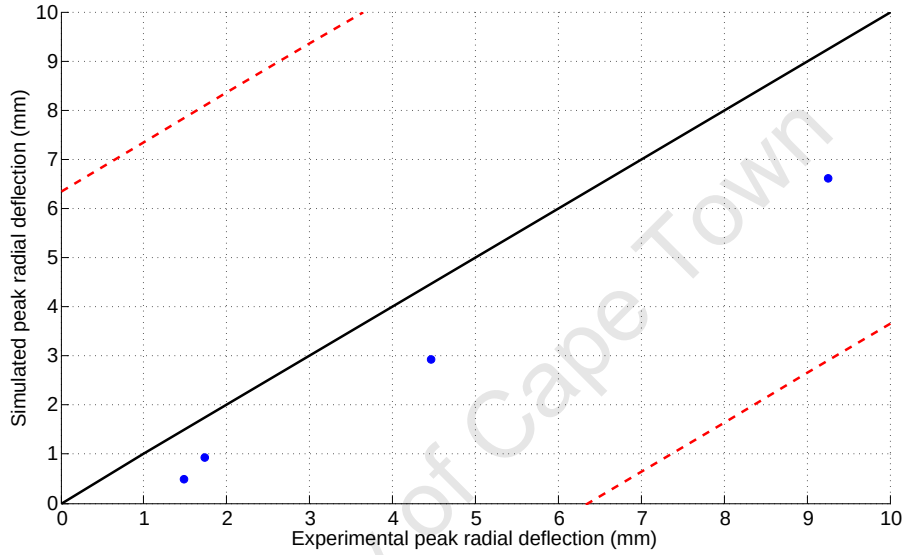

Figure 3.9: Experimental-simulated correlation of peak radial deflection values. Distance from the line $y = x$ is indicative of the deviation of the simulated values from those measured experimentally.

All the data points lie below the line $y = x$ indicating that all the simulations result in an underestimate for the peak radial deflection. Since the wall thickness of the cylinders used in the experiments (6.35mm) is thick relative to the measured deflections, it is unsurprising that all four simulated values fall within a single wall thickness. However the maximum divergence from perfect correlation is exhibited by test 4 (309.8g), which falls within approximately 0.4 of a wall thickness. The increasing divergence of the simulated results from perfect correlation with increasing charge mass suggests that the deviation may become even greater for larger charge masses. Considering the highly simplifying assumptions that are inherent in the numerical model, and since the experimental repeatability is likely to be low, the correlation between the simulated and experimental values is acceptable.

Based on the work reported by Feldgun et al [36] and Edri et al [25], it is likely that the additional experimental deformation in Figure 3.9 is due to the late-time afterburning effect (see Section 2.5.11) which is not captured in the simulations. The fully-confined

nature of the experiments, as well as the relatively large charge masses, are both factors that are likely to promote the afterburning phenomenon [25]. This is further suggested by the increasing experimental-simulation deviation at larger charge masses, where Benham and Duffey [5] have shown that the confinement effect becomes more influential.

While it would be ideal to include the effects of afterburning in the simulations, unlike AUTODYN [25], no readily available option exists for doing so in LS-DYNA. Consequently the only way of currently capturing the afterburning effect is to develop either a customised EOS, or an extension to the JWL EOS, both of which are beyond the scope of the present work. Consequently, while noted, the afterburning effect is not considered further in the simulations in this report.

In Figure 3.10, the simulated peak radial strains are overlaid on the analytical strain solutions of Section 3.1. The analytical curves are normalised by the ratios of their yield stresses to enable direct comparison of simulations with materials of different yield stresses. The simulated results are indicated by the data points, while the curves correspond to the analytical solutions.

For ease of reference:

- Curve 1 is the open-ended solution with a constant dynamic yield stress
- Curve 2 is the open-ended solution with a variable dynamic yield stress
- Curve 3 is the closed-ended solution with a variable dynamic yield stress.

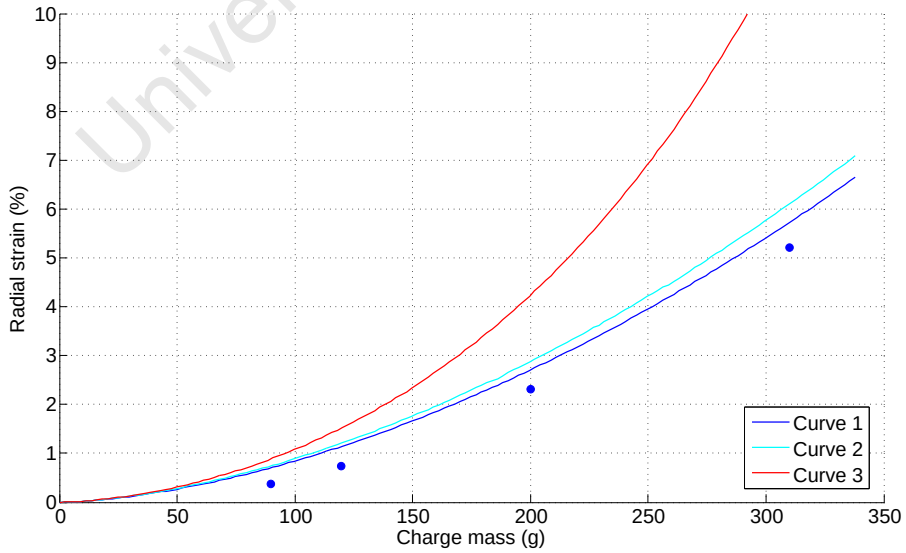

Figure 3.10: Analytical-simulated correlation of peak radial strain values.

Similar to Figure 3.9, the simulated peak radial strains consistently underestimate those predicted by the analytical solutions. Both the simulated results and the analytical

solutions exhibit an exponential increase with increasing charge mass. The discrepancy between the simulated results and that of Curve 1 is relatively constant as the simulated results follow the same general, exponential trend. The results of Figure 3.10 indicate that, over a large range of charge masses, an exponential relationship between charge mass and peak radial strain (or deflection) may be expected.

3.3 Cylinder geometry and material selection

The geometry of the cylinders chosen for the present work are informed by several parameters. It is desired that, from the range of available charge masses at BISRU, the cylinders in the present work achieve similar peak strains to those reported by Benham and Duffey [5]. Additionally, it is imperative for the symmetry of the numerical modelling that the cylinders used are seamless. This constraint significantly restricts the choice of locally available materials and geometries.

The strain ϵ experienced by the cylinders is a function of the cylinder radius a, wall thickness h, and charge mass W. Material properties, specifically the yield stress σ_y and plasticity behaviour λ, also significantly influence the structural response. Mathematically this is

$$\epsilon\phi\left(a, h, W, \sigma_y, \lambda\right) \tag{3.19}$$

where ϕ denotes "function of".

In general, all these parameters are informed by the local availability of material. The cylinder radius a and the charge mass W are coupled and chosen using Hopkinson-Cranz cube root scaling. These two parameters are then coupled to the cylinder wall thickness h, yield stress σ_y, and plasticity behaviour λ, and the latter three chosen based on a modified analytical solution. Details of these choices are presented briefly in this section.

3.3.1 Cylinder radius

It is desired that the peak strains in the present work be similar to those reported by Benham and Duffey [5]. In their experiments the authors used cylinders of inner radius 127mm and various charge masses up to a maximum of 350g.

Since the blast chamber at BISRU is rated for charge masses up to a maximum of only 75g, it is clear that smaller cylinders are required. In the case of a cylinder subjected to a blast from a centrally-located charge, the distance between the explosive source and the cylinder is the cylinder inner radius.

Using Hopkinson-Cranz cube root scaling, the cylinder radius and charge mass used by Benham and Duffey [5] are combined to give a scaled distance Z_{duffey}. This scaled distance must be approximately equal to that given by the combination of cylinder radius

and charge mass in the present work. Mathematically this is to say

$$Z_{\text{duffey}} = \frac{a}{\sqrt[3]{W_{\text{TNT}}}} = Z_{\text{present}} \tag{3.20}$$

where Z_{duffey} is the scaled distance from the Benham and Duffey [5] work, a is the distance from the centre of the blast source to the cylinder wall (i.e. inner radius), W_{TNT} is the equivalent TNT mass of the explosive, and Z_{present} is the desired scaled distance for the present work.

From the range of charge masses that are available at BISRU the inner radius a for the cylinders in the present work is taken to be 75mm.

3.3.2 Cylinder wall thickness

The strain experienced by the cylinder is inversely proportional to the cylinder wall thickness h, and there is no method of capturing the effect of the wall thickness in the cube root scaling presented in the previous section.

Consequently the cylinder wall thickness is chosen from the results of an analytical solution to the strain response of the cylinder. This analytical solution is based on that presented by Benham and Duffey [5] and is approximately modified according to the geometries and material properties in the present work. The solution methodology and results are presented in detail in Section 3.1.

The results in this section are a solution to Equation 3.11 as before, and the material response is again approximated by Equation 3.8 and Equation 3.9.

Subject to the constraint that the cylinders be both seamless and (readily) locally available, the choice is between mild steel cylinders of wall thickness 6.3mm and 304 stainless steel cylinders of wall thickness 2mm.

Results for mild steel cylinders

The result of the modified analytical solution for the mild steel cylinders is shown in Figure 3.11. The solution is a numerical solution to Equation 3.11 where the cylinder is taken to be open-ended, that is the quasi-static pressure $P_0 = 0$. (This solution technique is labelled Curve 2 in Section 3.1).

The mild steel cylinders are assumed to have a yield stress σ_y of approximately 250MPa, which is typical for mild steel and is also the value used by Benham and Duffey [5]. The

strain hardening parameter $\lambda = 0.01$ is in accordance with that used by the authors [5]. The cylinder radius $a = 75$mm and the wall thickness h is either 6.3mm, 3mm, or 2mm.

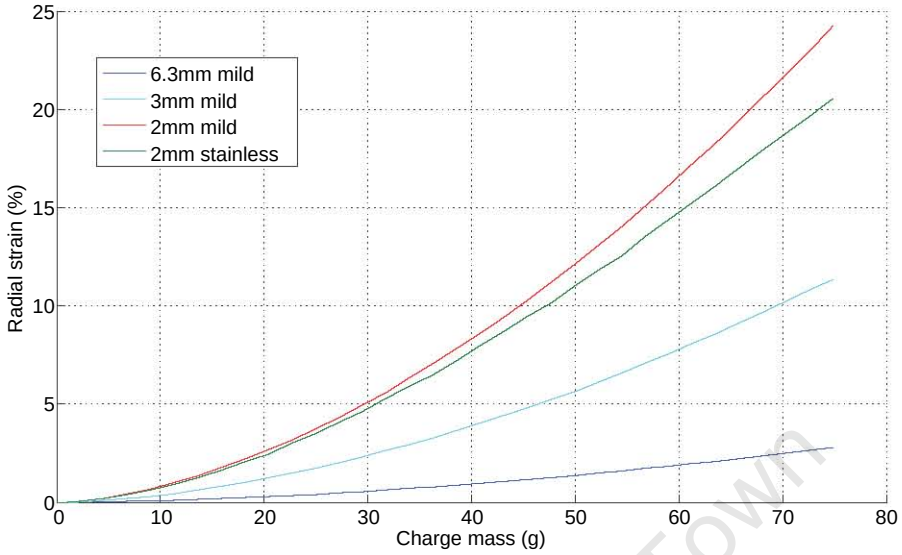

Figure 3.11: Results of modified Benham and Duffey [5] analytical solution for different materials and wall thickness.

It is clear from Figure 3.11 that radial strains for the 6.3mm wall thickness cylinder are very small, even at the high end of the charge mass range. Consequently using cylinders with a wall thickness of 6.3mm (material as delivered) is inadequate for the present work.

It is possible to machine the cylinder wall thickness down to a desired value. The cyan and red curves in Figure 3.11 are the results for the same cylinder with a 3mm and 2mm wall thickness respectively. In this case the magnitudes of the radial strains are acceptable and it appears plausible to use either such cylinder in the present work.

However the process of machining down the cylinder wall thickness is both time consuming and wasteful with such an extensive amount of the material being discarded.

Results for stainless steel cylinders

Figure 3.11 also shows the result of the modified analytical solution for the stainless steel cylinders. As for the case of the mild steel cylinders, the cylinders are taken to be open-ended with the quasi-static pressure $P_0 = 0$.

The stainless steel cylinders are assumed to have a yield stress $\sigma_y = 310$MPa which is approximately the value found from quasi-static tensile tests on the material as presented in Appendix B. The strain hardening parameter $\lambda = 1.95$ is in accordance with that reported by Duffey and Mitchell [30]. The cylinder radius $a = 75$mm and the wall thickness $h = 2$mm.

The radial strains predicted by the modified analytical solution for this configuration are adequately large for use in the present work. No circumferential machining is required as piping is readily available with a 2mm wall thickness. Considering this, in addition to the easier the availability of the stainless steel pipe, stainless steel cylinders with a wall thickness of 2mm are chosen for use in the present work.

3.3.3 Cylinder length

Since all the cylinders considered in the present work are partially-confined, with one large open end, the cylinder length l is is the least significant of the geometric parameters discussed in this section. Consequently the cylinder length is chosen based on a criterion taken from Proctor [44], who found that all significant deformation occurred within an axial length of 4 times the cylinder radius. Thus for a cylinder radius $a = 75$mm, the cylinder length l is taken as 300mm for all cylinders in the present work.

3.3.4 Cylinder material

The cylinders used in the present work are cut from 304 stainless steel "dairy" pipe with a wall thickness of 2mm (NW150×2). The pipe is supplied in 6m lengths by NDE Stainless Steel, Cape Town, and cut to the requisite length. As described in Section 3.3.2, 304 stainless steel pipe is chosen owing to its ready availability and its favourable as-delivered wall thickness.

The pipe has a certified yield strength of approximately 270MPa and an ultimate strength around 500MPa [57]. To characterise the material, quasi-static tensile tests are performed on specimens cut from the pipe both longitudinally and circumferentially. Neither case matches the certified strength values, though it is unspecified from which orientation the certification specimens are cut. The material characterisation procedure and results are presented in Appendix B.

3.3.5 Summary of cylinder geometry and material

The preceding sections have described the rationale which informs the geometry of the cylinders used in the present work. These are summarised in this section:

- the cylinder radius $a = 75$mm is scaled from the work of Benham and Duffey [5]
- the cylinder wall thickness $h = 2$mm is chosen based on a modified analytical solution to the response of cylinders to internal blast loading

- the cylinder length $l = 300$mm is chosen in accordance with a criterion suggested by Proctor [44]
- the cylinder material is 304 stainless steel chosen owing to its availability and favourable sizing.

3.4 Application of analytical solution

By adjusting certain parameters, the analytical solution developed by Benham and Duffey [5] and presented in Section 3.1 is modified to approximate the material and problem geometry in the present work. The fundamental solution mechanism is identical to that presented previously, only input parameters are changed. Details of these modifications are presented in this section, along with the resulting modified analytical predictions.

3.4.1 Details of modifications

The geometry of the cylinders in the present work is informed by several parameters, the details of which are presented in Section 3.3. The resulting cylinder geometry is reproduced here for ease of reference:

- the cylinder length $l = 300$mm
- the cylinders are of inner radius $a = 75$mm
- the cylinder wall thickness $h = 2$mm
- the cylinder yield stress is approximately $\sigma_y = 310$MPa.

The geometry is illustrated in Figure 3.12. The cylinders are cut from 304 stainless steel, seamless "dairy" tube, supplied by NDE Stainless Steel, Cape Town.

Following the methods described in Section 3.1, a vector **input** is defined, containing the initial conditions and other parameters that are used to solve the differential equations. The linear strain hardening parameter λ is taken as 1.95, as reported by Duffey and Mitchell [30] for 304 stainless steel. The Cowper-Symonds [47] strain rate sensitivity parameters, D and q, are defined as 100s^{-1} and 10 respectively, taken from work by Forrestal and Sagartz [58] and reported by Burgan [59]. The **input** vectors for each of the three analytical curves are summarised in Table 3.5.

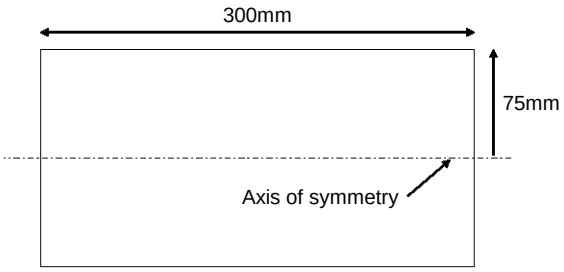

Figure 3.12: Geometry of cylinders for modified analytical solution.

Description	Symbol	Units	Curve 1	Curve 2	Curve 3
Charge mass	W	g	0 - 75		
Inner radius	a	mm	75		
Wall thickness	h	mm	2		
Static yield stress	σ_y	MPa	320		
Dynamic yield stress	σ_y^D	MPa	Equation 3.13[a]	Equation 3.9[a]	
Material density	ρ	kg.m^{-3}	7900		
Strain hardening	λ	-	1.95		
Cowper-Symonds 1	D	s^{-1}	100		
Cowper-Symonds 2	q	-	10		
Specific impulse	I_0	lbf.s.in^{-2}	Equation 3.6[a]		
Quasi-static pressure	P_0	atm	0	0	Equation 3.7[a]
Quasi-static delay time	T	s	0		
Initial displacement	$\omega(0)$	mm	0		
Initial velocity	$\mathrm{d}w(0)$	mm.s^{-1}	-	Equation 3.16[b]	
[a] Varies with charge mass.					

Table 3.5: Input parameters for modified analytical solutions.

3.4.2 Results of modified solution

Figure 3.13 presents the results of the three modified, analytical relationships between peak radial strain and charge mass. In accordance with Reference [5], these curves are labelled Curves 1 to 3. Again for ease of reference:

- Curve 1 is the open-ended solution with a constant dynamic yield stress
- Curve 2 is the open-ended solution with a variable dynamic yield stress
- Curve 3 is the closed-ended solution with a variable dynamic yield stress.

As expected and qualitatively similar to the solutions presented in Section 3.1, the curves exhibit an exponential increase in peak radial strain with increasing charge mass. Ignoring the region of very low charge masses, the relationship between peak radial strain and charge mass is approximately linear, particularly for Curves 1 and 2 between approximately 40g and 75g. The validity of Curve 3 is questionable owing to the large magnitudes

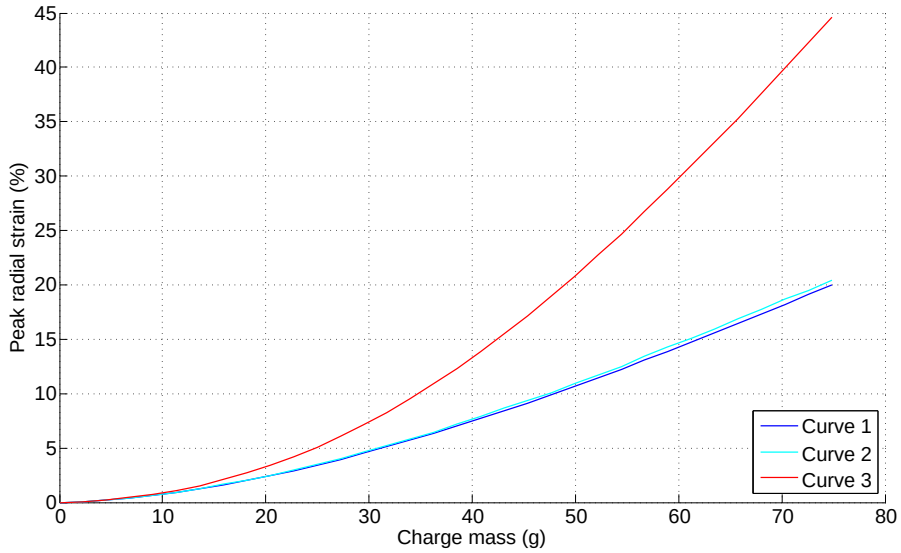

Figure 3.13: Analytically predicted peak radial strain as a function of charge mass from modified analytical solutions.

of its predicted peak radial strains, particularly at larger charge masses. Additionally the divergence between the curves is significantly larger than that in the Benham and Duffey [5] solution, though this is likely owing to the smaller enclosing volume and wall thickness for the cylinders under consideration.

Chapter 4

Experimental Details and Results

The previous sections have detailed the experimental design based on an analytical solution presented by Benham and Duffey [5]. The test rig design and full experimental procedure are described in this section, along with the experimental results and brief observations pertaining to the data sets.

4.1 Experimental details

In the experiments the cylinders are attached to a purpose-designed testing rig, which is in turn fixed to the horizontal ballistic pendulum at the Blast Impact and Survivability Research Unit (BISRU). This section presents details of the test rig design, and test arrangements and procedures.

4.1.1 Test rig

A sectioned 3D model of the full test rig used in the experiments and a photograph of the rig are shown in Figure 4.1 and Figure 4.2 respectively. The rig comprises five distinct constituent parts as indicated in the figures, specifically: the mounting plate, spacer rods, backing plate, boss member, and clamping members. All parts are manufactured from mild steel.

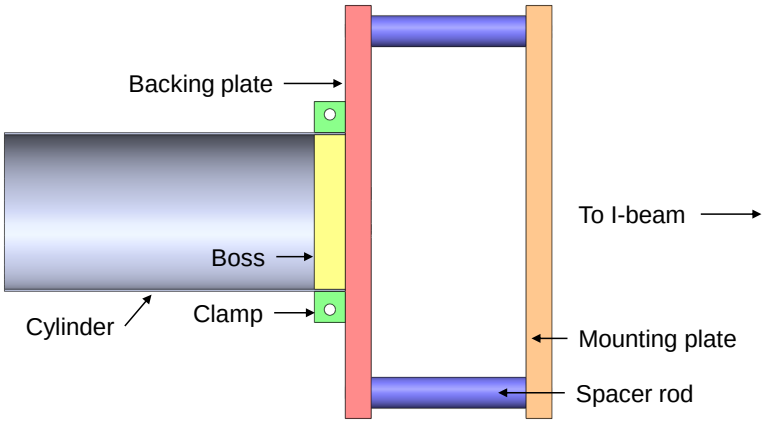

Figure 4.1: Sectioned 3D model of test rig.

The mounting plate of dimensions ($l \times w \times t$) 400mm×400mm×25mm is attached directly to the ballistic pendulum and serves to provide a surface onto which to attach the rest of the rig. Each of the four 150mm long spacer rods is attached at each corner of the mounting plate and provides a required access space between the mounting and backing plates, the latter of which is attached in a similar fashion. Similar to the mounting plate, the backing plate is also of dimensions 400mm×400mm×25mm, and serves to provide an approximately rigid backing surface against which to mount the boss member.

The boss member is a circular disc of dimensions ($\phi \times t$) 150mm×30mm with four threaded holes around its centre. The holes are used to fasten the boss member to the backing plate. The cylinders are placed over the boss member (so that the boss member is entirely inside the cylinder), and owing to its thickness relative to that of the cylinders, it acts as a relatively rigid surface for the closed end of the cylinders.

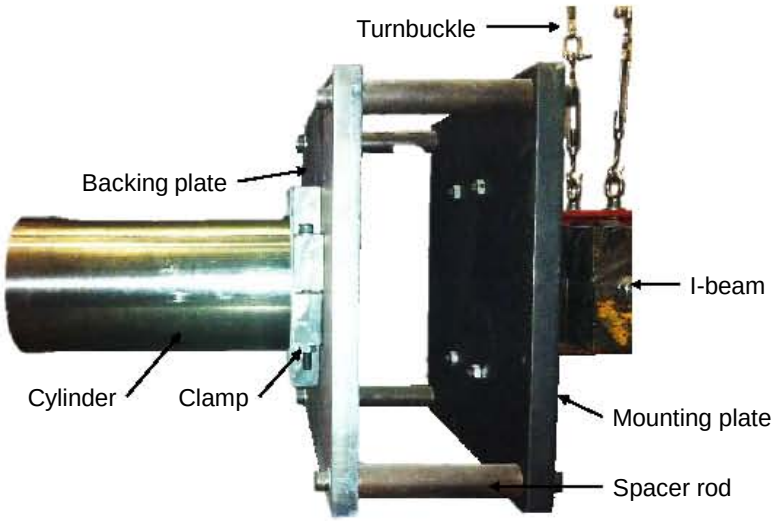

Figure 4.2: Photograph of test rig. (Boss member hidden).

The two clamp members are cut from 30mm thick steel and bored out so that the inner diameter of the clamp members is equivalent to the outer diameter of the cylinders (154mm). To allow the clamp members to be tightened around the cylinder, clearance holes are drilled through the length section of both members. A nut and bolt assembly is used to fasten the clamp around the cylinder. Additionally a small through-thickness cut is made from both clamp members to ensure a tight fit between the clamp members and the cylinder when the bolts are tightened. The thickness of the clamp is chosen to be equivalent to that of the boss member so that, when tightened around the cylinder, the clamp pressure is resisted entirely by the boss member and no bending of the cylinder occurs.

4.1.2 Ballistic pendulum

The test rig is mounted on the horizontal ballistic pendulum, which has been used to measure the impulse imparted to the experimental set ups in many studies [26–29]. The pendulum is shown in Figure 4.3.

The pendulum arrangement comprises a steel I-beam suspended by steel wires from a concrete ceiling and attached to the I-beam with adjustable turnbuckles. At one end of the pendulum the test rig is mounted, and balance masses of a similar total mass to that of the test rig, are attached at the other end to help balance the beam.

A felt-tipped marker is fastened to the beam at the end opposite to that of the test rig. The marker is in contact with tracing paper on a board below the beam, and traces the amplitude of the pendulum as it swings following a blast.

By taking the pendulum to have only a single degree of freedom, this traced amplitude

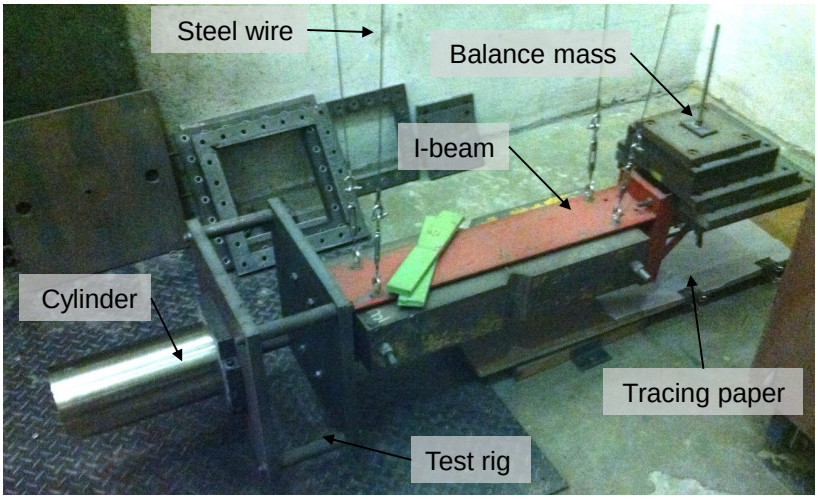

Figure 4.3: Photograph of the horizontal ballistic pendulum at BISRU.

may be directly related to the impulse imparted to the test rig. However this assumption requires that the I-beam be "perfectly" aligned both horizontally and laterally. This alignment is achieved by adjusting the turnbuckles and checking the orientation of the beam with a spirit level until satisfied. Additionally only the impulse in the direction parallel to the I-beam is recorded. The full pendulum-impulse theory is presented in Appendix A.

In previous experiments of this nature, the test rig is typically aligned so that the recorded impulse is in the same direction as the dominant deformation. For instance in the case of experiments on a flat steel plate, the plate normal is parallel to the I-beam, as is the dominant damage and recorded impulse.

However in the present work as shown in Figure 4.3, the cylinders are mounted on the test rig so that the cylinder axis is parallel to the I-beam, and the dominant damage is radial expansion of the cylinders. Consequently the impulse recorded by the pendulum is not that causing the structural deformation. Instead the impulse is used merely as a further metric against which to validate the numerical models, and no direct relationship between impulse and deformation is sought.

4.1.3 Test procedure

In each experiment the cylinder is loaded by detonating a known charge of plastic explosive 4 (PE4) inside the cylinder. To aid the symmetry of the experiments, the PE4 charges are rolled into a sphere and placed evenly in the hole of a polystyrene annulus, an example of which is shown in Figure 4.4.

The polystyrene annulus is cut from 12mm thick, expanded polystyrene and has an

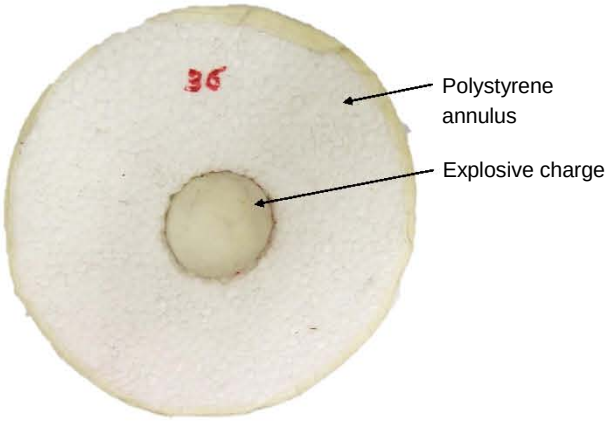

Figure 4.4: Typical polystyrene annulus with spherical charge used to position explosive charges in cylinders.

outer diameter of 150mm, corresponding to the inner diameter of the cylinders. The circumference of the polystyrene annulus is wrapped in a layer of masking tape to ensure a tight fit in the cylinders.[1]

An electrical detonator is inserted into the sphere of PE4 so that the front end of the detonator is approximately at the centre of the sphere. This is achieved by marking the sphere radius on the detonator and inserting the detonator up to the mark.

The charge and polystyrene annulus are inserted into the cylinder and the annulus is positioned at the desired axial location. This is shown in the schematic of Figure 4.5 for the two main axial charge positions in the present work. The axis of the detonator is aligned with that of the cylinder. The axial position of the annulus is checked at several locations to ensure that it is straight within the cylinder.

The charge is then detonated and this marks the completion of an experiment.

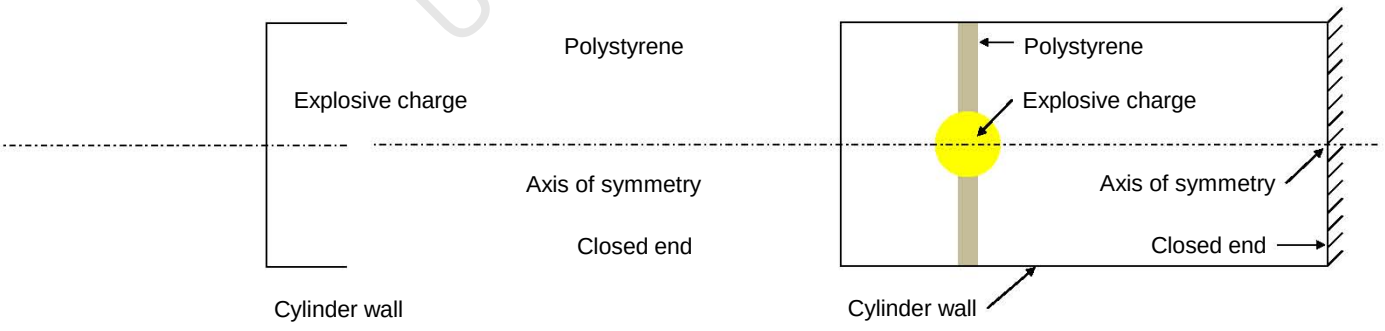

(a) Axial charge position $0.5l$. (b) Axial charge position $0.75l$.

Figure 4.5: Positioning of polystyrene and charge for different axial positions.

[1]The significance of the use of polystyrene in between the charge and the structure to be loaded is unclear. Such a procedure has been used in several experiments at BISRU [26–28, 60] where the role of the polystyrene has been thought to be negligible. The influence of the polystyrene is discussed further in Section 6.5.

4.1.4 Test parameters

In the present work the effect on the cylinder deformation of the following parameters is investigated:

- mass of explosive
- axial charge position
- influence of polystyrene annulus.

The majority of the experiments are performed with an axially-centred charge, that is a charge halfway along the the tube length l. This position is denoted $0.5l$ with the closed end of the cylinder as a reference. For these tests several different charge masses are used ranging between 25g and 75g.

The influence of the axial charge position is investigated by varying this position in some tests, where the charge is located either near the open end denoted by $0.75l$, or near the closed end $0.25l$. For the $0.75l$ experiments the charge mass is varied between 20g and 60g. Only a single experiment is performed with an axial charge position of $0.25l$ where the charge mass is 40g. This test failed and is not considered further.

Two experiments are performed to study the effect of the polystyrene annulus on the structural response of the cylinders. Instead of a full annulus, a half-disc is used to support the explosive charge such that there is no polystyrene between half the explosive and half the cylinder wall. Consequently a comparison of the symmetry of the cylinder response is indicative of the influence of the polystyrene. Only the $0.5l$ axial position is considered and two charge masses, 40g and 50g, are used.

Table 4.1 summarises the tests performed in the present work.

Test parameter	**Axial position (mm*)**	**Charge mass (g)**	**Polystyrene annulus**
Axial position (mm*)	$0.5l$	20g, 30g, 40g, 45g, 50g, 60g	Full
	$0.75l$		
Charge mass (g)	$0.5l$	25g, 30g, 40g, 45g, 50g, 55g, 60g, 75g	Full
	$0.75l$	20g, 30g, 40g, 45g, 50g, 60g	
Polystyrene annulus	$0.5l$	40g, 50g	Full
			Half
*In terms of tube length l taken from closed end.			

Table 4.1: Variation of test parameters in the present work.

4.2 Experimental measurement and notation

Several experimental parameters are recorded during and following testing, for instance the impulse imparted to the pendulum and the final cylinder deformation. Details on the measurement of these parameters are presented in this section, as well the experimental specimen designation used throughout the remainder of this work.

4.2.1 Cylinder deformation

The maximum diametric deformation δ of each cylinder is measured. This deformation is the difference between the original, untested cylinder diameter d_0, and the final, post-test cylinder diameter d_f, that is $\delta = d_f - d_0$. Outer diameters are used for all measurements. This is illustrated in Figure 4.6, where the cylinder is clamped and closed to the right of the clamp line. The left end corresponds to the open end of the cylinder, and the axial length l is as defined in Figure 4.6.

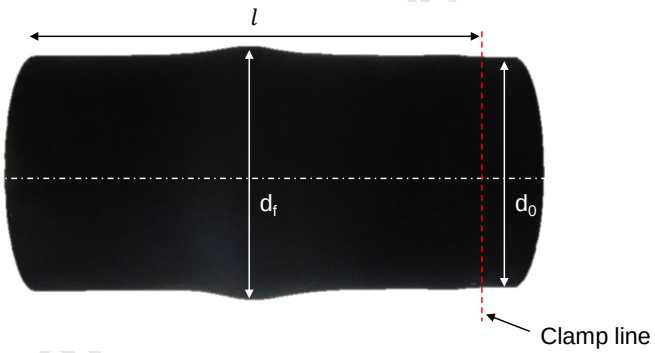

Figure 4.6: Definition of post-test diametric deformation. Cylinder is clamped and closed to the right of the clamp line.

Recall that the blast-exposed length of the cylinders $l = 300$mm, so that for tests where the charge is positioned midway along the cylinder length, the corresponding axial charge position is $0.5l = 150$mm, where the closed end of the cylinder is taken as the $0l$ reference. Similarly for tests where the explosive charge is positioned nearer to the opening, the corresponding axial charge position is $0.75l = 225$mm.

It is assumed that the maximum radial deformation occurs in line with the centre of the explosive charge. Using a large micrometer with an accuracy of 0.01mm, eight approximately equally-spaced diametric measurements d_i are recorded at the relevant axial position, that is either $0.5l$ or $0.75l$ depending on the test configuration. This is illustrated in Figure 4.7. Since the tests cannot be "perfectly" symmetrical, the average final

diameter $\bar{d_f}$ is taken as the mean of these eight measurements given by

$$\bar{d_f} = \frac{1}{8}\sum_{i=1}^{8} d_i \tag{4.1}$$

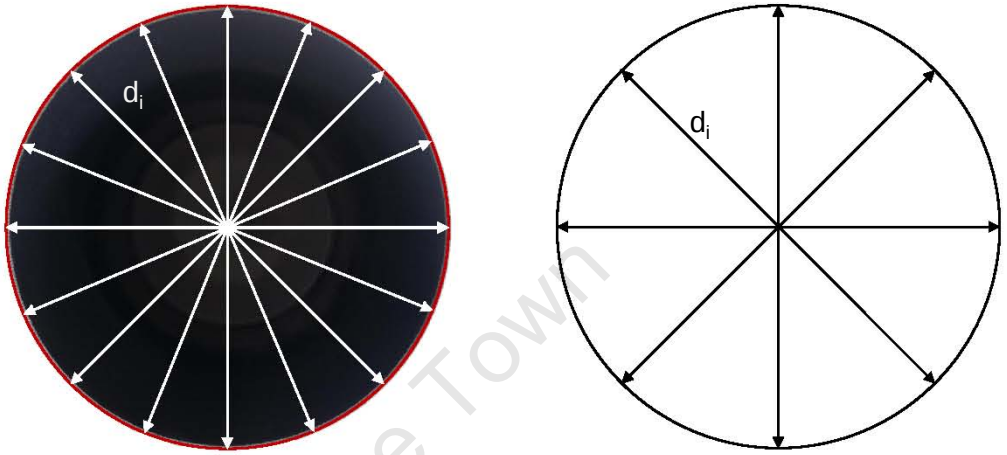

Figure 4.7: Definition of post-test final diameter.

The maximum diametric deformation δ as reported in the present work is thus the difference between the original, untested cylinder diameter d_0, and the average final, post-test cylinder diameter $\bar{d_f}$, given by

$$\delta = \bar{d_f} - d_0 \tag{4.2}$$

where in all cases $d_0 = 154$mm.

4.2.2 Impulse

As mentioned in Section 4.1.2, the impulse imparted to the "rigid" base of the cylinders is calculated from the recorded amplitude of the ballistic pendulum. The methodology for doing so is presented in full in Appendix A.

4.2.3 Cylinder notation

For ease of reference in this document, each experimental specimen is given a unique test designation. The designation captures the charge mass used in the test as well as the axial position of the charge. Where more than one experiment is performed with the same charge mass and position, a unique Latin letter is appended to the test designation, starting with 'a' and incrementing alphabetically.

For instance for an experiment performed with a charge mass of 50g located midway along the cylinder length, the test designation is given by

$$50g\_0.5l$$

If this test is repeated, the two designations become

$$50g\_0.5l\_a \qquad \text{and} \qquad 50g\_0.5l\_b$$

4.3 Experimental results

Following the experimental design detailed in Section 3.3, a series of experiments are conducted subjecting deformable cylinders to internal blast loads. An overview of the experimental results are presented in this section. Note that when referring to cylinder deformation, the diametric deformation is implied unless otherwise stated, and that the words deformation and deflection are used interchangeably in this section.

4.3.1 Results for experiments with axial charge position $0.5l$

The midpoint cylinder deformation as a function of charge mass is shown in Figure 4.8 for tests with a fixed axial charge position. All the tests are conducted with the charge mass midway along the tube length, that is $0.5l$ where the closed end is taken as the $0l$ reference. The data points represent the average of eight midpoint deflection measurements as detailed in Section 4.2, with the error bars indicating the maximum and minimum of these measurements. The error bars are indicative of the symmetry of the tests, where the shorter the error bars the closer is the test to being symmetrical.

The trend line in Figure 4.8 is a linear best-fit curve through all the data points except those which exhibited tearing as indicated in the figure. Note that the trend line is valid only for the range of charge masses which are presented in the figure, and that the deflection-charge mass response is unlikely to be linear for very small charge masses[2], which is suggested by the early exponential response of the modified analytical solution of Section 3.4.

In general the cylinders exhibit increasing midpoint deflection with increasing charge mass. Most of the cylinders exhibit large plastic deformations relative to the 2mm cylinder wall thickness, with the exception of the 25g and 30g responses which are within approximately 1.5 of a wall thickness. The photograph of Figure 4.9 shows the increasing radial deformation of the cylinders as they are subjected to blasts from larger charge masses.

It should be noted that the 25g and 30g results are out of trend, with the average deflection for the 30g test less than that for the 25g test. However a degree of variation may be expected as the experimental repeatability is more variable when the plastic deformations are relatively small than it is for larger deformations.

The other out of trend data points are the 55g and 60g results, where the midpoint deflection for one of the 60g tests is significantly less than that for the 55g test. In a

[2]This should be clear since a non-zero midpoint deflection for zero charge mass is invalid.

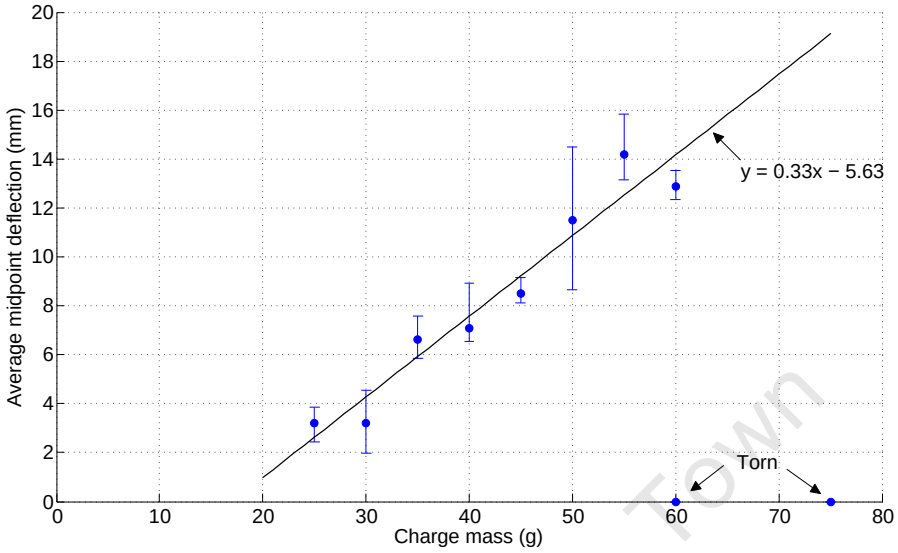

Figure 4.8: Experimental midpoint deflection of cylinders as a function of charge mass for cylinders tested with an axial charge position of $0.5l$.

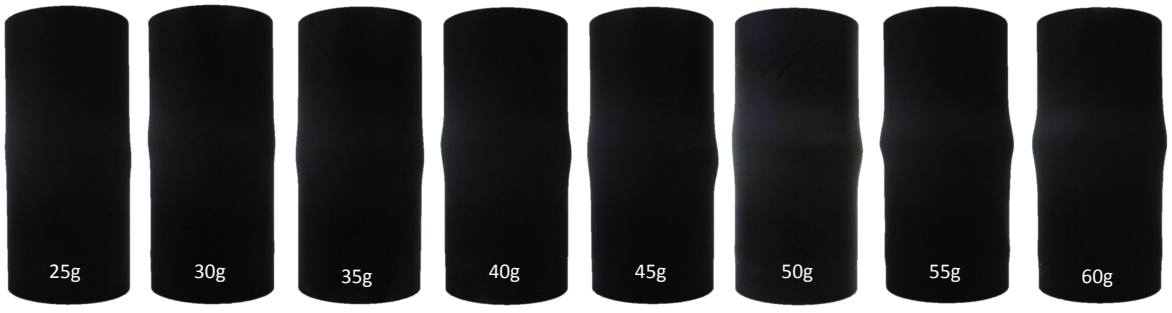

Figure 4.9: Increasing radial deformation of cylinders subjected to blasts from increasing charge masses. All tests conducted at an axial charge position of $0.5l$.

repeat test with a 60g charge mass, the cylinder exhibited a longitudinal tear on one side. This difference in results suggests that at charge masses near to 60g the cylinders are on the verge of failure, and consequently the material behaviour is less predictable than it is at smaller charge masses, which may explain the lower 60g deflection. The 75g test exhibited total failure, providing confirmation that the failure limit may be approximately 60g. Photographs of the torn and totally failed cylinders are shown in Figure 4.10.

(a) Longitudinal tear in cylinder subjected to blast from 60g charge mass ($60g\_0.5l\_a$).

(b) Total failure of cylinder subjected to blast from 75g charge mass ($75g\_0.5l$).

Figure 4.10: Photographs of the torn and totally failed cylinders.

In general the symmetry of the tests is acceptable, particularly in the mid-range of charge masses, as indicated by the relatively short error bars. The major exception is the 50g test where the diametric measurements vary by ±25%. This is illustrated in the photograph of Figure 4.11 which shows clearly the lack of diametric symmetry, with the deformation on one side significantly more pronounced than on the other. It should be noted that this was the first test performed in the present work, and could be owing to misalignment of the charge in the test arrangement.

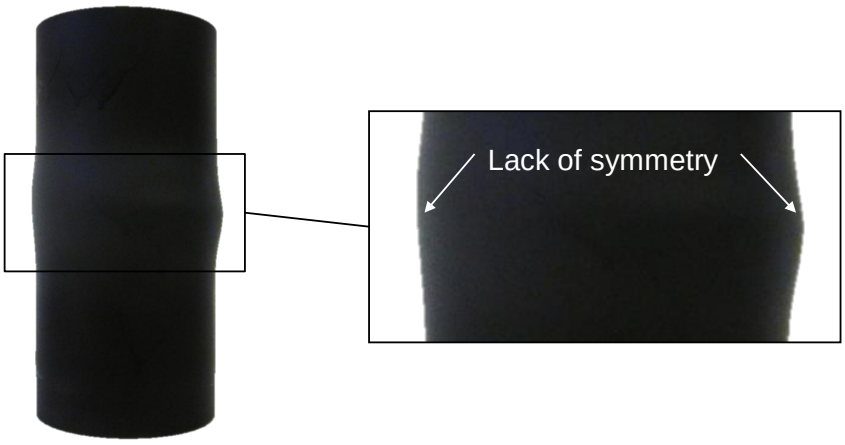

Figure 4.11: Lack of symmetry in diametric response for cylinder tested with 50g charge mass at an axial charge position of $0.5l$ ($50g\_0.5l$).

The cylinder responses for the 25g and 30g tests also exhibit relatively poor symmetry which may be expected, since in these cases the magnitudes of the plastic deformations are small.

Figure 4.12 presents the experimentally-measured cylinder profiles for all charge masses in this section. The profiles are created by axially sectioning the post-test cylinders and digitizing a trace of the profile using Engauge Digitizer 4.1. Note that since the 30mm clamped region is included in the figure, the original axial charge position is at 180mm. Also since these profiles are traced from cylinder sections, they represent the approximate *radial* deflection, and not the diametric deflection as reported previously. Owing to the biased aspect ratio of the profiles, the ratio of the x-y scale is 1:17.5 which significantly magnifies the deformations and disparities.

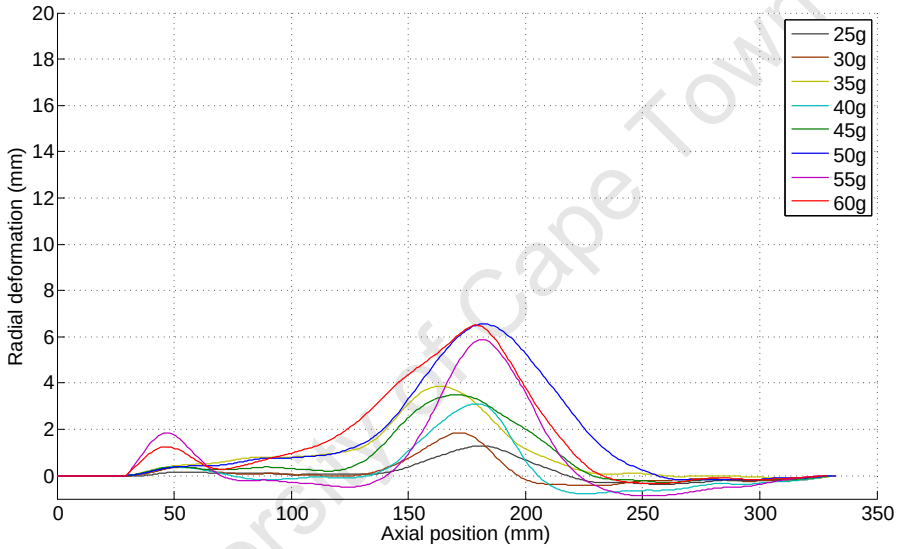

Figure 4.12: Experimental cylinder profiles for cylinders tested with various charge masses at an axial charge position of $0.5l$.

The general increase in deformation with increasing charge mass is evident in Figure 4.12. With the exception of the 35g test, the maximum deformations are relatively well aligned indicating a good degree of repeatability for the experimental procedure.

Figure 4.13 shows the impulse imparted to the "rigid" closed end of the cylinders as a function of charge mass. All the tests are conducted with the charge mass midway along the cylinder length, that is $0.5l$ where as usual the closed end is taken as the reference. The linear trend line is for all the data in Figure 4.13, and similarly to that presented previously, is only valid for the range of charge masses shown.

The impulse increases with increasing charge mass, and the charge mass-impulse ratio of approximately 1:2 is similar to that which has been found in many previous studies at BISRU [26, 28, 60, 61]. The good correlation of the impulse values to this linear trend is indicative of a sound experimental methodology and good repeatability. Note that

the linear best-fit curve is non-zero at zero charge mass. This is not unexpected since there are relatively few data points in the set and none whatsoever for very small charge masses. Consequently the intercept predicted by the linear curve is trivial.

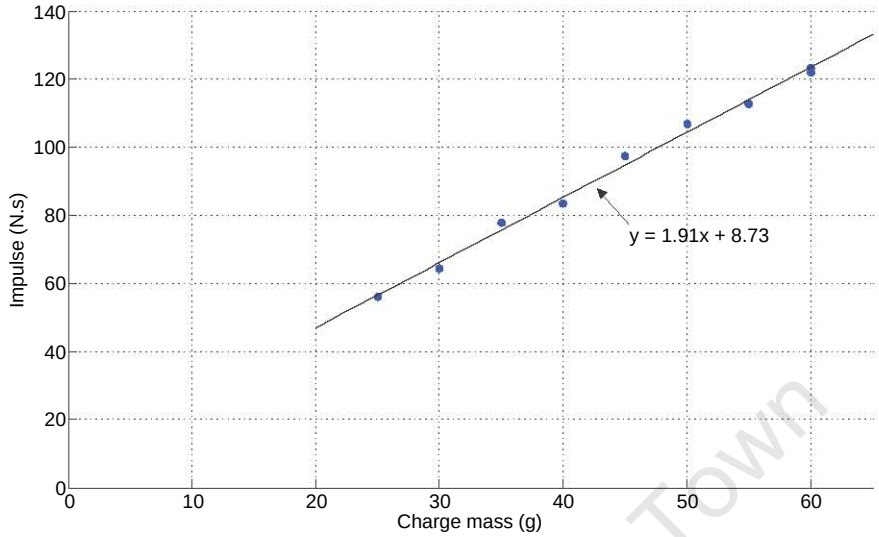

Figure 4.13: Impulse imparted to closed end of cylinders as a function of charge mass for cylinders tested with an axial charge position of $0.5l$.

4.3.2 Results for experiments with axial charge position $0.75l$

Figure 4.14 shows the diametric deflection as a function of charge mass for the six tests conducted with an axial charge position of $0.75l$. Recall that an axial charge position of $0.75l$ corresponds to a position nearer to the open end of the cylinders than presented previously. The trend line is a second order polynomial best-fit curve to all the data in the figure. Since the intercept predicted by the trend is greater than the three lower data points and considering that the response must pass through the origin, it should be clear that the trend is invalid beyond the range of charge masses presented[3]. In general the error bounds are short relative to the mean deflections, indicating adequate symmetry for this series of tests.

The cylinders exhibit an increase in deflection with increasing charge mass as expected. The increase in cylinder deflection with charge mass is rapid as indicated by the steep gradient of the curve, and since the response must pass through the origin, it appears qualitatively similar to the modified analytical solution in Section 3.4[4]. This immediately suggests that the effect of the cylinder confinement is greater for tests at this axial charge position, than it is for those presented previously.

[3]If the polynomial is considered for the full domain, the trend-predicted deflection decreases for charge masses from 0g to approximately 20g before increasing indefinitely, which is clearly nonsensical.

[4]A rapidly increasing exponential deflection-charge mass relationship.

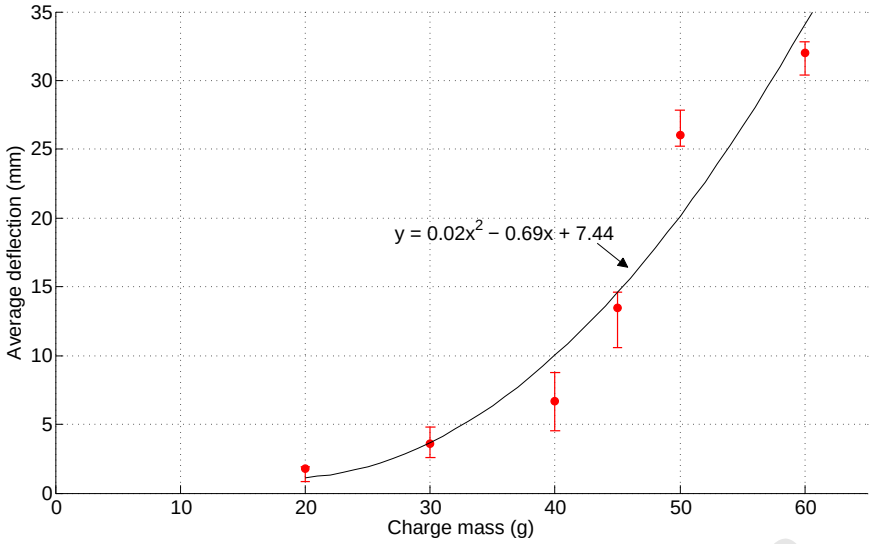

Figure 4.14: Experimental deflection of cylinders as a function of charge mass for cylinders tested with an axial charge position of $0.75l$.

The increasing deflection with charge mass is clear in the photograph of Figure 4.15, which has the cylinders tested in this section side-by-side. The rate of deformation increase is also evident in Figure 4.15, with the deformations in the 50g and 60g specimens significantly more pronounced than in the other tests. Additionally the post-test axial length of the 50g and 60g specimens is visibly shorter than that of the other specimens.

Figure 4.15: Increasing radial deformation of cylinders subjected to blasts from increasing charge masses. All tests conducted at an axial charge position of $0.75l$.

Also visible in the 50g and 60g specimens in Figure 4.15, is a significant "bulging" of the cylinders near the closed ends which corresponds to the bottom in the figure. This additional deformation, far from the position of the explosive charge, is indicative of the degree of pressure confinement in the system. The bulging on the 60g specimen is shown in more detail in Figure 4.16.

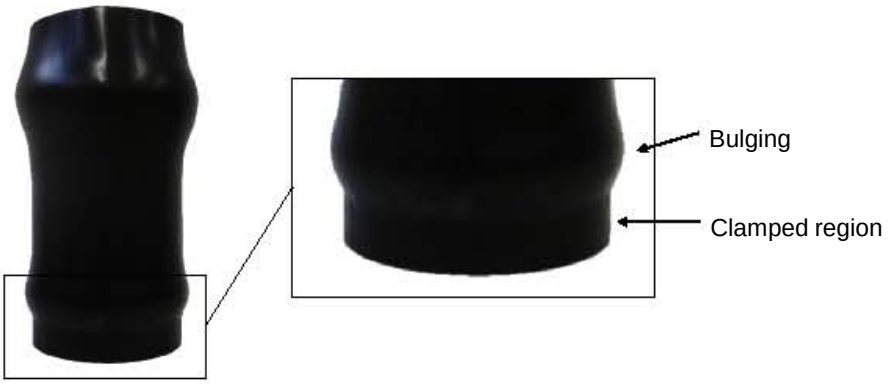

Figure 4.16: Bulging near closed end of cylinder subjected to blast load from 60g charge mass at an axial charge position of $0.75l$ ($60g\_0.75l$).

Figure 4.17 presents the experimentally-measured cylinder profiles for all charge masses in this section. The profiles are created by axially sectioning the post-test cylinders and digitizing a trace of the profile using Engauge Digitizer 4.1. Note that since the 30mm clamped region is included in the figure, the original axial charge position is at 255mm. Also since these profiles are traced from cylinder sections, they represent the approximate *radial* deflection, and not the diametric deflection as reported previously. Owing to the biased aspect ratio of the profiles, the ratio of the x-y scale is 1:8.75 which significantly magnifies the deformations and disparities.

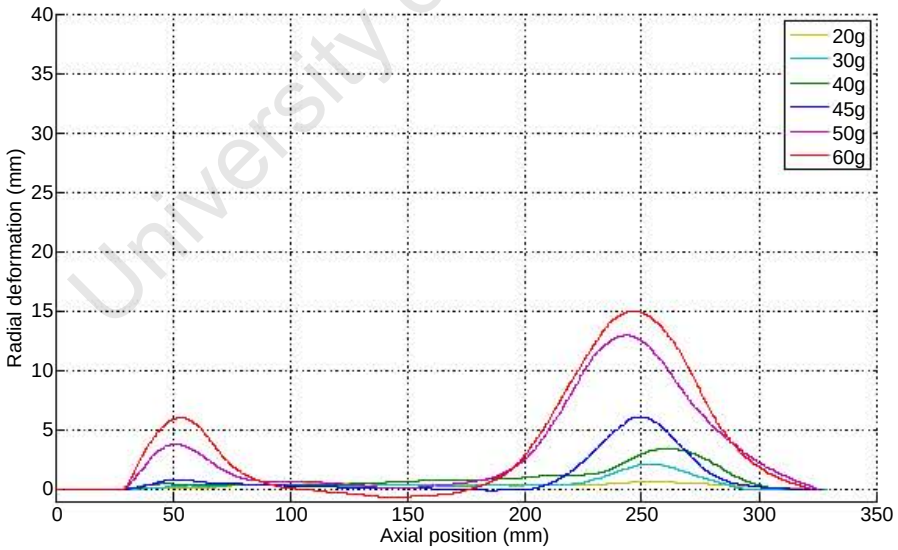

Figure 4.17: Experimental cylinder profiles for cylinders tested with various charge masses at an axial charge position of $0.75l$.

The general increase in deformation with increasing charge mass is evident in the figure, where the significant jump in deformation from 45g to 50g is clearly seen. With the exception of the 40g test, the maximum deformations are relatively well aligned indicating a good degree of repeatability for the experimental procedure.

The impulse imparted to the "rigid" closed end of the cylinders in this section is shown in Figure 4.18 as a function of charge mass. Similar to that shown previously, the impulse values exhibit an approximately linear increase with increasing charge mass, conforming to the charge mass-impulse ratio of 1:2 which is expected based on similar tests previously conducted at BISRU [26, 28, 60, 61]. The non-zero intercept for the linear trend is understandable given the small number of data points in the set, and the lack of any data below 20g.

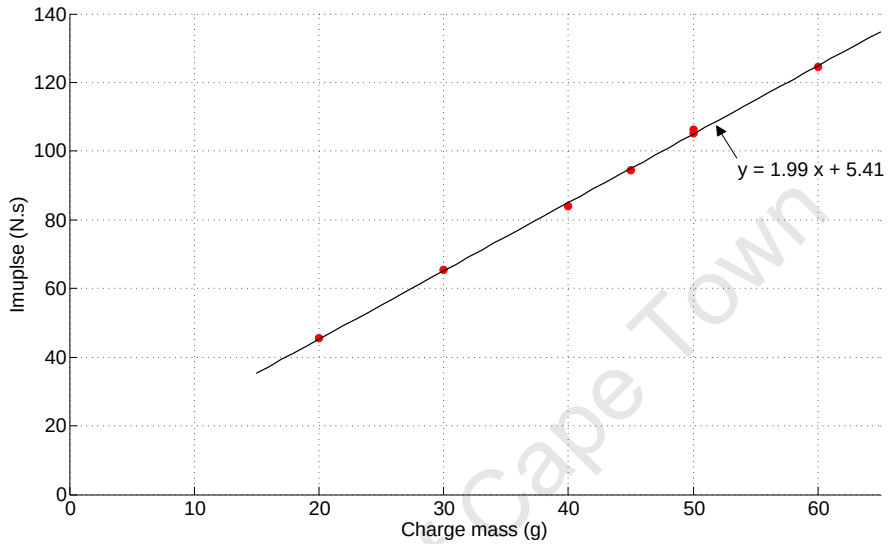

Figure 4.18: Impulse imparted to closed end of cylinders as a function of charge mass for cylinders tested with an axial charge position of $0.75l$.

Chapter 5

Numerical Details and Results

This section details the development of a computational model capable of simulating the experiments in the present work. The simulations are performed using LS-DYNA Release 6.0.0 at the Blast Impact and Survivability Research Unit (BISRU).

To avoid significant repetition, the common fundamental modelling techniques are presented first in this section. Unless explicitly stated otherwise, the methods detailed here are used for all simulations in the present work.

In order to develop a robust model, several preliminary investigations are performed to determine some of the required parameters. First a detonation is performed in 1D to gauge the reliability of the burn algorithm in LS-DYNA. In 2D the effect of mesh density on several parameters is considered. The results of these investigations are also presented briefly in this section, followed by details of the final model.

Following the development of the LS-DYNA computational model, the numerical results are presented in this section along with relevant, brief observations pertaining to the data sets.

5.1 General simulation formulations

The following sections describe several simulations where many of the fundamental modelling techniques are common. Since all the experiments in the present work involve explosive detonated in air, all the simulations comprise some Arbitrary-Lagrange-Euler (ALE) mesh filled with air and and/or explosive material. Additionally several simulations contain a Lagrange mesh representing a structural component.

The techniques used to build these simulations are generally similar, with only the geometries changing in most cases. Consequently to avoid significant repetition, this section presents general details on the meshes, formulations, material definitions, and other requirements used to define the simulations in the present work.

5.1.1 Air domain

The size of the air domain is chosen to represent the air in and around the system to be simulated. Thus in general the air domain is specified to be larger than the structure under consideration allowing space into which the structure may deform.

Since all structures and explosive charges in the present work are circular in section, the simulations are performed in 2D axisymmetry. This is preferred over modelling in 3D owing to its significant computational savings. In LS-DYNA the SECTION_ALE_2D card defines 2D ALE sections, and this card is used to create all the ALE domains in the present work. The axisymmetry is achieved by specifying the whole domain to comprise element formulation 14 (ELFORM=14), which is an axisymmetric solid element.

By specifying ALE formulation 11 (ALEFORM=11), the domain is meshed with multi-material (MM) elements. The MM formulation enables the mixing of different materials within a single ALE element, which in the present work is typically air and explosive products.

Note that LS-DYNA requires that the y-axis is used as the axis of symmetry. However since the geometry of the simulations is generally biased in the y-direction and considering the portrait orientation of this document, it is spatially beneficial to present simulation images rotated through 90°. Consequently in the figures in the present work the x-axis represents the axis of symmetry unless otherwise indicated.

To fill the whole domain with air, the entire domain is specified with the LS-DYNA material card MAT_NULL. Along with an appropriate equation of state (EOS), this material card is used to approximate the air as an ideal gas. To achieve this the linear polynomial EOS (EOS_LINEAR_POLYNOMIAL) is used in the present work with the

appropriately selected parameters. Details of the material model and EOS are presented in Section 5.1.4.

5.1.2 Explosive domain

For simulations that include explosive material, the MM nature of the ALE domain is invoked and a portion of the air domain is filled with explosive. This is achieved with the LS-DYNA card INITIAL_VOLUME_FRACTION_GEOMETRY which allows regions in an ALE domain to be filled with different materials of a chosen geometry.

If the axis of symmetry passes through the charge centre, spherical charges are represented as semi-circles in 2D axisymmetry. This is achieved by specifying container type 6 (CONTYP=6) on the INITIAL_VOLUME_FRACTION_GEOMETRY card, which defines the filled region as a circle (or sphere in 3D) and requires only a centre point and radius.

In several of the preliminary numerical simulations in Section 5.4, disc-shaped charges are used. If the axis of symmetry runs through the central axis of the disc, then representation is a rectangle in 2D. Container type 5 (CONTYP=5) is used in this case to define the end points of a rectangular region to be filled.

To fill the requisite regions with explosive material, the region is specified with the LS-DYNA material card MAT_HIGH_EXPLOSIVE_BURN, along with the Jones-Wilkins-Lee (JWL) EOS (EOS_JWL). Together these cards are typically used to simulate the burning of high explosives in LS-DYNA. Details of the material model and EOS are presented in Section 5.1.5.

Regardless of the filled geometry, a detonation point is necessary to initiate detonation of the explosive material. The detonation point is specified by defining its spatial position on the INITIAL_DETONATION card. In addition to its position the INITIAL_DETONATION card requires the explosive lighting time, that is the time in the simulation at which the explosive is lit. This is specified as 0μs for all the simulations in the present work unless otherwise indicated.

5.1.3 Cylinder domain

Most of the simulations in the present work involve a structural element that is loaded by the blast wave due to the detonation of the high explosive. The size of the structural domain is generally chosen to represent its physical geometry. In some cases geometric modifications are used to enable the application of boundary conditions, or because a portion of the physical structure is superfluous for the simulations.

All the structural domains are created using the SECTION_SHELL LS-DYNA card meshed with element formulation 14 (ELFORM=14), which defines the elements in the domain as 2D axisymmetric solids. As usual the y-axis is taken as the axis of symmetry[1]. By specifying the 2D solid element type 1 (SETYP=1) on the SECTION_SHELL card, the elements are defined as Lagrange elements, which are typically used for modelling relatively dense structural components. In the present work the Lagrange domain is used to model steels which are significantly denser than air.

To fill the Lagrange domain with the required material, the entire domain is specified with an appropriate LS-DYNA material card depending on the desired stress-strain relationship. For the majority of the models in the present work, a modified version of the Johnson-Cook [52] constitutive relationship is used and the material card MAT_JOHONSON_COOK (LS-DYNA MATERIAL 015) is specified accordingly. For solid elements with the Johnson-Cook [52] relationship, LS-DYNA requires an EOS and the Gruneisen (shock) EOS (EOS_GRUNEISEN) is used in the present work. Details of the material model and EOS are presented in Section 5.1.6.

The fluid-structure interaction (FSI) between the ALE domain and the Lagrange domain is defined using the powerful LS-DYNA coupling card CONSTRAINED_LAGRANGE_IN_SOLID. Coupling type 4 (CTYPE=4) is specified to achieve a penalty-based coupling between the two domains.

One of the inherent problems with FSI is material transport (leakage) through the Lagrange domain. In the present work this is identified as explosive material or significant pressure flowing *through* the Lagrange structure, where in reality it cannot do so. The most basic method of mitigating leakage is choosing an appropriate relative resolution between the ALE and Lagrange meshes, where ratios of 1:2 or 1:4 are typically found to be acceptable [62].

The CONSTRAINED_LAGRANGE_IN_SOLID card contains several other parameters that are used to mitigate the leakage including: the number of coupling points, leakage control, and the leakage control penalty factor. It is recommended to maintain *at least* two coupling points per each ALE element side length during the entire simulation duration [63]. However a balance must be found between the number of coupling points and the degree of leakage, since too many coupling points leads to numerical instability [63].

In the present work four coupling points (NQUAD=4) are distributed over the surface of each Lagrange element (that is 4×4). Leakage control (ILEAK=2) is specified, along with a penalty factor of 0.1 (PLEAK=0.1), which is the default value for this parameter as recommended [63].

[1]See note in Section 5.1.1

A further technique used to mitigate leakage is the specification of an additional CONSTRAINED_LAGRANGE_IN_SOLID card as used successfully by Geretto [62]. By using two coupling cards, the coupling between the air material and the Lagrange mesh is separated from that for the explosive material and the Lagrange mesh. This method is employed for all simulations in the present work.

5.1.4 Air material model

All air in the present work is modelled using a combination of the LS-DYNA material card MAT_NULL and the linear polynomial EOS (EOS_LINEAR_POLYNOMIAL). The reference mass density of air is specified on the material card as 1.184kg/m^3 which is typical for air at atmospheric pressure and 25°C.

The linear polynomial EOS requires values for its constant parameters, as well as the initial internal energy of air. The internal energy is used to calculate the initial air pressure at the beginning of the simulations.

To approximate an ideal gas, the EOS constant parameters C_4 and C_5 are specified as 0.4, while all other constants are set to zero as suggested in the LS-DYNA Keyword Manual [63] and by Alia and Souli [64]. This gives an initial internal energy for air of 253.3kJ/kg, at an atmospheric pressure of 101.3kPa. No strength model is required for air as it offers no resistance to shear distortion [65].

A specific ideal gas EOS (EOS_IDEAL_GAS) is available in LS-DYNA as an alternative approach to that detailed above. Several simulations were performed using this recently-added EOS instead of the linear polynomial EOS, with no difference in the results. However, the linear polynomial EOS is preferred in the present work since it has been used extensively in the literature to approximate air domains in blast applications [63, 64, 66, 67]. Additionally the relatively recent inclusion of the ideal gas EOS means it is less thoroughly tested than the linear polynomial EOS, and thus its use increases the probability of including some unknown numerical error in the simulations. Consequently the use of the ideal gas EOS is not considered further.

The material and EOS properties for air are summarised in Table 5.1.

ρ	e_0	C_0	C_1	C_2	C_3	C_4	C_5	C_6
kg/m^3	kJ/kg	-	-	-	-	-	-	-
1.184	253.3	0	0	0	0	0.4	0.4	0

Table 5.1: Material and linear polynomial EOS properties for air. Values from [63] and [64].

5.1.5 Explosive material model

The explosive material used in the experiments is Plastic Explosive 4 (PE4). PE4 has the same explosive characteristics as Composition 4 (C4), differing only in terms of the plasticisers [65]. Well-used material model data exists for C4 and thus the explosive material in the simulations is approximated as C4 instead. This substitution has been used successfully in several previous works at the Blast Impact and Survivability Research Unit (BISRU) [60, 65].

All explosive material in the present work is modelled using a combination of the LS-DYNA material card MAT_HIGH_EXPLOSIVE_BURN and the JWL EOS (EOS_JWL). The material card requires the mass density of the explosive ρ, the detonation velocity D, and the CJ pressure P_{CJ}. These are listed in Table 5.2.

The JWL EOS card requires several constant parameters. These parameters chosen for C4 explosive are taken from the LLNL Explosives Handbook [14] and listed in Table 5.2.

ρ	D	P_{CJ}	A	B	R_1	R_2	ω	e_0
kg/m^3	m/s	GPa	-	-	-	-	-	MJ/m^3
1.601	8193	28	609.77	12.95	4.5	1.4	0.25	9000

Table 5.2: Material properties and JWL EOS parameters for C4 explosive. Values from LLNL Explosives Handbook [14].

5.1.6 304 stainless steel material model

The material used in the present work is seamless, 304 stainless steel pipe. No published strength data exists for this material particularly as seamless pipe. Consequently to obtain its strength parameters, uni-axial tensile specimens cut from the pipe are tested on a Zwick/Roell 1484 tensile testing machine at the Centre for Materials Engineering (CME) at the University of Cape Town. The post-yield material behaviour is found from iterative simulations of the tensile tests in LS-DYNA. This process as well as tensile test details are presented in Appendix B.

At the commencement of the present work there was intention to subject the material to various high strain rate tests using a split-Hopkinson Bar. However fabricating accurate specimens, that are unaltered in their material properties, and can be used routinely for high strain rate split-Hopkinson Bar testing is made difficult by the pipe curvature. Consequently this is not attempted and the published data is used instead. It should be noted that 304 stainless steel is only moderately strain rate sensitive, and thus the strain rate parameters are less significant than they are in the case of mild steel [68].

All the stainless steel in the present work is modelled with a combination of the LS-DYNA material card MAT_JOHONSON_COOK (LS-DYNA MATERIAL 015), and the Gruneisen (shock) EOS (EOS_GRUNEISEN). The material card requires several inherent material properties, as well as strength and strain rate data. These are listed in Table 5.3. Parameters A, B, and n are found from the uni-axial tensile testing and simulations mentioned previously, while the strain rate constants, D and q are taken from published data [58,59].

Since the published strain rate data for 304 stainless steel [58, 59] is in terms of Cowper-Symonds [47] parameters, a modified version of the Johnson-Cook [52] constitutive relationship is used which employs a Cowper-Symonds-like formulation to capture the strain rate effects. This is achieved on the material card by specifying a viscoplastic formulation (VP=1), and setting the optional strain rate form to the Cowper-Symonds [47] formulation (RATEOP=3).

ρ	G	E	ν	A	B	n	D	q	T_{melt}	T_{room}
kg/m^3	GPa	GPa	-	MPa	MPa	-	s^{-1}	-	K	K
7900	81.8	200	0.3	310	1015	0.59	100	10	1673	298

Table 5.3: Material properties and Johnson-Cook [52] strength properties for 304 stainless steel.

The parameters specified for the EOS_GRUNEISEN card are taken from Steinberg [69] and listed in Table 5.4. No significant difference in structural response is exhibited whether using the Gruneisen or linear EOSs.

C_0	S_1	S_2	S_3	γ_0
m/s	-	-	-	-
4578	1.49	0	0	1.93

Table 5.4: Gruneisen EOS parameters for 304 stainless steel from Steinberg [69].

Note than in the case where other steels are used in the present work, the material specifications remain fundamentally the same, only the Johnson-Cook [52] and strain rate parameters are adjusted accordingly where necessary.

5.1.7 Boundary conditions

The boundary conditions used for the ALE domain in the present work may be considered as either symmetry boundary conditions or material transport boundary conditions. In general symmetry boundary conditions impose the constraints required to reduce the full 3D domain to its 2D (axi)symmetric projection, while material transport boundary conditions define how material behaves at the global boundaries of the domain. In

LS-DYNA these boundaries are specified by defining the appropriate nodal degrees of freedom (DoF) on the BOUNDARY_SPC_SET card.

A symmetry boundary condition is defined in the ALE domain along the entire axis of symmetry, which corresponds to the x-axis as presented in this report. Along this boundary the translational DoFs for the nodes that coincide with planes of symmetry are constrained, thus prohibiting material flow and/or pressure wave movement *across* this boundary.

The material transport boundary conditions used in the present work may be considered as either reflective or flow out. In general material flow is not permitted across reflective boundaries, while flow out boundaries do not inhibit material transport. In the models, reflective boundary conditions are defined by constraining all nodal DoFs along the boundary, while flow out boundaries are achieved by keeping the boundary DoFs unconstrained.

The flow out boundaries are used to truncate an infinite/near-infinite space, from which no material flow back *into* the model domain is expected. In the present work this boundary condition permits air and explosive product to flow out of the modelled domain, beyond which its history is lost to the simulation. Flow out boundaries are assigned to the ALE domain wherever it is truncated with the environment, that is outside the cylinders and ahead of the open end.

The reflective boundaries are used to approximate boundaries that are considered rigid relative to other components, and/or where structural deformation is negligible or unimportant. In the ALE domain in the present work, boundaries that are not open to the atmosphere are assigned a reflective boundary condition. This corresponds to the the "rigid" closed end in the experiments.

Like that for the ALE domain, the boundary conditions for the Lagrange domain are specified by constraining the appropriate nodal DoFs on the BOUNDARY_SPC_SET card. In the present work the only boundary conditions imposed on the Lagrange domain are those that approximate clamping in the experiments. This is achieved by setting the displacements/velocities at the required nodes to zero, in either the x- and/or y-directions as required.

5.2 Numerical measurement

In order to compare with the parameters measured experimentally, for instance the final cylinder deformation and the impulse imparted to the pendulum, the same parameters are required from the simulations. Details on the calculation of these parameters from the simulations are presented briefly in this section.

5.2.1 Deflection calculation

A typical radial deflection-time history for a point on the external surface of one of the Benham and Duffey [5] cylinders simulated in Section 3.2 is shown in Figure 5.1. The qualitative nature of the deflection history is similar for any significantly deformed point along the cylinder length.

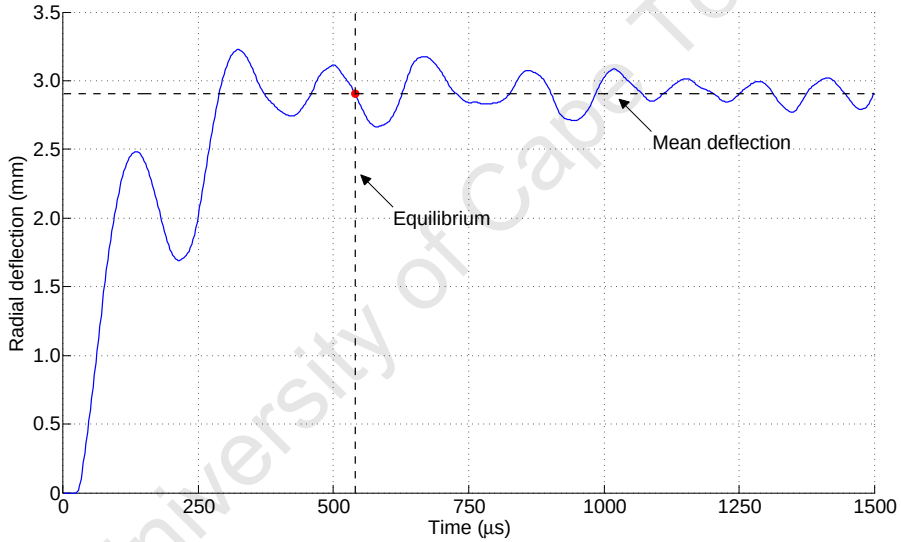

Figure 5.1: Definition of equilibrium point and final deformation for simulations.

It is clear in Figure 5.1 that the deflection values for a given point oscillate for longer than the duration of the simulation. Consequently specifying an exact final displacement value is generally difficult. To overcome this a mean deflection is calculated, from the time of equilibrium up to the end of the deflection-time history.

The structure is said to be in equilibrium when the change in amplitude of consecutive oscillations is negligible. The generic point of equilibrium is taken as midway between the preceding crest and trough as indicated by the red marker in Figure 5.1, and in this case the equilibrium is attained after 540μs. The final radial deflection is the mean of all deflection values beyond this equilibrium point, indicated by the horizontal, dashed line.

Since the *diametric* deformation is measured from the experimental specimens, the mean

value as indicated in Figure 5.1 is doubled and reported as the final simulated diametric deflection.

5.2.2 Impulse calculation

In order to calculate the impulse from the simulations, tracer points are defined in the ALE domain immediately ahead of the reflective boundary corresponding to the "rigid" closed end of the cylinders. The impulse recorded at this boundary corresponds to that measured in the experiments. The tracer points are fixed in space and distributed evenly from the axis of symmetry radially outwards to the cylinder wall. The positions of the tracer points as defined in the final model are indicated in Figure 5.2.

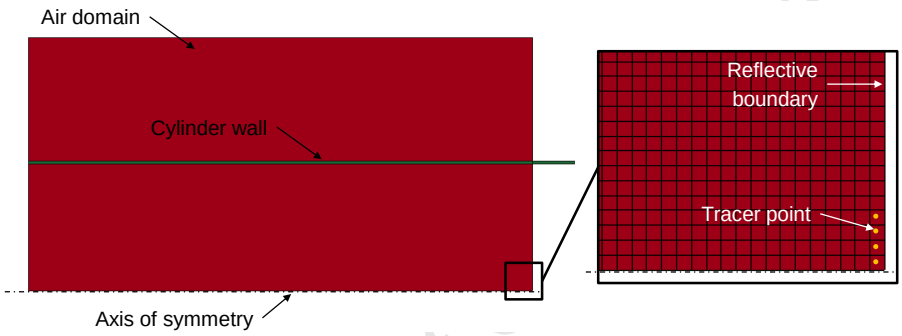

Figure 5.2: Positions of tracer points used to record pressure-time histories in simulations.

A typical pressure-time history from a tracer point near the axis of symmetry is shown in Figure 5.3. As described in Section 2.5.8, the integral of a pressure-time curve gives the specific impulse (impulse per unit area). Consequently the piece-wise simulated specific impulse i_k is found by numerically integrating the pressure-time history recorded at each tracer point. Since the pressure values reported by LS-DYNA represent absolute pressures, to get gauge pressures 101.3kPa is used as the reference pressure in the integration.

For a circular-section, axisymmetric domain as in the present work, the incremental area a_k is an annulus with outer radius R_k and inner radius r_k. The area of the annulus is given by

$$a_k = \pi \left(R_k^2 - r_k^2 \right) \tag{5.1}$$

where each tracer point is taken as midway between R_k and r_k, representing a spatial average over its area.

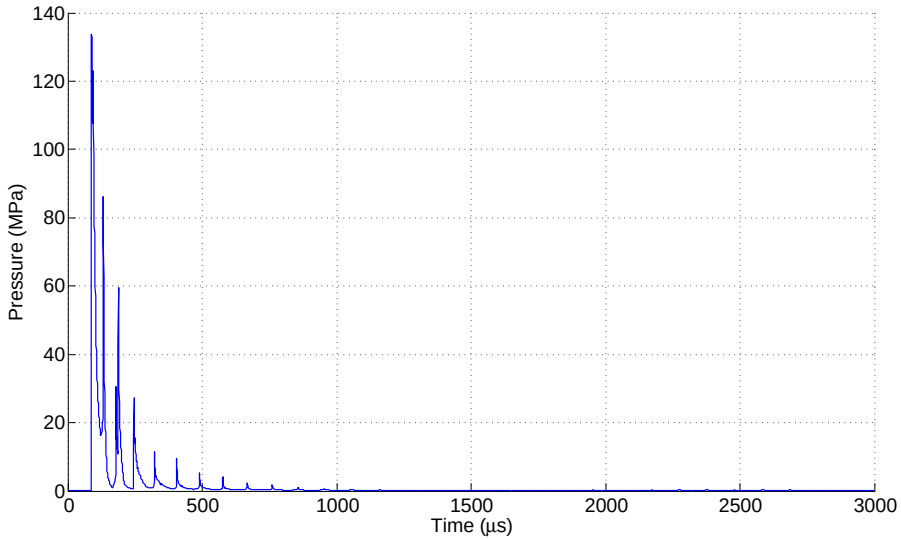

Figure 5.3: Typical simulated pressure-time history for a point near axis of symmetry.

By multiplying the specific impulse at each tracer point i_k by the area over which it acts a_k, the incremental impulse I_k is found. For n tracer points, the total impulse I_{total} is the sum of all the incremental impulses given by

$$I_{\text{total}} = \sum_{k=1}^{n} I_k = \sum_{k=1}^{n} i_k a_k \tag{5.2}$$

5.3 Preliminary 1D tests

In a previous numerical study in AUTODYN, Ozinsky [70] investigated the effect of mesh density on the detonation pressure and velocity in 1D. In the simple model, the detonation pressure is expected to asymptote towards the Chapman-Jouget (CJ) pressure as the mesh density is increased. However Ozinsky [70] found that beyond a certain mesh density, the detonation pressure exceeded the CJ pressure and continued to diverge increasingly rapidly from this value. Based on this Ozinsky [70] questioned the validity of the detonation-induced overpressures predicted by AUTODYN.

In the same investigation [70], the detonation velocity exhibited asymptotic behaviour toward the CJ velocity in accordance with the simple model.

In 1D the mesh density is defined as the number of elements/cells per unit length of the domain, while in 2D the mesh density is defined similarly on a per unit area basis. A low mesh density has a small number of large elements, while a higher mesh density, possibly referred to as a "more refined" mesh, has a greater number of smaller elements per unit area. The concept of mesh density is illustrated in 2D in the schematic of Figure 5.4, along with the definition of $x \times y$ notation used for all simulations.

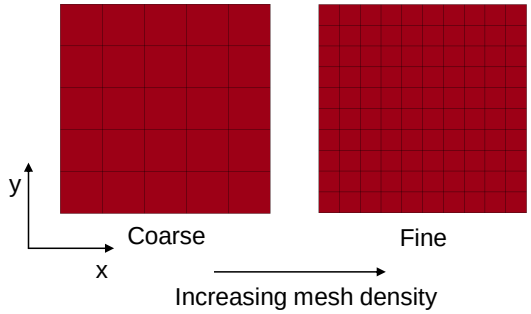

Figure 5.4: Definition of increasing mesh density.

To investigate the same phenomena in LS-DYNA, several 1D detonation tests are performed with different mesh densities. This section presents details of the 1D simulation set up, followed by the effects of the 1D mesh size on the detonation pressure and velocity.

5.3.1 1D preliminary simulation mesh details

To achieve an approximate 1D domain, a long, 2D domain is created with a dominant geometry in one dimension. Such a geometrically-biased domain is acceptable for approximating a 1D analysis. This method is preferred over a true 1D analysis since it enables the use of the same 2D element formulations that are described in Section 5.1.1 and used in the final models.

The domain is meshed with solid elements, using an ALE element formulation, and the whole domain is filled with the explosive material detailed in Section 5.1.5.

Table 5.5 shows the different mesh densities that are investigated. The state variables are recorded by tracers at the centre of each element, and a detonation point is defined at the left boundary. All boundaries for the detonation simulations are specified as reflective boundaries to approximate a confined detonation. Following initiation, the explosive is allowed to detonate and the simulation is stopped before the detonation wave can interact with the right boundary. A zoomed example of the set up is shown in Figure 5.5.

Mesh number	**Cell width**
-	mm
1	1
2	0.5
3	0.25
4	0.1

Table 5.5: Mesh sizes investigated for 1D preliminary detonation tests.

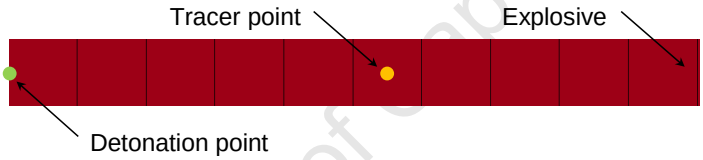

Figure 5.5: Simulation set up for 1D detonation tests. All boundaries are defined as reflective.

5.3.2 Effect of mesh density on 1D detonation pressure

Figure 5.6 shows the maximum detonation pressure as a function of distance for the four meshes tested. Ideally as the mesh is refined, the pressure is expected to converge towards a solution, which in this case is the CJ pressure. The CJ pressure of C4 explosive is approximately 28GPa and is indicated by the dashed horizontal in Figure 5.6.

As expected the detonation pressure increases with increasing mesh density. However the detonation pressure predicted by all four meshes is significantly below the CJ pressure of the explosive.

For Meshes 2 to 4, the rate of pressure increase (slope of the curve) slows significantly with increasing distance, and the curves are always concave down, which is indicative of asymptotic behaviour. In these three cases it appears as if the detonation pressure has quickly reached a steady-state pressure.

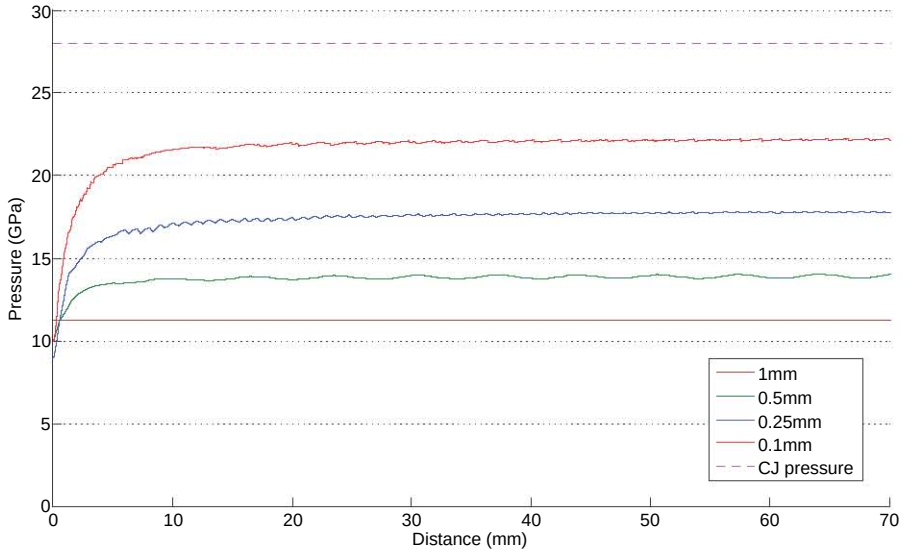

Figure 5.6: Variation of 1D detonation pressure with distance and mesh density.

Mesh 1, the coarsest of the four meshes, also appears to have reached a steady-state detonation pressure. However it exhibits no appreciable ramp-up distance, that is it requires no distance to reach its solution. This behaviour is unrealistic and is likely a result of having large cells with only a single, centrally-located integration point per cell.

For this simple case of a 1D detonation, it is clear that the detonation pressure is highly sensitive to mesh density. It appears as if the detonation pressure may approach the CJ pressure with further mesh refinement. However, the degree of under approximation even by the most refined of the four meshes is concerning, since it is computationally impractical to use a mesh of such refinement in a large scale simulation.

5.3.3 Effect of mesh density on 1D detonation velocity

In the simple model of detonation presented in Section 2.3.1, the detonation wave moves through the explosive at a constant velocity known as the detonation velocity. Ideally as the mesh is refined the detonation velocity should approach a solution, which in this case is the CJ velocity. The CJ velocity for C4 explosive is 8193m/s [14].

The detonation velocity is calculated using the time taken for the detonation wave to reach a fixed point in the mesh. If the detonation wave travels a distance Δx in a time Δt, then the detonation velocity is given simply by

$$D = \frac{\Delta x}{\Delta t} \tag{5.3}$$

A fixed tracer point is defined approximately midway along each mesh to record the pressure-time history at a fixed position. The arrival time Δt is defined as the time taken, from initiation, for the detonation wave to reach the tracer point. The detonation wave is assumed to have reached the tracer point when the pressure at that point increases sharply.

Table 5.6 presents the tracer point location, arrival time, and simulated detonation velocities for the four mesh sizes tested. As the mesh size is refined, the detonation velocity approaches the CJ velocity. The simulated detonation velocities are all near to the CJ velocity, which suggests that the simulated traversal of the detonation wave in LS-DYNA is in accordance with the simple model.

Even in the coarsest mesh, the error from the CJ velocity of approximately +2% is numerically good. The variation in detonation velocity between the meshes is approximately 2%, indicating that the detonation velocity is not sensitive to the mesh density.

Mesh number	**Cell width**	**Tracer point**	**Arrival time**	**Detonation velocity**	**Error**
-	mm	mm	μs	m/s	%
1	1	50.50	6.03	8374.8	+2.22
2	0.5	49.75	6.03	8250.4	+0.70
3	0.25	49.63	6.04	8216.1	+0.28
4	0.1	49.55	6.04	8203.6	+0.13

Table 5.6: Variation of detonation velocity with mesh density for 1D detonation tests.

5.3.4 Summary of 1D tests

This section presented the results of several 1D investigations into the effect of mesh density on the:

- detonation pressure
- detonation velocity.

The detonation pressure was shown to be highly sensitive to mesh density, and exhibited an increase with increasing mesh density. All four mesh sizes investigated significantly underpredicted the CJ pressure. That the finest mesh size underpredicted the CJ pressure by approximately 25% was concerning, as using such a fine mesh in a large scale simulation is computationally impractical. However the significance of the detonation pressure on the ability of the models to produce reasonable predictions is unclear.

The detonation velocity was shown to be largely independent of mesh density, will all four mesh densities predicting a detonation velocity within approximately 2% of the CJ velocity.

5.4 Preliminary 2D tests

In Section 5.3.2 the 1D simulated detonation pressure in the explosive was shown to be highly sensitive to mesh density. Consequently it is reasonable to expect the simulated air pressure due to such detonation of explosives to be similarly sensitive. This concern necessitates further investigation into the simulated detonation parameters in 2D before the models can be used reliably.

In this section the effects of mesh density on the 2D simulated detonation pressure, air pressure, and resulting impulse are detailed. Additionally the effects of mapping the detonation from an initially fine mesh to a less refined mesh are considered. Finally the effect of the Lagrange mesh density on the simulated structural deformation is investigated.

5.4.1 2D preliminary simulation mesh details

The simulations in this section are based on the results of experimental work performed by Rossiter [60]. As part of these experiments, Rossiter [60] detonated charges of PE4 explosive at one end of a thick-walled blast tube, and measured the impulse imparted to a thin plate at the other end. These measured impulse values are used to benchmark the simulations in this section.

The blast tube used by Rossiter [60] was circular in section, and of length and inner diameter 300mm and 106mm respectively. To approximate this in the simulations, a 2D axisymmetric domain is created with dimensions 300mm×53mm, where only the inner radius is required owing to the symmetry. A schematic of the geometry is shown in Figure 5.7.

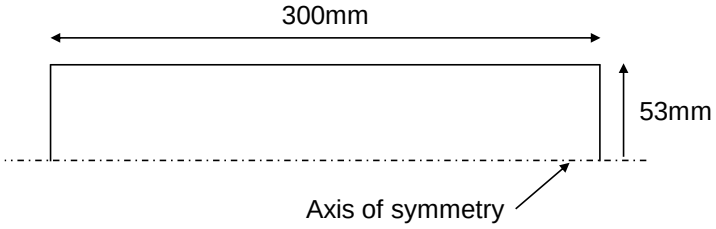

Figure 5.7: Schematic of 2D simulation domain geometry.

The domain is meshed with solid ALE elements with an MM formulation, and the whole domain is filled with air, in accordance with the methods detailed in Section 5.1.1 and Section 5.1.4.

The geometry of the explosive in the simulations is chosen to approximately replicate that used by Rossiter [60] in the experiments. Rossiter [60] used 34mm diameter, disc-shaped

charges of various masses to generate the blast loads. This charge is referred to as the bulk charge. An electrical detonator was attached to the bulk charge using a 6mm diameter, disc-shaped "leader" charge of mass 1g.

The bulk charge is modelled as a disc with radius 17mm and height determined by the desired charge mass. For a desired charge mass m_c of explosive with density ρ_c, the charge height is given by

$$h_c = 4\frac{m_c}{\pi \rho_c d_c^2} \tag{5.4}$$

where d_c is the charge diameter. The 1g leader charge is modelled similarly, except in this case the radius is 3mm.

The geometry of the charge is specified in the ALE mesh and the region is filled with the explosive material as described in Section 5.1.2 and illustrated in Figure 5.8. A detonation point is assigned at the free end of the leader charge, on the axis of symmetry, indicated by the green marker the Figure 5.8.

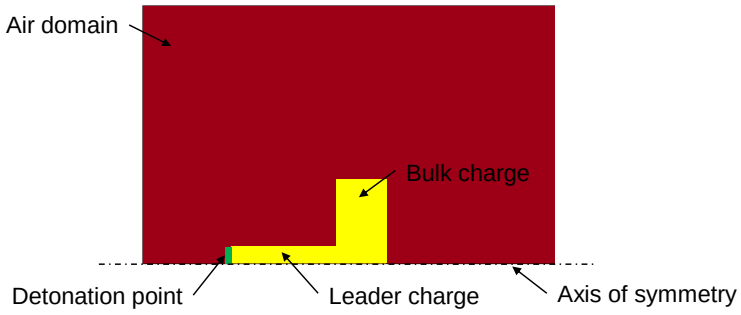

Figure 5.8: 2D axisymmetric charge geometry for preliminary 2D tests.

A typical model schematic for the simulations in this section is shown in Figure 5.9. In the figure, red represents air and yellow represents the explosive charge. As indicated, the walls of the blast tube, as well as the plate at the right end, are modelled using reflective boundaries.

The right end of the explosive charge is aligned with the opening of the blast tube, and thus the air in this region represents that which, in the experiments, is immediately in front of the blast tube. Since this region is open to the atmosphere, flow out boundaries are specified accordingly. The interface between the flow out and reflective boundaries represents the front end of the blast tube.

The different mesh sizes that are investigated are presented in Table 5.7, where the mesh sizes are specified in $x \times y$ notation in according to Figure 5.4.

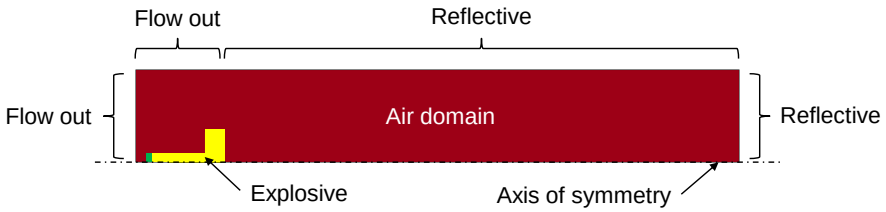

Figure 5.9: Boundary conditions for typical set up for 2D preliminary tests.

Mesh number	Cell size
-	mm×mm
1	1×1
2	0.5×0.5
3	0.25×0.25

Table 5.7: Mesh sizes investigated for 2D preliminary tests.

5.4.2 Effect of mesh density on 2D detonation pressure

To investigate the simulated 2D detonation pressure, several simulations are performed using meshes of different densities. The meshes are created and filled with explosive as described in the preceding sections. Tracer points are defined at the centre of each cell making up the explosive to record the detonation pressure at fixed positions in the explosive.

Three charge masses are investigated to approximately cover the range of charge masses used by Rossiter [60] in the experiments. Two of these charge masses were also investigated numerically in AUTODYN by Ozinsky [70], providing a further benchmark for the results of this section.

The maximum detonation pressure for each configuration is shown in Table 5.8. Similar to the 1D behaviour in Section 5.3.2, the detonation pressure increases with increasing mesh density. In each case the detonation pressure exhibits asymptotic behaviour as it approaches its maximum value.

Mesh number	Cell size	Maximum detonation pressure		
-	mm×mm	GPa		
		4+1g	10+1g	14+1g
1	1×1	15.89	16.23	16.32
2	0.5×0.5	18.53	19.47	19.47
3	0.25×0.25	20.56	21.37	21.39

Table 5.8: Detonation mesh sizes and variation of maximum detonation pressure with mesh density for 2D detonation tests.

Across all mesh sizes from all simulations, the variance in the maximum detonation pressure is approximately 35%. This indicates that the detonation pressure is sensitive to the mesh size in 2D, though not to the same degree as it is in 1D as shown in Section 5.3.2.

The simulated detonation pressures are within approximately 40% of the CJ pressure regardless of the mesh density. Such a disparity from CJ pressure is considered acceptable since the CJ pressure is given for a confined detonation, and the simulations in this case are unconfined [60]. The maximum detonation pressures consistently underestimate, by approximately 5%, those from similar simulations performed by Ozinsky [70] in AUTODYN.

Other than the mesh size dependence of the maximum detonation pressure, no significant conclusion can be made based on this investigation into the effect of mesh density on the maximum detonation pressure in the explosive. At this stage all three mesh sizes are potentially acceptable for use as detonation meshes in the final model.

5.4.3 Effect of mesh density on run time

To investigate the effect of mesh size on the 2D simulation run times, several simulations are performed using meshes of different densities. The meshes are created and filled with explosive as described in Sections 5.1.1 to 5.1.7.

Following from the previous sections, the same three charge masses and mesh sizes are investigated. In each case the simulations are run for 3ms, which is sufficient time to safely capture the initial pressure spike following the detonation, and the gradual return to approximately atmospheric pressure. Capturing these phenomena is necessary to simulate the impulse imparted to the plates in the experiments.

Figure 5.10 presents a comparison of the run times for the simulations using each mesh size and charge mass. The run time is determined by the size of the overall simulation domain and, as illustrated in Figure 5.10, the mesh density and to a lesser extent the charge mass.

As expected the run times increase with increasing mesh density. The maximum run times for the 1mm×1mm and 0.5mm×0.5mm meshes are approximately 1 hour and 13 hours respectively. Such run times are considered acceptable.

However the simulations using the 0.25mm×0.25mm mesh take up to approximately 140 hours to complete. For the large number of simulations that are required in the present work, the use of a mesh that is so computationally expensive is not practically feasible. Additionally the overall domain for the final models in the present work is likely

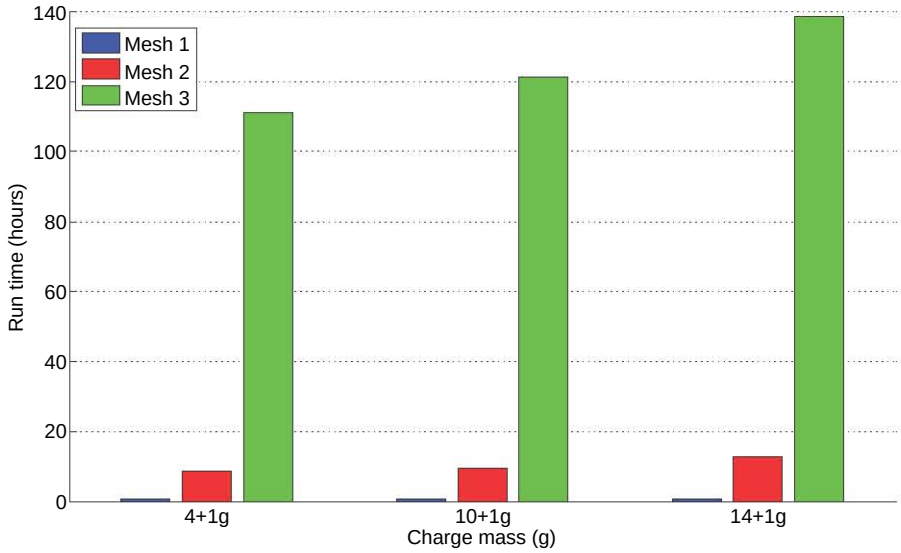

Figure 5.10: Comparison of run times for 2D preliminary simulations.

to be larger than those simulated in this section. Consequently the 0.25mm×0.25mm mesh is not considered for further use for the full simulation duration.

It should be noted that the simulations in this section comprise *only* an ALE domain, that is there is no complex FSI. The inclusion of FSI is expected to increase the simulation run times, further precluding the use of the 0.25mm×0.25mm mesh, and making the 1mm×1mm mesh increasingly attractive.

5.4.4 Effect of mesh density on 2D simulated impulse

To investigate the effect of mesh size on the simulated 2D impulse, several simulations are performed using meshes of different densities. The meshes are created and filled with explosive as described in Sections 5.1.1 to 5.1.7. It should be noted that using impulse as a metric largely ignores the spatial pressure distribution, however no such experimental data exists.

To record the pressure-time history in the air, tracer points are defined at the centre of each cell, along the reflective boundary at the right end of the model domain. These tracer points are indicated in Figure 5.11. This reflective boundary corresponds to the position of the test plates in the experiments by Rossiter [60].

The output from the simulations is a pressure-time history at the discrete tracer points. As described in Section 2.5.8, the integral of the pressure-time curve gives the specific impulse (impulse per unit area). Consequently the simulated specific impulse is found by numerically integrating the pressure-time history recorded at each tracer point. The total impulse is then the sum of each specific impulse multiplied by the area over which

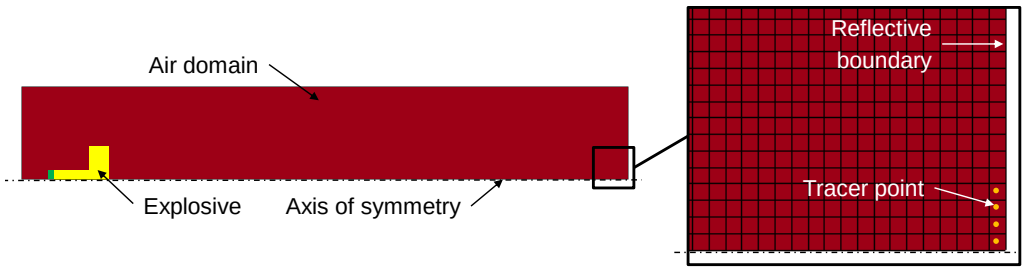

Figure 5.11: Positions of tracer points for 2D preliminary impulse simulations.

it acts. The method for calculating the total impulse from the simulated pressure-time history is described Section 5.2.2.

Following from the previous sections, the same three charge masses and mesh sizes are investigated. However owing to the impractical run time of the 0.25mm×0.25mm mesh, only a single charge mass is simulated as a reference. As described in the previous section, the simulations are run for 3ms, which is enough time to capture the pressure data required to simulate the impulse imparted to the plates in the experiments.

Table 5.9 compares the experimentally-measured impulse values reported by Rossiter [60], with the simulated values for each configuration.

Mesh number	**Cell size**	**Simulated impulse**		
-	mm×mm	N.s		
		4+1g	10+1g	14+1g
-	Experimental	12.1	24.7	31.8
1	1×1	10.53	22.56	30.87
2	0.5×0.5	10.85	23.11	32.43
3	0.25×0.25	-	25.48	-

Table 5.9: Mesh sizes and variation of simulated impulse with mesh density for 2D tests.

The table shows that the simulated impulse increases with increasing mesh density. This behaviour is expected since it was previously shown that the detonation pressure follows a similar trend.

Across all three charge masses, the disparity in the simulated impulse between the different meshes varies between 3% and 13%, with the maximum occurring in the 10+1g case. This indicates a small sensitivity to the mesh density, of the simulated impulse.

All the configurations result in simulated impulses that are relatively close to the experimentally-measured values. This is shown in Figure 5.12, where line $y = x$ represents prefect correlation between the experimental and simulated values, and the distance from this line is indicative of the disparity. The dashed lines are bounds of ±10% of the experimental values, chosen as an approximate quantitative threshold on acceptable impulse simulations.

The different mesh sizes are grouped by colour.

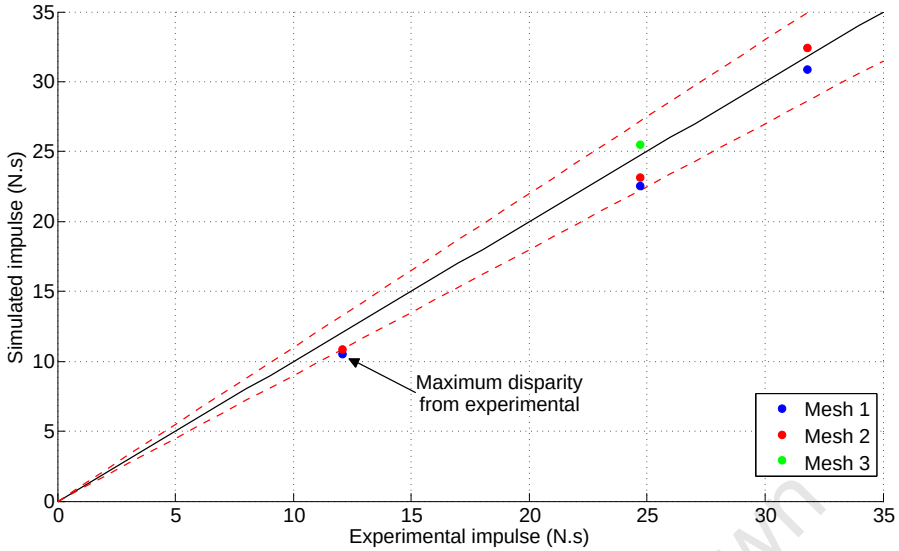

Figure 5.12: Comparison of experimental and simulated impulse values for 2D preliminary tests.

As indicated the maximum disparity is approximately 15% and occurs in the case of the 4+1g simulation with the 1mm×1mm mesh size. All the other simulations fall within or near to the ±10% confidence bounds. It should be noted that the reliability of the experimental impulse increases with increasing charge mass, and thus it is unsurprising that the maximum error occurs for the smallest charge mass with the coarsest mesh.

For the case of the 10+1g simulations, the simulated impulse that is closest to the experimental value is that from the 0.25mm×0.25mm mesh, which overestimates the experimental value by 3%. The 0.5mm×0.5mm mesh simulation underestimates the same experimental value by 7%. However as indicated in Section 5.4.3, the finer mesh requires almost 140 hours to run, compared with approximately 7 hours for the 0.5mm×0.5mm mesh.

The increase in computational expense is disproportionate to the potential increase in accuracy. This confirms the earlier decision to disregard the 0.25mm×0.25mm mesh for use in the final models. Instead, since the simulated impulse is relatively sensitive to the mesh density, but not so much so as to warrant the increased computational expense, either of the 1mm×1mm or 0.5mm×0.5mm meshes are from here on preferred.

5.4.5 Effect of mesh mapping on 2D simulated impulse

It has already been shown in Section 5.4.2, that the maximum detonation pressure in 2D is sensitive to the mesh density. Similarly the simulated impulses in Section 5.4.4 exhibited a small sensitivity to the mesh density, while the finer meshes were computationally very expensive. In all cases so far, both the early explosive detonation and the late-time pressure simulation have been modelled on meshes of the same degree of refinement.

It is plausible that only the early-time detonation need be modelled with a relatively fine mesh to achieve good detonation pressures, and that the late-time pressure modelling may be simulated with a coarser mesh. This would result in significant computational savings over modelling the entire duration with the finer mesh.

To achieve this, the state variables at a given time are transferred from the more refined detonation model to the coarser model for the remainder of the simulation. This process is known as mapping. Typically the mapping occurs very early relative to the overall simulated duration, so that the majority of the simulation occurs on the coarser, less computationally expensive, mesh.

To investigate the merits of using such a mapping technique, several simulations are performed using meshes of different densities. The simulated impulses for each combination of mapping time and mesh size are presented in Table 5.10. In the table, detonation mesh size refers to the mesh size in which the early detonation simulation takes place, while air mesh size refers to the mesh size in which the remainder of the simulation takes place. To save computation time, only the 10+1g charge mass is considered in this section.

As an additional parameter, the effect of the mapping time (i.e. the point in time at which the state variables are transferred from one mesh to the other) is investigated by using three different times in all of the simulations. These mapping times are listed in Table 5.10.

Across all detonation and air mesh sizes and all mapping points, the variation in the simulated impulses is less than 8%. This indicates that the simulated impulse is practically unaffected by the choice of mapping point.

For a given detonation mesh size, the disparity between simulated impulses generated using the various air mesh sizes never exceeds 7%. In general the finer air mesh sizes result in larger simulated impulse values, however the disparity is generally small relative to the total simulated impulse. The variation across mapping points is not considered significant.

For a given air mesh size, the variation between simulated impulses produced by the various detonation mesh sizes is below 6%. With the exception of the 1mm×1mm detonation

Detonation mesh size	**Remap time**	**Air mesh size (mm×mm)**		
mm×mm	μs	1×1	0.5×0.5	0.25×0.25
1×1	5	23.22		
	10	22.57		
	15	22.77		
0.5×0.5	5	22.71	23.40	
	10	22.98	23.26	
	15	23.02	23.58	
0.25×0.25	5	23.16	23.35	23.24
	10	22.85	23.20	23.34
	15	21.83	23.18	22.25
	Experimental impulse: 24.7 N.s			

Table 5.10: Effect of remapping on simulated impulse for 2D preliminary tests.

mesh mapped at 5μs, the finer detonation meshes result in larger simulated impulse values. This is unsurprising since it was shown in Section 5.4.3 that the detonation pressure is inversely proportional to the size of the detonation mesh. However the simulated impulse disparity between detonation mesh sizes is not large enough to be considered significant.

The results of this section indicate that there is no computational benefit or accuracy gain from mapping the simulation from a finer to a coarser mesh at any given time. That is, using even the least refined detonation and air mesh results in a simulated impulse value that is acceptable relative to those from other configurations. Consequently, the mapping process is not considered further for the final models. Further for the mesh sizes tested, the simulated impulse is not significantly affected by the choice of either the detonation or air mesh, hence both the 1mm×1mm and 0.5mm×0.5mm mesh sizes are remain acceptable for the final models.

5.4.6 Effect of Lagrange mesh density on simulated deformation

The preceding mesh density investigations have focussed solely on the mesh density of the ALE domain and its resulting ability to simulate the air/pressure-related phenomena. However the models in the present work are required to provide an estimation of the deformation of a cylinder wall which necessitates the inclusion of a Lagrange domain as described in Section 5.1.3. Consequently the effect of the Lagrange mesh density on its resulting predictions is important.

A parameter study is performed to investigate the effect of the Lagrange mesh size on the cylinder deformation profile. With the Benham and Duffey [5] model of Section 3.2 as a basis, simulations are performed with Lagrange domains of different mesh destinies. All

simulations are performed for a centrally-located, spherical 0.441lb (200.0g) charge mass, in an ALE domain with element size 1mm×1mm. Table 5.11 lists the four Lagrange mesh sizes investigated in this section, along with their respective midpoint deformations.

Mesh number	**Cell size**	**Midpoint deformation**
-	mm×mm	mm
1	1×1	2.77
2	0.5×0.5	2.86
3	0.25×0.25	2.92
4	0.1×0.1	2.95

Table 5.11: Mesh sizes and deformations for 2D Lagrange domain tests.

It is clear that the midpoint deformation of the cylinders increases with increasing mesh density. However the variation across all four mesh sizes is approximately 6.5%, which is disproportionately small compared to the relative element sizes in the domains. That is a 90% change in the Lagrange mesh density results in only a 6.5% change in the simulated deformation.

Figure 5.13 shows the deformation profiles for the four mesh sizes, where the deformations are exaggerated by the approximate 1:100 x-y scale. For all the profiles, the first and last 25mm represent the constrained ends of the cylinders, and the midpoint is at approximately 290mm. All the profiles are similar, both near the clamped ends and at the midpoint, suggesting that the cylinder deformation is not highly sensitive to the Lagrange mesh density.

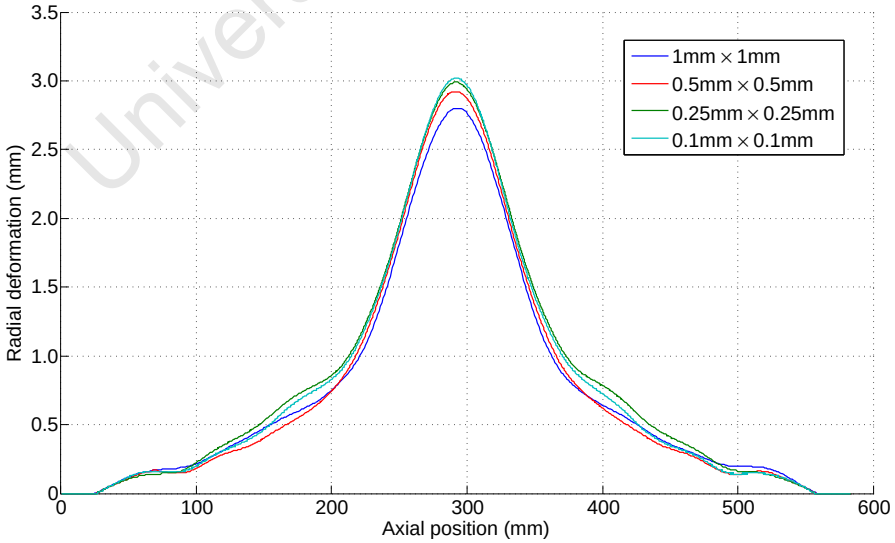

Figure 5.13: Effect of Lagrange mesh density on deformation profile.

Figure 5.14 shows the material locations for two simulations with different Lagrange mesh densities 280μs after detonation. All other parameters are identical. In the figures the air is represented by yellow and brown corresponds to explosive material. As indicated in Figure 5.14a for the case of the 0.5mm×0.5mm Lagrange mesh, explosive material has travelled *through* the solid Lagrange domain. This is known as material leakage and clearly represents an unrealistic phenomenon that must be mitigated. Such mitigation may be achieved by increasing the Lagrange mesh density as shown in Figure 5.14b where there is no leakage for a Lagrange mesh with dimensions 0.25mm×0.25mm.

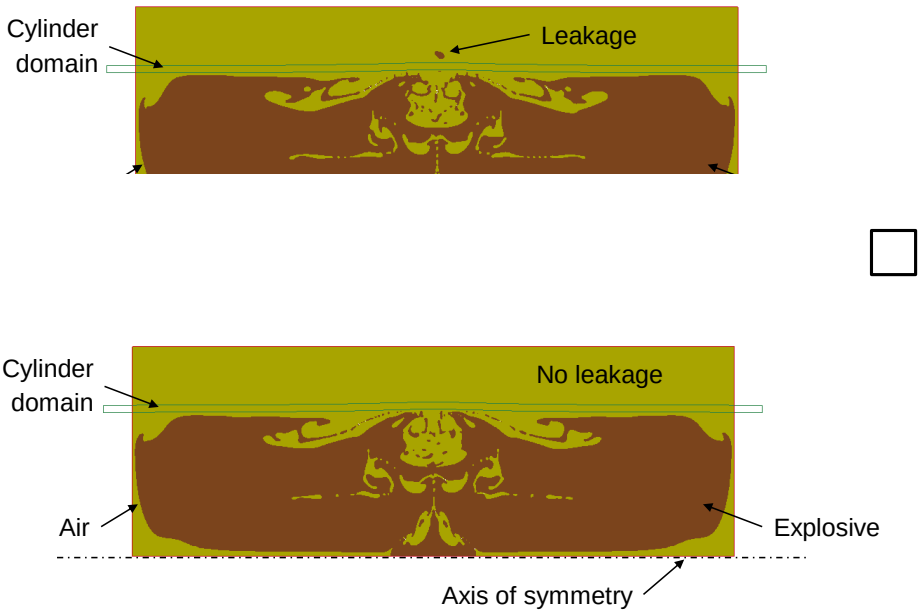

(b) No leakage for Lagrange elements of dimensions 0.25mm×0.25mm.

Figure 5.14: Comparison of leakage of explosive material through the cylinder domain for Lagrange meshes of different densities. Both images 280μs after detonation.

In Section 5.4.3 the run times for several simulations with different mesh densities were compared and it was shown that the run time increases significantly with mesh density. However in Section 5.4.3, the simulations employ no FSI which is expected to add an additional computation cost, increasing the run times even further.

Figure 5.15 compares the run times for the four simulations in this section which *do* consider the FSI. Recall that the ALE mesh density of 1mm×1mm is constant in this section, only that of the Lagrange domain is varied. As expected the run times increase with increasing mesh density with the maximum run time approximately 70 hours for the 0.1mm×0.1mm Lagrange mesh.

In Section 5.4.3, the *maximum* run time for the ALE mesh with dimensions 1mm×1mm is approximately 1 hour, while the *minimum* run time in this section is approximately 5 hours. However the simulation time in Section 5.4.3 is 3ms compared to 1ms for those

in this section. Thus even though the simulation time in this section is 33% of that in Section 5.4.3, for the *best* case the inclusion of FSI has increased the run time by a factor of 5. This significant increase justifies the preference for the 1mm×1mm ALE mesh as alluded to in Section 5.4.3.

Based on the balance between appropriate simulation run time and the mitigation of leakage through the Lagrange domain, the 0.25mm×0.25mm Lagrange mesh is used in the present work with, along with 1mm×1mm ALE meshes.

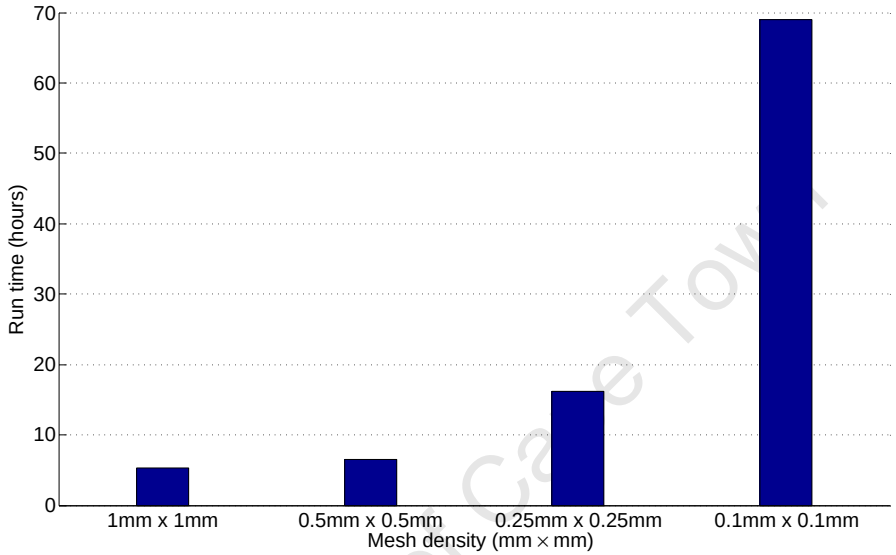

Figure 5.15: Effect of Lagrange mesh density on simulation run time for constant ALE mesh density of 1mm×1mm.

5.4.7 Summary of 2D tests

This section presented the results of several 2D investigations into the effect of:

- mesh density on the detonation pressure
- mesh density on the simulation run time
- mesh density on the simulated impulse
- mesh mapping on the simulated impulse
- Lagrange mesh density on simulated deformation.

The detonation pressure exhibited a small sensitivity to mesh density, increasing moderately with increasing mesh density. All three mesh sizes investigated significantly underpredicted the CJ pressure, though this was deemed to be acceptable since the simulations

in this section were unconfined and the CJ pressure is quoted for confined detonations. However the underprediction of the detonation pressure was later shown to be practically unimportant, as all the simulations predicted impulses that were near to the respective experimentally-derived values.

As expected, the run times for the simulations were highly sensitive to the mesh density, exhibiting a significant increase in run time with increasing mesh density. The 0.25mm×0.25mm mesh size was practically infeasible, requiring approximately 140 hours for 3ms of simulation time. Using impulse as a metric, the small increase in accuracy using this mesh was later shown to be highly disproportionate to the significant increase in computation time. The run times were affected by the charge mass in the simulations, with larger charges resulting in increased run times.

The simulated impulse exhibited a small increase with increasing mesh density, and the majority of the simulations predicted impulses within ±10% of the respective experimental values. Either of the 1mm×1mm or 0.5mm×0.5mm mesh sizes were preferred for the final models as they offered the best balance of accuracy and computation time.

A mapping technique was trialled where the state variables at a given time were transferred from a refined detonation model to a coarser model for the remainder of the simulations. No significant accuracy gain or computational benefit was derived from using the mapping technique. It was also shown that the choice of mapping time did not practically affect the simulated results.

Finally several simulations were performed with Lagrange domains of different mesh densities. Across all the mesh sizes, the simulated midpoint deformations were within approximately 6.5% of each other, and qualitatively the simulated cylinder profiles were all similar. Consequently no significant accuracy gain was achieved by using finer Lagrange meshes. However the coarser Lagrange mesh sizes exhibited material leakage through the Lagrange domain, thus the 0.25mm×0.25mm Lagrange mesh was used in the present work as it offered good leakage mitigation and acceptable simulation run times.

5.5 The final model

In the preceding sections, several preliminary investigations were performed on parameters that are important in the final model. The results of these investigations inform the decisions that are made for the final model.

This section presents details of the final LS-DYNA model used in the present work. First the overall model geometry and constraints are described, followed by an outline of the experiments that are simulated.

The simulations in the present work are based on the experiments detailed in Section 4.1, which consider thin-walled, right-circular, stainless steel cylinders subjected to internal blast loads. In the experiments both the charge mass, and its axial position within the cylinders are varied.

The cylinder geometry and material is described in Section 3.3, and is summarised here for ease of reference:

- the cylinders are of radius $a = 75$mm
- the cylinder wall thickness $h = 2$mm
- the cylinder length $l = 300$mm
- the cylinder material is 304 stainless steel.

5.5.1 Air and explosive model

In the preceding sections the deformation of a Lagrange mesh has not been considered, and thus the dimensions of the ALE domain have typically coincided with the dimensions of the structures under consideration. However the cylinders in the final model are expected to deform, and consequently the ALE domain must be extended sufficiently beyond the cylinder dimensions, such that the cylinders are always entirely contained within the ALE domain.

The resulting ALE domain is of dimensions 300mm×150mm, where the 300mm corresponds to the length of the cylinders and the 150mm provides adequate space into which the structure may deform "radially" outwards. Recall that only the cylinder radius is required owing to the symmetry. The ALE domain is meshed with solid MM elements, and the whole region is filled with air, following the methods detailed in Section 5.1. The air material parameters and linear polynomial EOS parameters are listed in Table 5.1.

The element size for the ALE domain is chosen as 1mm×1mm since elements of this size have been shown in Section 5.4 to produce acceptable numerical results. Additionally such an element size is computationally practical for use in FSI relative to smaller ALE elements.

For the experiments in the present work, radially-centred spherical charges are used in all the tests. An electrical detonator is attached to the bulk charge by pushing it into the sphere of PE4 until the front end of the detonator is approximately centred within the sphere. The geometry of the explosive in the simulations is chosen to replicate this, where the 2D axisymmetric projection of a sphere is a semi-circle centred on the axis of symmetry. The required charge mass is specified by adjusting the semi-circle radius, and the semi-circle centre, while constrained to the axis of symmetry, is adjusted according to the required axial charge position. For a desired charge mass m_c of explosive with density ρ_c, the sphere/semi-circle radius is given by

$$r = \left[\frac{3}{4}\frac{m_c}{\pi\rho_c}\right]^{1/3} \tag{5.5}$$

The electrical detonator is modelled by defining a detonation point at the centre of the charge. This is indicated by the green marker in Figure 5.16, which shows the ALE domain and qualitative charge geometry for the final model.

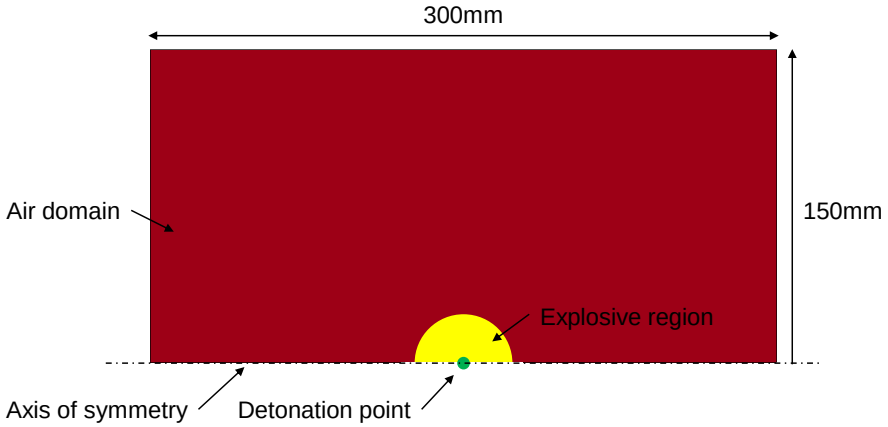

Figure 5.16: ALE domain and qualitative charge geometry for final model.

The material properties and JWL EOS parameters for C4 explosive are presented previously in Table 5.2.

5.5.2 Cylinder model

The 2D axisymmetric projection of an axial section of a cylinder is a rectangle, where the rectangle is a cylinder inner radius away from the axis of symmetry. Consequently in order to include the cylinder in the final model, a rectangular Lagrange domain is created in accordance with the methods described in Section 5.1.

In the simulations only that part of the Lagrange domain that is contained in the ALE domain is subjected to blast loading. That is the axial length of the cylinder that is loaded may be controlled by restricting the ALE domain to a length equal to the internal axial length of the cylinder. This informs the choice of 300mm for the length of the ALE domain as detailed previously.

However the Lagrange domain must be extended beyond the ALE domain to allow for the application of the necessary boundary conditions that approximate the clamping of the cylinder in the experiments. Hence the length of the Lagrange domain is specified as 325mm, and not 300mm. Since the extended portion of the Lagrange domain is beyond the boundary of the ALE domain, the axial length of the cylinder subjected to blasting remains unchanged. The resulting Lagrange domain is of dimensions 325mm×2mm, where 2mm is chosen to correspond directly to a cylinder wall thickness. The Lagrange domain is illustrated in Figure 5.17.

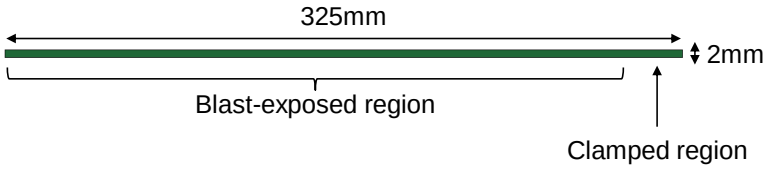

Figure 5.17: Lagrange domain for final model.

The element size for the Lagrange domain is specified to be a quarter that of the ALE domain, that is 0.25mm×0.25mm. As shown in Section 5.4.6, elements of this size have produced acceptable structural responses relative to smaller elements, in addition to minimising material transport (leakage) through the cylinder domain.

The 304 stainless steel material properties, Johnson-Cook [52] strength properties, and Gruneisen EOS parameters are listed previously in Table 5.3 and Table 5.4.

5.5.3 Boundary conditions

Figure 5.18 shows a typical schematic for the final model. The boundaries of the ALE domain are modelled as either flow out or reflective boundaries, depending on whether material may or may not flow across a given boundary. This is detailed in Section 5.1.7.

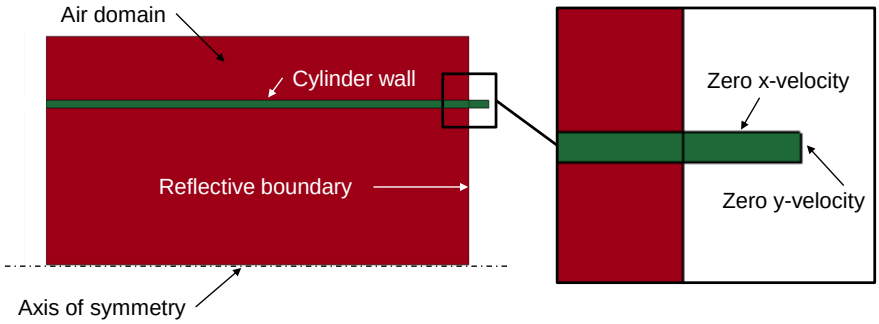

Figure 5.18: Typical boundary condition set up for final model.

For all the experiments in the present work, the end of the cylinder that is clamped is closed while the other end remains open to the atmosphere. This must be captured in the simulations and consequently a reflective boundary is specified at the end of the ALE domain that corresponds to the closed end of the cylinder, while material flow is permitted across the opposite boundary. This is illustrated in Figure 5.18, where all boundaries are flow out except those indicated otherwise.

Figure 5.18 also shows the application of boundary conditions to the extended portion of the Lagrange domain. In this case the velocities of the boundaries of the extended section are specified as zero in either the x- or y-directions. Such a method has been used successfully to approximate clamped structures in previous studies at BISRU [60, 70].

Additionally several simulations were performed where the ALE domain was extended in front of the open end of the cylinder, representing a better approximation of the flow-out boundary condition. The deformation results from these simulations exhibited no significant difference relative to those from simulations with the boundary conditions as described in Figure 5.18. Consequently the configuration of Figure 5.18 is preferred for its smaller ALE domain.

5.5.4 Decoupled model details

One of the advantages of LS-DYNA over the other similar hydrocode AUTODYN, is its improved handling of FSI sensors. In LS-DYNA it is possible to define a tracer point in a moving Lagrange mesh that records state variables in the ALE/Eulerian mesh in which is contained at any given time. This cannot be achieved in AUTODYN [60, 70].

Specifically by implementing the FSI_SENSOR card, it is possible to record the air pressure immediately ahead of the cylinder wall *even* as the cylinder wall deforms. However the output files produced using this method contain only 0s for the air pressures even though the spatial history of the tracer points is recorded correctly in the same output files. The problem occurs whether running the simulations in LS-DYNA Release 5.1.1 or LS-DYNA Release 6.0.0, thus eliminating the possibility of a software "bug" in the .0 release.

A similar simulation is performed in 3D where the output file records non-zero entries for the pressures. Thus it appears at this stage that the ability of LS-DYNA to record ALE/Eularian state variables that contain a moving Lagrange domain, is limited to the 3D case.

Consequently, a modified approach similar to that used in AUTODYN, is required to achieve a pressure-time history of the points immediately ahead of the cylinder wall. Rossiter [60] proposed three methods to overcome this limitation in AUTODYN:

- the pressure history is recorded at the position of the original surface of the structure, even as it deforms
- the structure is fixed in position by specifying a zero-velocity constraint and the pressure history immediately ahead of the structure is recorded
- the ALE/Eulerian domain is truncated at the original surface of the structure, the structure is replaced with a reflective boundary condition, and the pressure history immediately ahead of the boundary is recorded.

The three methods are shown schematically in Figure 5.19, where the ALE domain is represented by blue, the Lagrange domain is indicated by grey, and the red dots correspond to the tracer points used to record the state variables. From tests with a 4+1g charge mass, Rossiter [60] found that using the reflective boundary condition produced an impulse that was closest to that measured experimentally. Consequently where required, the same method is used to record the pressure-time histories in the present work.

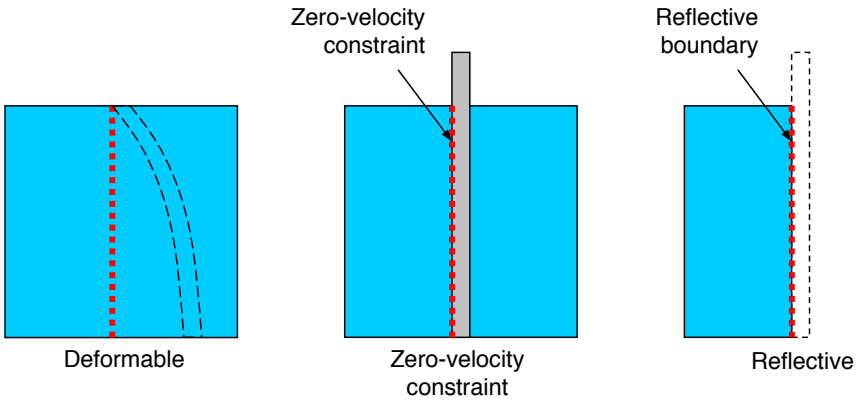

Figure 5.19: Possible tracer point positioning for recording pressure-time histories in air ahead of a deforming Lagrange domain. Image adapted from Rossiter [60].

5.5.5 Summary of final model dimensions

In the preceding sections details were presented of the final LS-DYNA model used to simulate the experiments in the present work. The dimensions and element sizes are summarised below:

- the ALE domain is of dimensions 300mm×150mm,
  with element sizes of 1mm×1mm
- the Lagrange domain is of dimensions 325mm×2mm,
  with element sizes of 0.25mm×0.25mm.

5.6 Numerical results

Following the simulation methods detailed in Section 5.1, the experiments in the present work are simulated in LS-DYNA. An overview of the simulation results are presented in this section. Note that when referring to cylinder deformation, the diametric deformation is implied unless otherwise stated. Also the words deformation and deflection are used interchangeably in this section.

5.6.1 Results for simulations with axial charge position $0.5l$

Figure 5.20 shows the simulated midpoint deflection as a function of charge mass for several tests with a constant axial charge position. In all these simulations, the axial charge is located midway along the cylinder length, that is $0.5l$ relative to the $0l$ closed end. The trend line is a linear best-fit curve to all but the circled data points presented in the figure.

As expected the simulated midpoint deflection increases with increasing charge mass. Excepting the two smaller charge masses (circled), the deflection-charge mass relationship conforms closely to the linear trend for the majority of the charge masses presented. It is clear that the linear trend line is valid only for approximately the range of charge masses for which it is presented, as the global cylinder response appears to be highly non-linear if the region of small charge masses is included.

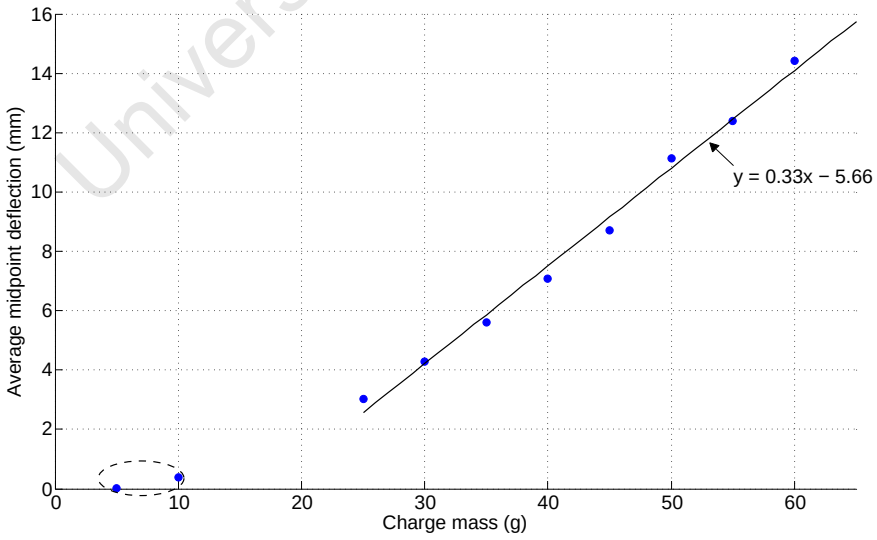

Figure 5.20: Simulated midpoint deflection of cylinders as a function of charge mass for simulations with an axial charge position of $0.5l$.

Figure 5.21 presents the simulated cylinder profiles for all charge masses in this section. The profiles are created by plotting the final x, y coordinates of the cylinders in the simulations, and thus they represent the approximate *radial* deflection, and not the diametric deflection as reported previously. Note that since the 30mm clamped region is included in the figure, the original axial charge position is at 180mm. Also owing to the biased aspect ratio of the profiles, the ratio of the x-y scale is 1:17.5 which significantly magnifies the deformations and disparities.

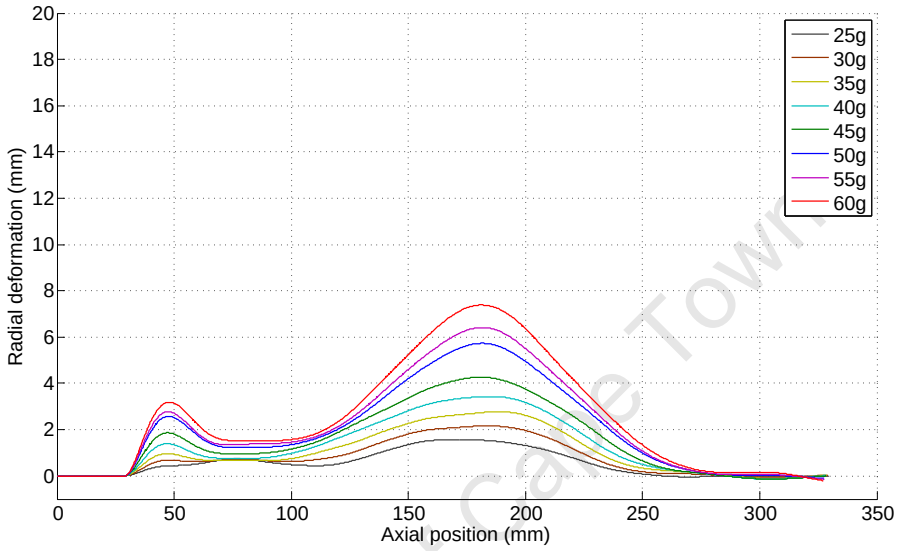

Figure 5.21: Simulated cylinder profiles for simulations with various charge masses at an axial charge position of $0.5l$.

Figure 5.21 shows the gradual increase in radial deformation with increasing charge mass and the qualitative similarity between the profiles. Since the axial length of the deformed regions are all similar, it suggests that the region of deformation is independent of charge mass. The bulging at the region near the constrained end becomes increasingly significant for larger charge masses.

The simulated impulse as a function of charge mass is shown in Figure 5.22 for all the simulations in this section. The trend line is a linear best-fit curve to all the data points.

The simulated impulse exhibits the expected linear increase with increasing charge mass based on previously conducted experimental work at BISRU [26, 28, 60, 61], as well as that in the present work. All the simulated values conform very closely with this approximate 1:2 charge mass-impulse ratio. The non-zero impulse intercept predicted by the linear trend is not unreasonable given the few data points near zero charge mass. However the predicted impulse of 3.59N.s is appropriately small.

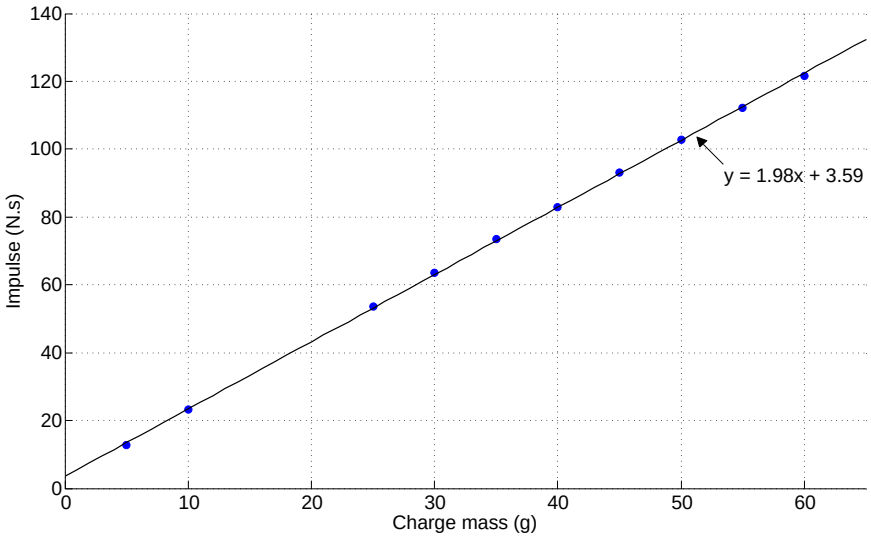

Figure 5.22: Simulated impulse imparted to closed end of cylinders as a function of charge mass for simulations with an axial charge position of $0.5l$.

5.6.2 Results for simulations with axial charge position $0.75l$

The cylinder deflection as a function of charge mass is presented in Figure 5.23 for several simulations with a constant axial charge mass position. All these simulations are performed with the charge mass located at $0.75l$, which is nearer to the open end of the cylinder when the closed end is taken as the $0l$ reference. The trend line is a linear best-fit curve to all the data presented in the figure.

Similar to the responses seen previously, the deflection exhibits an approximately regular increase with increasing charge mass. The linear trend is only valid for approximately the range of charge masses presented, as the cylinder response is unlikely to be linear for very small charge masses as shown for the $0.5l$ simulations. Consequently the negative intercept predicted by the linear trend is trivial.

Figure 5.24 presents the simulated cylinder profiles for all charge masses in this section. The profiles are created by plotting the final x, y coordinates of the cylinders in the simulations, and thus they represent the approximate *radial* deflection, and not the diametric deflection as reported previously. Note that since the 30mm clamped region is included in the figure, the original axial charge position is at 255mm. Also owing to the biased aspect ratio of the profiles, the ratio of the x-y scale is 1:17.5 which significantly magnifies the deformations and disparities.

Figure 5.24 shows the increase in radial deformation with increasing charge mass and the qualitative similarity between the profiles. The degree of deformation of the 60g profile appears disproportionate relative to the others, particularly for the bulged region near the constrained end. Similar to that seen in the $0.5l$ profiles, the distribution of the

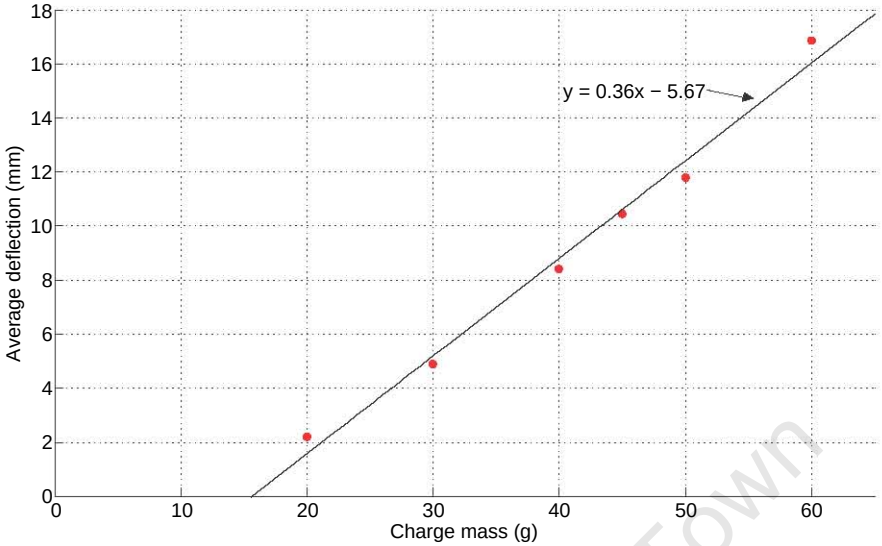

Figure 5.23: Simulated deflection of cylinders as a function of charge mass for simulations with an axial charge position of $0.75l$.

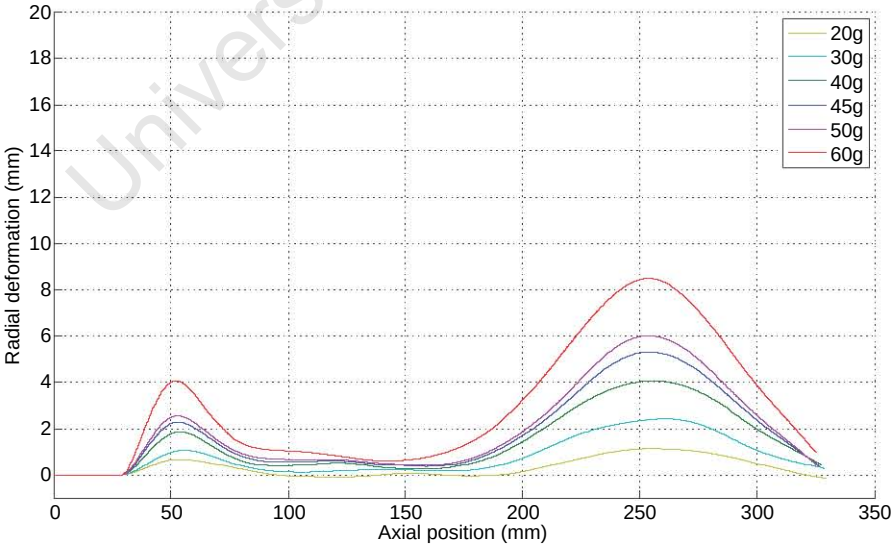

Figure 5.24: Simulated cylinder profiles for simulations with various charge masses at an axial charge position of $0.75l$.

deformation appears to be independent of the charge mass, with the deformed regions all similar in axial length.

Figure 5.25 shows the simulated impulse as a function of charge mass for all the simulations in this section. The linear trend line is a best-fit to the data points, and is valid only for approximately the range of charge masses to which it is fit. The non-zero intercept predicted by the trend line is owing to the lack of data points near zero charge mass.

The simulated impulse increases regularly with increasing charge mass, conforming closely to the linear trend.

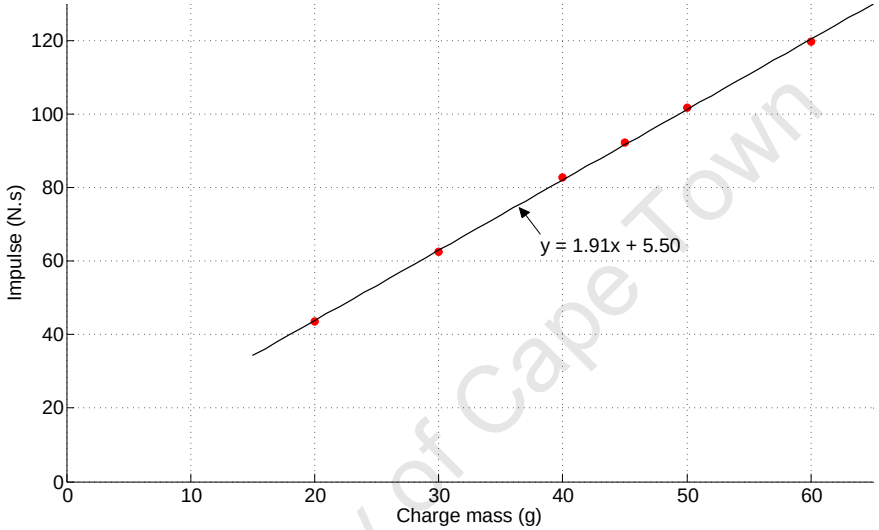

Figure 5.25: Simulated impulse imparted to closed end of cylinders as a function of charge mass for simulations with an axial charge position of $0.75l$.

Chapter 6

Discussion

Based on the results of the experiments and simulations presented previously, this section presents an analysis of the deformation mechanisms in the cylinder systems. First an experimental-simulation correlation is presented, then the effect of the axial charge position is considered. A brief comparison is made between the results in the present work and the modified analytical solution of Section 3.4. Finally the influence of the polystyrene annulus on the cylinder response is briefly discussed.

6.1 Summary of results

A summary of all the experimental and numerical results detailed in the preceding sections are presented in Table 6.1 to Table 6.4 for ease of reference. Further comment is provided in later in this chapter.

6.1.1 Summary of deflection results

Table 6.1 and Table 6.2 summarise the various cylinder deflections in the present work.

Test designation	**Charge mass**	**Charge position**	**Experimental deflection**	**Simulated deflection**
-	g	-	mm	mm
$25g\_0.5l$	25	$0.5l$	3.22	3.04
$30g\_0.5l$	30	$0.5l$	3.19	4.29
$35g\_0.5l$	35	$0.5l$	6.63	5.61
$40g\_0.5l$	40	$0.5l$	7.07	7.08
$45g\_0.5l$	45	$0.5l$	8.51	8.70
$50g\_0.5l$	50	$0.5l$	11.50	11.13
$55g\_0.5l$	55	$0.5l$	14.20	12.40
$60g\_0.5l\_a$	60	$0.5l$	Torn	-
$60g\_0.5l\_b$	60	$0.5l$	12.86	14.41
$75g\_0.5l$	75	$0.5l$	Torn	-

Table 6.1: Summary of deflection results for tests with an axial charge position of $0.5l$.

Test designation	**Charge mass**	**Charge position**	**Experimental deflection**	**Simulated deflection**
-	g	-	mm	mm
$20g\_0.75l$	20	$0.75l$	1.79	2.20
$30g\_0.75l$	30	$0.75l$	3.61	4.88
$40g\_0.75l$	40	$0.75l$	6.67	8.41
$45g\_0.75l$	45	$0.75l$	13.50	10.45
$50g\_0.75l\_a$	50	$0.75l$	Asymmetric	-
$50g\_0.75l\_b$	50	$0.75l$	26.05	11.84
$60g\_0.75l$	60	$0.75l$	32.03	16.87

Table 6.2: Summary of deflection results for tests with an axial charge position of $0.75l$.

6.1.2 Summary of impulse results

Table 6.3 and Table 6.4 summarise the various impulses measured in the present work.

Test designation	**Charge mass**	**Charge position**	**Experimental impulse**	**Simulated impulse**
-	g	-	N.s	N.s
$25g\_0.5l$	25	$0.5l$	55.95	53.66
$30g\_0.5l$	30	$0.5l$	64.31	63.51
$35g\_0.5l$	35	$0.5l$	77.90	73.31
$40g\_0.5l$	40	$0.5l$	83.37	82.96
$45g\_0.5l$	45	$0.5l$	97.46	92.77
$50g\_0.5l$	50	$0.5l$	106.71	102.66
$55g\_0.5l$	55	$0.5l$	112.81	112.30
$60g\_0.5l\_a$	60	$0.5l$	Torn	-
$60g\_0.5l\_b$	60	$0.5l$	123.33	121.64
$75g\_0.5l$	75	$0.5l$	Torn	-

Table 6.3: Summary of impulse results for tests with an axial charge position of $0.5l$.

Test designation	**Charge mass**	**Charge position**	**Experimental impulse**	**Simulated impulse**
-	g	-	N.s	N.s
$20g\_0.75l$	20	$0.75l$	45.51	43.44
$30g\_0.75l$	30	$0.75l$	65.30	62.61
$40g\_0.75l$	40	$0.75l$	83.94	82.63
$45g\_0.75l$	45	$0.75l$	97.46	92.14
$50g\_0.75l\_a$	50	$0.75l$	105.14	101.61
$50g\_0.75l\_b$	50	$0.75l$	106.25	101.61
$60g\_0.75l$	60	$0.75l$	124.63	119.53

Table 6.4: Summary of impulse results for tests with an axial charge position of $0.75l$.

6.2 Experimental-simulation correlation

In order to quantitatively determine how well the simulations replicate the experiments in the present work, the simulated cylinder deformations and impulses are compared with the corresponding experimentally-measured values. These are presented in this section, where the comparisons are disaggregated according to axial charge position.

In both sections, a figure compares the experimental and simulated cylinder deformation values, with all the data points at a fixed axial charge position. The experimental results are shown on the x-axis and the the simulated values are shown on the y-axis. The solid black line represents the line $y = x$ which is the line of perfect correlation. Data points above the line $y = x$ are thus overestimates of the experimental values, while data points below the line are underestimates. The distance of the data points from this line is indicative of the degree of correlation between the experimental and simulated values, where the nearer the simulated values are to this line the closer is the correlation.

For the figures comparing deformations, the two dashed, red lines represent confidence bounds of ± 1 cylinder wall thickness. For experiments on flat plates, the level of experimental repeatability at the Blast Impact and Survivability Research Unit (BISRU) is typically ± 1 plate thickness. In the present work, the analogue of plate thickness is the cylinder wall thickness, and consequently simulated values within these bounds are considered accurate. It should be noted that since the results being compared are diametric measurements, the directly analogous confidence interval is ± 2 wall thickness[1]. However owing to the good accuracy of the simulated results in most instances, ± 1 wall thickness is used instead.

For the case of impulse comparisons, the two dashed, red lines represent confidence bounds of $\pm 5\%$ of the experimental values.

As detailed in Section 4.2, the experimental deformation values are *averages* of several diametric measurements. However since the simulations are performed in 2D axisymmetry, the simulated deformation results are inherently symmetrical. Thus owing to the discrepancy between the averaged experimental measurements and the perfectly symmetrical simulated values, it is reasonable to expect an increased degree of variation between the results relative to similar experimental-simulation correlations for flat plates.

[1]Since each diametric measurement spans two cylinder wall thickness.

6.2.1 Experimental-simulation correlation for axial charge position $0.5l$

Figure 6.1 compares the simulated cylinder deformations with the corresponding experimental values for all tests conducted with an axial charge position of $0.5l$.

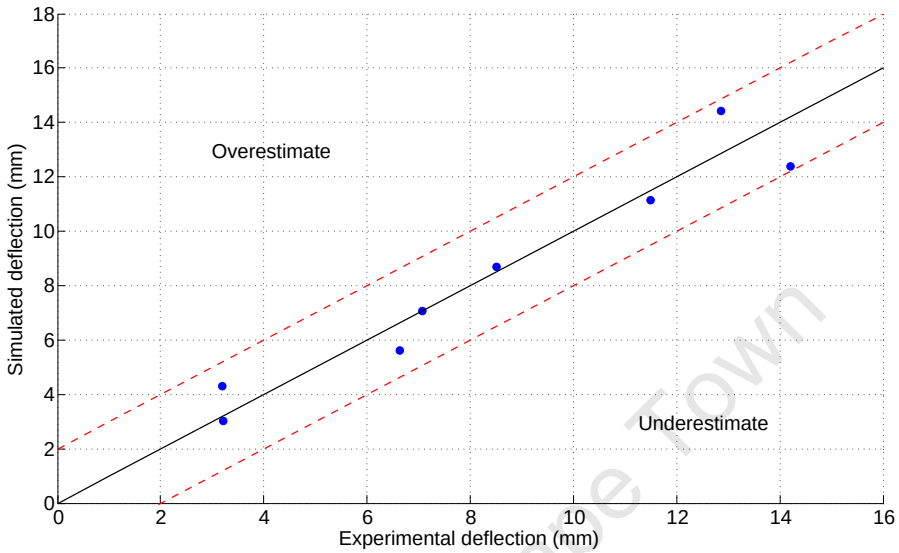

Figure 6.1: Experimental-simulation correlation of deflection values for axial charge position $0.5l$.

All the data points fall within the ± 1 cylinder wall thickness confidence bounds indicating good correlation between the simulated and experimental values, with the majority of the data points lying close to the line $y = x$. With the exception of two data points, the disparity from perfect correlation varies between -0.5 and +0.6 of a cylinder wall thickness.

The simulations that fall outside of this range are the 55g and 60g simulations which vary from perfect correlation by less than 0.9 of a cylinder wall thickness.

In Section 4.3 it was shown that in general the cylinder deformation exhibits linearly increasing behaviour with increasing charge mass. However the 55g and 60g tests are out of trend, with the 60g test experimental deformation approximately 10% *less* than that for the 55g test. This anomalous behaviour is not replicated in the simulations where the cylinder response conforms very closely to the linear trend, though it should be noted that no failure criteria are included in the numerical model.

It has already been suggested that the load imparted to the cylinder from a 60g charge mass is near to the failure threshold of the cylinder, making its structural response less predictable in this region. This may explain the significant divergence exhibited by the 55g and 60g tests, as well as the relatively poor simulation-experimental correlation for these tests.

The experimental and simulated impulse values are compared in Figure 6.2 for tests with various charge masses with an axial charge position of $0.5l$. All the simulated impulse values underestimate their corresponding experimental impulse values.

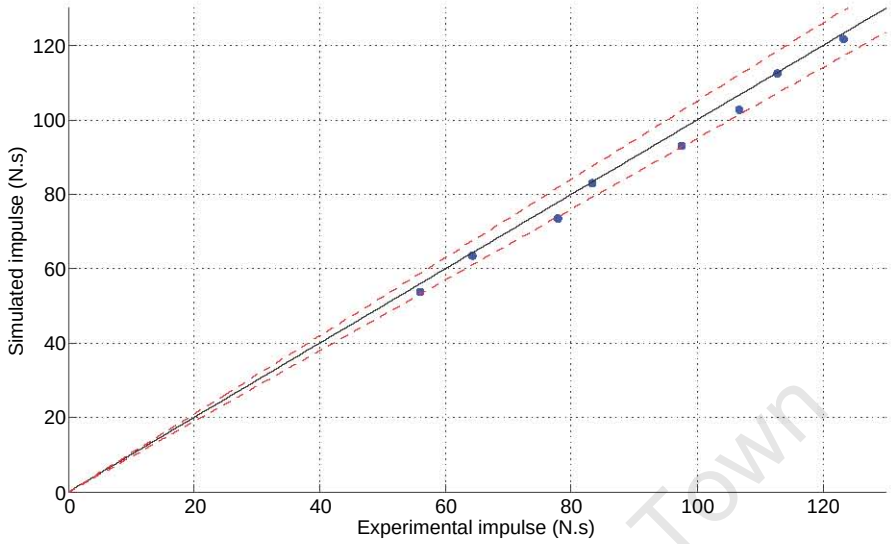

Figure 6.2: Experimental-simulation correlation of impulse values for axial charge position $0.5l$.

The majority of the data points lie close to the line $y = x$, while the others fall within or close to the -5% confidence bound. This indicates accurate agreement between the simulated impulse values and those found experimentally. The difference between the simulated and experimental values ranges between -0.5% and -6.0%.

The values in this section are summarised in Table 6.5 and Table 6.6, where the deflection difference is the disparity of the simulated values from the corresponding experimental values in fractions of a cylinder wall thickness. The difference in impulse values is the percentage difference of the simulated impulse values from the corresponding experimental impulses.

Test designation	**Experimental deflection**	**Simulated deflection**	**Disparity[a]**
-	mm	mm	-
$25g\_0.5l$	3.22	3.04	-0.1
$30g\_0.5l$	3.19	4.29	+0.6
$35g\_0.5l$	6.63	5.61	-0.5
$40g\_0.5l$	7.07	7.08	+0.0
$45g\_0.5l$	8.51	8.70	+0.1
$50g\_0.5l$	11.50	11.13	-0.2
$55g\_0.5l$	14.20	12.40	-0.9
$60g\_0.5l\_b$	12.86	14.41	+0.8
[a]Disparity of simulated values from experimental values in cylinder wall thickness.			

Table 6.5: Summary of deflection experimental-simulation correlation for axial charge position $0.5l$.

Test designation	**Experimental impulse**	**Simulated impulse**	**Disparity[a]**
-	N.s	N.s	%
$25g\_0.5l$	55.94	53.66	-4.3%
$30g\_0.5l$	64.31	63.51	-1.3%
$35g\_0.5l$	77.90	73.49	-6.0%
$40g\_0.5l$	83.37	82.96	-0.5%
$45g\_0.5l$	97.46	93.03	-4.8%
$50g\_0.5l$	106.71	102.66	-3.9%
$55g\_0.5l$	112.81	112.30	-0.5%
$60g\_0.5l\_b$	123.33	121.64	-1.4%
[a]Percentage disparity of simulated values from experimental values.			

Table 6.6: Summary of impulse experimental-simulation correlation for axial charge position $0.5l$.

6.2.2 Experimental-simulation correlation for axial charge position $0.75l$

Figure 6.3 compares the simulated cylinder deformations with the corresponding experimental values for all tests conducted with an axial charge position of $0.75l$.

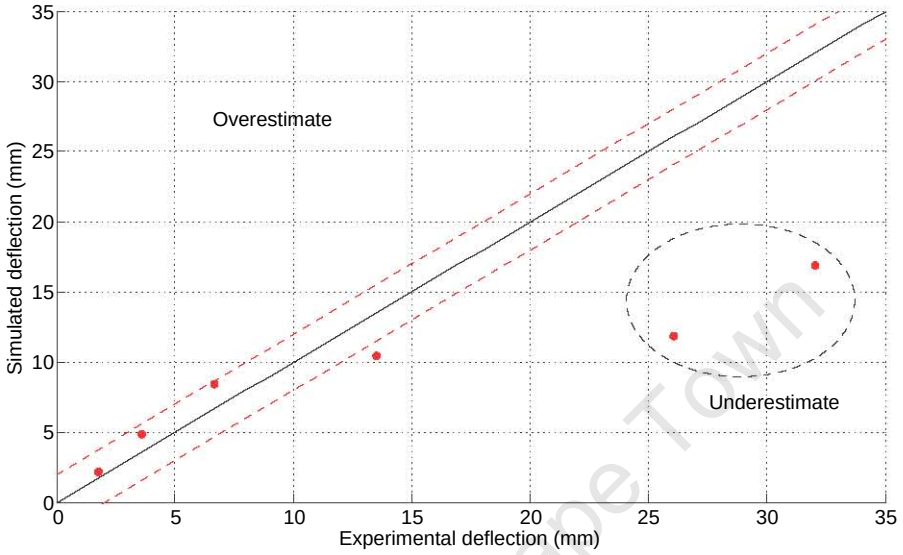

Figure 6.3: Experimental-simulation correlation of deflection values for axial charge position $0.75l$.

For the purpose of this discussion, the response is considered in two regions: the lower four data points, and the upper two which are circled in Figure 6.3. For the lower four data points, the agreement between the simulated deflection values and those measured experimentally is adequate with all four simulated values falling within or relatively near to the ± 1 cylinder wall thickness confidence bounds. For these simulations the disparity from perfect correlation varies between -1.5 and +0.9 of a cylinder wall thickness.

For the case of the two upper, circled data points the correlation between the simulated deflections and those measured experimentally is poor, with the simulated deflections significantly underestimating their corresponding experimental values. Both simulations are approximately -7 times the cylinder wall thickness from their respective experimental values.

The lack of experimental-numerical agreement for the circled tests is concerning as it precludes significant use of these models for further analysis and undermines their reliability. However the adequate experimental-numerical deformation correlation for the four lower data points, coupled with the good agreement of the respective impulse values, suggests that the modelling of the structural response is fundamentally sound. Thus it appears that beyond a given charge mass in the 45g - 50g range, some loading phenomenon, for

instance additional dynamic pressure effects, is not captured in the simulations resulting in lower than expected deformations.

Another reason considered herein for the discrepancy may be a degree of uncertainty in the material model used in the simulations. However, considering that using the same material model results in generally accurate experimental-numerical correlation elsewhere in the present work, it appears more likely that this lack of agreement is due to some loading phenomenon that is not captured in the simulations.

The experimental and simulated impulse values are compared in Figure 6.4 for tests with various charge masses with an axial charge position of $0.75l$. Similar to that seen in the $0.5l$ case, all the simulated impulse values underestimate their corresponding experimental impulse values.

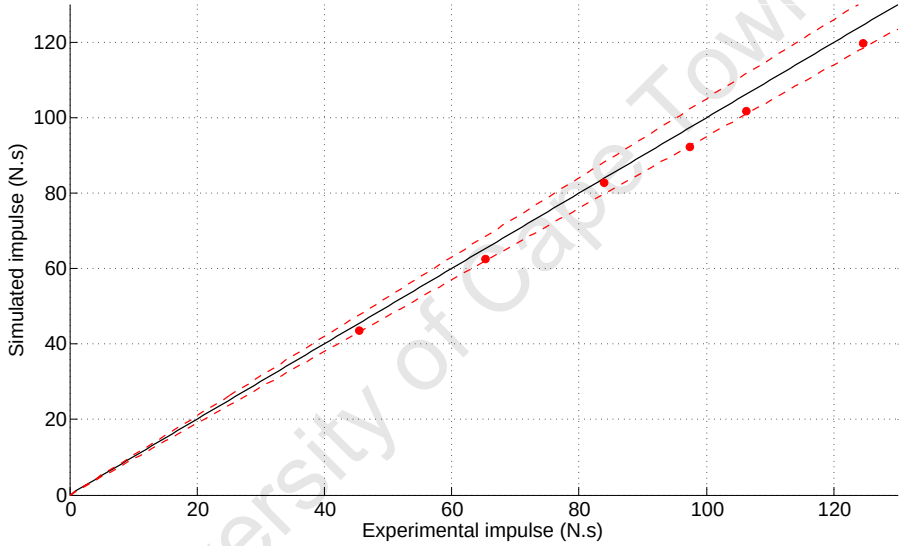

Figure 6.4: Experimental-simulation correlation of impulse values for axial charge position $0.75l$.

All the data points lie close to or within the -5% confidence bound. This indicates accurate agreement between the simulated impulse values and those found experimentally. The difference between the simulated and experimental values ranges between -1.6% and -5.8%.

The values in this section are summarised in Table 6.7 and Table 6.8, where the deflection difference is the disparity of the simulated values from the corresponding experimental values in fractions of a cylinder wall thickness. The difference in impulse values is the percentage difference of the simulated impulse values from the corresponding experimental impulses.

Test designation	**Experimental deflection**	**Simulated deflection**	**Disparity[a]**
-	mm	mm	-
$20g\_0.75l$	1.79	2.20	+0.2
$30g\_0.75l$	3.61	4.88	+0.6
$40g\_0.75l$	6.67	8.41	+0.9
$45g\_0.75l$	13.50	10.45	-1.5
$50g\_0.75l\_b$	26.05	11.84	-7.1
$60g\_0.75l$	32.03	16.87	-7.6
[a]Disparity of simulated values from experimental values in cylinder wall thickness.			

Table 6.7: Summary of deflection experimental-simulation correlation for axial charge position $0.75l$.

Test designation	**Experimental impulse**	**Simulated impulse**	**Disparity[a]**
-	N.s	N.s	-
$20g\_0.75l$	45.51	43.44	-4.8%
$30g\_0.75l$	65.30	62.61	-4.3%
$40g\_0.75l$	83.94	82.63	-1.6%
$45g\_0.75l$	97.46	92.14	-5.8%
$50g\_0.75l\_b$	106.25	101.61	-4.6%
$60g\_0.75l$	124.63	119.53	-4.3%
[a]Percentage disparity of simulated values from experimental values.			

Table 6.8: Summary of impulse experimental-simulation correlation for axial charge position $0.75l$.

6.3 Effect of axial charge position

As shown in the experimental results of Section 4.3, the cylinder response appears to be highly sensitive to the axial position of the explosive charge. This is investigated further in this section.

First the experimental and numerical results are compared for tests with the same charge mass at the different axial positions. Across these two positions the 30g and 50g tests exhibit distinct behaviour and a detailed pressure analysis is presented for these tests. Finally using the same tests, the experimental and simulated post-test cylinder profiles are compared.

6.3.1 Experimental comparison

Figure 6.5 shows the experimental deflection as a function of charge mass and axial charge position. The two axial charge positions $0.5l$ and $0.75l$ are separated by colour, where the closed end of the cylinder is taken as a reference so that $0.5l$ is midway along the cylinder length and $0.75l$ is nearer to the opening. Recall that the data points represent the average of several diametric measurements, and each data point is bounded by error bars indicating the minimum and maximum of the measured deflections. Consequently the error bars are indicative of the symmetry of the tests, where the shorter the error bars the closer is the test to being symmetrical. In some cases the data is skewed significantly in one direction.

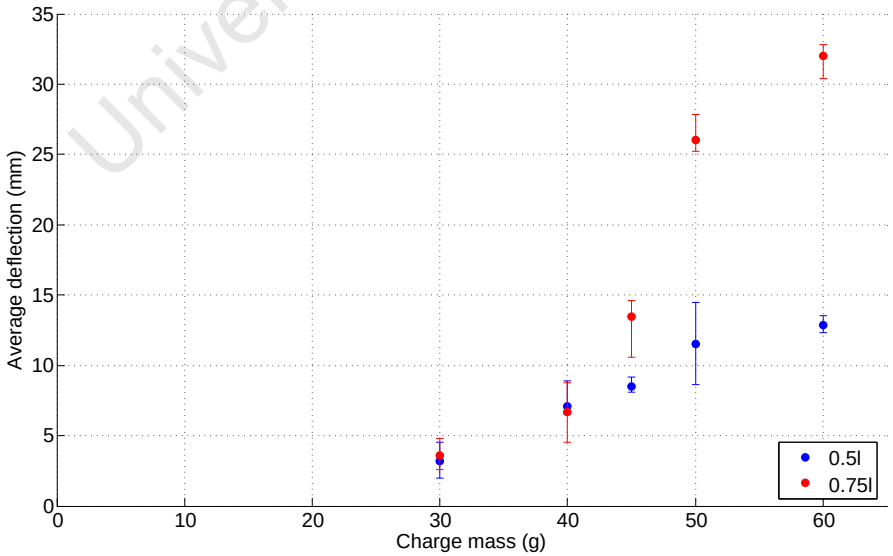

Figure 6.5: Experimental deflection as a function of charge mass for different axial charge positions.

As shown in Section 4.3.1 the average deflection increases with charge mass regardless

of axial position. For the 30g and 40g tests, both deflections from the different axial charge positions are near to each other varying by less than approximately 10%, though it should be noted that the confidence interval for the 40g, 0.75l result is relatively large.

For the three larger charge masses, there is a significant disparity between the deflections from the different axial charge positions, with the deflections from the 0.75l tests greater in all cases. For these tests the deflection disparity varies between approximately 60% and 150%, and becomes increasingly divergent with increasing charge mass. This indicates that, beyond a given loading threshold, the cylinder response is highly sensitive to the axial location of the charge, and that this sensitivity is more effectual as the charge mass is increased.

Photographs comparing these ten cylinders are shown in Figure 6.6. The two different axial positions are again separated by colour, where blue represents those tested with an axial charge position of 0.5l and red corresponds to 0.75l. Cylinders tested with the same charge mass are aligned vertically.

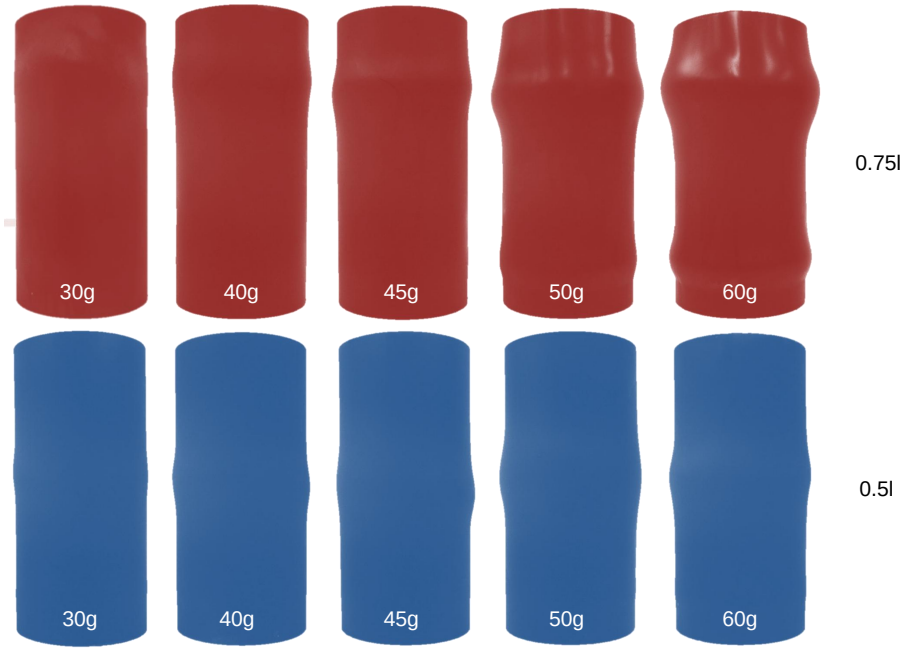

Figure 6.6: Difference in experimental deformation for cylinders tested at different axial charge positions.

For the tests conducted with an axial charge position of 0.75l, significantly larger cylinder deformation is evident, as discussed previously. Additionally these tests exhibit noticeable bulging near the closed end of the cylinders (bottom end in the figure) which is far more pronounced than in the tests with an axial charge position of 0.5l. Both of these features, the larger deformations and the marked bulging, suggest that the quasi-static pressure effects are more significant when the charge is nearer to the opening of the cylinder. This is examined further by considering the transient response of the cylinders in Section 6.3.2.

Figure 6.7 shows the experimental impulse imparted to the "rigid" closed end of the cylinders as a function of charge mass and axial charge position. Consistent with the rest of this section, the two axial positions are separated by colour, and data points that are vertically aligned represent values from tests with the same charge mass at different axial positions[2]. Since the two data sets exhibit very similar behaviour, the linear trend line is for the combination of both data sets.

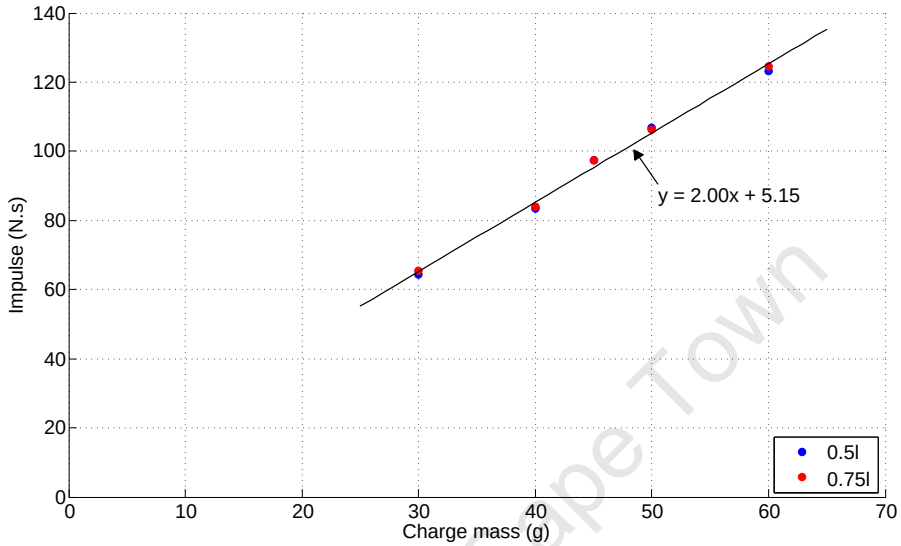

Figure 6.7: Experimental impulse as a function of charge mass for different axial charge positions.

The agreement between the impulse values from tests with the same charge mass at different axial positions is very good, with the maximum variation below approximately 1%. Thus it is clear that the measured impulse is not sensitive to a variation in the axial position of the charge.

Such close agreement between impulse values indicates consistency in the test method, and that in terms of the measured impulse at least, the tests have a high level of repeatability. The charge mass-impulse ratio of approximately 1:2 is similar to that which has been found by many others at BISRU [26, 28, 60, 61]. Note that the linear best-fit curve is non-zero at zero charge mass. This is not unexpected since there are relatively few data points in the set and thus the relationship may not be valid beyond the given range of charge masses.

It should also be noted that since the impulse largely ignores the spatial pressure distribution, the measured impulse is not significantly affected by the symmetry/lack of symmetry of the tests. This is further evidenced by comparing the midpoint deflections and impulses of Figures 6.5 and 6.7 respectively. Where the impulses show good agree-

[2]There are actually two coincident data points for the 45g charge mass, with one being obscured by the other.

ment at the same charge mass, the structural responses of the cylinders are markedly different.

6.3.2 Simulated comparison

In Section 6.3.1 the influence of the axial charge position on the deformation response of the cylinders was compared. It was shown that, beyond a given loading threshold, the average deformation of two cylinders subjected to blasts from equal charges at different axial positions is distinctly different.

In order to understand the difference, cylinder response pairs are investigated numerically in this section, where a pair comprises two simulations with equal charges at the two different axial positions. Two simulation pairs are presented, one each from the low end and high end of the range of charge masses. In the 30g tests the cylinder responses are similar across the two axial charge positions in both the experiments and the simulations. In the 50g tests there is a marked difference in the experimental cylinder responses across the charge positions. This difference is also apparent in the simulations, though significantly less pronounced. These tests are chosen since they exhibit generally distinct behaviour.

At this point it should be noted that the experimental-numerical agreement for the 50g, $0.75l$ test is not as good as it is for most of the other tests attributed to loading effects not adequately captured in the LS-DYNA model.

30g tests

Figure 6.8 shows the simulated radial deformation-time history for cylinders subjected to loads from a 30g charge at different axial charge positions. The charge positions are separated by colour where blue represents a charge located midway along the tube length $0.5l$, and red corresponds to the axial position nearer the open end $0.75l$. In both cases the deformation-time history is recorded at a point on the external surface of the cylinder directly in line with the original centre of the charge. Time $t = 0$ corresponds to detonation of the explosive.

The deformation histories are qualitatively similar with both simulations exhibiting rapid initial deformation before oscillating, with similar frequencies, about some equilibrium deformation level. In both cases there is no significant increase in deformation beyond the initial peak, which is indicative of a purely impulsive response typically seen in unconfined structural responses. Both curves exhibit the strain growth phenomenon mentioned in Section 2.7, where the relatively late-time deformation amplitudes increase without further loading. This suggests that for the given configuration loaded by a blast from a 30g

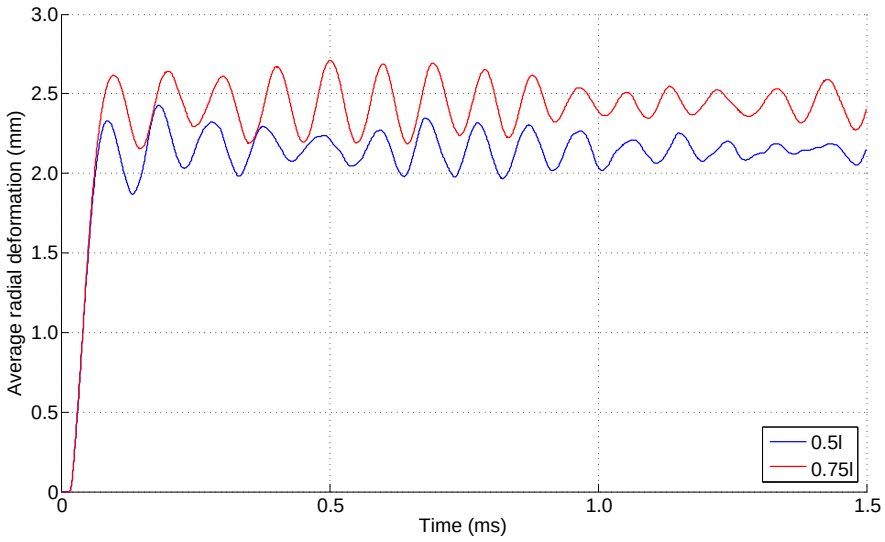

Figure 6.8: Simulated radial deformation histories for simulations with a 30g charge at different axial positions.

explosive charge, the effect of the confinement on the structural response of the cylinder is insignificant.

The equilibrium deformation of the $0.75l$ simulation is larger than that exhibited by the $0.5l$ simulation, which is expected by virtue of its being nearer to the unconfined boundary of the cylinder. Quantitatively the difference between the two is approximately 13%, which is the same as that that measured experimentally. Thus it is clear that for a relatively small charge mass, the cylinder response is not *highly* sensitive to a change in the axial position of the charge.

Figure 6.9 shows the specific impulse distribution as a function of axial position for both load cases. The specific impulse distributions are taken from the decoupled simulations as detailed in Section 5.5.4. As in Figure 6.8, the two axial charge positions are separated by colour with blue representing the $0.5l$ configuration and red the $0.75l$ configuration. The two square markers show graphically the axial charge position for the respective simulations. For the axial position of the cylinder, 0mm corresponds to the closed and restrained end $0l$, and 300mm corresponds to the open end $1l$.

Excepting the position of the local peaks, the specific impulse distributions exhibited by the curves for both axial charge positions are both qualitatively and quantitatively similar. This indicates that in general, the magnitudes of the forces experienced by the cylinders are similar in both cases. The exception is the different positions of these local peaks, which are indicative of larger forces in the respective regions. This results in the maximum radial deformation occurring in the same region as the peak, which is the case exhibited both numerically and experimentally, and expected due to the charge mass location.

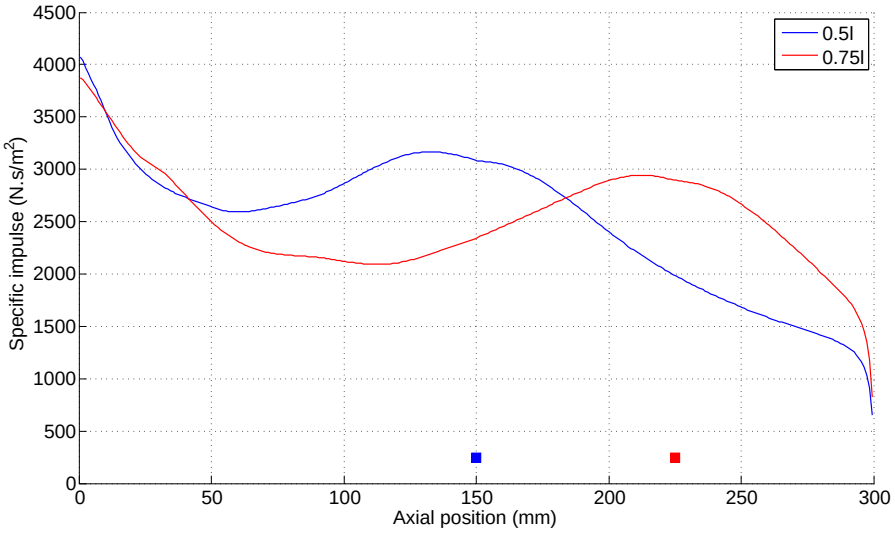

Figure 6.9: Simulated specific impulse distributions for simulations with a 30g charge at different axial positions.

In the case of the $0.75l$ simulation, the local specific impulse peak occurs further from the constrained end of the cylinder than it does in the $0.5l$ simulation. Consequently, while the forces experienced in both cases are similar, the additional 75mm from the constrained end in the $0.75l$ case results in a larger magnitude of deformation. Thus it is expected that the further is the charge mass from the constrained end, the larger is the deformation.

The maximum specific impulse occurs nearest to the closed end of the cylinders in both cases, where the cylinder wall interfaces with the "rigid" base. The high level of confinement in this region causes increased pressure accumulation relative to the rest of the system, which gives rise to the spike in specific impulse. In both cases the peak specific impulse is approximately 4000N.s/m^2. However this region is also nearest to the clamped boundary of the cylinder. Consequently, while the force at this position is relatively high, the deformation is limited by its proximity to the constrained end.

50g tests

Figure 6.10 shows the simulated radial deformation-time history for cylinders subjected to loads from a 50g charge at different axial charge positions. Consistent with the rest of this section, the charge positions are separated by colour where blue represents a charge located at $0.5l$, and red corresponds to $0.75l$.

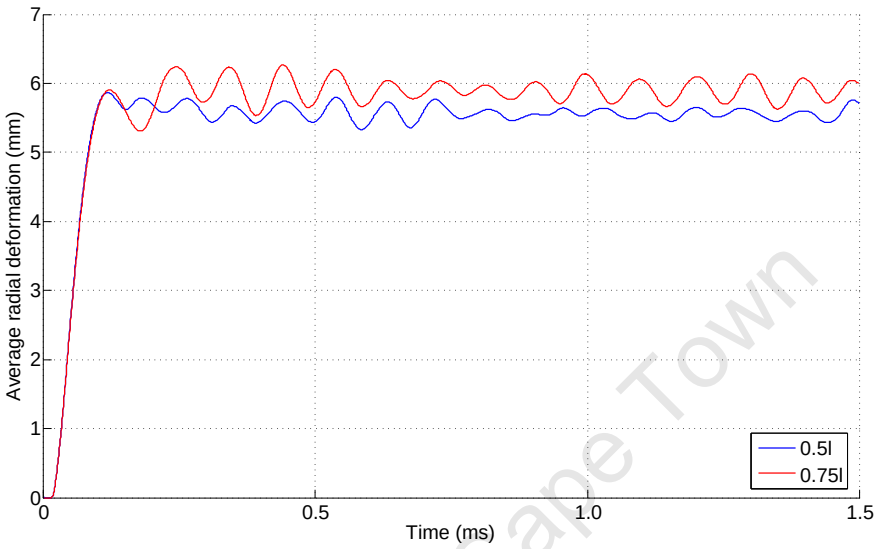

Figure 6.10: Simulated radial deformation histories for simulations with a 50g charge at different axial positions.

Both deformation histories exhibit a rapid initial deformation, however unlike for the 30g tests (where the two curves are qualitatively similar), here there is a marked distinction between the two following the initial deformation peak.

For the $0.5l$ simulation there is no significant difference in deformation beyond the initial peak, which is the behaviour expected from a purely impulsive response in an unconfined structure. This is similar to the response seen previously in both 30g simulations. Following the initial peak, the deformation continues to oscillate about some equilibrium with small variations.

In the response of the $0.75l$ simulation, there is a significant increase in the magnitude of the deformation following the initial peak. This type of response is a combination of impulsive and dynamic effects, typically seen in the response of confined structures as described in Section 2.5. The initial rapid increase in deformation is the impulsive effect and occurs as a result of the impulse imparted to the cylinder from the blast wave. The later increase in deformation is the dynamic effect due to the accumulation of quasi-static gas pressure within the structure. The more significant the quasi-static pressure, the larger the late, second deformation increase is expected to be.

Comparing the two responses reveals another possible reason for the cylinder response

sensitivity to the axial position of the charge mass. It is clear that in the $0.5l$ case there is no significant accumulation of quasi-static pressure, and the effect of confinement does not contribute to any additional deformation. Conversely the different structural response in the $0.75l$ simulation is due to more significant quasi-static pressure retention in the structure. Thus it appears that that for the given configuration loaded by a blast from a 50g explosive charge, there is a significant confinement effect on the structural response of the cylinder, provided the explosive charge is located sufficiently far from the closed end.

The specific impulse distributions as a function of axial position are presented in Figure 6.11, where the two axial charge positions, $0.5l$ and $0.75l$, are represented by the blue and red curves respectively. The specific impulse distributions are taken from the decoupled simulations as detailed in Section 5.5.4. As usual 0mm corresponds to the constrained end of the cylinder $0l$, and 300mm corresponds to the free end $1l$. The two square markers indicate graphically the axial charge positions for the respective simulations.

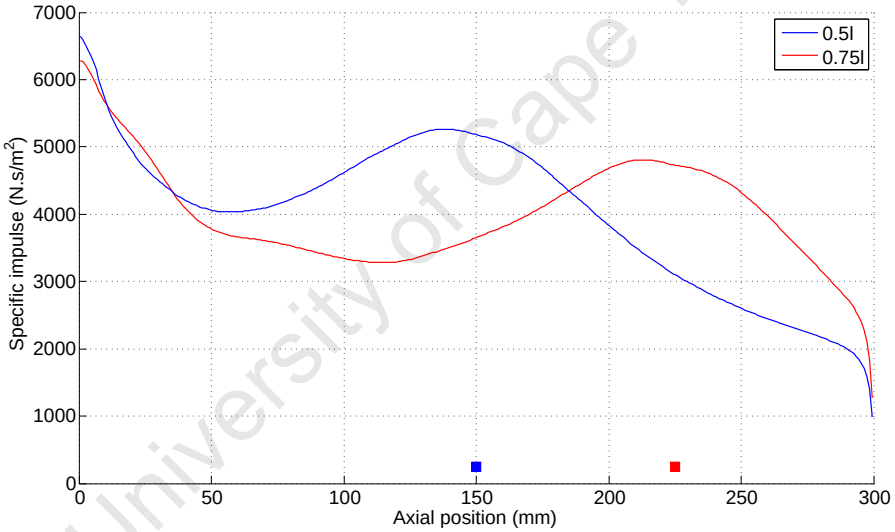

Figure 6.11: Simulated specific impulse distributions for simulations with a 50g charge at different axial positions.

Similar to that seen for the 30g tests, the curves are both generally qualitatively and quantitatively similar, with the exception of the position of the local specific impulse peaks. For the case of the $0.75l$ simulation, the local peak in specific impulse occurs further from the restrained end of the cylinder than it does in the $0.5l$ simulation. Consequently, in accordance with that seen in the 30g tests, a larger magnitude of deformation may be expected. However in Figure 6.10 the magnitudes of the impulsive deformations, represented by the first deformation peak, are similar, indicating that for larger charge masses the impulsive response of the cylinders is not highly sensitive to a change in the axial charge position.

The peak specific impulse for both cases is quantitatively similar and occurs nearest to the closed end of the cylinders, at the cylinder wall-"rigid" base interface. The specific impulse spike of approximately 6500N.s/m^2 is attributed to the additional pressure retention in this region owing to the high level of confinement. It is this large magnitude specific impulse that gives rise to the significant bulging exhibited by some cylinders in Section 4.3. However this region is also nearest to the clamp boundary limiting the deformation in this region.

At this point it should be noted that the preceding discussion is *not* undermined by the lack of agreement between the experimental and simulated deformation results for the $0.75l$ test in this section[3]. Instead the close correlation between the experimentally-measured and simulated impulse values suggests that the impulsive portion of the loading/response is correctly captured in the simulations. Thus it confirms that the discrepancy is owing to failure of the simulations to correctly capture the dynamic portion of the loading, that is the quasi-static gas pressure. The additional deformation exhibited experimentally is attributed to these dynamic effects.

6.3.3 Comparison of pressure behaviour

The distinctions between the responses from the two axial charge positions may be further understood by investigating the pressure behaviour inside the cylinders. A series of simulated pressure contours at certain times are presented in this section with a view to highlighting discrepancies between the pressure behaviours. For all the pressure contours, the time point specified is relative to detonation of the explosive at 0μs.

Following from the previous section two charge masses, 30g and 50g, are investigated at both axial charge positions. These charge masses are chosen as they exhibit distinctive behaviour ideal for the illustrative nature of this section. The magnitudes of the pressures for the 30g tests are generally lower than those for the 50g tests, since for a given explosive the pressure is a function of primarily charge mass, and other factors which remain constant across the tests.

Following the pressure contours, several figures are presented for both axial charge positions which overlay the pressure-time and deflection-time histories for points in the air immediately ahead of the cylinder wall and in the Lagrange domain on the cylinder wall respectively. These points are taken to be in line with the original centre of the charge mass, that is at 150mm and 225mm for the $0.5l$ and $0.75l$ tests respectively, relative to 0mm at the closed end. The pressure-time histories are taken from the decoupled models as detailed in Section 5.5.4.

[3]Recall that experimentally the diametric deformation for the 50g test with an axial charge position of $0.75l$ is 26.05mm compared to 11.84mm from the corresponding simulation.

Figure 6.12 shows a schematic orienting the pressure contours in this section. The domain inside and outside the cylinder is indicated in the figure, and the right end corresponds to the "rigid" closed end in all the figures. Note that the colour bars in this section refer to the air pressures, and that the green colour of the cylinder walls is not indicative of the pressure.

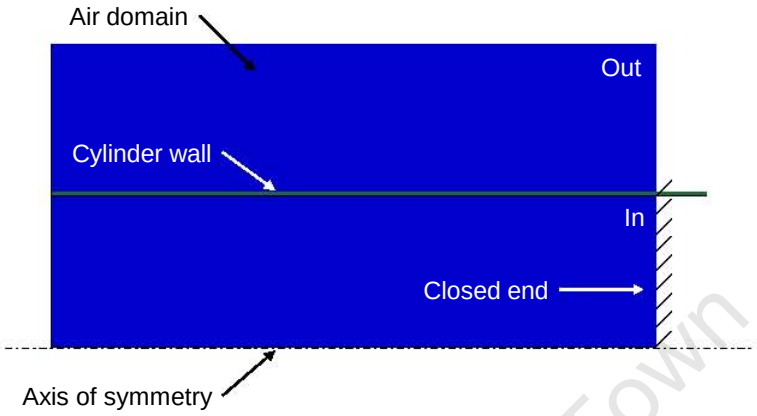

Figure 6.12: Orientation of figures for pressure contour investigation.

30g tests

The pressure contours 15μs after detonation are shown in Figure 6.13a and Figure 6.14a for simulations with an axial charge position of 0.5l and 0.75l respectively. In both cases the explosive charge mass is 30g. 15μs after detonation the blast wave is expanding spherically outwards from its point of detonation in accordance with the simple model. Figure 6.13a and Figure 6.14a show the point just before the incident blast wave interacts with the cylinder wall. Since there is as yet no boundary interaction, and the geometries in the two configurations are the same, the blast wave in both cases is similar, merely offset axially according to the original axial position of the charge. In Figure 6.14a for the 0.75l axial position simulation, a portion of the blast wave is in the verge of exhausting from the open end of the cylinder and this pressure will be lost from the system without causing any structural damage. This is not the case in the 0.5l simulation where the blast wave is entirely contained within the structure at this time.

Following 15μs the blast wave contacts the cylinder wall and the blast pressure accumulates in the region between the wall and the source of the blast. This causes the formation of a localised region of relatively high pressure as shown in Figure 6.13b and Figure 6.14b, for both axial charge positions 20μs after detonation. The accumulated pressure regions in both figures are similar, as the regions are similar in size and the pressure magnitudes against the cylinder walls are both approximately 70MPa - 80MPa. In both cases the loading on the cylinder wall is symmetrical about a line through the respective charge

centres. The overall pressure distribution is not symmetrical in Figure 6.14b for the $0.75l$ axial position simulation, where a portion of the blast pressure continues to vent from the open end of the cylinder.

Gas continues to be driven from the blast source towards the cylinder wall further developing the localised, high pressure region there. Though it is not apparent from the figures owing to the limited graphical resolution (10 discrete pressure increments), the region behind the incident blast wave is significantly above atmospheric pressure in accordance with that presented in Section 2.6.2. Thus the lowest pressure regions are near the ends of the cylinder, and consequently the accumulated pressure region expands in this direction, "laterally" (axially outwards) along the cylinder wall. This is shown in Figure 6.13c and Figure 6.14c 30μs after detonation.

In Figure 6.13c for the simulation with the $0.5l$ axial charge position, the entire blast wave remains contained within the structure, resulting in a loading on the cylinder wall that is symmetrical about a line through the original charge centre. This is not the case in Figure 6.14c for the $0.75l$ simulation where the loading on the wall remains unsymmetrical as before. In both cases the accumulated pressure region decreases outwards along the cylinder wall, from a maximum of approximately 40MPa in line with the respective charge positions. The early formation of a reflected stem is also evident at the incident wave front, near the cylinder walls in both figures. This reflection is significant since it will drive gas towards the centre of the cylinder as it grows.

Figure 6.13d shows the pressure contours for the simulation with a $0.5l$ axial charge position 40μs after detonation. This point corresponds to the time immediately before the incident blast wave reaches the "rigid" closed end of the cylinder. The high pressure region in front of the cylinder wall has expanded further, and the distribution and loading on the cylinder wall remain symmetrical about a line through the point of detonation, decreasing gradually from approximately 20MPa at the centre. The reflected portion of the blast wave has grown relative to that seen previously, however the majority of the wave front, at both the open and closed ends, comprises the relatively uniform, vertical incident portion of the blast wave. Figure 6.14d shows the pressure contours at the same time for the $0.75l$ axial charge position simulation. Since the only boundary interactions as yet are the same in both cases, the pressure distribution is qualitatively and quantitatively similar to that in the $0.5l$ simulation, only shifted axially as a function of the original charge position.

For the case of the simulation with a $0.75l$ charge position, as the blast wave traverses the length of the cylinder the reflected portion of the incident blast wave grows driving gas towards the central axis. This is shown in Figure 6.14e after 65μs, immediately before the incident wave reaches the "rigid" closed end. This occurs later than the $0.5l$ simulation

since the incident wave must travel 75mm further in this case. By this time the majority of the wave front comprises the reflected stem which has overtaken the the incident portion, and the magnitude of the pressure behind the wave front is approximately the same everywhere across the radius. The high pressure region ahead of the cylinder wall is approximately uniform with a magnitude in the order of 5MPa. By this time this region is expanding predominately back towards to the central axis of the cylinder.

In the case of the $0.5l$ simulation, first contact with the closed end boundary is made by the reflected portion of the wave front, immediately after that shown in Figure 6.13d and the initial accumulation of pressure occurs at the cylinder wall-"rigid" boundary interface. The high pressure region then expands radially inwards towards the central axis of the cylinder where it eventually converges. Figure 6.13e shows the $0.5l$ simulation 65μs after detonation, by which stage the significant high pressure region is that accumulated in front of the closed end. The accumulated pressure expands back axially towards the open end of the cylinder, where as seen in the figure, the reflected wave front is highly non-uniform in profile and magnitude.

Figure 6.13f and Figure 6.14f show both axial position configurations 100μs after detonation. For the $0.75l$ simulation the accumulated pressure at the closed end of the cylinder has developed similarly to that described previously for the simulation with an axial charge position of $0.5l$. In both instances, the reflected pressure near the closed end of the cylinder expands towards the opening, reloading the cylinder wall as it proceeds. Note that the reflected blast wave is more advanced in the $0.5l$ case which is expected since it arrived at the closed end sooner.

A relatively uniform, higher pressure region is evident along the central axis of both cylinders in Figure 6.13f and Figure 6.14f. This region is caused by convergence as the accumulated pressure ahead of the cylinder walls expands radially inwards. In the $0.5l$ case the accumulation of pressure in this region is also aided by additional convergence near the opening. This occurs only in the $0.5l$ simulation since the incident blast wave first interacts with the cylinder wall further from the opening than in the $0.75l$ case, and there is thus sufficient time for the reflected stem to grow and drive gas towards the central axis of the cylinder.

Following 100μs the reflected pressure continues to traverse the cylinder towards the open end, however the general behaviour is quite distinct for the two different axial charge positions. The pressure contours for both cases are shown in Figure 6.13g and Figure 6.14g 150μs after detonation. For the simulation with the $0.5l$ charge position the higher pressure region has moved radially outward from near the central axis, to ahead of the cylinder wall. There is a significant pressure differential in the radial direction, causing the high pressure regions to flow to and from the central axis and cylinder wall as

the pressure expands towards the opening. There is no such radial pressure gradient in the $0.75l$ case with the radial pressure distribution approximately uniform in magnitude. The predominant pressure movement is along the cylinder axis towards the open end. The localised high pressure region in this case is caused by the convergence of the pressure reflected from the "rigid" closed end and the high pressure region previously seen along the central axis.

Figure 6.13h and Figure 6.14h show the pressure contours at 400μs after detonation. The pressure magnitudes are generally low in both cases relative to those seen previously, with the maximum pressure across both axial charge positions approximately 2MPa. The pressure decay indicates that there is no significant recirculation/pressure retention in either case. The radial pressure gradient is still clear in the $0.5l$ simulation, and in the $0.75l$ simulation a higher pressure region remains near the closed end of the cylinder. From thin-walled cylinder theory[4], the minimum required static pressure to cause radial deformation is approximately 8MPa. Thus in both cases the magnitudes of the pressure are too small to cause further structural damage.

By 1500μs after detonation, there is no significant residual pressure in either configuration and the systems have vented to ambient conditions with the maximum pressure across both simulations approximately 150kPa.

[4]For a thin-walled cylindrical vessel, the hoop stress induced by a static pressure p is $\sigma_h = \frac{pa}{h}$.

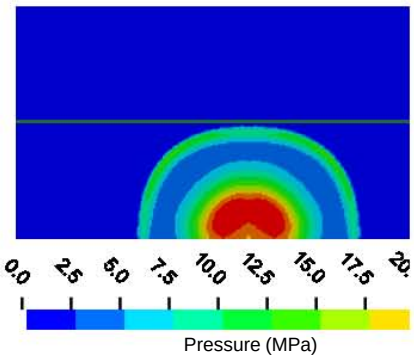

(a) Axial charge position $0.5l$, 15μs.

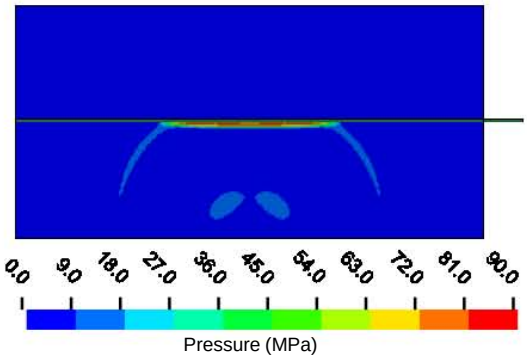

(b) Axial charge position $0.5l$, 20μs.

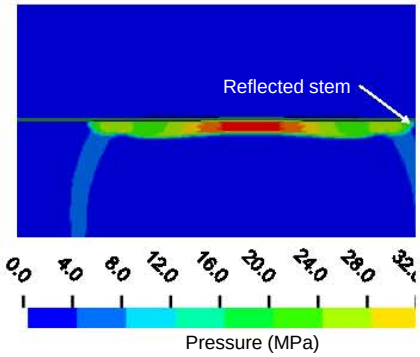

(c) Axial charge position $0.5l$, 30μs.

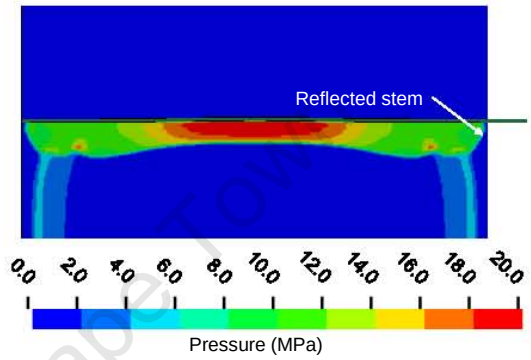

(d) Axial charge position $0.5l$, 40μs.

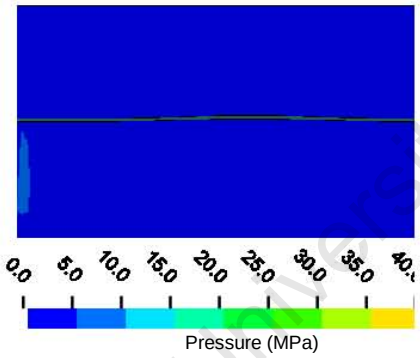

(e) Axial charge position $0.5l$, 65μs.

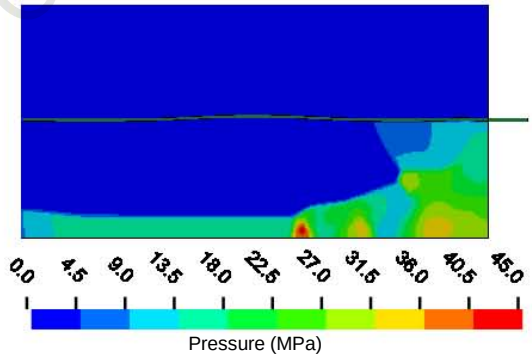

(f) Axial charge position $0.5l$, 100μs.

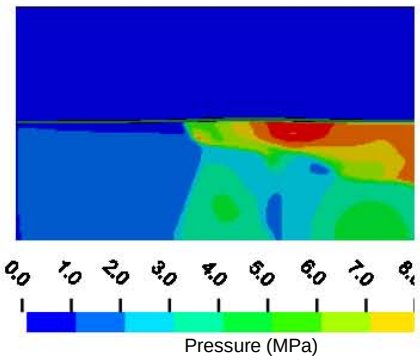

(g) Axial charge position $0.5l$, 150μs.

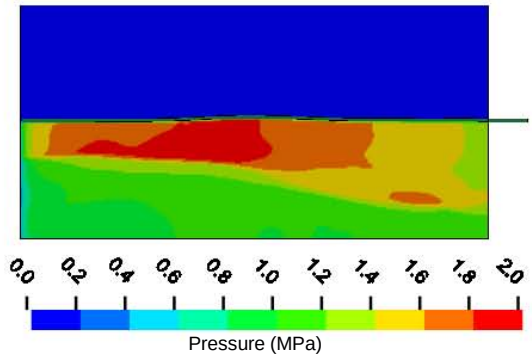

(h) Axial charge position $0.5l$, 400μs.

Figure 6.13: Time series of simulated pressure contours for 30g tests with an axial charge position of $0.5l$.

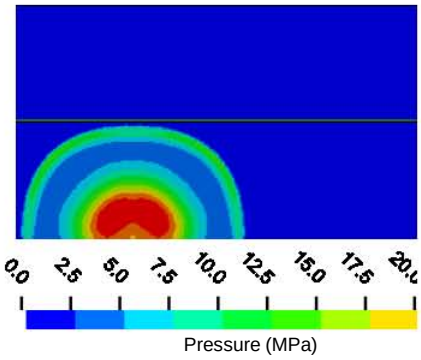

(a) Axial charge position $0.75l$, 15μs.

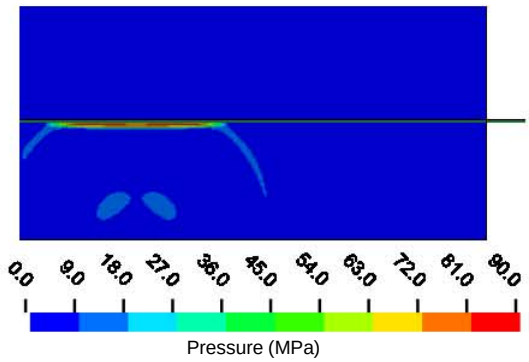

(b) Axial charge position $0.75l$, 20μs.

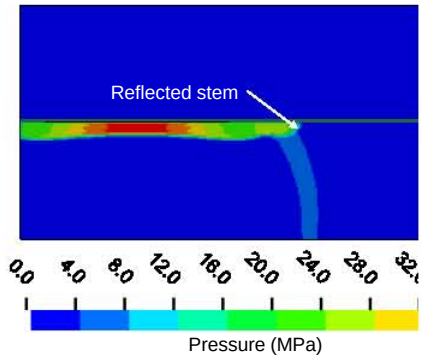

(c) Axial charge position $0.75l$, 30μs.

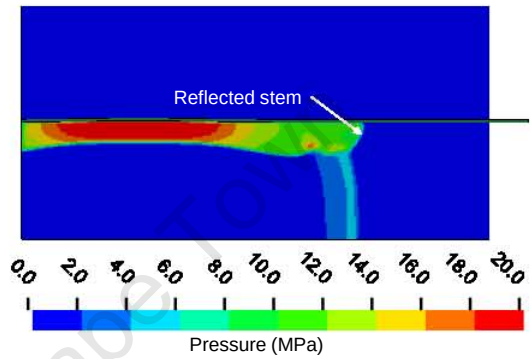

(d) Axial charge position $0.75l$, 40μs.

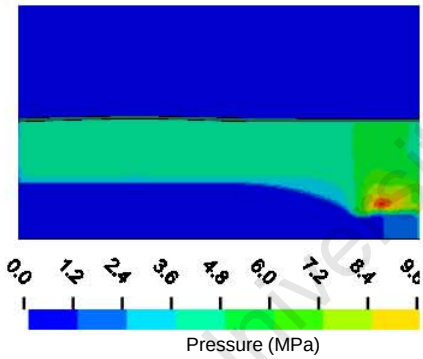

(e) Axial charge position $0.75l$, 65μs.

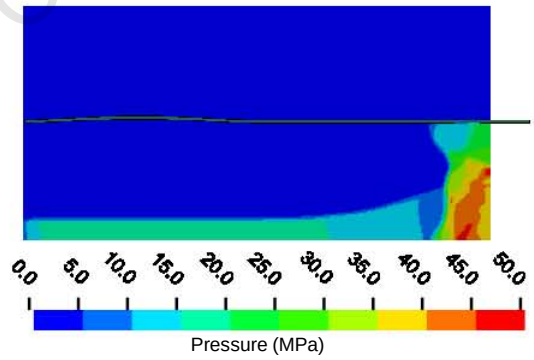

(f) Axial charge position $0.75l$, 100μs.

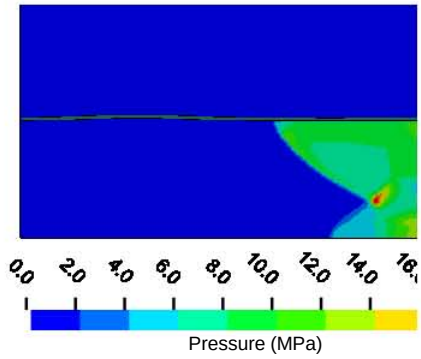

(g) Axial charge position $0.75l$, 150μs.

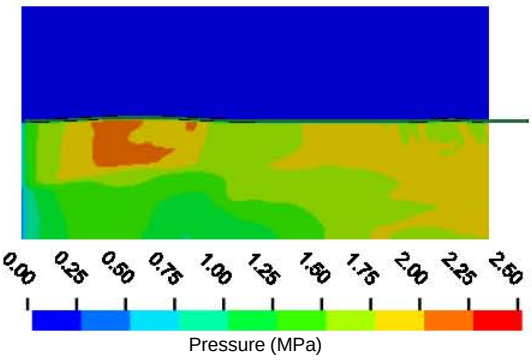

(h) Axial charge position $0.75l$, 400μs.

Figure 6.14: Time series of simulated pressure contours for 30g tests with an axial charge position of $0.75l$.

Figure 6.15a and Figure 6.15b present overlays of the pressure-time histories for a point in the air immediately in front of the cylinder wall in line with the original charge position, and the deflection-time histories of the cylinder wall at the same point. Figure 6.15a is for the $0.5l$ axial charge position and Figure 6.15b for the $0.75l$ case. In both figures the pressure is presented on the primary y-axis as either blue or red depending on the axial charge position, and the deflection on the secondary y-axis in green. Consistent with the rest of this section, the times on the x-axis are relative to detonation at 0μs. The pressure traces are taken from the decoupled models as detailed in Section 5.5.4. The qualitative pressure response is typical for most points along the axial length of the cylinder, with the exception of those near the closed end.

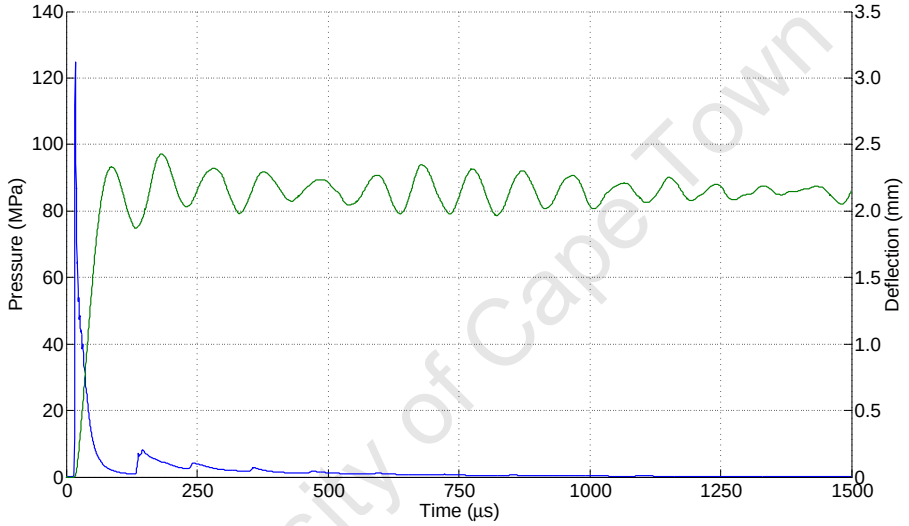

(a) Axial charge position $0.5l$.

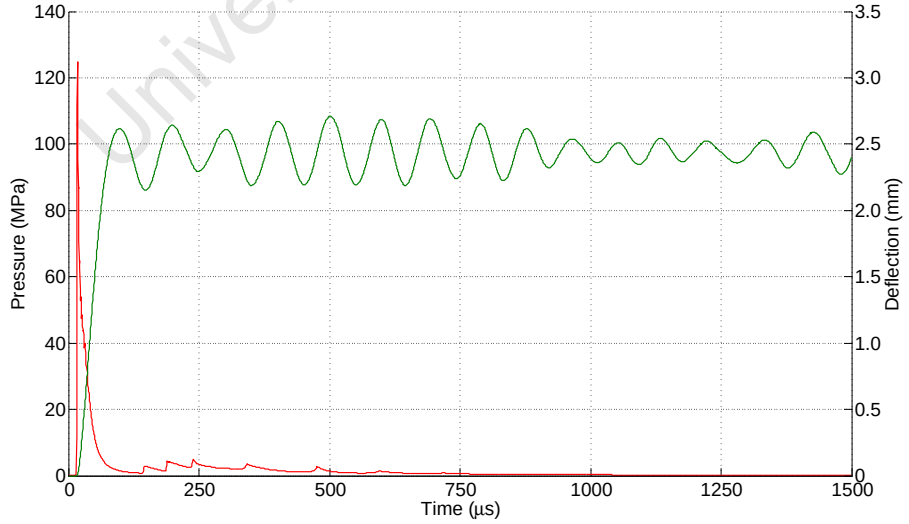

(b) Axial charge position $0.75l$.

Figure 6.15: Simulated pressure and deflection histories for tests with a 30g charge at both axial charge positions.

Similar to that shown by Karpp et al [34], the pressure histories may be considered in two regions: the initial, large pressure spike followed by a series of significantly smaller reflected pressure spikes. These two distinct phenomena are evident in both figures.

In both cases the initial pressure spike and decay is qualitatively and quantitatively the same up to approximately 100μs, with both pressures peaking at approximately 120MPa and decaying at the same rate. Quantitatively the initial pressure spike shows extremely close correlation with the approximation proposed by Mills [22] and presented in Section 2.5. This similarity is expected since, for the given geometries, the initial pressure spike is a function of only the charge mass and the distance to the cylinder wall, both of which are the same regardless of the axial charge position.

The initial, large pressure spikes subject the cylinder walls to a significant force, causing the walls to accelerate in the direction of the impulse, in this case radially outward. This causes an almost instantaneous increase in the wall displacement following the onset of the significant pressure spike. This is the impulsive part of the structural response.

Even though the initial pressure spikes and impulsive loads are similar, the initial deflection histories are quantitatively different, with the first deflection peak 12% larger in Figure 6.15b for the 0.75l simulation. This discrepancy is likely due to the larger distance from the constrained end, that is the deformation point of interest is 75mm further from the clamped end of the cylinder than in the 0.5l case.

The relatively late-time pressure reflections for the two axial charge positions are distinct. This is particularly evident 100μs - 250μs after detonation. In the case of the 0.5l simulation, the first reflected pressure spike is of approximate magnitude 6.5MPa, which decays gradually until approximately 250μs after detonation. This reflected pressure spike exhibits the "double-peak" identified by Karpp et al [34]. The reflection does appear to have a small effect on the structural response of the cylinder, with the deformation response exhibiting a small increase following this additional loading. However the effect on the permanent cylinder deformation is insignificant with the peaks of the deformation response immediately thereafter returning to approximately the same magnitude as the initial, impulsive peak. Following 250μs the pressure response exhibits several very small reflected peaks as it decays quickly towards ambient conditions, with no visible effect on the cylinder deformation.

In the case of the 0.75l simulation, the first reflected pressure peak is of magnitude 2MPa after 140μs, which then decays for a short time before before exhibiting two further reflected peaks of increasing magnitudes before 250μs. This qualitative difference relative to the 0.5l case, is due to the additional time required for the blast wave reflected from the closed end of the cylinder to reach this point. That is the pressure reflections from both the closed end and central axis of the cylinder, are captured as separate reflected spikes in

Figure 6.15b. This is distinct from the $0.5l$ case, where both reflected phenomena arrive at the cylinder wall at nominally the same time, resulting in a single reflected pressure peak of larger magnitude.

The small pressure reflections in the $0.75l$ case appear to have no effect on the deformation response of the cylinder, with no significant change in the deflection peaks following any of the reflected pressure spikes. The late-time deformation response exhibits the elastic strain growth phenomenon mentioned in Section 2.7.3, where the deflection peaks increase without further loading of the cylinder. However this has no effect on the final cylinder deflection, as the deformation amplitude scales about an approximately constant mean value.

Comparing the deformation histories for the two axial charge positions, it is clear that for a 30g charge mass, the cylinder deformation is not sensitive to an axial change in the charge position. The only significant differences between the two responses, are the larger magnitude in the $0.75l$ case as a result of this point being further from the restrained end of the cylinder, and the earlier onset of strain growth in the $0.5l$ case. Since there is no deformation increase beyond the initial peak in both cases, it suggests that there is no confinement effect for the given charge mass, regardless of the axial charge position.

50g tests

Figure 6.16a and Figure 6.17a show the simulated pressure contours 15μs after detonation, just before significant contact with the cylinder wall for both the 0.5l and 0.75l axial charge positions respectively. At this point the blast wave is symmetrical and expanding spherically outward as expected from a spherical charge. Since there is as yet no boundary interaction and the two geometries are same, the blast wave is similar in both figures, merely offset according to the original charge position. In Figure 6.17a for the simulation with the 0.75l axial charge position, a significant portion of the blast wave is on the verge of exhausting from the open end of the cylinder at this time, and this pressure is thus lost from the system before causing any structural damage. This is distinct from the 0.5l simulation where the blast wave remains entirely contained within the structure at this time.

Between 15μs and 20μs after detonation, the blast pressure accumulates against the cylinder wall, causing the formation of a relatively localised high pressure region as shown in Figure 6.16b and Figure 6.17b which both occur 20μs after detonation. At this time the pressure responses from both axial charge positions are similar, where the magnitudes of the pressures against the cylinder walls are approximately 100MPa and the sizes of the regions are similar. The loading on both cylinder walls is symmetrical about a line through the respective original charge centres, though the overall pressure distribution is not symmetrical in Figure 6.17b for the 0.75l simulation, since a portion of the blast pressure vents from the open end of the cylinder.

The high pressure region continues to develop as further gas is driven from the source of the detonation towards the cylinder wall. Though not visible owing to the limited graphical resolution, the region behind the blast wave remains significantly above atmospheric pressure, and consequently the only room for expansion of the accumulated high pressure region is "laterally" (axially outwards) along the cylinder wall towards the low pressure region at the ends of the cylinders. This development is shown in Figure 6.16c and Figure 6.17c for both axial charge positions 30μs after detonation. The accumulated pressure travels symmetrically in both directions along the cylinder and the gas pressure reduces as it expands.

In Figure 6.16c for the case of the 0.5l simulation, the loading on the cylinder wall remains symmetrical about a line through the point of detonation. The entire blast wave remains contained within the structure at this time. This is opposed to the behaviour in Figure 6.17c for the 0.75l simulation, where owing to the pressure venting from the open end of the cylinder, the loading on the wall is no longer symmetrical about a line through the charge centre. In both cases the accumulated pressure decreases gradually in magnitude from the localised high pressure region of approximately 60MPa in line with

the charge, outward towards the ends of the cylinders. Also evident in both figures at the incident wave front, is the early formation of a reflected stem due to the interaction of the incident pressure with cylinder wall. This reflection is significant, since as the high pressure region behind the reflection expands, it drives gas radially inwards towards the central axis of the cylinders.

Figure 6.16d and Figure 6.17d show the pressure contours for simulations with both axial charge positions 37μs after detonation. This point is chosen since it corresponds to the point immediately before the incident blast waves reaches the "rigid" closed end of the cylinder in the the 0.5l simulation. In this case the high pressure region ahead of the cylinder wall has expanded further, decreasing gradually outwards from a maximum of approximately 45MPa at the centre. Since there has been no unbalanced boundary interaction, the pressure distribution on the cylinder wall remains symmetrical about a line through the original charge centre. The reflected portion of the incident wave front has grown relative to that seen previously, however the wave front still comprises predominately the relatively uniform, vertical incident portion. In Figure 6.17d for the 0.75l simulation, since the boundary interactions are so far the same as those in the 0.5l case, the pressure distribution that remains in the system is qualitatively and quantitatively similar, only shifted axially owing to the different original charge positions.

In the case of the 0.75l simulation, the reflected portion of the incident blast wave continues to expand, driving gas towards the central axis of the cylinder as it does so. This is shown in Figure 6.17e which occurs 58μs after detonation and corresponds to the point in time for this configuration immediately before the incident wave reaches the closed end of the cylinder. This occurs later in time compared to that for the 0.5l simulation, since the blast wave in this case travels 75mm further to reach the same point. By this time the majority of the wave front comprises the reflected stem, which has significantly overtaken the incident portion of the wave front. The radial pressure distribution behind the wave front is relatively even, with magnitudes in the order of 10MPa, which is distinct from the 0.5l case in Figure 6.16d where it is localised to a small region near the cylinder wall-"rigid" base interface. The majority of the high pressure is limited to the region ahead of the cylinder wall that is expanding back towards the central axis of the cylinder.

Figure 6.16e shows the 0.5l simulation at the same time, 58μs after detonation. By this time the incident blast wave has reached the closed end of the cylinder, with the first interaction occurring at the interface of the cylinder wall and "rigid" boundary. Following this interaction, a localised high pressure region develops at the boundary-cylinder wall interface in the 0.5l simulation. As further gas accumulates here, this high pressure region is driven towards the central axis of the cylinder while the accumulated pressure begins to expand back towards the cylinder opening. This is shown in Figure 6.16e. The reflected wave is highly non-uniform in both magnitude and profile. At this time there remains

a higher pressure region near the cylinder wall which is expanding back towards to the central axis of the cylinder, driving gas with it as it does so. The loading on the cylinder wall is no longer uniform, with a higher load experienced near the accumulated pressure region at the closed end.

Pressure contours for both axial charge positions are shown in Figure 6.16f and Figure 6.17f 100μs after detonation. For the 0.75l simulation the accumulated pressure at the closed end of the cylinder has developed similarly to that described previously for the simulation with an axial charge position of 0.5l. However owing to the blast wave profile before just contact with the boundary, there is a more uniform accumulation of pressure at the closed end compared to that in the 0.5l case, resulting in a more vertical reflected wave front which is evident in the figure. In both instances, the reflected pressure near the closed end of the cylinder expands towards the opening, reloading the cylinder wall as it proceeds. Note that the reflected blast wave is more advanced in the 0.5l case which is expected since it arrived at the closed end approximately 20μs earlier.

By this time a higher pressure region is evident along the central axis of the cylinders in both figures. This higher pressure develops as the accumulated pressure regions ahead of the cylinder walls expand radially inwards and converge near the central axis. In the case of the 0.5l simulation by the time shown in Figure 6.16f, this central pressure region is expanding back towards the cylinder wall. The localised high pressure region of approximately 70MPa is the interaction of the reflected pressure expanding from the closed end and that expanding from the central axis towards the cylinder wall. Since there exists a significant pressure differential in the radial direction, the gas in the cylinder is driven predominantly radially outwards towards the cylinder wall, loading it further and inhibiting the trapped pressure deeper in the cylinder from venting.

The behaviour is distinct in the 0.75l case where the higher pressure region along the central axis, visible in Figure 6.17f, is lower in magnitude than that in the 0.5l simulation. At this time the significant pressure differential is in the axial direction, and thus the gas in the cylinder is driven predominantly laterally towards to the cylinder opening. The wave front in this case is significantly more vertical and uniform compared to that in the 0.5l case, further promoting pressure flow in the axial direction.

Following 100μs the reflected pressure continues to traverse the cylinder towards the open end in both cases, however the 0.5l case exhibits significant radial pressure movement not seen in the 0.75l simulation. Pressure contours for both axial charge positions are shown in Figure 6.16g and Figure 6.17g 150μs after detonation. For the 0.5l simulation, the higher pressure region has moved radially outward from near the central axis to the cylinder wall. The significant pressure differential remains in the radial direction, causing the pressure to reflect between the central axis and the cylinder wall as it expands

towards the opening. In the simulation with the $0.75l$ axial charge position, the radial pressure distribution is relatively even, with the significant pressure gradient in the axial direction. Consequently the predominant pressure flow is axially towards the open end of the cylinder. The localised high pressure region of 35MPa evident in Figure 6.17g, is a result of the convergence of the pressure reflected from the closed end and that previously seen along the central axis.

At this point the fundamental distinction between the pressure behaviours for the two axial positions is evident. The pressure may be considered in two regimes: that incident on/reflected off the cylinder wall, and that incident on/reflected from the "rigid" closed end of the cylinder. In general these two pressure mechanisms move predominantly radially and axially respectively, as seen in the figures, where the axial pressure movement appears to drive gas out of the open end of the cylinders.

The significant structural damage is caused by the pressure impinging radially against the cylinder wall and its subsequent radial movement within the cylinder. This is particularly clear for the initial impulsive loading in both cases. For both axial positions, the radially reflected pressure takes nominally the same amount of time to reach the cylinder wall and continue reflecting in the radial direction.

However, in the simulations with the axial charge position of $0.75l$, the incident pressure must axially travel 75mm further than in the $0.5l$ simulations, before it is reflected from the closed end. Consequently, this axially-reflected pressure takes longer to return to its original axial position than it does in the $0.5l$ case. In the $0.75l$ simulation, this additional time is sufficient to allow the radially moving pressure to reflect from the high pressure region at the central axis and reload the cylinder wall *before* it is driven out by the axially moving pressure. This reloading is the cause of the additional deformation.

In the $0.5l$ case, the axially moving pressure reaches the midpoint prior to the waves propagating radially, preventing the reflected radial pressure from impinging on the cylinder wall unhindered, which precludes any further deformation of the cylinder wall.

The pressure continues to vent in both cases with the flow direction predominantly more axial in the $0.75l$ simulation. The pressure contours after 400μs are shown for both simulations in Figure 6.16h and Figure 6.17h, by which time the pressure magnitude is well below the approximately 8MPa required to cause permanent damage in the cylinders. In both cases the axial pressure distribution is relatively uniform in the cylinders, with magnitudes in the order of single megapascals, and the maximum pressure across both simulations is below 4.5MPa. There remains a small radial pressure gradient in the $0.5l$ simulation and a similarly small axial gradient in the $0.75l$ simulation, which are functions of the different venting behaviour.

By 1500μs after detonation, the cylinders are fully vented with no significant residual pressure in either system. The maximum pressure across both cases is below 250kPa.

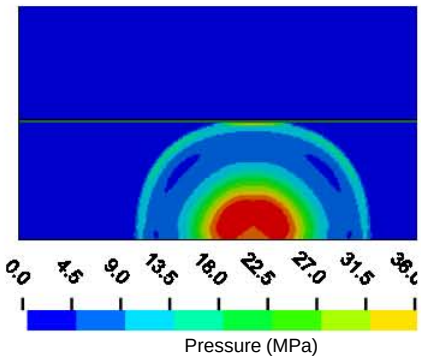

(a) Axial charge position $0.5l$, 15μs.

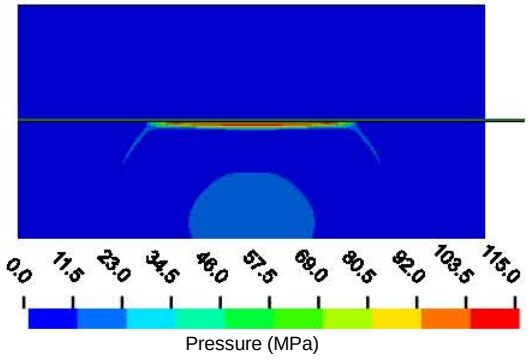

(b) Axial charge position $0.5l$, 20μs.

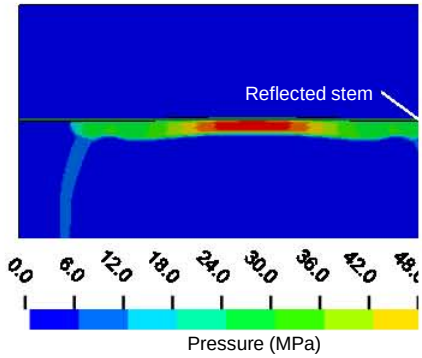

(c) Axial charge position $0.5l$, 30μs.

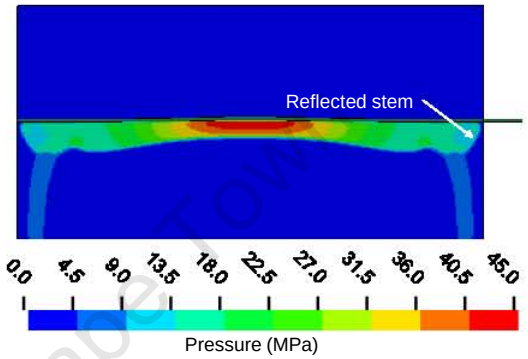

(d) Axial charge position $0.5l$, 37μs.

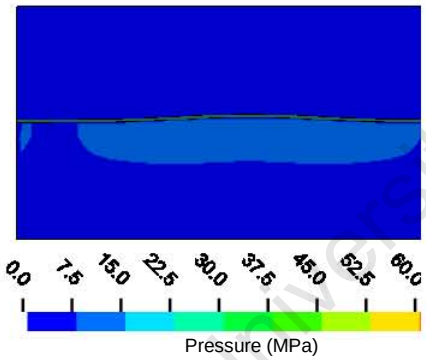

(e) Axial charge position $0.5l$, 58μs.

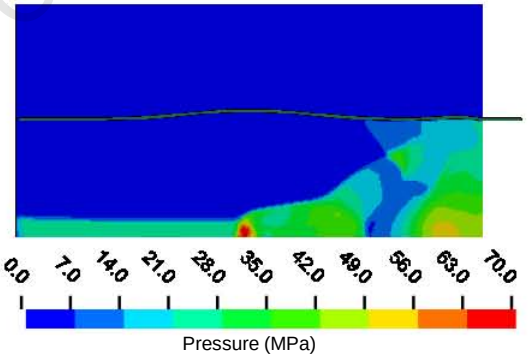

(f) Axial charge position $0.5l$, 100μs.

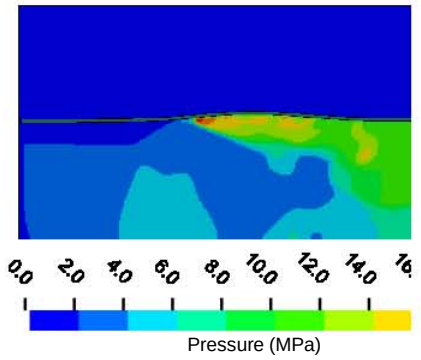

(g) Axial charge position $0.5l$, 150μs.

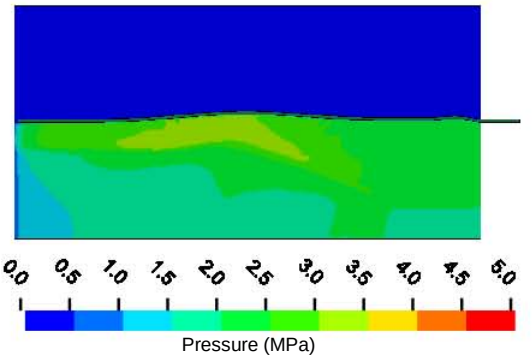

(h) Axial charge position $0.5l$, 400μs.

Figure 6.16: Time series of simulated pressure contours for 50g tests with an axial charge position of $0.5l$.

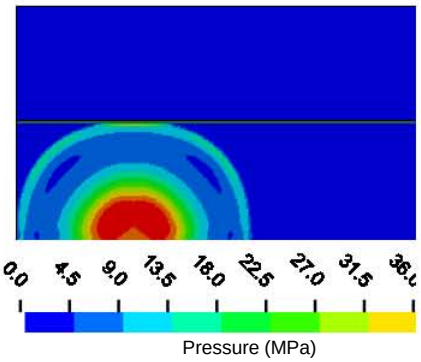

(a) Axial charge position $0.75l$, 15μs.

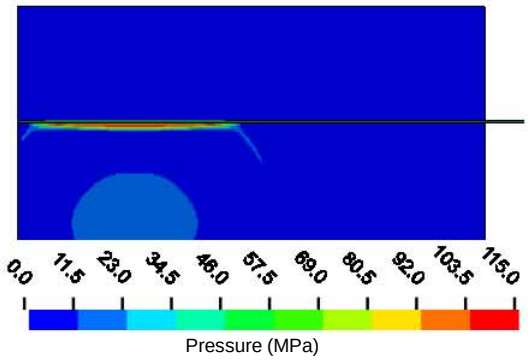

(b) Axial charge position $0.75l$, 20μs.

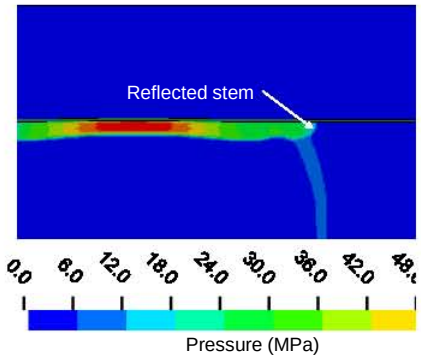

(c) Axial charge position $0.75l$, 30μs.

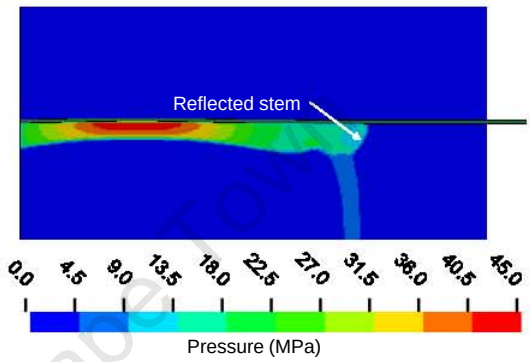

(d) Axial charge position $0.75l$, 37μs.

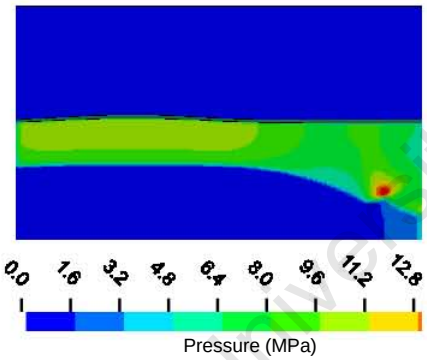

(e) Axial charge position $0.75l$, 58μs.

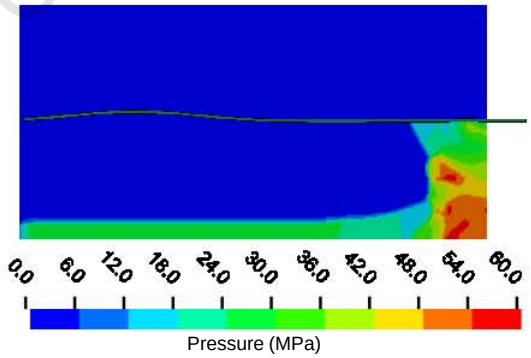

(f) Axial charge position $0.75l$, 100μs.

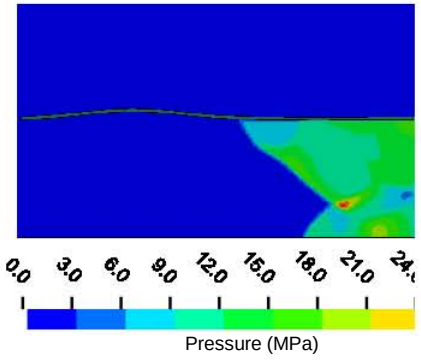

(g) Axial charge position $0.75l$, 150μs.

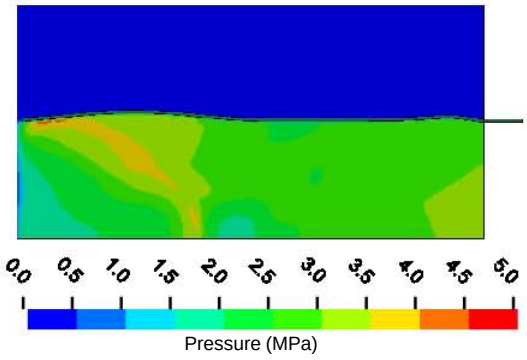

(h) Axial charge position $0.75l$, 400μs.

Figure 6.17: Time series of simulated pressure contours for 50g tests with an axial charge position of $0.75l$.

The pressure-time histories for a point in the air immediately in front of the cylinder wall in line with the original charge position, and the deflection-time histories of the cylinder wall at the same point, are overlaid in Figure 6.18a and Figure 6.18b. The pressure is presented on the primary y-axis as blue in Figure 6.18a for the $0.5l$ axial charge position, and as red in Figure 6.18b for the $0.75l$ case. In both figures the deflection is shown on the secondary y-axis in green, and consistent with the rest of this section, the times on the x-axis are relative to detonation at 0μs. The qualitative pressure response is typical for most points along the axial length of the cylinder, with the exception of those near the closed end.

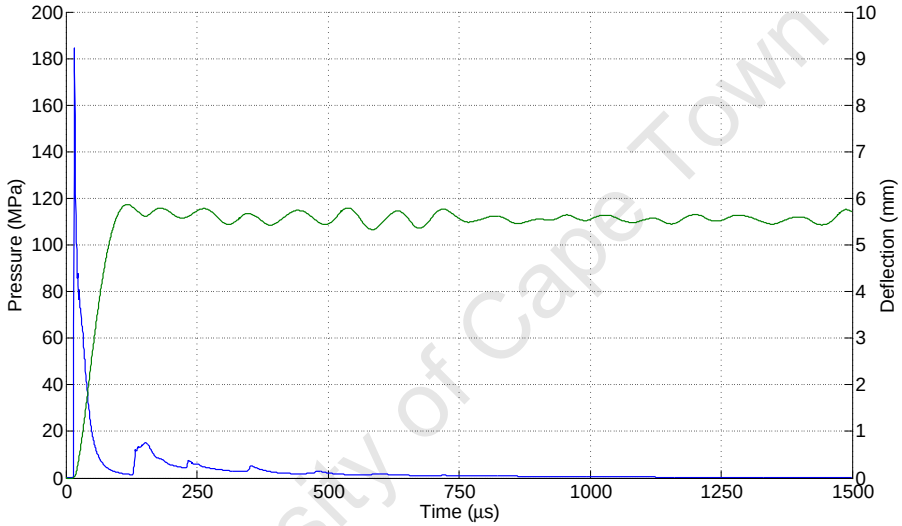

(a) Axial charge position $0.5l$.

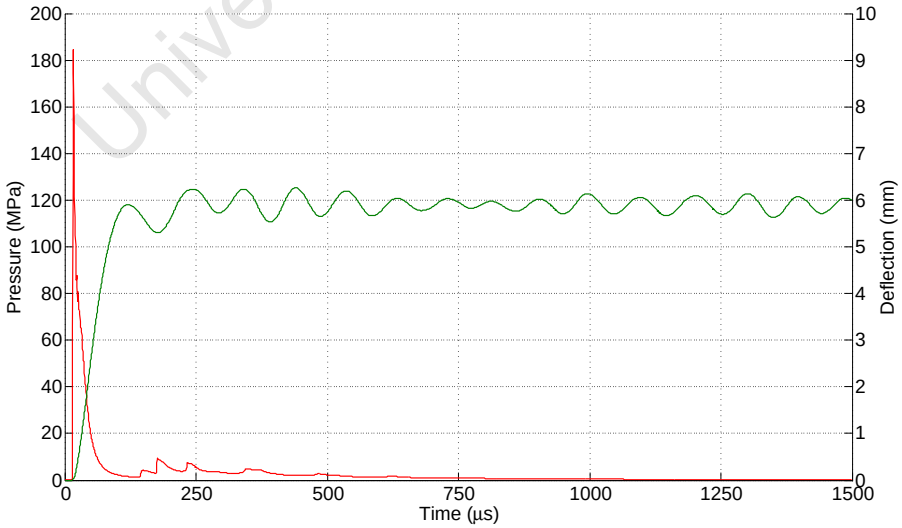

(b) Axial charge position $0.75l$.

Figure 6.18: Simulated pressure and deflection histories for tests with a 50g charge at both axial charge positions.

Like the pressure-time histories for the 30g tests and as suggested by Karpp et al [34], the pressure histories are considered in two regions: the initial, large pressure spike and a series of significantly smaller reflected pressure spikes. These distinct phenomena are evident in both figures.

The initial pressure spike is qualitatively and quantitatively similar in both axial charge position cases, peaking at approximately 180MPa and decaying at the same rate. Since for the given geometries the initial pressure spike is a function of only the charge mass and the distance to the cylinder wall, it is expected that the two axial charge cases produce very similar results. The magnitude of the initial pressure spike is in close agreement with that predicted by the analytical solution of Mills [22], presented in Section 2.5.

In both cases the initial pressure spikes impart a large force to the cylinder walls, causing the point of interest to accelerate in the direction of the impulse, in this case radially outward. The pressure spike results in the dynamic displacement which rapidly increases following the onset of significant pressure. This early regime of the structural response is purely impulsive with the confinement of the cylinders having no effect at this point.

For the 30g tests the impulsive deformation response of the $0.75l$ simulation is appreciably larger than that for the $0.5l$ simulation. However at 50g the initial deformation peaks are similar here varying by approximately 0.6%. Since the point of interest for the deformation in the $0.75l$ simulation is further from the constrained end of the cylinder, it is surprising that its initial deformation peak is not more than 0.6% larger than that for the $0.5l$ simulation.

Similar to that seen in the 30g tests, the reflected pressure responses for the two axial charge positions are distinct, particularly between approximately 100μs and 250μs. In the case of the simulation with the $0.5l$ axial charge position, the first reflected pressure spike is of magnitude 15MPa and decays gradually until just before 250μs where a second reflected pressure spike is experienced. These reflections appear to have no effect of the cylinder deformation, with the deformation response exhibiting no increase following this additional loading. Following 250μs the pressure response exhibits several very small reflected peaks as it decays quickly towards ambient conditions, with no visible effect on the cylinder deformation. The increased amplitudes of the deformation response at approximately 500μs and late on at approximately 1500μs are evidence of elastic strain growth as presented in Section 2.7.3. Since the mean deformation remains the same, this strain growth does not significantly affect the final cylinder deformation.

In the case of the $0.75l$ simulation, the first reflected pressure peak is of magnitude 4.5MPa after 150μs, which then decays for a short time before before exhibiting two further reflected peaks of increasing magnitudes before 250μs. This difference in qualitative behaviour, also evident in the 30g tests, is due to the additional time required for the

blast wave reflected from the closed end of the cylinder to reach this point where the pressure is being recorded in the $0.75l$ case. That is the pressure reflections from both the closed end and central axis of the cylinder, are captured as separate reflected spikes in Figure 6.18b. This is distinct from the $0.5l$ case shown previously, where both reflected phenomena arrive at the cylinder wall at near the same time, resulting in a nearly-single reflected pressure peak of larger magnitude.

In Figure 6.18b for the $0.75l$ simulation, following the initial, impulsive deformation peak, there is a clear increase in the magnitude of the deformation response. The second deformation peak as well as those subsequently, are approximately 6% larger than the initial peak. This behaviour is typically indicative of a quasi-static pressure effect, that is the above-ambient, confined pressure is causing additional structural deformation above that caused by the initial impulsive loading. This is significant because this additional quasi-static deformation is not exhibited by the $0.5l$ simulation, nor is it evident in the 30g simulations at *either* axial charge position.

A deformation increase of 6% may not seem significant where the amplitude changes owing to elastic strain growth show similar variance. However it is the qualitative nature of this increase, that is its occurrence immediately after the first deformation peak and at near the same time as the arrival of the reflected pressure at this point, that suggests it *is* owing to the effects of quasi-static pressure. Additionally it appears that a significant portion of the quasi-static pressure is *not* correctly captured in the LS-DYNA models, which explains the significant underestimation of the simulations where the quasi-static pressure appears to be significant. Consequently the difference between the first and subsequent deformation peaks would be significantly larger, if the quasi-static pressure was better accounted for.

This is confirmed by examining deformation-time history of Figure 6.19, where the simulation is modified to be closed on *both* ends thus exaggerating the effect of the quasi-static pressure. The deformation-time history exhibits the same qualitative features in this case, except that the increased deformation due to the dynamic response is significantly larger than that seen previously.

Following 250μs the pressure history in Figure 6.18b exhibits several small reflection spikes as it decays to ambient conditions. These reflections have no effect on the deformation response of the cylinder. Similar to that seen previously, the late-time deformation response exhibits the elastic strain growth phenomenon mentioned in Section 2.7.3, where the deflection peaks increase without further loading on the cylinder. However this has no effect of the final cylinder deflection, as the deformation amplitude scales about an approximately constant mean value.

Comparing the deformation histories for the two axial charge positions, it is clear that

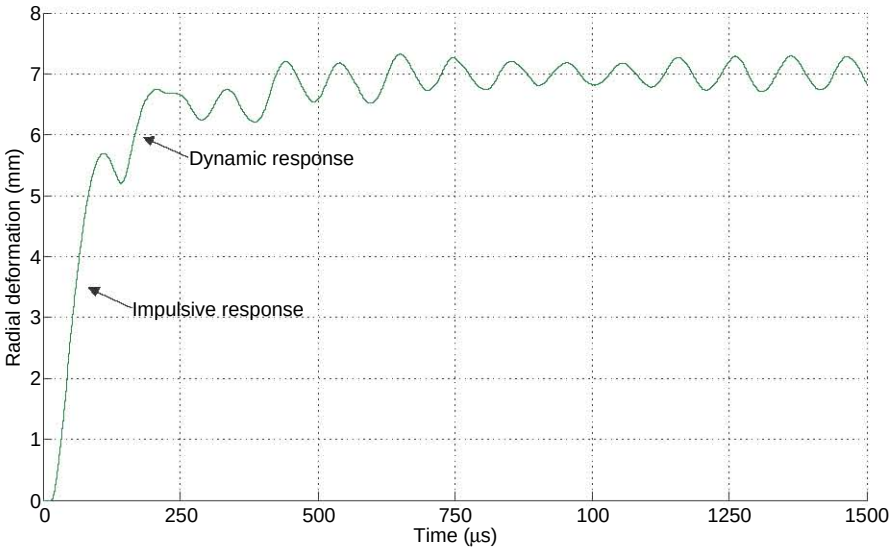

Figure 6.19: Simulated deformation-time history for a test with a 50g charge mass at an axial charge position of $0.5l$. Test is closed on *both* ends and exhibits an exaggerated response to the quasi-static pressure.

for a 50g charge mass the cylinder deformation is sensitive to a change in the axial charge position. In the case of the $0.5l$ axial charge position the quasi-static pressure appears to have no effect on the structural response, while the effect is significant in the $0.75l$ case. The result is that the final cylinder deformation is larger in the case of the $0.75l$ simulation. Consequently it suggests that, for the given geometry, there is a significant confinement effect if the charge mass is far enough from the closed end of the cylinder.

6.3.4 Comparison of cylinder profiles

This section presents an experimental-numerical correlation for the sectioned cylinder profiles in the present work. Following from the previous section the profiles from the 30g and 50g tests are presented at both axial charge positions. In general the magnitude of the profile deformation is larger for the 50g tests which is expected since it has already been shown that the radial deformation increases with increasing charge mass.

In all the figures in this section, the experimental profiles are represented by blue, while red corresponds to the simulated profiles. Note that there may exist a small discrepancy between the simulated profile deformation and that reported in the results of Section 4.3. This is since the values reported in the results are the equilibrium values, that is the mean of the deformation-time histories which do not necessarily correspond with the values at exactly time $t = 1.5$ms. This is opposed to the profiles in this section which are taken from the x and y coordinates of the cylinders at exactly time $t = 1.5$ms.

Note that since the 30mm clamped region is included in the figures in this section, the

original charge position is at 180mm for the $0.5l$ case and 255mm for the case of the $0.75l$ axial charge position.

30g tests

Figure 6.20a and Figure 6.20b show overlays of the experimental and simulated final cylinder profiles for the 30g tests at axial charge positions of $0.5l$ and $0.75l$ respectively.

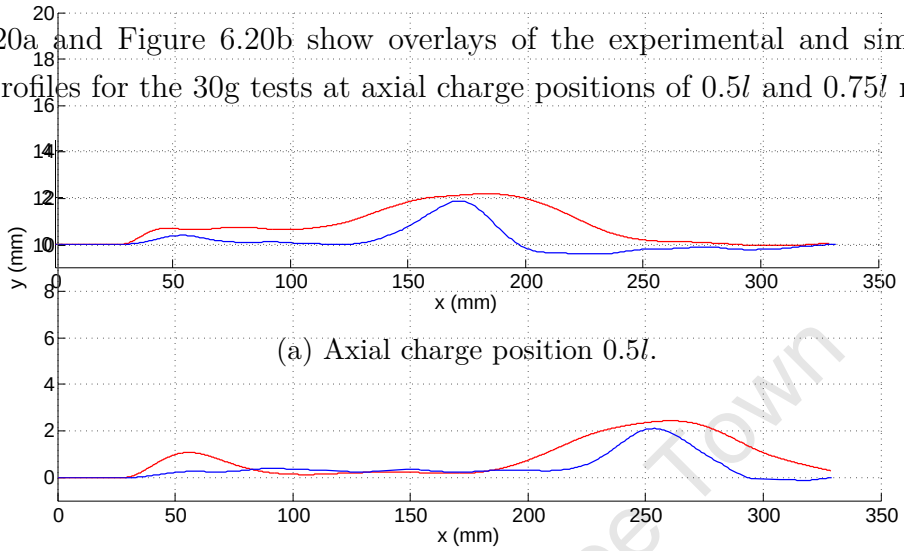

(a) Axial charge position $0.5l$.

(b) Axial charge position $0.75l$.

Figure 6.20: Experimental-simulated profile comparison for 30g tests with different axial charge positions. Experimental profile is represented by blue, while red corresponds to the simulated profile.

In general the quantitative correlation between the experimental and simulated profiles is good with the largest disparity between the two being approximately one cylinder wall thickness. Note that owing to the biased aspect ratio of the profiles, the ratio of the x-y scale in the figures is 1:17.5 and thus the deformation and disparities are significantly magnified.

It is clear in both figures that the experimental profiles exhibit significantly more localised deformations than those seen in the simulations. That is the deformation in the simulated profiles is more distributed along the cylinder length, particularly in the $0.5l$ case which exhibits significant and relatively constant deformation from 30mm to approximately 100mm. It is plausible that the localised nature of this deformation is a result of the polystyrene annuli that are used to position the charges in the experiments.

It is also evident that the bulging near the constrained ends is significantly larger in the simulated profiles than in the experimental ones. Such a disparity in this region is understandable since the simulated boundary conditions do not replicate *perfectly* the physical clamping in the experiments, and the effect of the boundary conditions in the simulations is more influential for deformation nearer to the boundary conditions.

50g tests

The experimental and simulated final cylinder profiles are overlaid in Figure 6.21a and Figure 6.21b for the 50g tests at axial charge positions of $0.5l$ and $0.75l$ respectively.

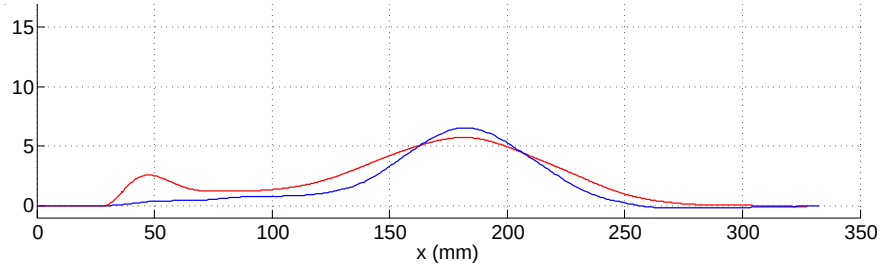

(a) Axial charge position $0.5l$.

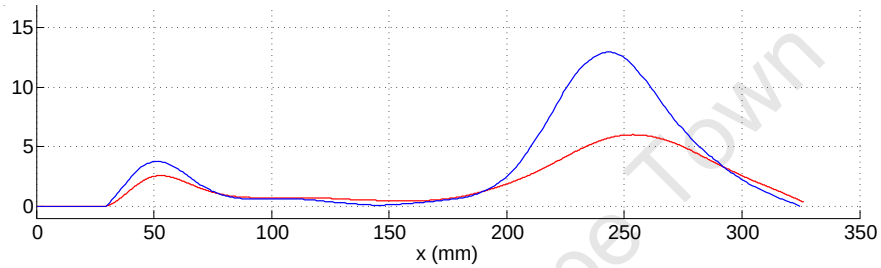

(b) Axial charge position $0.75l$.

Figure 6.21: Experimental-simulated profile comparison for 50g tests with different axial charge positions. Experimental profile is represented by blue, while red corresponds to the simulated profile.

In Figure 6.21a for the $0.5l$ axial charge position, the quantitative agreement between the experimental and simulated profiles is generally good, with the disparities everywhere within a single cylinder wall thickness. This is distinct from Figure 6.21b for the $0.75l$ case, where the quantitative agreement between the two profiles is poor in the region of maximum deformation. However outside of this region the profiles exhibit extremely good correlation with the disparities well within a cylinder wall thickness. Similar to that seen for the 30g tests, the experimental profiles exhibit more localised deformations than the simulated profiles. It should also be noted that the ratio of the x-y scale in the figures is 1:8.75 and thus the deformation and disparities are significantly magnified.

6.4 Comparison with modified analytical solution

In Section 3.4 a modified version of Benham and Duffey's [5] analytical solution for the deformation response of cylinders subjected to internal blast loads was presented. This modified analytical solution is based on that presented by the authors [5] for mild steel, and adjusted to suit the geometric and material parameters in the present work.

Figure 6.22 shows both the experimental and simulated results overlaid on the modified Benham and Duffey [5] analytical solution at an axial charge position of $0.5l$. The experimental data are represented by the solid blue data points, and the simulated results are represented by the red diamonds.

Recall that the three curves are derived from three different solution methods where:

- Curve 1 is the closed-form solution to an open-ended geometry with a constant dynamic yield stress
- Curve 2 is a numerical solution to an open-ended geometry with a variable dynamic yield stress
- Curve 3 is a numerical solution to a closed-ended geometry with a variable dynamic yield stress.

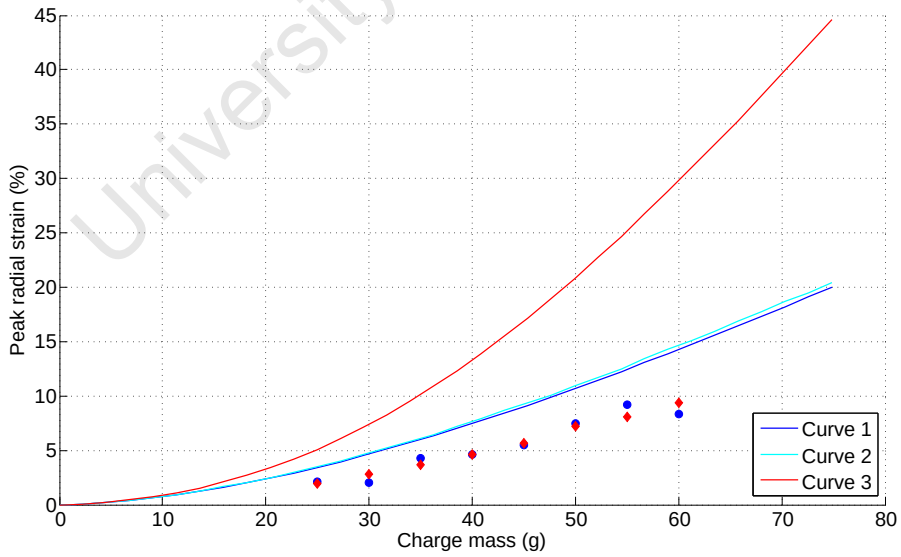

Figure 6.22: Comparison of experimental and simulated results with analytically predicted peak radial strain as a function of charge mass from modified analytical solutions.

Since all configurations in the present work are partially-confined, that is one open end and one closed, it is reasonable to expect the results to fall somewhere between Curve 1 and Curve 3. In this section both the experimental and numerical results for tests with an axially-centred charge are compared with these analytical solutions.

In general and considering the variation in experimental measurement, both the experimental and the simulated results follow the general trend predicted by Curves 1 and 2. That is an approximately linear increase in radial strain with increasing charge mass in the range 40g-75g.

All the results fall below the analytical solution of Curve 1, which is unexpected given that Curve 1 is for an open-ended configuration and thus it does not consider effects due to the accumulation of quasi-static pressure. However it is shown in the numerical analysis in the preceding sections that the quasi-static gas pressure appears to have no significant effect on the cylinder deformation for the $0.5l$ configuration. Consequently it is reasonable that the experimental and simulated results should lie near to Curves 1 and 2 which represent the purely impulsive solutions. However the degree of underestimation is surprising given the remarkable agreement between the analytical solutions and the experimental work reported by Benham and Duffey [5].

Furthermore in Section 3.2, where the work of Benham and Duffey [5] is simulated and compared with their analytical solutions, there is a similar disparity between the results with the simulations consistently underestimating that predicted analytically, even though the simulations in this case are closed on both ends. This further suggests that the quasi-static pressure retention is not correctly captured in the LS-DYNA models.

It should also be noted that the modified analytical solution here presented is unverified and merely adapted from an existing solution for larger, mild steel cylinders. The 304 stainless steel material is approximated as rigid-plastic with linear strain hardening and non-linear strain rate sensitivity. The linear strain hardening parameter $\lambda = 1.95$ may not be representative of the material in the present work. Consequently there is inherent uncertainty regarding the modified material approximation and it is thus plausible that the modified solution overestimates the cylinder deformation.

6.5 Effect of polystyrene annuli

In Section 4.1 the experimental procedure was detailed, including a description of the use of polystyrene annuli for positioning the explosive charges in the experiments. An example of one such polystyrene annulus is shown in Figure 6.23.

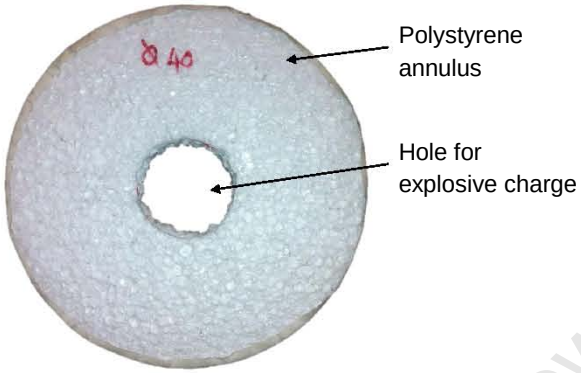

Figure 6.23: Photograph of a typical polystyrene annulus used to support the charge in the experiments.

To date the influence of the polystyrene on the structural response is not well known, though it is thought to be negligible. One possibility is that following detonation the polystyrene burns up completely, without significantly impeding the blast wave, and that by the time the blast wave loads the structure of interest, there is no polystyrene remaining between the two. A second possibility is that some of the polystyrene remains between the explosive and the structure during the early-time wave propagation.

This section presents the details of two experiments designed to provide some preliminary insight into the effect of the polystyrene on the structural response.

6.5.1 Modified experimental set up

As a means of qualifying the effect of the polystyrene in this work, two additional experiments are performed. Both a 40g and 50g charge mass are used and the experimental procedure is identical to that detailed in Section 4.1. However for these tests only half a polystyrene annulus is used to position the charge. Thus on one side of the central axis there is polystyrene between the explosive charge and the cylinder wall as before, while on the other side there is only air between the two. This is shown in the schematic of Figure 6.24.

Assuming that using the full annulus set up used hitherto results in a relatively symmetrical deformation response, then the disparity between the diametrically opposed points labelled 'a' and 'b' in Figure 6.24 gives a relative indication of the effect of the polystyrene on the cylinder deformation.

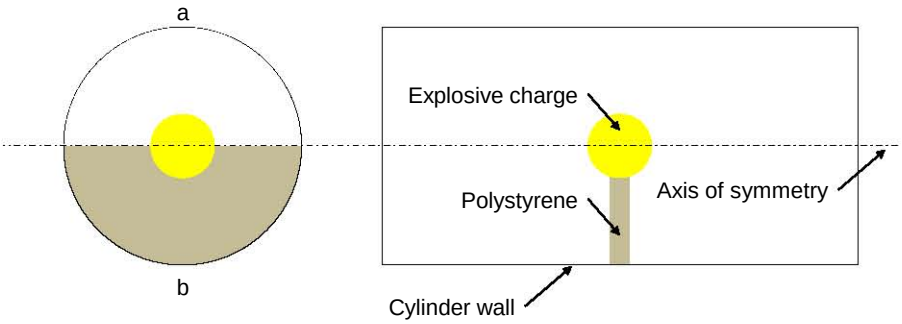

Figure 6.24: Modified experimental set up for tests with polystyrene half-annulus.

6.5.2 Experimental results

In Section 4.3.1 and Section 5.6.2, the reported post-test deformation is a measure of the final cylinder diameter which assumes a certain degree of symmetry in the response. However since the methodology in this section relies on the *disparity* between diametrically opposed points relative to the central axis, no such diametric measurement can be made. Consequently the results in this section are based on photographic observation.

Figure 6.25 shows photographs of the post-test response of the two cylinders tested in this section. In both cases the cylinders are positioned to illustrate any diametric disparity, and the orientation of points 'a' and 'b' is as indicated in the figure.

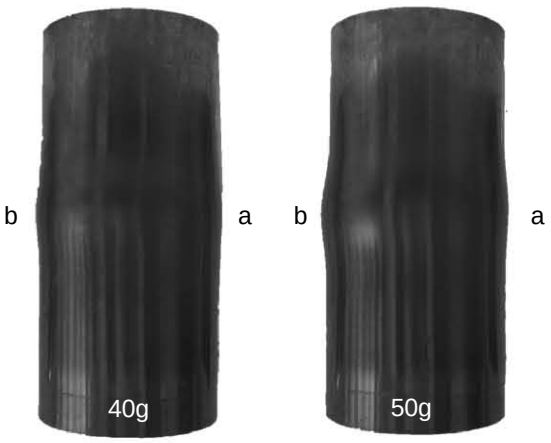

Figure 6.25: Results of modified tests conducted with half a polystyrene annulus. 'a' and 'b' denote sides without and with polystyrene respectively.

In both cases, though particularly in the 50g test, it is clear that the deformation of side 'b' is more pronounced than that of side 'a'. The exaggeration in the 50g test is aided by the generally larger plastic deformations for this mass of explosive. Since side 'b' is that side aligned with the polystyrene it initially appears that the use of polystyrene increases the level of deformation seen by the structure.

In Figure 6.26, the cylinders of this section are shown side-by-side with those from Section 4.3.1 where a full polystyrene annulus is used. In the figure the simulations with the half-annulus are indicated by the asterisk. Based only on this figure, the diametric variation for the cylinders of this section appears significantly larger than that for the full-annulus tests. It should be noted that the symmetry for both the 40g and 50g tests from Section 4.3.1 is worse than the majority of the other tests, consequently the asymmetric deformation seen in this section may be due to the inherent experimental variation. However, that both the half-annulus tests exhibit deformation bias on the side *with* polystyrene, it seems less likely that the asymmetric deformation is due to experimental variation, and more likely due to the use of the polystyrene in between the explosive and the loaded structure. The effect of polystyrene on loading and the structural deformation is worthy of further investigation, which is beyond the scope of the present work.

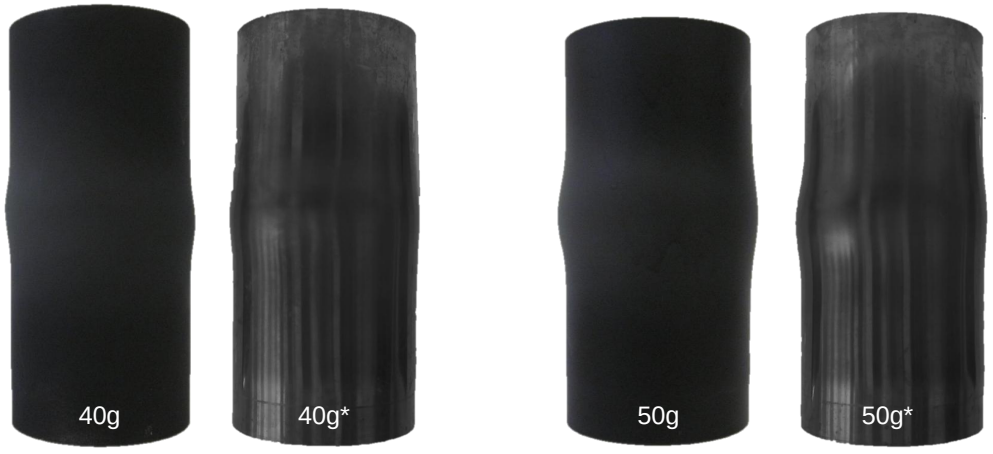

Figure 6.26: Comparison of tests conducted with full and half polystyrene annuli. Half-annulus tests denoted by *.

Chapter 7

Conclusions

The response of structures to internal blast loading is an increasingly important field. The present work investigates the response of partially-confined, right-circular cylinders to internal blast loads from radially-centred PE4 explosives. In these experiments two primary parameters are varied: the mass of explosive, and the axial position of the explosive. As an additional parameter, two experiments are conducted with a modified experimental set up that employed only half an annulus of polystyrene. The radial deformation of the cylinders is used to gauge the effectiveness of the various configurations.

Computational models are developed in LS-DYNA Release 6.0.0 and validated against the experimental results. The intention of the models is to provide further insight into the behaviour of the systems, particularly the transient behaviour that is not captured in the experiments.

This section briefly presents conclusions based on the findings of both the experimental and numerical investigations.

7.1 Sensitivity of experimental configuration

The experimental set up and methodology exhibits good repeatability, indicated by the majority of the deformation results fitting closely to their respective trends. Additionally comparing the sectioned profiles of the cylinders sees the maximum deformations relatively well aligned, indicating a robust experimental procedure. The good repeatability is further confirmed by the strong adherence of all the measured impulse values to the expected linear trend.

7.2 Validity of computational models

The deformation results of the simulations are compared with those found experimentally for validation. In general the correlation between the two is very good particularly with respect to the deformation in line with the original charge centre (axial positions of 150mm and 225mm relative to 0mm at the closed end in the $0.5l$ and $0.75l$ tests respectively). The exceptions are the deformations for the $0.75l$ tests with larger charge masses, where the simulations significantly underestimate the experimental deformation. This underestimation is believed to be due to the poor simulation of the quasi-static pressure in the models, and supported by similar underestimation for simulations of the work of Behnam and Duffey [5], in which the cylinder deformations are known to be highly dependent on the quasi-static pressure. Based on work by Edri et al [25], this is likely due to absence of the afterburning effect in the simulations which cannot be readily captured in LS-DYNA at this time.

The correlation between the deformed cylinder profiles and those from the simulations is good, particularly for larger plastic deformations. Qualitatively the simulated profiles for the 30g tests exhibit less localised deformations than those in the experimental profiles. It is possible that this localisation is due to the polystyrene used to position the charges in the experiments. The simulations generally overestimate the bulging near the closed end of the cylinders, except in the case of the $0.75l$ tests with larger charge masses, further suggesting that the quasi-static pressure is not adequately captured.

The validity of the computational models is further confirmed by the very good correlation between the simulated impulse values and those measured experimentally across all tests.

7.3 Effect of charge mass on structural response

The cylinders exhibit an increase in deformation with increasing mass of explosive. In the case of the $0.5l$ tests this relationship is linear, while the $0.75l$ experiments exhibit an exponential relationship between deformation and charge mass if the full range of charge mass is considered. The maximum permissible charge mass before failure appears to be approximately 60g, based on tests at 60g resulting in tearing in one case, and no tearing in others.

For tests in the region above 50g-55g, there is significant bulging of the cylinders near the clamped end. This bulging is indicative of the level of quasi-static pressure within the system, and thus it suggests that the quasi-static pressure is too low to cause significant structural damage for charge masses below this range, and that the response for charge masses below this range is thus purely impulsive.

This is confirmed by examining the deformation-time histories for simulations with a charge mass from both ends of the range tested, specifically 30g and 50g. The transient response in the 30g simulations exhibits no evidence of dynamic effects, that is no relatively late-time increase in deformation typical of high quasi-static pressure. Consequently for smaller charge masses the late-time pressure is too low to cause additional structural deformation.

The measured impulse increases linearly with charge mass.

7.4 Effect of charge position on structural response

Since all the tests in the present work concern charges that are radially-centred within the cylinders, the effective stand off distance between the cylinders and the explosive remains constant in all tests. Consequently for responses where the cylinder confinement has no effect, the deformation from a given charge mass is expected to be the same regardless of the axial charge position. For charge masses in the range 20g-45g, the deformations of the cylinders tested with different axial charge positions are qualitatively and quantitatively similar.

However, the deformation response between the two axial positions becomes increasingly divergent with increasing charge mass. Above 45g, the deformations from tests with an axial charge position of $0.75l$ are significantly larger than those from the $0.5l$ tests. Since all the parameters except the axial position remain the same, this suggests that the confinement effect of the cylinders is a function of the axial charge position, and that the confinement is more influential when the charge is located nearer the open end of the

cylinders. Additionally the effect of confinement only affects the structural deformation beyond a given mass of explosive.

This is confirmed by comparing the deformation-time histories for the 30g and 50g simulations at the two different axial charge positions. For the lower charge masses there is no significant difference in the simulated transient responses between the two axial positions. For the larger charge masses, the initial impulsive portion of the transient response is similar for both axial charge positions which is expected as detailed previously. However the $0.75l$ simulation exhibits a relatively late-time deformation increase indicative of the deformation due to high quasi-static pressure, and this increase is *not* evident in the $0.5l$ case.

This behaviour is further explicated by investigating the simulated pressure behaviour in the cylinder systems. The major pressure mechanisms comprise two parts: the pressure incident on/reflected off the cylinder wall, and that incident on/reflected from the closed end. It appears that the significant damage mechanism is the pressure incident on the cylinder wall and its subsequent radial movement inside the cylinder. The pressure reflected from the closed end travels predominately axially within the cylinder, eventually expelling gas from the open end.

In the case of the $0.75l$ simulations the pressure reflected from the closed end takes longer to return to the original charge position than in the $0.5l$ case. Consequently the pressure on the cylinder wall in this region has longer to act before it is driven out of the system, causing additional late-time deformation. This is contrasted with the $0.5l$ case where the pressure is expelled from the system *before* it has a chance to cause late-time midpoint deformation. However when the charge masses are relatively small, despite the added time in the $0.75l$ simulations, the late-time pressure is too low to cause additional damage.

The measured impulses across both axial charge positions are similar and are thus unaffected by changes in the axial charge position within the range tested.

7.5 Effect of polystyrene on structural response

In the experiments, the explosive charge is positioned and supported using an annulus of polystyrene, however there remains uncertainty over the possible influence of the polystyrene on the structural response.

Two tests are conducted with a half-annulus of polystyrene to provide initial insight into its role in the present work. Relative to the tests performed with the full annulus, these tests exhibit larger radial disparities and poorer symmetry. For both test cases,

the radial deformations are biased to the side *with* polystyrene. This suggests that for the configurations in the present work, placing polystyrene between the explosive and cylinder wall to be loaded, increases the level of deformation exhibited by the structure.

Chapter 8

Recommendations

Based on the findings and conclusions of the present work, the following is recommended:

- Further experimental investigation with a view to measuring transient pressures during a blast test. Having some experimental pressure-time histories would provide insight into the validity of the same simulated phenomena. This would also be valuable in evaluating the ability of LS-DYNA to simulate blast wave reflection.
- Additionally the use of high-speed cameras and digital image correlation (DIC) should be investigated as a further means of recording some transient structural deformation data during testing.
- The simulations should be repeated in AUTODYN where the afterburning effect can be incorporated and the results compared with those from the present work.
- The test rig should be redesigned so that it can be used for both confined and unconfined experiments. This may mean designing a rig that is unconstrained (i.e. not attached to the pendulum) in the blast chamber. An alternative method of positioning the charge within the cylinders should also be considered.
- Future experiments on cylinders should employ a more robust method of post-test diameter measurement. For instance the use of 3D scanning technology could improve the accuracy of the post-test measurements.
- As additional parameters, future experiments should consider the effects on the structural response of filling the cylinders with various materials, as well the effect of the fill level.
- Eventually cylinders should be fabricated from composite materials, and their response compared with that for monolithic steels.

- Further experimental investigation into the role of polystyrene on structural deformation when it is placed between the explosive and the structure to be loaded. Using a well-understood set up, for instance blast loading of thin quadrangular plates, several tests should be conducted both with and without polystyrene. Any disparity in the results will provide a measure of the role of the polystyrene on the structural response.

References

[1] M. Silvestrini, B. Genova, and F.J. Leon Trujillo. Energy concentration factor. a simple concept for the prediction of blast propagation in partially confined geometries. *Journal of Loss Prevention in the Process Industries*, 22(4):449 – 454, 2009.

[2] M. Flegenheimer. M.T.A. expands an effort to decrease subway trash. `http://www.nytimes.com/2012/08/31/nyregion/mta-expands-an-effort-to-remove-trash-cans.html`, August 2012.

[3] C.A. Berrick. *Passenger rail security enhanced federal leadership needed to prioritize and guide security efforts : testimony before the Committee on Commerce, Science, and Transportation, U.S. Senate*. Passenger rail security. Government Accountability Office, 2007.

[4] P. Sylvester. England - is it safe from terrorism? `http://journals.worldnomads.com/safetyhub/story/73286/United-Kingdom/England-Is-It-Safe-From-Terrorism`, June 2011.

[5] R.A. Benham and T.A. Duffey. Experimental-theoretical correlation on the containment of explosions in closed cylindrical vessels. *International Journal of Mechanical Sciences*, 16(8):549 – 558, 1974.

[6] W.E. Baker. *Explosions in Air*. Austin: London University of Texas Press, 1973.

[7] G.F. Kinney. *Explosive shocks in air*. Macmillan, 1962.

[8] R.J. Martin, A. Reza, and L.W. Anderson. What is an explosion? a case history of an investigation for the insurance industry. *Journal of Loss Prevention in the Process Industries*, 13(6):491 – 497, 2000.

[9] P.D. Smith and J. G. Hetherington. *Blast and Ballistic Loading of Structures*. Butterworth Heinemann, 1994.

[10] Factory Mutual Insurance Company. *Causes and Effects of Fires and Explosions*, 2006.

[11] P.W. Cooper. *Explosives engineering*. Wiley-VCH, 1996.

[12] USDOD. Structures to Resist the Effects of Accidental Explosions. Document No. UFC 3-340-02. Technical report, US Department of Defense (USDOD), 2008.

[13] J.A. Zukas and W.P. Walters. *Explosive Effects and Applications*. High Pressure Shock Compression of Condensed Matter. Springer, 2002.

[14] B.M. Dobratz and P.C. Crawford. *LLNL Explosives Handbook*. Natl Technical Information, 1985.

[15] ANSYS. *Release 13.0 ANSYS AUTODYN User's Manual*, November 2010.

[16] T. Ngo, P. Mendis, A. Gupta, and J. Ramsay. Blast loading and blast effects on structures an overview. *Electronic Journal of Structural Engineering Special Issue: Loading on Structures*, 2007.

[17] J.S. Rinehart and J. Pearson. *Explosive working of metals*. Macmillan, 1963.

[18] S. Mannan and F.P. Lees. *Lee's Loss Prevention in the Process Industries: Hazard Identification, Assessment, and Control*. Number v. 1 in Lee's Loss Prevention in the Process Industries: Hazard Identification, Assessment, and Control. Elsevier Butterworth-Heinemann, 2005.

[19] W. Baker, P. Cox, P. Westine, J. Kulesz, and R. Strehlow. *Explosion Hazards and Evaluation*, chapter Loading from blast waves. Elsevier, 1983.

[20] B. Luccioni and D. Ambrosini. Numerical assessment of blast effects scaling procedures. *Mechanica Computational*, XXIX(12), 2010.

[21] H.L. Brode. Numerical solutions of spherical blast waves. *Journal of Applied Physics*, 26(6):766–775, 1955.

[22] C.A. Mills. The design of concrete structure to resist explosions and weapon effects. In *Conference on concrete for hazard protections*, 1987.

[23] C.M. Harris. *Shock and vibration handbook*. Mechanical engineering. McGraw-Hill, 1996.

[24] The effects of simplification of the explosion pressure-time history. Technical report, Steel Construction Institute, 1991.

[25] I. Edri, V.R. Feldgun, Y.S. Karinski, and D.Z. Yankelevsky. On blast pressure analysis due to a partially confined explosion: III. afterburning effect. *International Journal of Protective Structures*, 3(3):311 – 332, 2012.

[26] G.S. Langdon, I.B. Rossiter, V.H. Balden, and G.N. Nurick. Performance of mild steel perforated plates as a blast wave mitigation technique: Experimental and numerical investigation. *International Journal of Impact Engineering*, 37(10):1021 – 1036, 2010.

[27] G.S. Langdon, G.N. Nurick, and N.J. du Plessis. The influence of separation distance on the performance of perforated plates as a blast wave shielding technique. *Engineering Structures*, 33(12):3537 – 3545, 2011.

[28] N. Jacob, G.N. Nurick, and G.S. Langdon. The effect of stand-off distance on the failure of fully clamped circular mild steel plates subjected to blast loads. *Engineering Structures*, 29(10):2723 – 2736, 2007.

[29] N. Jacob, S. Chung Kim Yuen, G.N. Nurick, D. Bonorchis, S.A. Desai, and D. Tait. Scaling aspects of quadrangular plates subjected to localised blast loads - experiments and predictions. *International Journal of Impact Engineering*, 30(8-9):1179 – 1208, 2004. Eighth International Symposium on Plasticity and Impact Mechanics (IMPLAST 2003).

[30] T.A. Duffey and D. Mitchell. Containment of explosions in cylindrical shells. *International Journal of Mechanical Sciences*, 15(3):237 – 249, 1973.

[31] W.E. Baker, C.E. Anderson, B.L. Morris, and D.K. Wauters. Quasi-static pressure, duration, and impulse for explosions (e.g. HE) in structures. Technical Report 6, SOUTHWEST RESEARCH INST SAN ANTONIO TX, 1982.

[32] H.R.W. Weibull. Pressures recorded in partially closed chambers at explosion of TNT charges. *Annals of the New York Academy of Sciences*, 152(1):357–361, 1968.

[33] C. Kingery, R. Schumacher, and W. Ewing. Internal pressure from explosions in suppressive structures. Technical report, ARMY BALLISTIC RESEARCH LAB ABERDEEN PROVING GROUND MD, 1978.

[34] R.R. Karpp, T.A. Duffey, T.R. Neal, and Los Alamos National Laboratory. *Response of containment vessels to explosive blast loading*. Los Alamos National Laboratory. Los Alamos National Laboratory, 1980.

[35] I. Edri, Z. Savir, V.R. Feldgun, Y.S. Karinski, and D.Z. Yankelevsky. On blast pressure analysis due to a partially confined explosion: I. experimental studies. *International Journal of Protective Structures*, 2(1):1 – 20, 2011.

[36] V.R. Feldgun, Y.S. Karinski, I. Edri, D. Tsemakh, and D.Z. Yankelevsky. On blast pressure analysis due to a partially confined explosion: II. numerical studies. *International Journal of Protective Structures*, 3(1):61 – 80, 2012.

[37] V.R. Feldgun, Y.S. Karinski, and D.Z. Yankelevsky. A simplified model with lumped parameters for explosion venting simulation. *International Journal of Impact Engineering*, 38(12):964 – 975, 2011.

[38] T.A. Duffey and E.A. Rodriguez. Overview of pressure vessel design criteria for internal detonation (blast) loading. Technical report, Los Alamos National Lab, 2001.

[39] W.E. Baker and F.J. Allen. *The Response of Elastic Spherical Shells to Spherically Symmetric Internal Blast Loading*. Office of technical services, U.S. Department of Commerce, 1957.

[40] W.E. Baker. The elastic-plastic response of thin spherical shells to internal blast loading. *Journal of Applied Mechanics*, 27(1):139–144, 1960.

[41] A.J. Hoffman, S.N. Mills, and U.S. Army Ballistic Research Laboratory. *Air Blast Measurements about Explosive Charges at Side-on and Normal Incidence*. BRL report. Ballistic Research Laboratories, 1956.

[42] M. Giglio. Spherical vessel subjected to explosive detonation loading. *International Journal of Pressure Vessels and Piping*, 74(2):83 – 88, 1997.

[43] Q. Dong, Q.M. Li, and J.Y. Zheng. Interactive mechanisms between the internal blast loading and the dynamic elastic response of spherical containment vessels. *International Journal of Impact Engineering*, 37(4):349 – 358, 2010.

[44] J Proctor. Containment of explosions in water-filled right-circular cylinders. *Experimental Mechanics*, 10:458–466, 1970. 10.1007/BF02327673.

[45] C.K. Youngdahl. The equivalence of dynamic loads for the final plastic deformation of a tube. In *Proceedings of the first international conference on pressure vessel technology, CONF690906*, 1969.

[46] H.J. Goodman. *Compiled Free-air Blast Data on Bare Spherical Pentolite*. Defense Technical Information Center, 1960.

[47] G.R. Cowper and P.S. Symonds. *Strain-hardening and strain-rate effects in the impact loading of cantilever beams*. Providence, R.I. : Division of Applied Mathematics, Brown University., 1957.

[48] W.R. Wise and J.F. Proctor. *Explosion Containment Laws for Nuclear Reactor Vessels*. Defense Technical Information Center, 1965.

[49] N. Rushton, G.K. Schleyer, A.M. Clayton, and S. Thompson. Internal explosive loading of steel pipes. *Thin-Walled Structures*, 46(7 - 9):870 – 877, 2008. A special issue to mark the Retiral of Professor Jim Rhodes, Founding Editor.

[50] F. Fanous and L. Greimann. Simplified analysis for impulsively loaded shells. *Journal of Structural Engineering*, 114(4):885–899, 1988.

[51] A.M. Clayton. Preliminary design of vessels to contain explosions. *ASME Conference Proceedings*, 2006(4756X):111–115, 2006.

[52] G.R. Johnson and W.H. Cook. A constiutive model and data for metals subjected to large strains, high strain rates and high temperatures. In *Proceedings of the 7th International Symposium on Ballistics*, volume 21, pages 541–547. The Hague, Netherlands: International Ballistics Committee, 1983.

[53] US Department of the Army. Structures to Resist the Effects of Accidental Explosions. Army TM5-1300, Navy NAVFAC P-397, Airforce AFR 88-22. Technical report, Departments of the Army, Navy and Air Force, 1990.

[54] G.S. Collins. An introduction to hydrocode modeling. Unpublished lecture notes. `http://amcg.ese.ic.ac.uk/~gsc/publications/sales_2/download/intro.pdf`, August 2002.

[55] G.E. Fairlie. The numerical simiulation of high explosives using AUTODYN-2D & 3D. In *Explo 98. Institute of Explosive Engineeris Fourth Biannual Symposium*, 1998.

[56] L.P. Orlenko. *Physics of Explosion (In Russian).* Fizmatlit, Russia, Third edition, 2002.

[57] Everbest Valves & Fittings. *Inspection Certificate: Stainless Steel Dairy Tube*, April 2012.

[58] M.J. Forrestal and M.J. Sagartz. Elastic-plastic response of 304 stainless steel beams to impulse loads. *Journal of Applied Mechanics*, 45(3):685–687, 1978.

[59] B.A. Burgan. *Elevated Temperature and High Strain Rate Properties of Offshore Steels.* Offshore Technology Report Series. HSE Books, 2001.

[60] I.B. Rossiter. Performance of mild steel perforated plates as a blast wave mitigation technique. Master's thesis, University of Cape Town, 2008.

[61] G.S. Langdon, S. Chung Kim Yuen, and G.N. Nurick. Experimental and numerical studies on the response of quadrangular stiffened plates. part II: localised blast loading. *International Journal of Impact Engineering*, 31(1):85 – 111, 2005.

[62] C. Geretto. Private commuication. 2012.

[63] LTSC. *LS-DYNA Keyword User's Manual Volume I*, March 2012.

[64] A. Alia and M. Souli. High explosive simulation using multi-material formulations. *Applied Thermal Engineering*, 26(10):1032 – 1042, 2006.

[65] E.G. Pickering. The response of quadrangular plates to buried charges. Master's thesis, University of Cape Town, 2011.

[66] C. Soutis, G. Mohamed, and A. Hodzicgay. Modelling the structural response of GLARE panels to blast load. *Composite Structures*, 94(1):267 – 276, 2011.

[67] C.F. Zhao, J.Y. Chen, Y. Wang, and S.J. Lu. Damage mechanism and response of reinforced concrete containment structure under internal blast loading. *Theoretical and Applied Fracture Mechanics*, 61(0):12 – 20, 2012.

[68] G.S. Langdon and G.K. Schleyer. Unusual strain rate sensitive behaviour of aisi 316l austenitic stainless steel. *The Journal of Strain Analysis for Engineering Design*, 39(1):71–86, 2004.

[69] D.J. Steinberg. *Equation of State and Strength Properties of Selected Materials: Change 1, Feb. 13, 1996*. UCRL-MA. Lawrence Livermore National Laboratories, 1996.

[70] A. Ozinsky. A numerical investigation into the behaviour of perforated plates as blast wave mitigation devices. 2011.

[71] S. Chung Kim Yuen. *The effects of blast induced imperfections on the energy absorption characteristics of square tubes*. PhD thesis, University of Cape Town, 2006.

[72] M.D. Theobald. *Blast loading of sandwich panels with thin-walled tube cores*. PhD thesis, University of Cape Town, 2007.

[73] T.J. Cloete. Constructing true stress vs. true strain curves from load vs. deflection data. 2004.

[74] ASTM Standard E8M - Standard Test Methods for Tension Testing of Metallic Materials, 2011.

[75] D. Bonorchis. *Analysis and Simulation of Welded Plates Subjected to Blast Loading*. PhD thesis, University of Cape Town, 2007.

[76] S. Lee, F. Barthelat, J.W. Hutchinson, and H.D. Espinosa. Dynamic failure of metallic pyramidal truss core materials: Experiments and modeling. *International Journal of Plasticity*, 22(11):2118 – 2145, 2006.

Appendix A

Impulse Theory

In Section 4.1.2 the horizontal ballistic pendulum used at the Blast Impact and Survivability Research Unit (BISRU) was introduced. During a blast test, the pendulum traces the amplitude of its swing from which the impulse imparted to it may be calculated. Taking into account the geometry of the pendulum set up, this section presents details of the necessary calculations based on that presented by Chung Kim Yuen [71] and Theobald [72].

A.1 Horizontal pendulum theory

The geometry of the horizontal pendulum set up is shown in Figure A.1.

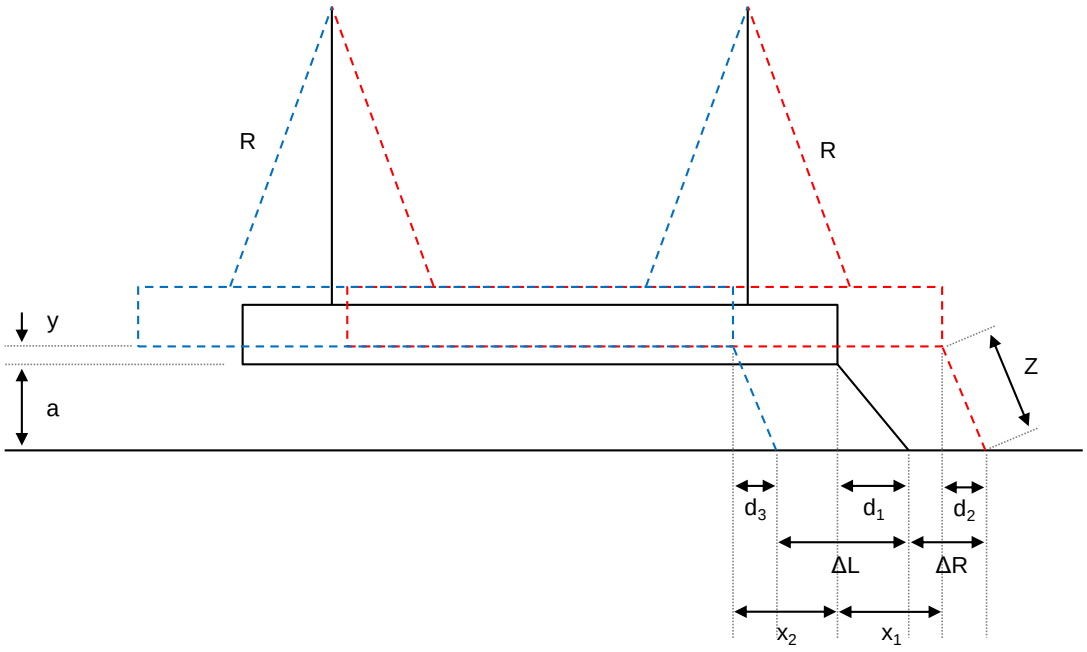

Figure A.1: Geometry of the horizontal ballistic pendulum.

The linearised equation of motion for a simple pendulum is

$$\ddot{x} + 2\beta\dot{x} + \omega_n^2 = 0 \tag{A.1}$$

where

$$\beta = \frac{C}{2m_p} \tag{A.2}$$

and

$$\omega_n = \frac{2\pi}{T} \tag{A.3}$$

In the above equations β is the damping constant, C is the damping coefficient, m_p is the total mass of pendulum including clamping rig, specimen and balancing masses, and T is the natural period of pendulum.

The solution to the second order differential equation of Equation A.1 is

$$x = \frac{\left(e^{-\beta t}\right) \dot{x_0} \sin\left(\omega_d t\right)}{\omega_d} \tag{A.4}$$

where $\dot{x_0}$ is the initial velocity of the pendulum and $\omega_d = \sqrt{\omega_n^2 - \beta^2}$.

If x_1 is the maximum forward horizontal displacement of the pendulum occurring at time $t = T/4$, and x_2 is the maximum backward horizontal displacement of the pendulum occurring at time $t = 3T/4$, then substituting into Equation A.4 gives

$$x_1 = \frac{\dot{x_0} T}{2\pi} e^{-\beta T/4} \tag{A.5}$$

and

$$x_2 = -\frac{\dot{x_0} T}{2\pi} e^{-3\beta T/4} \tag{A.6}$$

Solving for β in terms of x_1 and x_2 gives

$$\beta = \frac{2}{T} \ln\left(\frac{x_1}{x_2}\right) \tag{A.7}$$

and the initial velocity of the pendulum $\dot{x_0}$ is found by putting Equation A.7 into Equation A.5 giving

$$\dot{x_0} = \frac{2\pi}{T} x_1 e^{-\beta T/4} \tag{A.8}$$

Finally the impulse imparted to the pendulum is found by

$$I = m_p \dot{x_0} \tag{A.9}$$

The natural period of the pendulum T is found by perturbing the pendulum and averaging the time taken for a number of oscillations. It should be noted, that owing to the geometry of the set up, the maximum forward ΔR and backward ΔL translations of the pen tip do not correspond to the maximum forward x_1 and backward x_2 displacements of the pendulum. Consequently these must be related by taking into account the geometry of the pendulum.

The horizontal distance between the initial position of the pendulum and the tip of the pen is

$$d_1 = \sqrt{Z^2 - a^2} \tag{A.10}$$

and when the pendulum is at its maximum amplitude, this distance has been reduced to

$$d_2 = \sqrt{Z^2 - (a + y)^2} \tag{A.11}$$

It is reasonable to assume that the angle of oscillation of the pendulum θ is small, so that $x_1 = R\theta$ and $y = R\theta^2/2$ where R is the length of the wires from which the pendulum is hung. Combining these relationships gives

$$y = \frac{x_1^2}{2R} \tag{A.12}$$

which when substituted into Equation A.11 results in

$$d_2 = \sqrt{Z^2 - \left(a + \frac{x_1^2}{2R}\right)^2} \tag{A.13}$$

From the geometry of Figure A.1 it is clear that

$$x_1 = \Delta R + d_1 - d_2 \tag{A.14}$$

and

$$x_2 = \Delta L - d_1 + d_2 \tag{A.15}$$

Substituting for d_1 and d_2 gives

$$x_1 = \Delta R + \sqrt{Z^2 - a^2} - \sqrt{Z^2 - \left(a + \frac{x_1^2}{2R}\right)^2} \tag{A.16}$$

and

$$x_2 = \Delta L - \sqrt{Z^2 - a^2} + \sqrt{Z^2 - \left(a + \frac{x_1^2}{2R}\right)^2} \tag{A.17}$$

If ΔR, ΔL, Z, a, and R are measured, then Equation A.16 and Equation A.17 may be solved iteratively using MATLAB or the solver add-in for Microsoft Excel. The damping constant may then be calculated, followed by the initial velocity of the pendulum $\dot{x}_0$. Finally the impulse is found from Equation A.9.

Appendix B

Material Characterisation

In order to simulate the cylinder response, information about the material stress, strain and strain rate behaviour is required. This information may be acquired through various material characterisation tests, for instance quasi-static tensile testing and split Hopkinson bar testing.

This section first presents the background to the material strength models used in the simulations in the present work. The results of the quasi-static tensile testing are then briefly presented, along with a discussion of the inherent complications. Finally the methods for calibrating the required material model parameters are detailed.

B.1 Material strength models

The real phenomena that are described by empirical material tests can only be approximated in the computational model. Many constitutive relationships have been proposed to do so, each with a different level of complexity. Typically the complexity increases as the constitutive relationship incorporates more factors affecting the material behaviour, for instance strain, strain rate and temperature effects. In general, these constitutive relationships are referred to as material strength models.

The strength behaviour may be adequately approximated from quasi-static tensile test data. However in order to capture the strain rate behaviour, material data is required across a range of strain rates; ideally from quasi static through to high strain rate. Thermal softening effects may be approximated from material tests at elevated temperatures.

For the 304 stainless steel in the present work, quasi-static tensile tests are conducted at a single cross-head speed of 6mm/min. Consequently the strain rate dependency of the material cannot be adequately approximated. However the effects of stain rate are not insignificant and cannot be ignored. In order to achieve *some* approximation of the strain rate behaviour, it is assumed that the behaviour is similar to that of other 304 stainless steels of comparable strength. Strain rate data is available for such materials [58, 59].

In the present work a modified version of the Johnson-Cook [52] constitutive relationship is used to approximate the material response. This modified model along with the background to its constituent parts are presented in the following sections.

B.1.1 Power law hardening

When the stress in a material exceeds its elastic limit, irrecoverable deformation is exhibited by the material. This deformation is known as plastic deformation, during which the material is said to experience plastic flow. The stress at which plastic flow is initiated is the yield stress, often referred to as the flow stress.

When the true stress in a material is plotted against the true strain, the resulting curve is known as the flow curve. For a given set of conditions, the flow curve gives the stress required to cause the material to flow plastically to a given extent of strain.

The flow behaviour of metals may be described by the Holloman equation

$$\sigma = K\epsilon^n \tag{B.1}$$

where σ is the true stress, K is a strength coefficient, ϵ is the total true strain, and n is the strain hardening exponent. The strain hardening exponent has limiting values of 0 and 1, which describe the two limiting cases of a perfectly-plastic material and a perfectly-elastic material respectively.

If only the plastic portion of the flow curve is considered, the flow behaviour may be described by the Ludwig equation

$$\sigma = A + B\epsilon_p^n \tag{B.2}$$

where A is the yield stress at zero plastic strain, B is the strain hardening coefficient, and ϵ_p is the plastic portion of the total strain tensor. This portion of the plastic strain may be found by decomposing the total strain tensor ϵ into its elastic and plastic parts, according to

$$\epsilon_p = \epsilon - \epsilon_e$$

In the Johnson-Cook [52] constitutive model, the effect of strain hardening is captured according to Equation B.2. Values for A, B and n are typically found by fitting true stress-strain data to the curve produced by Equation B.2. The method for doing so is presented in more detail in Section B.2.

B.1.2 Cowper-Symonds strain rate

The Cowper-Symonds [47] relationship relates the material static σ and dynamic σ^D stresses to the uni-axial strain rate $\dot{\epsilon}$ according to

$$\frac{\sigma^D}{\sigma} = \left[1 + \left(\frac{\dot{\epsilon}}{D}\right)^{1/q}\right] \tag{B.3}$$

where D and q are empirically-derived material parameters. These are chosen to best describe the material sensitivity to strain rate.

To specify values for D and q, a series of tensile tests at different strain rates must be performed. A stress measure, for instance the yield stress, is taken to be the flow stress, and this is measured at the various strain rates. The dynamic yield stresses may then

be plotted against their respective strain rates to determine the two required material parameters.

With D and q known, the dynamic yield stress σ_y^D for any strain rate $\dot{\epsilon}$ may be predicted using Equation B.3. However, the material parameters are only valid for the dynamic stress level from which they were derived. Consequently for the prediction of any other dynamic stress level, for instance the ultimate stress, new values for D and q are required.

In the standard Johnson-Cook [52] constitutive model, the strain rate effects are captured differently from that presented here. However in the modified Johnson-Cook [52] relationship as used in the present work, the strain rate term is replaced by Equation B.3. This modification is detailed in the following section.

B.1.3 Modified Johnson-Cook relationship

The standard Johnson-Cook [52] constitutive model defines the yield surface by considering the multiplicative effects of three terms according to

$$\sigma_y = \left[A + B\epsilon_p^n\right]\left[1 + C\ln\left(\dot{\epsilon}_p^*\right)\right]\left[1 - T_H^m\right] \tag{B.4}$$

The first term incorporates the effects of strain hardening where A, B, and n are determined from quasi-static tensile tests at a reference strain rate $\dot{\epsilon}_0$. This is detailed in Section B.1.1.

The second bracket represents the strain rate dependency where C is the strain hardening coefficient, and $\dot{\epsilon}_p^*$ is the dimensionless plastic strain rate. To determine C, several tensile tests at different strain rates are required. If the ratio of dynamic yield stress to static yield stress σ_y^D/σ_y is plotted against the natural logarithm of strain rate $\ln(\dot{\epsilon})$, the slope the linear fit gives the value for C.

The dimensionless plastic strain rate $\dot{\epsilon}_p^*$ is given by

$$\dot{\epsilon}_p^* = \frac{\dot{\epsilon}}{\dot{\epsilon}_0}$$

where $\dot{\epsilon}$ is the current strain rate and $\dot{\epsilon}_0$ is the reference strain rate at which the quasi-static tests were performed. Note that any value may be chosen for $\dot{\epsilon}_0$, however the values for A, B, and n must then be adjusted accordingly. This method was used by Johnson and Cook [52] to achieve a reference strain rate $\dot{\epsilon}_0 = 1\text{s}^{-1}$.

The third term couples the effect of thermal softening where T_H is the homologous temperature, and m is the thermal softening exponent. The homologous temperature is given by

$$T_H^m = \frac{T - T_{\text{room}}}{T_{\text{melt}} - T_{\text{room}}}$$

where T is the current temperature, and T_{room} and T_{melt} are the room and melting temperatures respectively. Note than when $T = T_{\text{melt}}$, the thermal softening term becomes zero so that the yield stress defined by Equation B.4 drops to zero accordingly.

In LS-DYNA a modified version of the Johnson-Cook [52] model is available which approximates the strain rate behaviour with a Cowper-Symonds-like formulation. In this case the middle term is replaced by $\left[1 + (\dot{\epsilon}/D)^{1/q}\right]$, so that the yield surface is then approximated by

$$\sigma_y = \left[A + B\epsilon_p^n\right]\left[1 + \left(\frac{\dot{\epsilon}}{D}\right)^{1/q}\right][1 - T_H^m] \tag{B.5}$$

where the first and third terms remain as before, and the second term is in accordance with that detailed in Section B.1.2.

B.2 Derivation of the Johnson-Cook parameters

In the present work, quasi-static, uni-axial tensile tests are used to determine the material strength properties. The post-ultimate stress behaviour is found by iterative simulation and the resulting stress-strain behaviour is used to derive the parameters required for the modified Johnson-Cook [52] material model.

Before the Johnson-Cook [52] parameters may be found, several preliminary procedures are performed on the raw data recorded by the tensile testing machine. Details of these procedures based on similar methods used by Pickering [65] and Cloete [73] are presented in this section.

B.2.1 Quasi-static tensile testing

The quasi-static tensile tests are conducted on the Zwick/Roell 1484 tensile testing machine at the Centre for Materials Engineering (CME), University of Cape Town. The tests provide the force-displacement data from which the stress-strain curves up to the ultimate stress for the material are formulated.

Several test specimens are cut from the cylinders along the cylinder axis. These specimens are sized according to ASTM E8M - Standard Test Methods for Tension Testing of Metallic Materials [74], and a schematic of these so-called "dog bone" specimens is shown in Figure B.1a. However owing to the manner in which the tubes are manufactured, the final material is highly anisotropic, and specimens cut from the longitudinal orientation *do not* provide relevant strength data when the deformation of interest is predominantly radial.

(a) "Dog bone" specimen. (b) Curved specimen.

Figure B.1: Schematics of different specimens used for quasi-static tensile testing.

Consequently additional circumferentially-orientated specimens are cut from the cylinders. However owing to the cylinder curvature, it is not possible to cut the desired circumferential "dog bone" specimens out of the cylinders and consequently curved, uniform-thickness specimens are used instead as shown in Figure B.1b. Since these specimens are both curved and of uniform thickness, there is no clear definition of gauge length for such specimens and this introduces a degree of uncertainty in calculating the specimen strain from the recorded force-displacement data.

The curved tensile specimens are manufactured by cutting rings from the tube of width 15mm. These rings are then cut along a diameter and small feet of length approximately 30mm are bent at both ends for gripping in the tensile testing machine. The thickness of the specimens is everywhere 2mm.

For the longitudinal "dog bone" specimens, all tests are conducted at a crosshead displacement speed of 3.6mm/min. However owing to the larger thickness of the curved specimens, the crosshead speed is increased to 6.0mm/min for these tests. Typical force-displacement outputs for both specimens are shown in Figure B.2a and Figure B.2b. Only the curved specimens are considered further.

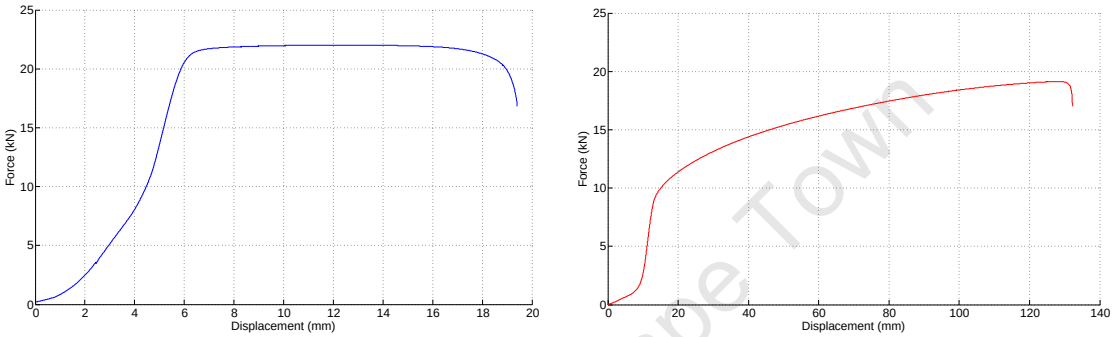

(a) Longitudinally-cut specimens tested at 3.6mm/min.

(b) Circumferentially-cut specimens tested at 6.0mm/min.

Figure B.2: Typical force-displacement output from tensile tests for different specimens.

B.2.2 Removal of machine compliance

In Figure B.2b the initial portion of the curve is non-linear and the gradient of this portion is significantly lower than the Young's modulus of stainless steel. These discrepancies are due to the initial "bedding in" and take up of the curved specimens as well as the testing machine compliance, all of which must be removed to achieve a true estimation of the specimen stress-strain behaviour. In the case of the curved specimens, the bedding in portion of the response is larger relative to that exhibited by typical "dog bone" specimens, as the bent grips straighten out during the early phase of the test. This is indicated in Figure B.3.

The initial portion of the curve is adjusted so that it conforms to the expected linear rise of force with displacement. This is achieved by fitting a linear slope through the mid to upper "linear" portion of the force-displacement curve, and extending it until it intercepts the x-axis at zero displacement. The entire curve is then shifted such that the zero displacement corresponds to the origin, that is the zero force-displacement point.

This procedure corrects for the initial force-displacement response, but it does not account

for the testing machine compliance, that is the elastic displacement of the machine itself during the test. Though the effect of this compliance is small it must still be removed. Bonorchis [75] proposed a method for doing so where the force at each data point is divided by the gradient of the linear portion of the curve, and subtracted from the corresponding displacement value.

However Pickering [65] commented that the above approach assumes that the stiffness of the testing machine is equal to that of the machine *and* the specimen in series. Consequently Pickering [65] proposed an alternative method which is used in the present work and detailed below.

The test specimen is assigned a stiffness k_{specimen} and a Young's modulus $E = 200\text{GPa}$; typical for 304 stainless steel [76]. By assuming that the testing machine and the specimen are in *parallel*, the slope of the force-displacement curve recorded during the test represents the combined/effective stiffness k_{eff} of both the machine and the specimen. Consequently the specimen and machine stiffness k_{machine} may be decomposed according to

$$\frac{1}{k_{\text{eff}}} = \frac{1}{k_{\text{specimen}}} + \frac{1}{k_{\text{machine}}} \tag{B.6}$$

Rearranging this gives

$$k_{\text{machine}} = \left[\frac{1}{k_{\text{eff}}} - \frac{1}{k_{\text{specimen}}}\right]^{-1} \tag{B.7}$$

From Hooke's Law it can be shown that the uni-axial stiffness of the specimen $k_{\text{specimen}} = AE/L$, and recalling that the effective stiffness k_{eff} is the slope of the recorded force-displacement curve, by making these substitutions Equation B.7 becomes

$$k_{\text{machine}} = \left[\frac{1}{\text{gradient}} - \frac{L}{AE}\right]^{-1} \tag{B.8}$$

Thus by subtracting the displacement at a given data point d_i by its corresponding force divided by the machine stiffness F_i/k_{machine}, the compliance of the testing machine can

be better removed. Mathematically this is

$$d_i^{\text{corrected}} = d_i - \frac{F_i}{k_{\text{machine}}} \tag{B.9}$$

An example of an adjusted force-displacement curve for a curved tensile specimen is shown in Figure B.3.

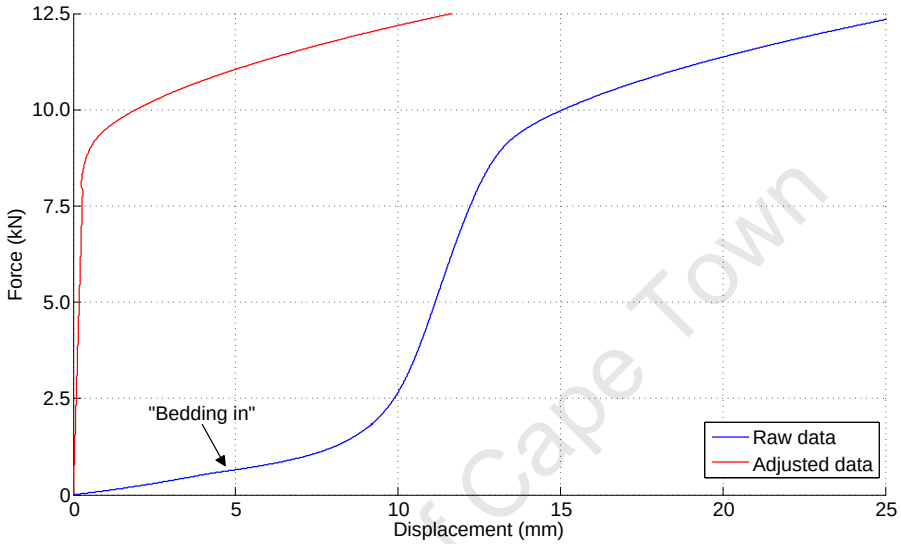

Figure B.3: Linearisation and removal of machine compliance for tensile tests on curved specimens.

B.2.3 Engineering stress and strain

The post-processed force-displacement data are converted to stress and strain values. If the cross sectional area A of the test specimen is assumed constant for the duration of the test, then the engineering stress and strain are given respectively by

$$\sigma_{\text{eng}} = \frac{F}{A} \tag{B.10}$$

$$\epsilon_{\text{eng}} = \frac{\Delta x}{L} \tag{B.11}$$

where F is the force recorded in the test, Δx is the associated crosshead displacement value, and L is the original gauge length of the specimen. Since for the curved tensile

specimens there is no clear definition of gauge length, it is assumed to be the distance between the platens of the testing machine (≈200mm).

B.2.4 Yielding and true stress and strain

For the models it is necessary to determine the yielding point of the material, that is where its response changes from linear to non-linear, which in many cases may be read directly from the stress-strain curve. However in the *unadjusted* data for the material in the present work, there is no distinct change from linear to non-linear, rather a smooth transition between the two regimes[1]. This subjectivity introduces uncertainty for specifying the yield point in a consistent manner.

To overcome this inconsistency, the 0.2% offset strain method is used to determine the yield point. In this method a line with gradient equal to that of the linear portion of the stress-strain curve is offset by 0.2% strain, and extended until it intercepts the experimental stress-strain curve. The point of interception is defined as the yield point. This method is favourable as it may be applied consistently and routinely to all tensile tests, and is illustrated in Figure B.4.

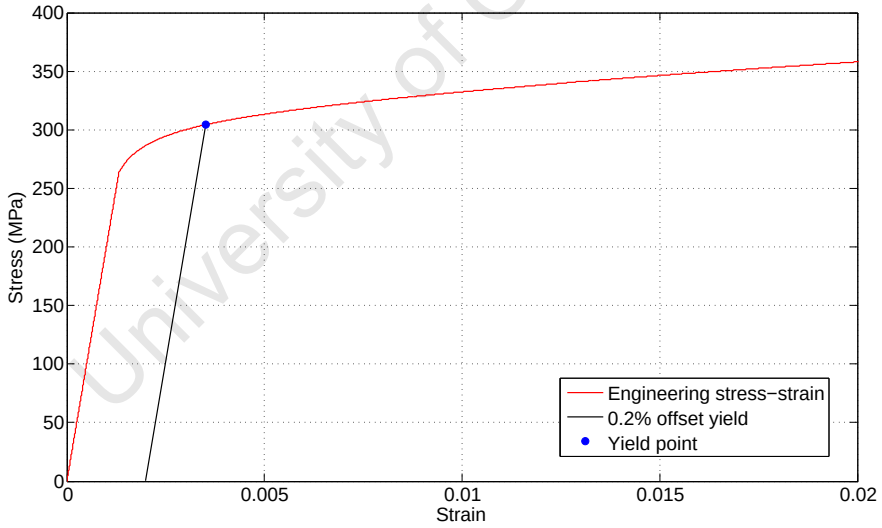

Figure B.4: 0.2% offset method used to routinely determine yield point.

The models require the true strain ϵ_{true} and stress σ_{true} values as these give a more accurate indication of the deformation characteristics of the material. In the calculation of the true values, the cross sectional area of the specimen is *not* assumed constant during the

[1]Clearly a distinct transition is introduced following linearisation, however this point depends entirely on where the linear region is chosen to end and is consequently not necessarily indicative of the yield point.

test. The true strain and stress values may be found from the corresponding engineering values, given respectively by

$$\epsilon_{\text{true}} = \ln(1 + \epsilon_p) \tag{B.12}$$

$$\sigma_{\text{true}} = \sigma_{\text{eng}}(1 + \epsilon_{\text{true}}) \tag{B.13}$$

where ϵ_p is the plastic portion of the total strain, that is the strain that occurs beyond yield.

B.2.5 Post-ultimate stress behaviour

At some point during the plastic deformation of the specimen, a strain increment leads to a *decrease* in the load. This point is known as the point of necking and corresponds with the ultimate tensile strength (UTS), which is taken as the maximum stress on the engineering stress-strain curve.

The cross sectional area of the specimen changes substantially after necking, and since this change cannot be accounted for by the tensile testing machine, the results from the tensile tests cannot be used beyond the point of necking.

Consequently the post-UTS behaviour is found by simulating a tensile test in LS-DYNA, and comparing the simulated force-displacement data with that recorded experimentally. Depending on the level of correlation between the two, the stress-strain data input to the model is adjusted and the simulations are repeated until the force-displacement agreement is satisfactory.

However the full stress-strain curve is required as in input for the models, that is both the pre- and post-UTS stress-strain. Two options for the qualitative nature of the post-UTS curve are investigated: a linear curve and a power curve. Similar to that reported by Pickering [65], the results from the linear curve are unsatisfactory and not considered further in this section.

B.2.6 Simulation of tensile tests

Consistent with the other simulations in the present work, the tensile tests are simulated in LS-DYNA Release 6.0.0. However unlike the blasting simulations which employ the explicit method, the tensile tests are simulated using the implicit method. The implicit method can use larger timesteps than the explicit method, resulting in a significant reduction in runtime.

Specimen model and boundary conditions

Recall that the curved tensile specimens are cut from rings of the cylinder material and have dimensions as follows:

- width = 15mm
- thickness = 2mm
- grip length = 2×30mm
- curved length ≈ 180mm
- inner radius = 75mm.

The 3D Lagrange domain used to model the specimens exploits the symmetry of the test specimens. Consequently the Lagrange domain is sized to match that presented above, except for the curved length which is halved to approximately 90mm. Constant stress solid elements (ELFORM=1) are used of dimensions 0.5mm×0.5mm×0.5mm.

Since the tensile specimen is modelled in half-symmetry the experimental cross head velocity is halved in the simulations. That is the velocity boundary condition applied to the upper boundary of the gripped region of the specimen is specified as 3mm/min, corresponding to the 6mm/min used experimentally. The only other constraint is the symmetry boundary condition, where the face cut through the length is constrained to have zero y-displacement. The model domain as well as the boundary conditions are indicated in Figure B.5.

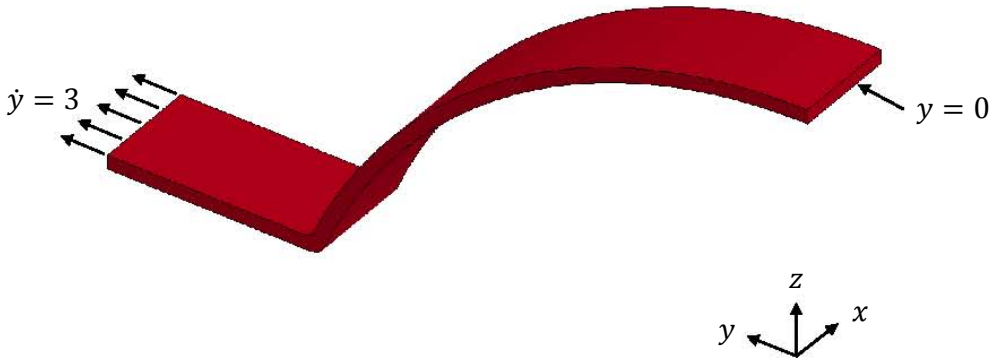

Figure B.5: Tensile specimen model and boundary conditions in half-symmetry.

Simulation input and results

As mentioned in Section B.2.5, the full stress-strain behaviour is required as an input to the models, however only that up to UTS can be reliably taken from the tensile tests. It is assumed that the post-UTS behaviour conforms to a power law relationship similar to that described in Section B.1.1.

To approximate the post-UTS behaviour, the stress at a late-strain point (300% strain) is estimated and a power curve is fit from the experimental UTS to this estimated point. The initial gradient of the post-UTS portion of the curve is set to be equal to that near the end of the pre-UTS portion, ensuring a smooth transition between the two regimes of the stress-strain curve

To investigate the sensitivity of the simulations to the choice of the chosen stress value at the late-strain point, the 300% strain point is kept constant and several simulations are performed with different corresponding stress values. The resulting force-displacement curves from the simulations exhibit no significant sensitivity to changes of the stress value in the order of ±20%. The chosen curve fitting point is 2000MPa at 300% strain.

Recall that for the curved tensile specimens there is no clear definition of gauge length. Consequently, the initially estimated gauge length of 200mm is adjusted iteratively, resulting in an adjusted stress-strain curve used as the input to the models. This procedure is repeated until the force-displacement output from the simulations matches that recorded in the experiments. The corresponding gauge length is 220mm which is reasonable considering that the *entire* grip regions of the specimen are not taken up in the platens of the test machine.

The true stress-strain curves for different gauge lengths that are used as inputs to the model are shown in Figure B.6. The force-displacement output from the model with a 220mm gauge length is compared to the experimental curve in Figure B.7.

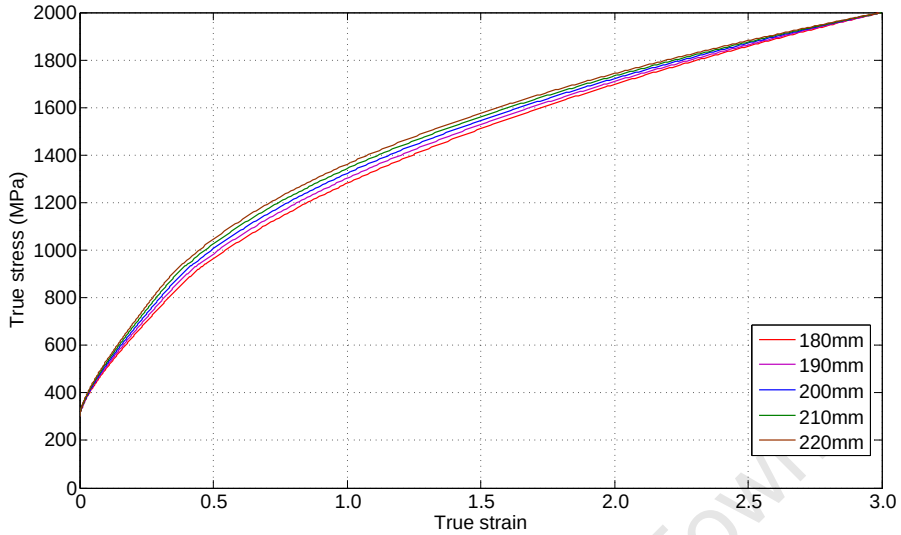

Figure B.6: True stress-strain curves with different gauge lengths used as inputs to the model.

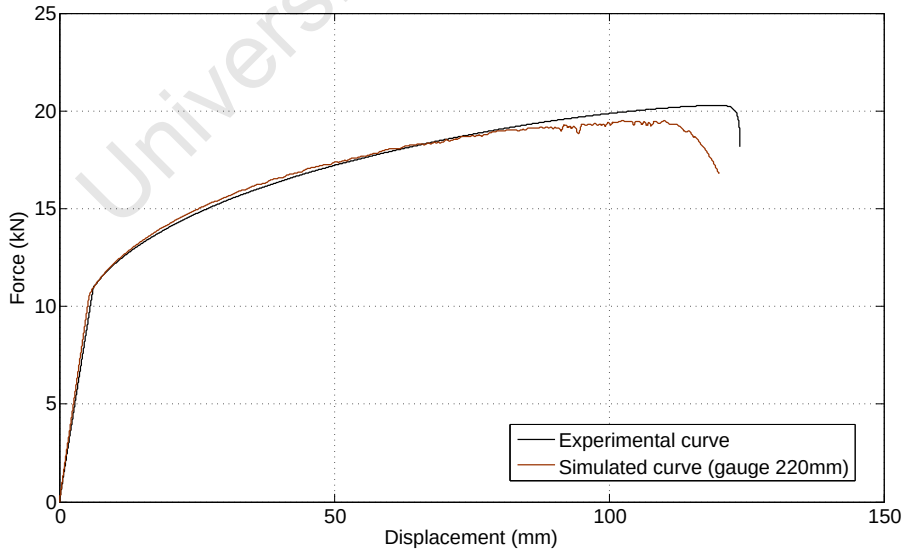

Figure B.7: Comparison of experimental and simulated force-displacement curves from tensile tests. For the simulated curve gauge length = 220mm.

Finding A, B, and n

The Johnson-Cook [52] strength parameter A corresponds to the yield stress of the material. This is found using the 0.2% offset method detailed in Section B.2.4. The yield stress for the material in the present work is taken to be approximately 310MPa.

With A fixed, the strain hardening parameters B and n are determined in MATLAB by fitting a power curve, conforming to $A + B\epsilon^n$, to the estimated true stress-strain data with a specimen gauge length of 220mm. The fit is shown in Figure B.8 and the strength parameters used in the present work are summarised in Table B.1.

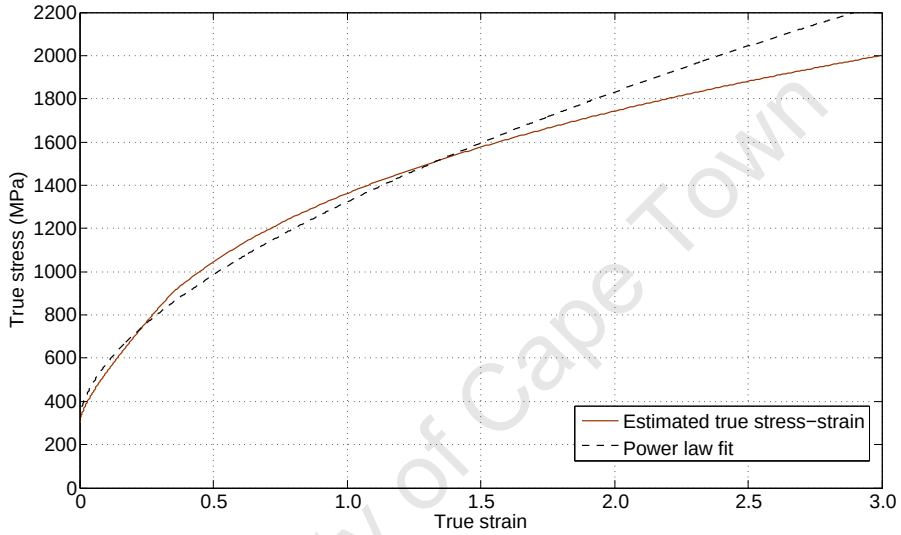

Figure B.8: Power law fit ($A + B\epsilon^n$) used to determine strength parameters for Johnson-Cook [52] material model. $A = 310$MPa, $B = 1015$MPa, and $n = 0.59$.

Finding D and q

Recall that a modified Johnson-Cook [52] material model is used in the present work, where the strain rate effects are captured with a Cowper-Symonds-like relationship. Consequently the strain rate parameters D and q are required.

Values for D and q are taken from published data [58] for 304 stainless steel as reported in Elevated Temperature and High Strain Rate Properties of Offshore Steels [59]. These values are summarised in Table B.1.

A	B	n	D	q
MPa	MPa	-	s^{-1}	-
310	1015	0.59	100	10

Table B.1: Johnson-Cook [52] strength and strain rate properties for 304 stainless steel.

Appendix C

Design Drawings

This section presents design drawings for the test rig and cylinder specimens.

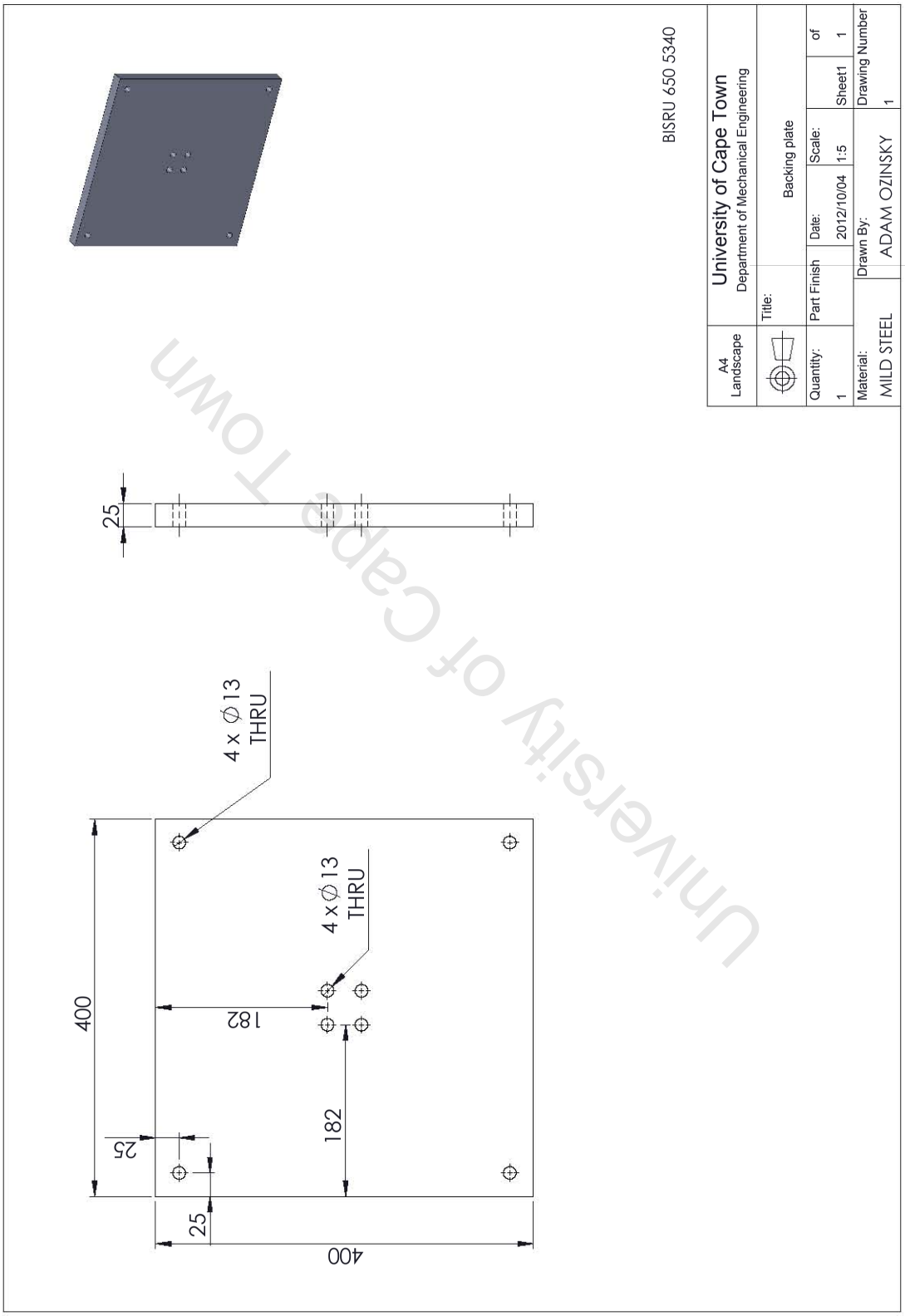

Figure C.1: Drawing of backing and mounting plates.

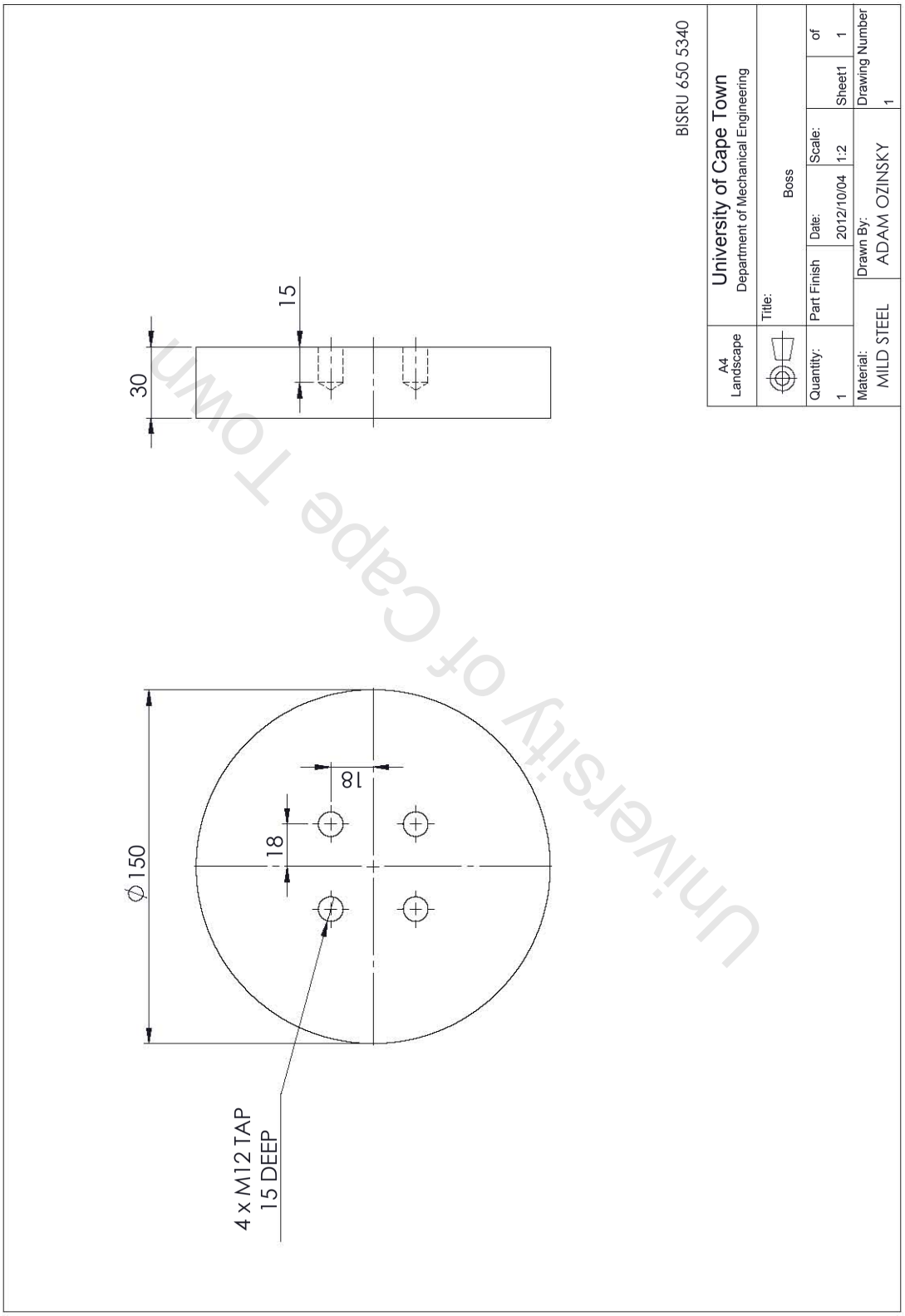

Figure C.2: Drawing of boss member.

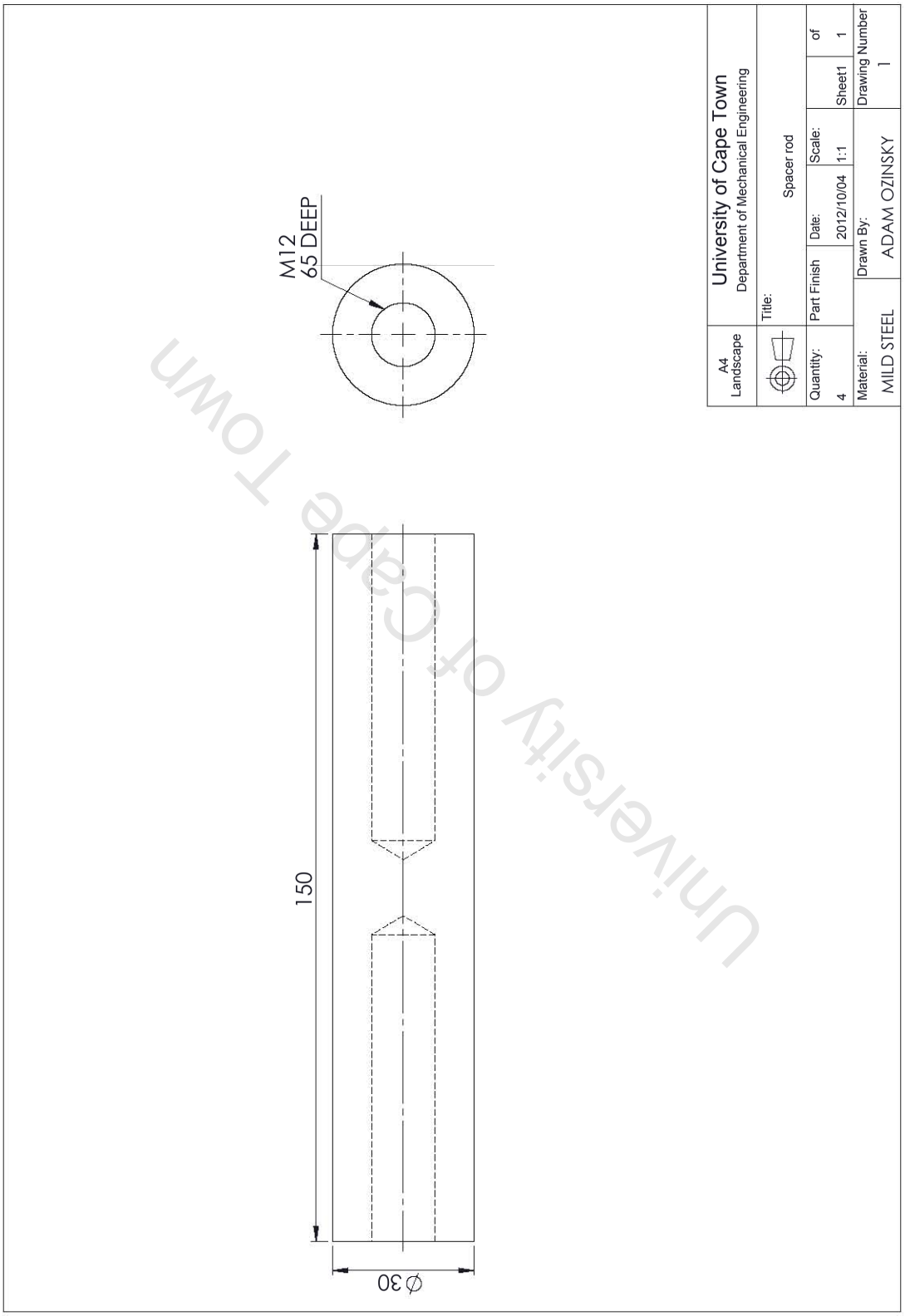

Figure C.3: Drawing of spacer rod.

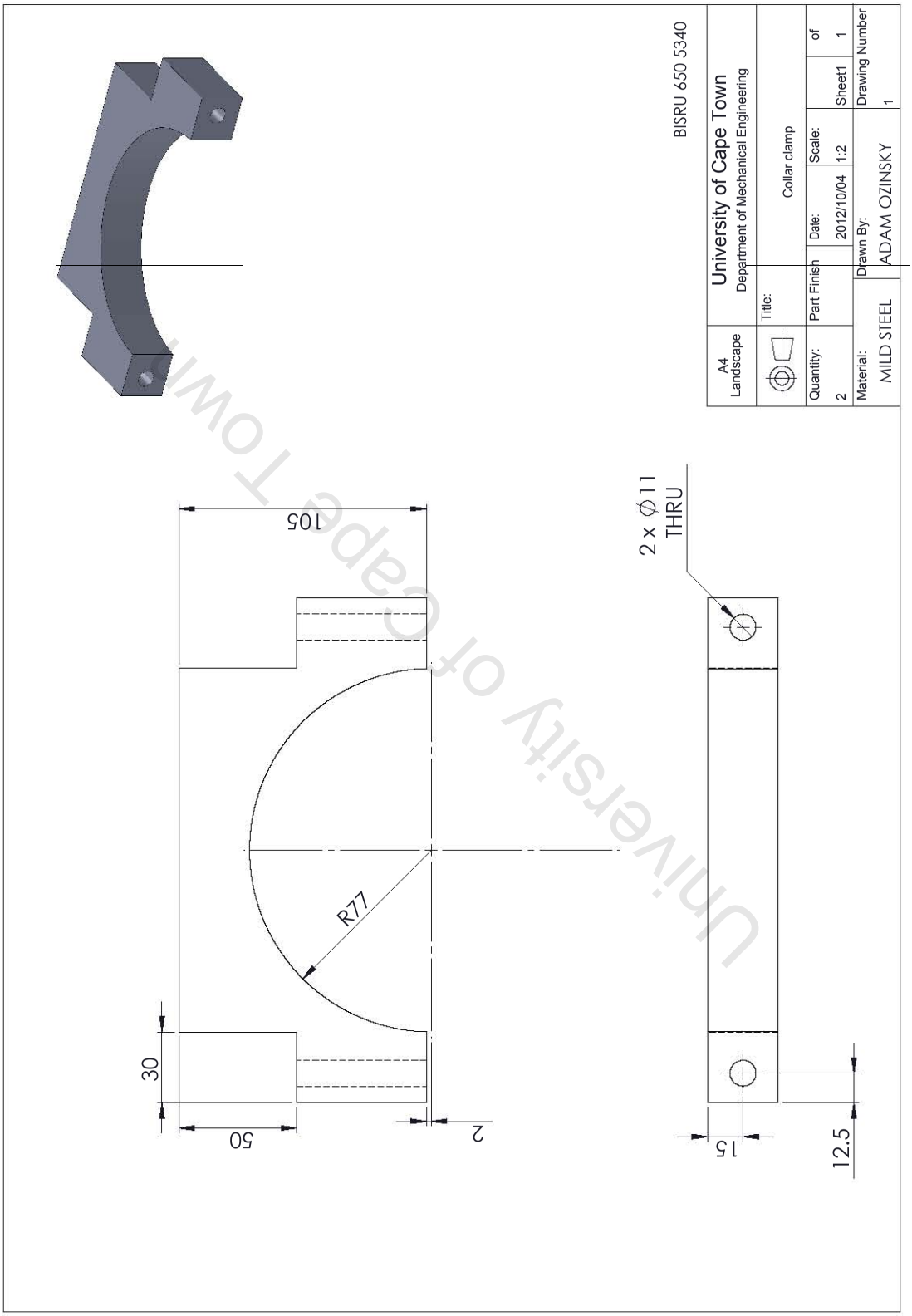

Figure C.4: Drawing of collar clamp.

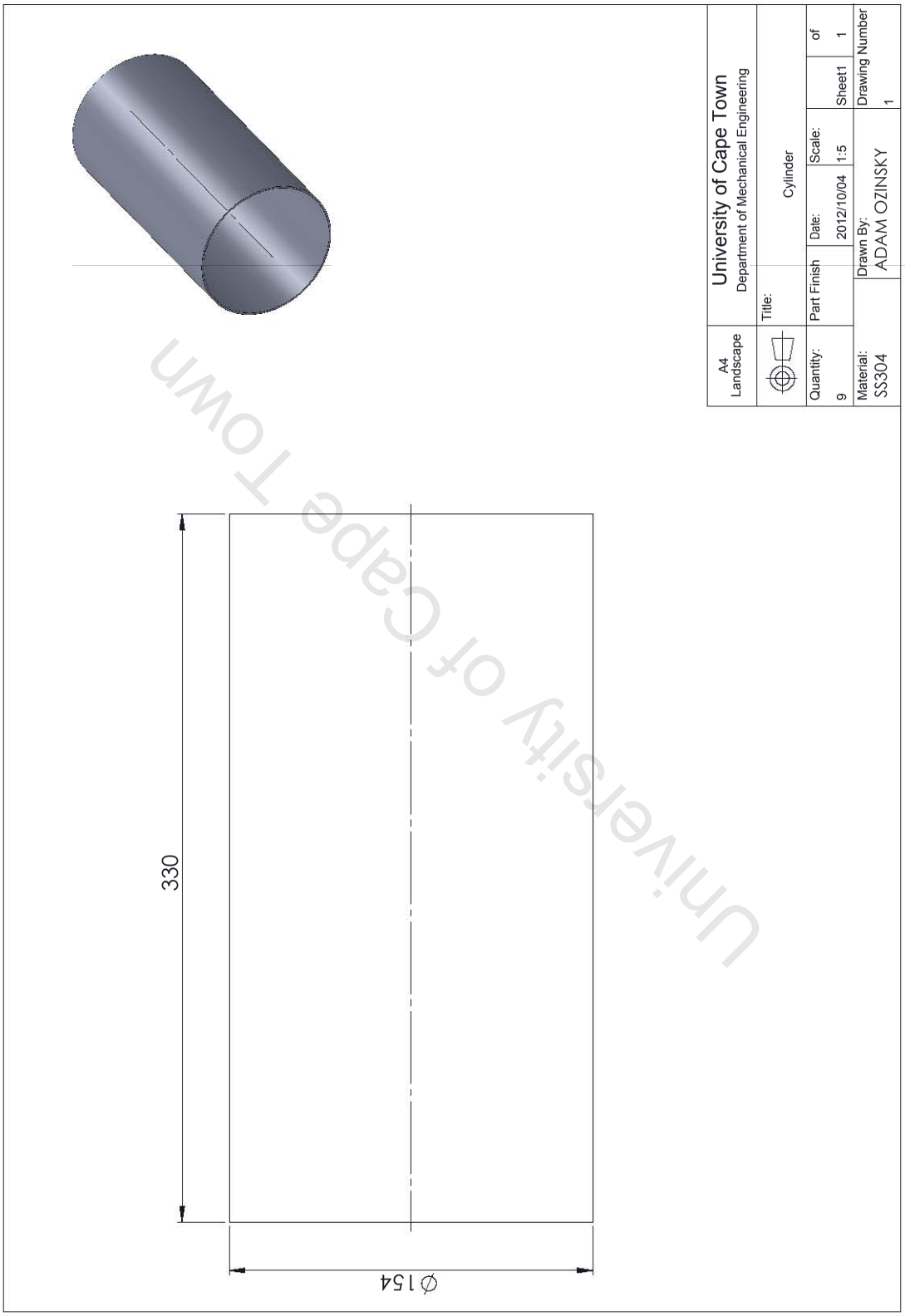

Figure C.5: Drawing of cylinder specimen.

Appendix D

Ethics Declaration

This section presents the ethics declaration required by the Faculty of Engineering and the Built Environment, University of Cape Town.

EBE Faculty: Assessment of Ethics in Research Projects (Rev2)

Any person planning to undertake research in the Faculty of Engineering and the Built Environment at the University of Cape Town is required to complete this form before collecting or analysing data. When completed it should be submitted to the supervisor (where applicable) and from there to the Head of Department. If any of the questions below have been answered YES, and the applicant is NOT a fourth year student, the Head should forward this form for approval by the Faculty EIR committee: submit to Ms Zulpha Geyer (Zulpha.Geyer@uct.ac.za; Chem Eng Building, Ph 021 650 4791).
NB: A copy of this signed form must be included with the thesis/dissertation/report when it is submitted for examination

This form must only be completed once the most recent revision EBE EiR Handbook has been read.

Name of Principal Researcher/Student: Adam Ozinsky Department: Mechanical Engineering

Preferred email address of the applicant: adam dot ozinsky at uct dot ac dot za

If a Student: Degree: MSc (Mechanical Engineering) Supervisor: A/Prof Genevieve Langdon

If a Research Contract indicate source of funding/sponsorship: NRF

Research Project Title: The Response of Partially-confined Right-circular Cylinders to Internal Blast Loading

Overview of ethics issues in your research project:

Question 1: Is there a possibility that your research could cause harm to a third party (i.e. a person not involved in your project)?		NO
Question 2: Is your research making use of human subjects as sources of data? If your answer is YES, please complete Addendum 2.		NO
Question 3: Does your research involve the participation of or provision of services to communities? If your answer is YES, please complete Addendum 3.		NO
Question 4: If your research is sponsored, is there any potential for conflicts of interest? If your answer is YES, please complete Addendum 4.		NO

If you have answered YES to any of the above questions, please append a copy of your research proposal, as well as any interview schedules or questionnaires (Addendum 1) and please complete further addenda as appropriate. Ensure that you refer to the EiR Handbook to assist you in completing the documentation requirements for this form.

I hereby undertake to carry out my research in such a way that

- there is no apparent legal objection to the nature or the method of research; and
- the research will not compromise staff or students or the other responsibilities of the University;
- the stated objective will be achieved, and the findings will have a high degree of validity;
- limitations and alternative interpretations will be considered;
- the findings could be subject to peer review and publicly available; and
- I will comply with the conventions of copyright and avoid any practice that would constitute plagiarism.

Signed by:

	Full name and signature	Date
Principal Researcher/Student:	Adam Ozinsky	18/10/2012

This application is approved by:

Supervisor (if applicable):	A/Prof Genevieve Langdon	18/10/2012
HOD (or delegated nominee): *Final authority for all assessments with NO to all questions and for all undergraduate research.*	Prof Gerald Nurick (Acting HOD)	18/10/2012
Chair : Faculty EIR Committee For applicants other than undergraduate students who have answered YES to any of the above questions.		